brighton and sussex medical school

Brighton
ISMRM | British & Irish CHAPTER
2025

BIC - ISMRM 2025
30th Annual Meeting
British & Irish Chapter

Brighton & Sussex Medical School
University of Sussex, Brighton
9 - 11 September 2025

ISMRM | British & Irish CHAPTER

ABSTRACT BOOK

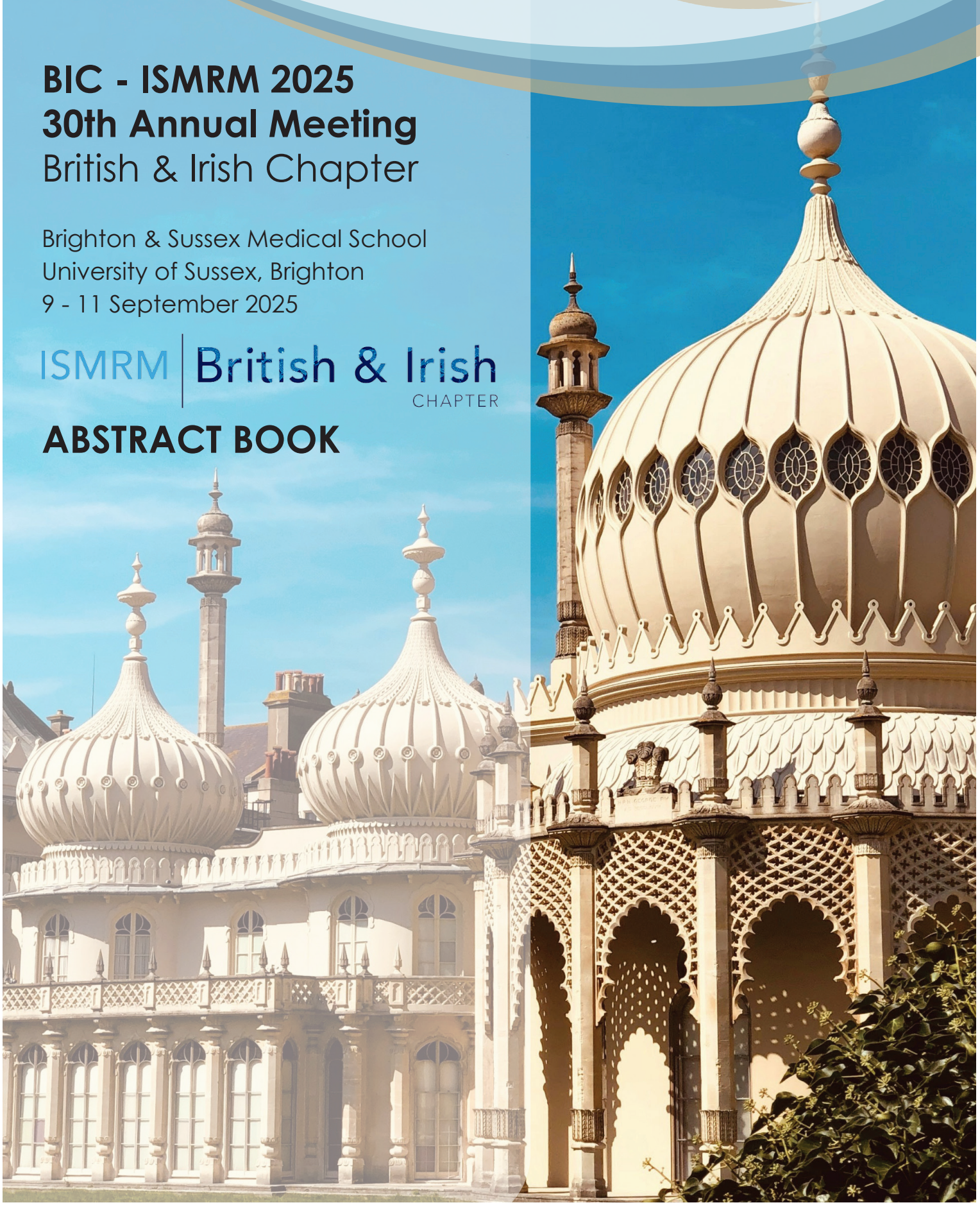

WELCOME

A warm welcome to all delegates to the 30th annual meeting of the British and Irish Chapter of the International Society of Magnetic Resonance in Medicine (BIC-ISMRM).

This year's meeting takes place on the verdant campus of the University of Sussex, and is hosted by the Brighton and Sussex Medical School (BSMS), a top-notch medical school sponsored by University of Sussex and University of Brighton. Since the inception of the Clinical Imaging Sciences Centre in 2006, both Universities as well as BSMS have been hubs for innovative MRI research. CISC has been a beacon of neuroimaging research, generating stellar research output that ranges from methodological innovations in quantitative MR to collaborative work with the vast and diverse group of neuroimaging researchers across both campuses. Collaborative research extends beyond campus limits, and CISC researchers are engaged in collaborations with groups across the country and abroad.

The meeting program reflects the vast range and high quality of MR research across the UK and Ireland: human, animal and in vitro systems; focus on brain, heart and a variety of other organs; from basic science to clinical applications; methodological innovations in acquisition, processing and analysis; a wide variety of observed nuclei and finally - a massive range of magnetic fields. There is something for everyone, and we hope that the annual meeting, as well as the workshop that precedes it, will fulfill their purpose as highly enjoyable opportunities to learn, network, meet old friends and make new ones.

We are thankful to the BIC-ISMRM board for choosing us to host the annual meeting of the BIC-ISMRM, and are looking forward to hosting all delegates and invited speakers in Brighton for this exciting event.

Prof. Itamar Ronen
Chair of the Local Organising Committee

OUR SPONSORS

Our sincere thanks to all of the sponsors of this annual meeting

GOLD

Multiwave Technologies

SIEMENS Healthineers

PHILIPS

NVISION

SILVER

Xiel. A MIS Healthcare company

GOLD STANDARD PHANTOMS

MR SOLUTIONS

GE HealthCare

skope

TeqRF RF Coil Innovation

BRONZE

tesla

Perspectum

WORKSHOP

BRUKER

SCIENTIFIC ADVISORS

Prof Itamar Ronen, Chair in Medical Physics &
Academic Director of the Clinical Imaging Science Centre, BSMS

Dr Nicholas Dowell, Associate Professor in Imaging Physics, BSMS

Dr Samira Bouyagoub, MRI Physicist, University of Sussex

Dr Anne Josset, Research Fellow in MR Physics, BSMS

LOCAL ORGANISERS

Matt Bemment, Senior Communications Officer, BSMS
Robyn Dillon, Senior MRI Radiographer & Clinical fMRI Lead, CISC
Kathy Sleigh, Administrator, CISC
Laura Arnold, Senior Administrator, Clinical Neuroscience, BSMS
Jan Bush, Head of Radiography, CISC
Juliet Kneller, Operations Officer, BSMS
Dawn Hanna, Senior Operations Manager, BSMS
Beatrice Ramunno, Research Coordinator, BSMS
Tyler Jones, Research Coordinator, BSMS
Louise Hopkins, Administrator, Clinical Neuroscience, BSMS
Ruby Loughman, Administrator, Clinical Neuroscience, BSMS
Dr Anne Josset, Research Fellow, BSMS
Kristen Jakobsen, PhD student, BSMS
Kennis Lau, Administrator, BSMS
Prof Andrew Dilley, Prof of Neuroanatomy &
Head of Clinical Neuroscience

DAY ONE
WORKSHOP

Advanced in vivo MRS Methods for Studying Metabolism, Physiology and Cytomorphology

Jeanine Prompers,

University Medical Center Utrecht
and Maastricht University,
The Netherlands

Advances in Phosphorus and Deuterium Metabolic Imaging: Paving the Way to Clinical Translation

Prof. Dr. Prompers is Professor of Organ-Specific Metabolic Imaging in the Department of Human Biology at the NUTRIM Institute of Nutrition and Translational Research in Metabolism of Maastricht University Medical Centre+. Her research focuses on the development of multi-nuclear MRS and MRI methods for the in vivo study of tissue metabolism in metabolic diseases. She has a strong track record on the application of ultra-high field MRS to measure energy and lipid metabolism in skeletal muscle, liver and heart, in particular in the setting of obesity-related diseases. She is one of the pioneers of deuterium metabolic imaging and was the first to perform this technique in human brain and liver at ultra-high field. Since 2024,
Prof. Prompers is also CEO of Scannexus, the ultra-high field MRI facility on the Brightlands campus in Maastricht. Prof. Prompers has published over 90 papers and has supervised 15 PhD students as (co-)promotor.

Assaf Tal,

Aviv University, Israel

Having the Spectroscopic Cake and Eating It Too: The Case for Multiparametric MRS

Prof. Assaf Tal graduated with a B.Sc. in physics from the Hebrew University in 2001 before gradually taking an interest in biomedical imaging and neurophysiology. Following a postdoctoral stay at NYU in 2013, he has served as a faculty member at the Weizmann Institute and NYU School of Medicine before recently joining the School of Biomedical Engineering at Tel-Aviv University in 2024, where his lab focuses on developing new MRS neuroimaging methodologies for understanding brain plasticity and motor learning, as well as measuring changes to cellular morphology and composition

Myriam M. Chaumeil,

Nvision Imaging Technologies, Germany & Ulm University, Germany & University of California San Francisco, USA

Advances in Hyperpolarized 13C MR: Emerging technologies and Applications in Neurological Disorders

Myriam Chaumeil is the Head of Research, HP MRI applied science, at NVision Imaging Technologies, as well as Adjunct Professor at the University of California San Francisco, and Honorary Professor at Ulm University. She received her PhD in Physics from the University of Paris-Sud. Her expertise is on developing and validating Hyperpolarized 13C-MR based methods for in vivo measurement of metabolism, in physiological and pathological conditions, in preclinical models and in patients. She has experience in studies of glioblastoma, Huntington's disease, Multiple Sclerosis, Alzheimer's disease, Traumatic Brain Injury, cerebral small vascular diseases and CNS lymphoma.

Paul Mullins,

Bangor University, UK

Using MRS to probe cerebral function and physiology - examples from research in hypoxia

Paul Mullins is Professor of Neuroimaging and Senior Physicist at the Bangor Imaging Centre in the School of Psychology and Sports Science.

Paul's research falls into three broad areas: the use of magnetic resonance imaging and spectroscopy to investigate basic neurologic and physiologic processes in health and disease; the use of these techniques to measure changes associated with neurotransmission and neural activity in health and disease; and investigating the impacts of physiologic challenges (e.g. hypoxia, concussion, exercise) on the brain.

Paul also interacts with colleagues from the College of Medicine and Health Sciences on MRI study design, data acquisition and processing and the resources available to help with their research questions, and his aim is to keep the Bangor Imaging Unit a world-class centre for neuroimaging research in North Wales.

Itamar Ronen,

Brighton and Sussex Medical School, UK

And Yet They Move – What Does Metabolite Diffusion Tell Us About Cell Structure and physiology?

Itamar obtained his PhD in Physical Chemistry from Tel Aviv University, where he worked with on developing a method for indirect NMR detection of 17-O with potential for metabolic imaging. He did his post-doctoral research at the Centre for Magnetic Resonance Research at the University of Minnesota, where he developed a strong interest in diffusion-based contrast in MR. Itamar obtained his first academic position at the Boston University School of Medicine, where he developed an interest in metabolite diffusion as potential marker for cell-specific microstructure and metabolism. In 2009 Itamar moved to the Netherlands, where he joined the Gorter Center for MRI at the Leiden University Medical Center (LUMC) as Associate Professor of Radiology, developing spectroscopic methods for ultrahigh and ultralow field MR. He moved to Brighton in the UK in 2021, where he holds the positions of Academic Director of the Clinical Imaging Science Centre (CISC) and Chair in Medical Physics at the Brighton and Sussex Medical School.

DAYS TWO & THREE
Annual Meeting

Plenary Speaker:

Bill Moore Lecture:
Prof Mark Lythgoe,
University College London

Prof Mark Lythgoe is the Founder and Director of the Centre for Advanced Biomedical Imaging (CABI) at UCL, which is a multidisciplinary research centre for experimental imaging. The Centre now hosts 12 state-of-the-art imaging modalities and 50 researchers. Mark is also Deputy Director of the UCL Department of Imaging and Director of Biomedical Imaging Research at the Francis Crick Institute.

Mark has a long-standing track record in the development and application of biomedical imaging techniques and has been awarded £45 million for his collaborative programme of imaging research. He has published over 300 papers including publications in Nature, Nature Photonics, Nature Medicine and The Lancet. Mark has translated his research findings into clinical radiological practice and established a training programme with University College Hospital in biomedical imaging. He is Co-director of MSc in Advanced Biomedical Imaging and Co-founder the UCL Centre for Doctoral Training in Medical Imaging.

In 2023, Mark was awarded the prestigious IET Achievement Medal for a major and distinguished contribution in Medical Imaging; the award was presented at the 'Global Engineering Oscars' by the Institution of Engineering and Technology. In 2021, Mark received the Royal Society of Medicine Ellison–Cliffe Award, for his contribution of fundamental science to the advancement of medicine. In 2013 Mark received the Davies Medal from the Royal Photographic Society for a significant contribution to the field of imaging science. Mark has also received the Alumni Achievement Award, which is given to the University of Salford's most notable and successful graduates.

Mark is committed to the public engagement of science. During his tenure as Director of the Cheltenham Science Festival, it has become one of the largest science festivals in the world. For his contributions to communicating science, Mark was awarded the Neuroscience Prize for Public Understanding from the British Neuroscience Association, Dorothy Hodgkin Award, Biosciences Federation Science Communication Award and was made a Fellow of the British Science Association.

Session Moderators

Session 1: MRI & MRS: Brain Physiology

Laura Parkes,
University of Manchester

With a background in both physics (MPhys Oxford, 1997) and neuroscience (MSc, UCL 1999) **Laura's** research is focussed on developing novel methodology to study brain function. Following a PhD on quantitative measurements of cerebral blood flow (UCL, 2002), Laura moved to the Netherlands to |complete postdoctoral research using fMRI and MEG. In 2005 she returned to the UK, first to the University of Liverpool and, since 2008, the Manchester University. One principle area of reseach concerns mechanisms of brain plasticity following a New Investigators Award from the Medical Research Council in 2006. Laura continues to study the cerebro-vascular system, and has developed quantitative measurements of cerebral blood flow, microvessel structure, oxygen metabolism and blood-brain barrier integrity. Key applications are in ageing, cerebral small vessel disease, stroke, Parkinson's disease and Alzheimer's Disease with an aim to understand mechanisms of cognitive decline.

Session 2: MRI: Image Analysis and Machine Learning

Ivor Simpson,
University of Sussex

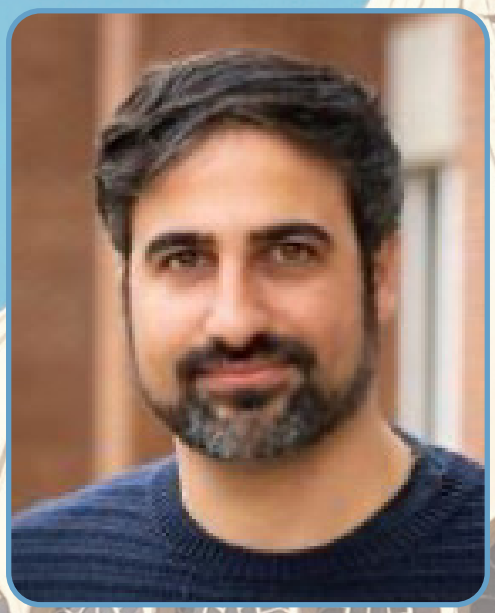

Ivor is an Associate Professor in Artificial Intelligence within the AI research group in the department of Informatics. He is also the Academic Lead for Sussex AI and the convenor of the MRes in Advanced Artificial Intelligence.

Ivor's research focuses on the development of novel machine learning and statistical inference methodologies applied to imaging and temporal data, with a particular interest in applications in medical image analysis, computer vision and ecological monitoring. Ivor's team aims to create methods that reliably characterise the uncertainty in predictions, require fewer labelled data, and offer a greater degree of interpretability than classic deep learning approaches. He is currently the primary supervisor for 6 PhD students in these areas, and secondary supervisor for several others. Much of Ivor's research requires interdisciplinary collaboration, and he works closely with a variety of colleagues across the university and externally. He is also open to new academic and industrial collaborations in areas related to his research.

Session 3: MRI and MRS: Preclinical Studies and Cancer

Bernard Siow,
Francis Crick Institute

Dr. Bernard Siow is the Head of MRI at the In Vivo Imaging (IVI) facility at the Francis Crick Institute, where he oversaw the design and development of the MRI unit and the installation of its preclinical scanner. His passion lies in using the principles of MRI physics to push the boundaries of diffusion MRI and microstructure imaging to answer fundamental biomedical questions. He has a particular interest in developing advanced techniques, including double diffusion encoding and diffusion-weighted magnetic resonance spectroscopy. Given the breadth of cancer expertise and research at the Crick, he has found this collaborative environment particularly enriching for his work.

Session 4: MRI, MRS and other modalities: Neuro

Harish Poptani,
University of Liverpool

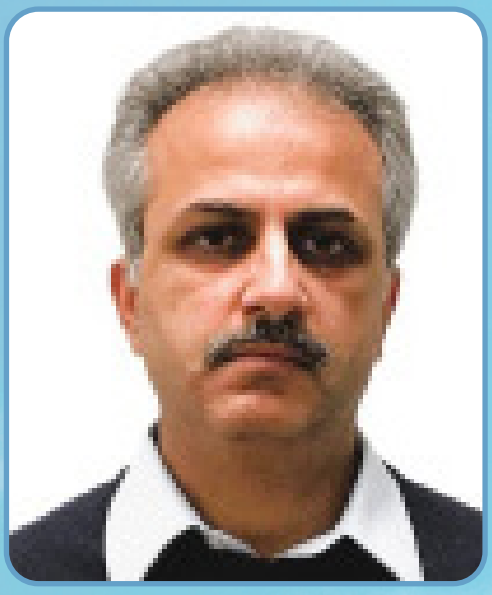

Professor Poptani is the Chair of the Centre for Preclinical Imaging (CPI) at the University of Liverpool with a research focus on developing cutting-edge non-invasive imaging biomarkers for assessing early treatment response in cancer. His work is highly translational in nature and his group has been credited with identifying several imaging markers for diagnosis or early treatment response which are currently used in the clinic.

He has published 162 papers and was awarded the Senior Fellowship from the International Society of Magnetic Resonance in Medicine (ISMRM) for his significant contributions to the field in 2021. He currently serves as the Chair of the British and Irish chapter of ISMRM. His research has been funded by various grants including funding from the UKRI as well as UK based charities such as the Wellcome Trust and the North West Cancer Research.

Session 5: Body MRI and MRS

MODERATOR: **Jeanine Prompers** (See Workshop for bio)

Session 6: Hardware, pulse and protocol design

Mara Cercignani,
Cardiff University

Professor Mara Cercignani is Head of MRI at the Cardiff University Brain Research Imaging Centre. She earned her engineering degree from Politecnico di Milano and her PhD from University College London. Her expertise lies in quantitative MRI—especially diffusion MRI and magnetization transfer imaging—with a focus on translating imaging physics into clinical applications. Her research spans neurodegeneration, neuroinflammation, and psychiatric conditions.

Since 2019, Professor Cercignani has been a Senior Fellow of the International Society for Magnetic Resonance in Medicine (ISMRM) and has served as a Deputy Editor for Magnetic Resonance in Medicine since 2014. She has published over 200 papers in peer-reviewed journals, and several book chapters. She edited the text "Quantiative MRI of the Brain: Principles of Physical Measurement".

ORAL ABSTRACTS

In order of programme

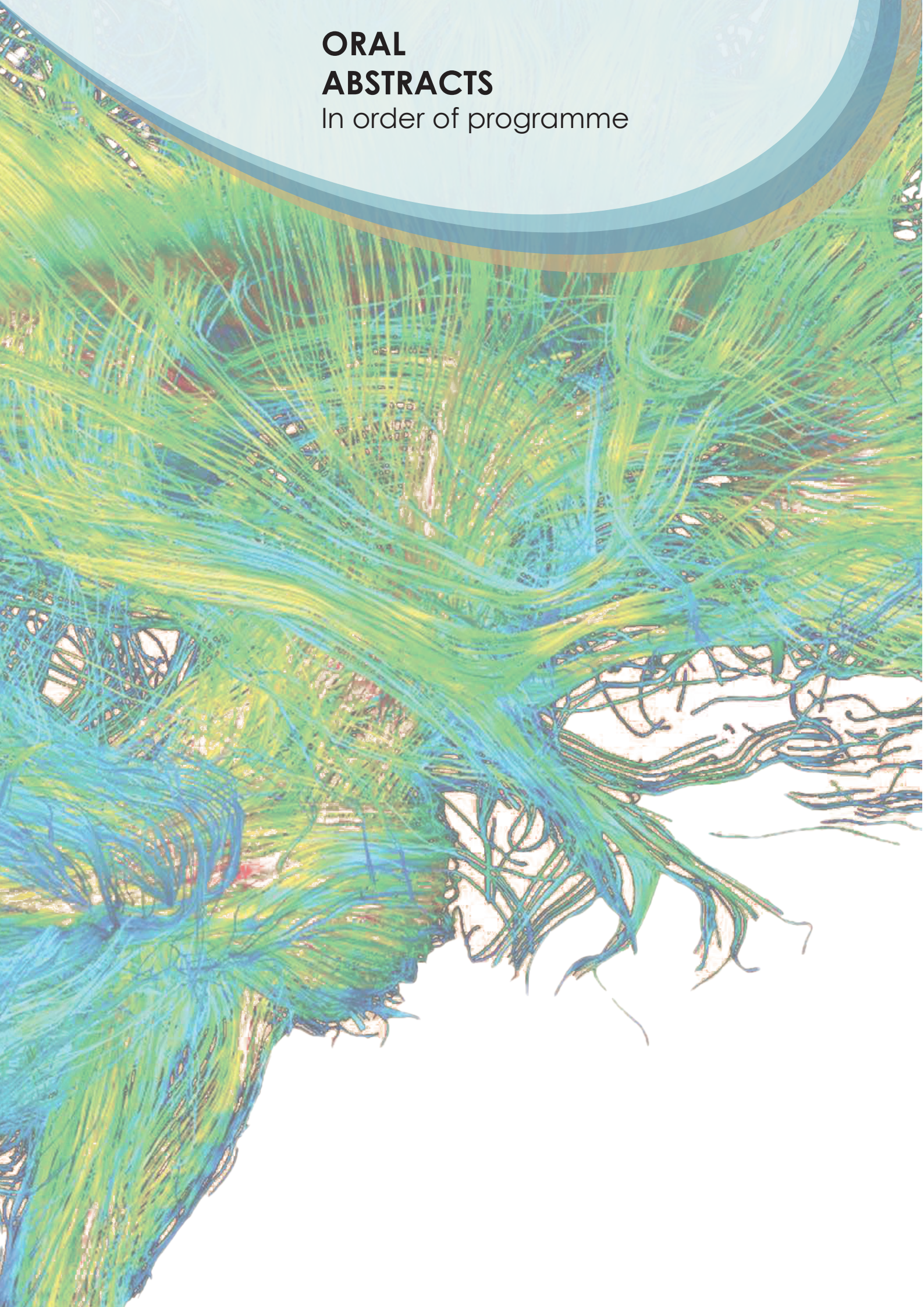

Evaluation of Single Breath-Hold Calibrated fMRI for Baseline $CMRO_2$ and OEF Measurement in Grey Matter.

Elizabeth J. Fear[1,2], Davide Di Censo[1,2], Sara Pomante[1,2], Francesca Graziano[1,2], Manuela Carriero[1,2], Stefano Censi[1,2], Emma Biondetti[1,2], Alessandra S. Caporale[1,2], Valentina Tomassini[1,2], Antonello M. Chiarelli[1,2], Richard G. Wise[1,2]

[1]Department of Neuroscience, Imaging, and Clinical Sciences, University G. d'Annunzio of Chieti-Pescara, Chieti, Italy

[2]Institute for Advanced Biomedical Technologies (ITAB), University G. d'Annunzio of Chieti-Pescara, Chieti, Italy

Introduction: The cerebral metabolic rate of oxygen consumption ($CMRO_2$) is a key indicator of neuronal activity energy expenditure whilst oxygen extraction fraction (OEF) represents the fraction of oxygen extracted from the blood by the brain, reflecting the balance between oxygen supply and demand. These two parameters may be altered in neurological conditions where blood supply or oxygen metabolism is compromised [1].

The recently developed technique of breath-hold calibrated fMRI (BHC-fMRI) can be used to map $CMRO_2$ and oxygen extraction (OEF) in the human brain [2]. Measurements of BOLD and arterial spin labelling (ASL) cerebral blood flow (CBF) signals are made during repeated BHs that induce cyclic hypercapnia and thus vasodilation. An oxygen transport model combined with a phenomenological model of the BOLD signal are used to estimate OEF and $CMRO_2$. We have previously demonstrated the use of a dual excitation pseudo-continuous arterial spin labelling (DEXI)pCASL sequence enabling simultaneous BOLD and ASL acquisitions during 10 BH repetitions over an 11-minute acquisition window [3]. This approach provides robust mapping of $CMRO_2$ without the need for external gas challenges. Here we investigate the possibility of estimating global grey matter (GM) OEF and $CMRO_2$ from single breath-holds with the aim of reducing acquisition times and understanding the stability of the estimated parameters. Eventually a streamlined approach would minimise participant burden, thereby increasing tolerance and compliance in patient populations.

Methods: ***MRI acquisition:*** Data were acquired on 53 healthy subjects (26 females, 27 males; age: 33 ± 6 years) using a 3T MAGNETOM Prisma scanner (Siemens Healthineers AG, Forchheim, Germany) with a 32-channel receive-only head coil. The protocol included a T1-weighted MP2RAGE scan for anatomical reference (1mm isotropic resolution), an Inversion Recovery (IR) sequence with GE-EPI readout to calculate haemoglobin concentration from the blood of the sagittal sinus and a DEXI pCASL acquisition to collect, during BH cycles, simultaneous ASL (TE1=10 ms) and GE-EPI BOLD (TE2=30 ms) data in the transverse plane (TR=4400ms, FA=90°, matrix=64*64*15, res=3.4*3.4*7mm, GRAPPA=3, PF=1, Labelling duration=1500ms, Post labelling delay=1500ms). Pre-labelling saturation and two inversion pulses for background suppression were included. M_0 images were acquired in blip-up/blip-down modality for field distortion correction. Subjects performed 10 repeated BHs with a 20s/40s BH/recovery cycle. CO_2 and O_2 end-tidal traces were recorded using a nasal cannula through a sampling line into a gas analyser system (ADInstruments, Dunedin, New Zealand). Resting data were collected for 44s before BHs began to enable estimation of baseline CBF. ***MRI pre-processing:*** MP2RAGE was used for spatial normalization into MNI space using Syn transformations (antsRegistration, ANTs) and for tissue segmentation (FAST, FSL). The two M_0s were used for susceptibility distortion (Topup,FSL) and intensity correction (N4biasfieldcorrection, ANTs). The M_0 corrected image was registered with the T1-weighted image and the transformation matrix inverted to bring the grey matter (GM) partial volume into the M_0 space and thresholded at 0.5 to obtain a GM mask. GE BOLD-ASL fMRI images were preprocessed using FSL-FLIRT for motion correction. The motion corrected versions were registered to M_0 and then distortion corrected (ApplyTopup,FSL). ***$CMRO_2$ and OEF analysis:*** BOLD/ASL data and CO_2 end-tidal partial pressure ($P_{ET}CO_2$) traces collected during repeated BH were truncated into individual BHs, corresponding to data samples of 60s, and used to calculate $CMRO_2$ and OEF in the GM using a modified Davis model [2] with both the global BOLD signal and $P_{ET}CO_2$ traces used as separate regressors to identify BH induced signal variation.

Results: Results show (Fig.1a) mean $CMRO_2$ = 110.3±2.3 µmol/100g/min (BOLD-regressor) and 108.8±2.3 µmol/100g/min ($P_{ET}CO_2$-regressor) and (Fig.1b) mean OEF = 0.346±0.006 (BOLD-regressor) and 0.338±0.006 ($P_{ET}CO_2$-regressor) across the 10 individual BHs. These are compared with values of OEF = 0.366±0.007 (BOLD-regressor) 0.356±0.007 ($P_{ET}CO_2$-regressor) and $CMRO_2$ = 120.3±2.5 µmol/100g/min (BOLD regressor) 118.1±2.6 µmol/100g/min ($P_{ET}CO_2$-regressor) using the combined 10 BHs together.

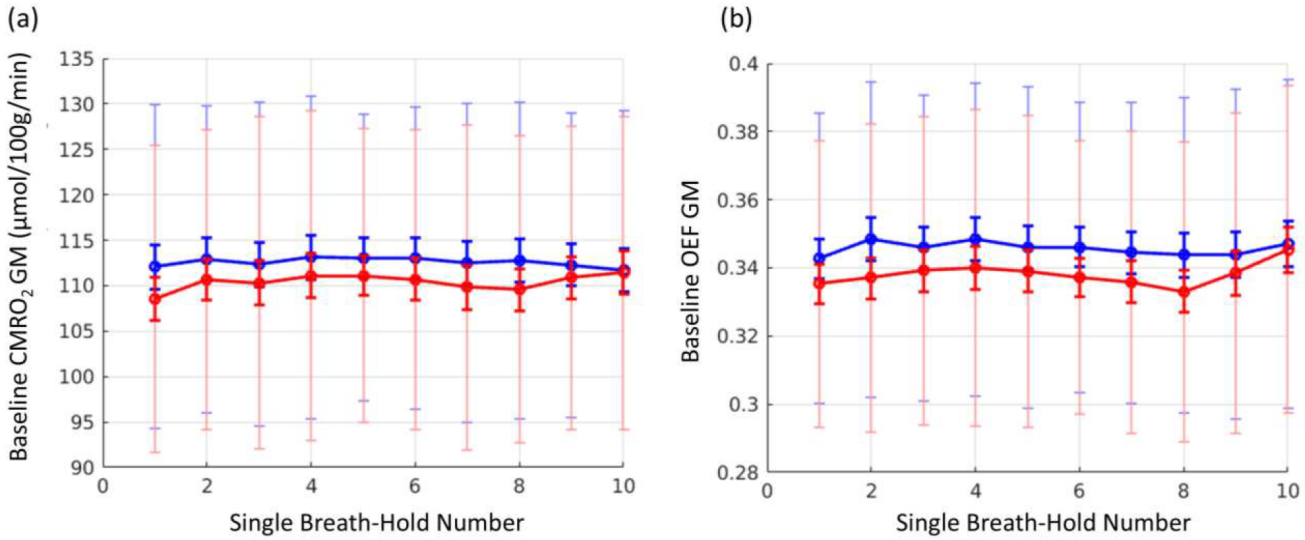

Fig. 1. Calculated baseline $CMRO_2$ and OEF average values across GM using calibrated fMRI data from 10 single BHs across 53 healthy controls. (a) $CMRO_2$ and (b) OEF calculated using individual breath-holds (1-10) using the BOLD signal as regressor (blue) and $P_{ET}CO_2$ as regressor (red) for identifying BH-induced signal variation. Light colours identify standard deviation, and bold colours identify standard error values across subjects

Discussion: The relative consistency of global grey matter $CMRO_2$ and OEF values calculated using each single BH suggests that one BH may be sufficient. However, there is a small bias (approximately 6% underestimate) when comparing to estimates made from all 10 BHs together. The agreements between estimates achieved using the global BOLD signal as a regressor and those using $P_{ET}CO_2$ as regressor to identify BH-induced signal variation, suggest that CO_2 monitoring may not be essential. The quality of OEF and $CMRO_2$ maps from single breath-holds remains to be explored.

Conclusions: We present a simplified protocol that permits estimation of absolute baseline of $CMRO_2$ and OEF in global GM using just one BH potentially without CO_2 monitoring, which would greatly decrease MRI scan time and the demands made on participants undergoing the procedure.

Acknowledgements: Funding provided by the following projects:

1) European Union-NextGenerationEU (NGEU)- Italian Ministry of University and Research (MUR), National Plan for Recovery and Resilience (PNRR) and Projects of National Relevance (PRIN), Project Code: P2022ESHT4, Project Title: "Advancing MRI biomarkers of brain tissue microstructure and energetics in Multiple Sclerosis." Funding call No. 1409 of 14.09.2022, Concession decree No. 1367 of 01.09.2023 adopted by MUR, ERC Panel LS5 "Neuroscience and Disorders of the Nervous System". CUP: D53D23019210001; 2) NGEU PNRR, Mission 4 Component 2 – M4C2, Investment 1.5 – Call for tender No. 3277 of 30.12.2021 MUR Award Number: ECS00000041, Project Title: "VITALITY - Innovation, digitalization and sustainability for the diffused economy in Central Italy," Concession Decree No. 1057 of 23.06.2022 adopted by MUR. CUP D73C22000840006; 3) NGEU MUR, Research National Program (PNR) and PRIN, Project Code: 2022BERM2F, Project Title: "Mapping Mitochondrial Function and Oxygen Metabolism in the Human Brain with Magnetic Resonance Imaging." Funding call No. 104 of 02.02.2022, Concession decree No. 1065 of 18.07.2023 adopted by MUR, ERC Panel LS7 "Prevention, Diagnosis and Treatment of Human Diseases". CUP: D53D23013410001

References

[1] D. Paling, X. Golay, C. Wheeler-Kingshott, R. Kapoor, D. Miller. *J Neurol.* **258**(12), 2113–2127 (2011)

[2] A. M. Chiarelli, M. Germuska, H.L. Chandler, R. Stickland, E. Patitucci, E. Biondetti, D. Mascali, N. Saxena, S. Khot, J. Steventon, C.Foster *et al.*, *J Cereb Blood Flow Metab.***42**(7), 1192–1209 (2022)

[3] I. D. Driver, A. M. Chiarelli, H. L. Chandler, H. Thomas, S. Manolova, H. Lu, R.G. Wise, M. Germuska, *Imaging Neurosci (Camb)*, **2**, 1–14 (2024)

Resting-State Functional Electrical Properties Tomography (rsfEPT)

Jierong Luo and Karin Shmueli
Department of Medical Physics and Biomedical Engineering, University College London, London, United Kingdom

Introduction: Tissue electrical conductivity can be calculated from non-invasive measurements of the B_1 transceive phase using MR electrical properties tomography (EPT) [1]. Recent advances have enabled EPT to characterise tissue conductivity distributions in healthy and diseased brains in vivo [2]. Although the underlying neurophysiological substrates remain unclear, functional EPT (fEPT) has revealed repeatable task-evoked activations and showed patterns distinct from conventional BOLD fMRI [3-6]. Influenced by dynamic changes in the concentration and mobility of intra- and extracellular ions [1, 7-9], fEPT time-series acquired in the resting state may reveal unique neuronal networks in the brain. Therefore, we present the first resting-state fEPT (rsfEPT), using both seed-based and independent component analysis (ICA).

Methods: Data acquisition: 70 multi-echo (ME) 2D GRE-EPI [10] volumes were acquired in three healthy volunteers (HVs) at 3T (Prisma, Siemens) using a 64-channel head coil with: GRAPPA=4, MB=3, TR=4034 ms, TEs=15.6, 41.6, 67.6 ms, and 1.3-mm isotropic resolution. Structural T1-weighted images were acquired using MPRAGE. Image processing for each volume: Magnitude echo images were combined [11] for optimal BOLD contrast sensitivity. The transceive phase (φ_0) was calculated from the complex ME-EPI data by non-linear fitting [12] and extrapolation, followed by unwrapping [13] and slice-to-slice artifact correction [14]. EPT maps were then calculated from φ_0 using integral-form MagSeg [15] using T1-weighted images for magnitude weighting and GM/WM/CSF segmentation [16], to preserve boundaries and minimise noise (Fig. 1). Functional analysis using seed-based connectivity and ICA: Echo-combined magnitude image volumes were aligned to the first volume [17], and the same transformation was applied to register the EPTs. For each subject, seed-based connectivity analysis was performed using CONN toolbox [18], and ICA was performed using FSL MELODIC [19] on skull-stripped [20] rsfMRI and rsfEPT data. All data were spatially and temporally filtered with default settings. Comparison of rsfMRI and rsfEPT: rsfMRI and rsfEPT networks and ROI-to-ROI connectivity derived from the seed-based analysis were compared. For ICA, the default mode network (DMN) in rsfMRI was identified according to [21], and DICE scores of spatial overlaps between the DMN and each independent component (IC) in rsfEPT (both defined as regions with |z|-score > 3) were calculated for each HV. For each IC, the maximum peak height and its frequency were extracted from the power spectrum, and the number of peaks were calculated as the number of local maxima in the spectrum. Any difference in these measurements between rsfMRI and rsfEPT was tested using a two-sample t-test ($p<0.01$).

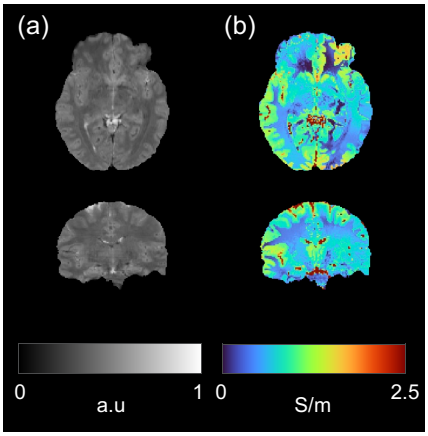

Fig. 1. (a) Echo-combined magnitude image and (b) reconstructed EPT.

Results and discussion: For rsfMRI, seed-based connectivity revealed the DMN in all subjects, while for rsfEPT the medial prefrontal cortex seed was mainly correlated with the frontal brain grey matter, with fewer correlations extending to the posterior cingul ate cortex and angular gyrus (Fig. 2). Compared the rsfMRI, the ROI-to-ROI

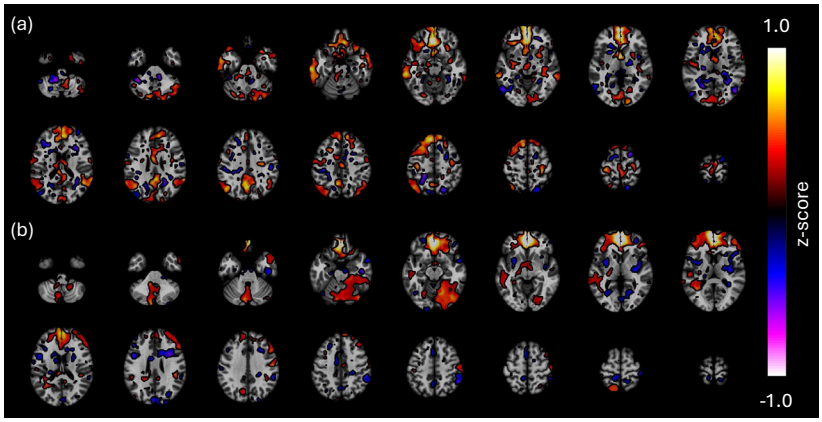

Fig. 2. Seed-based (a) rsfMRI and (b) rsfEPT connectivity with a seed in the medial prefrontal cortex (DMN) from a healthy volunteer.

connectivity matrices showed overall weaker connectivity in rsfEPT in HVs (Fig. 3).

Using ICA, we identified more ICs in rsfEPT (39, 42 and 52) than in rsfMRI (21, 12 and 10) for each subject, respectively. The DMN [18] was observed in rsfMRI, but ICs in rsfEPT did not show a spatial distribution comparable to the DMN, illustrated by the low DICE scores (<0.25) between the rsfMRI DMN and rsfEPT ICs (Fig. 4a). In all HVs, ICs found in rsfEPT showed significantly weaker peak powers ($p<0.01$), compared with ICs in rsfMRI (Fig. 4b). We found rsfMRI ICs had relatively low frequencies, while the frequency of rsfEPT ICs showed broader spectra (Fig. 4c).

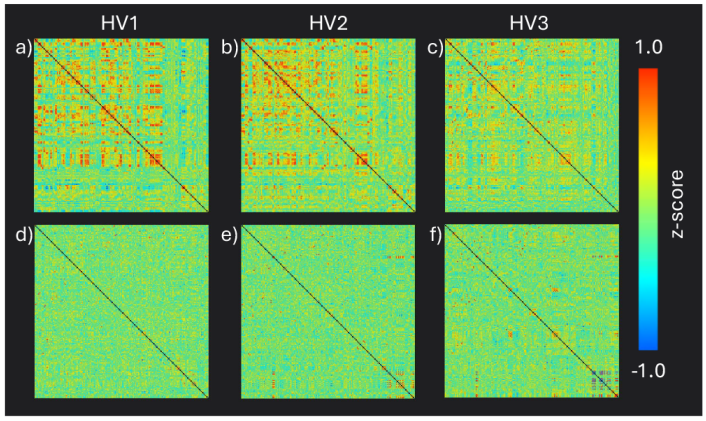

Fig. 3. ROI-to-ROI matrices of (a-c) rsfMRI and (d-f) rsfEPT from all three healthy volunteers (HV1-3).

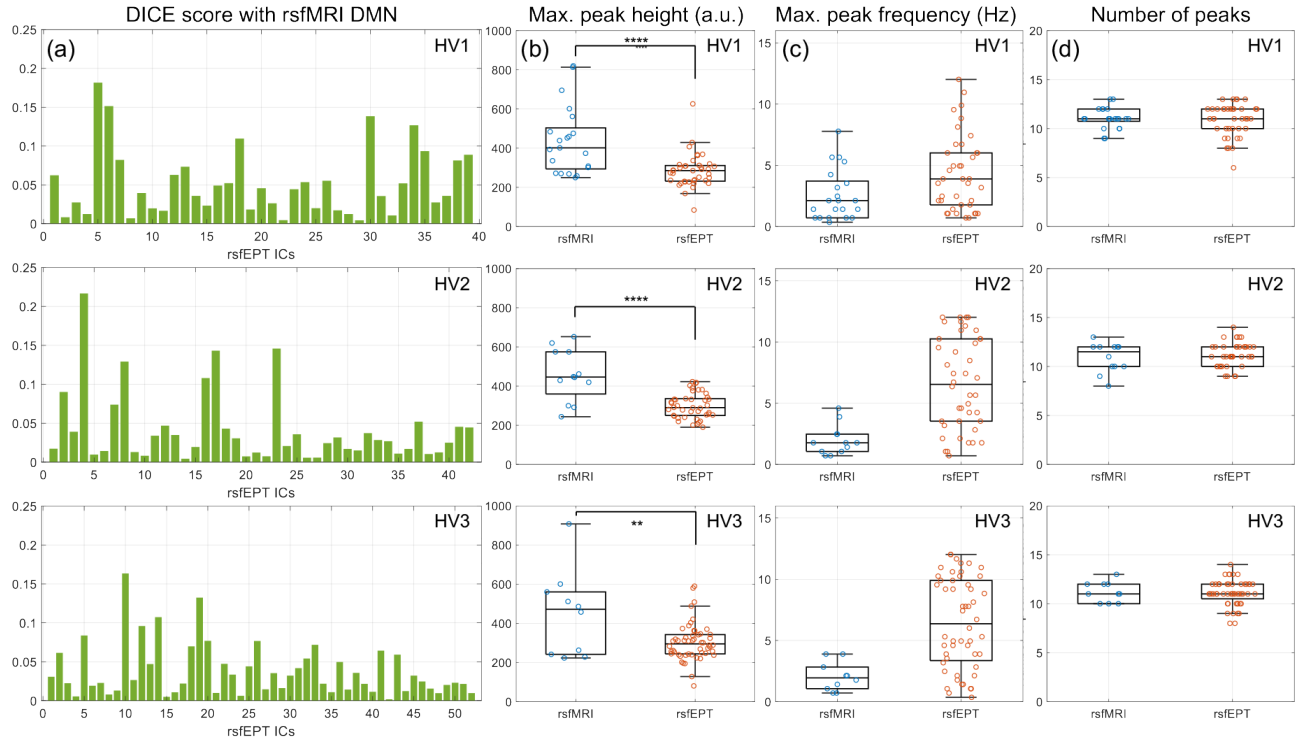

Fig. 4. Comparison between rsfMRI and rsfEPT in each healthy volunteer (HV1-3): (a) DICE similarity score between the rsfMRI default mode network (DMN) and each independent component (IC) found in rsfEPT. (b-d) Comparison between rsfMRI and rsfEPT ICs in terms of (b) maximum peak height, (d) frequency of the maximum peak, and (d) total number of peaks found in each IC. **p<0.01, ****p< 0.0001.

Conclusions: We demonstrated rsfEPT for the first time in three healthy subjects using both seed-based analysis and ICA. Compared with simultaneous rsfMRI, seed-based connectivity and ICA of rsfEPT showed different connectivity patterns, although with some similarity to the DMN. Future studies with larger cohorts are needed to further investigate rsfEPT.

References: [1] U Katscher, et al. NMR Biomed. 2017. [2] AL van Lier, et al. Magn Reson Med. 2014. [3] J Cao, et al. Phys Eng Sci Med. 2024. [4] M Helle, et al. Proc ISMRM 2019; 3759. [5] R Schmidt. Proc ISMRM 2019; 3777. [6] KJ Jung, et al. Proc ISMRM 2023; 0922. [7] AE Hoetink, et al. IEEE Trans Biomed Eng. 2004. [8] N Antonov, et al. Clin Hemorheol. Micro. 2008. [9] RL Gaw, et al. IEEE Trans Biomed Eng. 2008. [10] OC Kiersnowski, et al. Proc ISMRM 2024; 188. [11] B A Poser, et al. Magn Reson Med. 2006. [12] T Liu, et al. Magn Reson Med. 2012. [13] A Karsa, et al. IEEE Trans Med Imaging. 2018. [14] OV Arsenov, et al. Proc ISMRM 2024, 3675. [15] A Karsa, et al. Proc ISMRM 2021; 3774. [16] J Ashburner, et al. Neuroimage. 2005. [17] S Ourselin, et al. Image and Vision Comp. 2001. [18] S Whitfield-Gabrieli et al. Brain Connect. 2012. [19] CF Beckmann, et al. IEEE Trans Med Imaging. 2004. [20] SM Smith. Hum Brain Mapp. 2002. [21] SM Smith, et al. PNAS 2009.

Complex-Valued Magnetic Resonance Fingerprinting for Simultaneous Estimation of Magnetic Field Perturbations and Transverse Relaxation

Kevin McNally,[1] Patrick S. Fuchs,[1] Karin Shmueli,[1] Matthew T. Cherukara[1]
[1]*Department of Medical Physics and Biomedical Engineering, University College London, London, UK*

Introduction: Quantitative susceptibility mapping (QSM) uses the complex MRI signal to calculate distributions of magnetic susceptibility [1]. QSM reconstruction involves multiple processing steps, and these stages are susceptible to error propagation. Magnetic resonance fingerprinting (MRF) is a quantitative technique that enables simultaneous estimation of multiple tissue properties through MR signal pattern recognition [2]. We applied an MRF technique to complex-valued MRI data (CV-MRF) to simultaneously estimate transverse relaxation rate (R_2^*) and frequency (proportional to magnetic field) perturbations (Δf) which are the required input for QSM reconstruction. Here, we validated CV-MRF using a digital phantom, and compared it with recommended methods *in vivo*.

Methods: The observed complex-valued MR signal from a multi-echo GRE sequence is given by:

$$S(TE) = M_0 \cdot e^{-R_2^* \cdot TE + i(2\pi\Delta f \cdot TE + \phi_0)} \quad (1)$$

where M_0 is the signal magnitude and ϕ_0 is the phase offset, both at $TE = 0$. Typically, R_2^* is estimated by fitting the magnitude of this complex signal over TEs, and Δf (and ϕ_0) is estimated from the phase. For CV-MRF, a dictionary was generated by simulating MR signals (Eq. 1) for all combinations of R_2^* in the range 10:1:70 s^{-1} and Δf in the range −100:1:100 Hz, for the required TE values. For pattern matching, the dot product was used to compare the normalised MR signal from each voxel with every dictionary entry to identify the best match.

For validation, a 128×128 synthetic MR image was simulated using a digital phantom [3], with R_2^* and Δf values assigned to regions in the range 10:1:70 s^{-1} and −50:1:50 Hz respectively, for echo times between 0 and 50 ms. Gaussian noise was added to the real and imaginary signal components independently for SNR levels 0:10:100 dB. In vivo data were acquired from a healthy volunteer (male, aged 32 years) under local ethics committee approval, using a 3T Siemens Prisma. 3D multi-echo GRE was acquired, at 1 mm isotropic resolution, with 5 echoes ($TE_1 = \Delta TE = 4.92$ ms), aligning with consensus recommendations [4]. A T_1-weighted MP-RAGE data set was also acquired for tissue segmentation, performed using FSL FAST [5]. CV-MRF was compared against consensus recommended methods: R_2^* estimation using auto-regression on linear operators (ARLO) [6], and Δf estimation using non-linear complex field fitting (NLCFF) from the MEDI toolbox [7].

Results: Fig. 1 shows CV-MRF against ground truth results in the digital phantom at SNR = 30 dB. Mean percentage error (MPE) was 0.05% and 0.01% in R_2^* and Δf respectively. Between 0 and 20 dB, MPE increased noticeably, reaching 30.4% and 1.8% for R_2^* and Δf respectively at SNR = 0 dB.

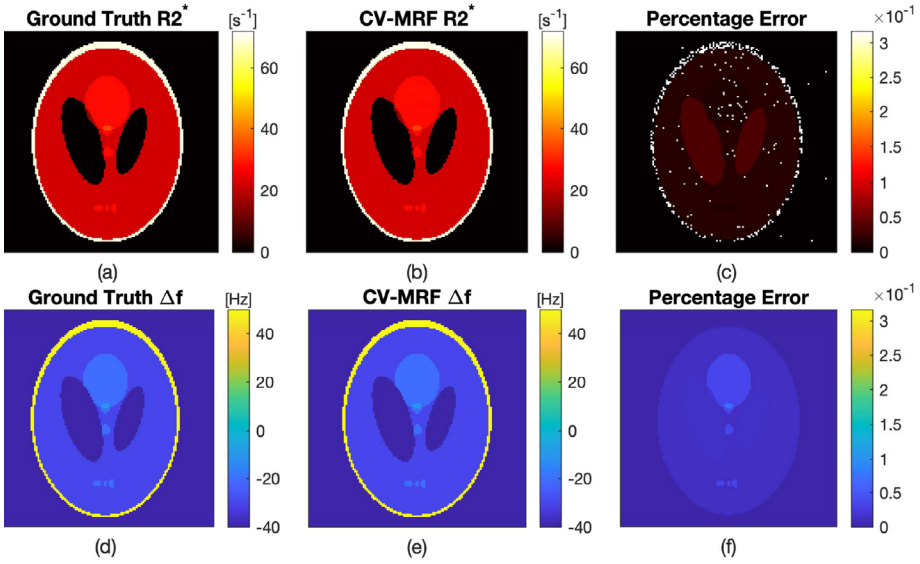

Fig 1. CV-MRF vs ground truth results in the digital phantom.

Fig. 2 shows in vivo results of CV-MRF and recommended methods. Across the brain, the MPE between the methods was 0.01% and 1.87% in R_2^* and Δf respectively. There were no significant differences in estimates of R_2^* and Δf in white matter, but CV-MRF estimated significantly higher R_2^* values than ARLO, and significantly lower Δf than NLCFF, in both CSF and grey matter.

In the in vivo data set, consensus methods ran in 127 seconds (ARLO: 7.4s; NLCFF: 120s), whereas CV-MRF took 112 seconds (dictionary generation: 0.85s; pattern matching: 111s).

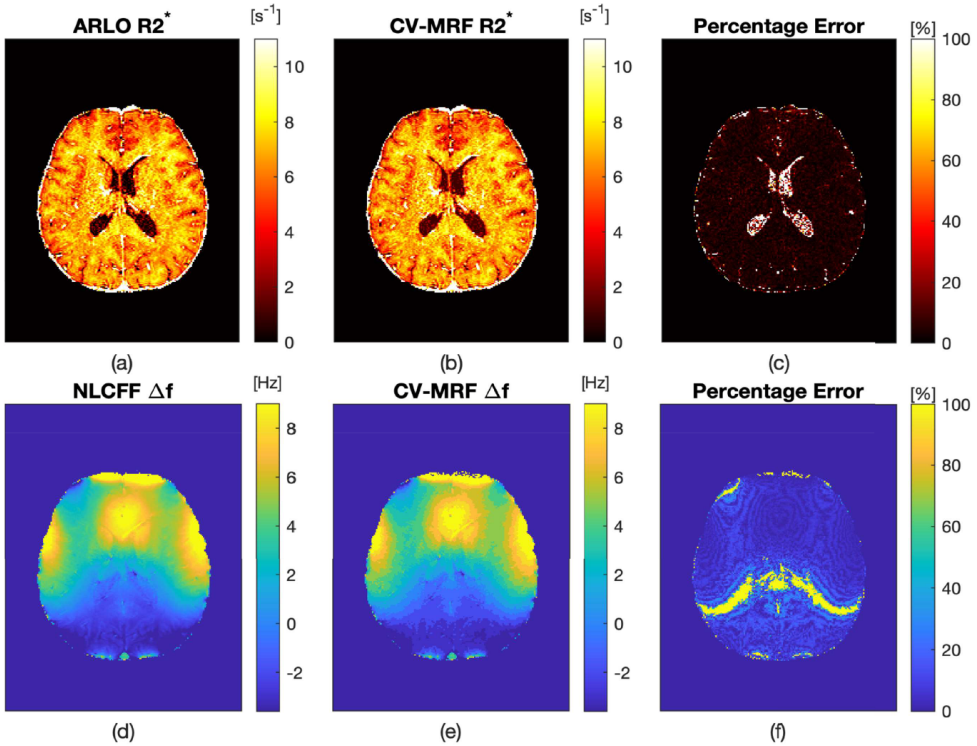

Fig 2. R_2^* and Δf using CV-MRF vs consensus methods in a healthy volunteer.

Discussion: Using the complex MR signal model (Eq. 1), we implemented a dictionary matching method (CV-MRF) to estimate R_2^* and Δf from complex-valued multi-echo GRE data. The performance of the method was demonstrated in synthetic data with ground truth R_2^* and Δf. CV-MRF was able to recover these values with high accuracy, under typical SNR conditions. At higher noise levels, the accuracy of CV-MRF decreased, in line with results found using other dictionary-based methods [8].

When applying CV-MRF in a healthy volunteer, only minor differences were seen between CV-MRF results and those from currently used methods. Notably, elevated percentage errors were observed in a region where Δf values approached zero. Differences were more pronounced in CSF and grey matter but were not significant in white matter. Despite these modest differences, the CV-MRF method provides robust parameter estimates that correlate closely with estimates from current widely used methods.

CV-MRF also provided an improvement in run time of 12%, relative to combined ARLO and NLCFF. CV-MRF computation times for dictionary generation and pattern matching are consistent with other studies of dictionary-based parameter estimation in other applications [8].

The CV-MRF method is limited by the model in Eq. 1. It represents an idealised case and does not account for differences in T1 (which may limit accuracy across tissue types) or for the presence of a phase offset ϕ_0. Incorporating the latter would offer the possibility of using CV-MRF within phase-based electrical properties tomography [9]. Validation of CV-MRF in a broader range of synthetic and in vivo datasets is also necessary.

Conclusions: Here we developed CV-MRF: a dictionary matching approach to determine R_2^* and Δf from complex multi-echo GRE data. CV-MRF parameter maps are closely comparable with those obtained from current methods, and there is significant potential for expanding the method to other parameters.

References

[1] Shmueli K, 2020. *Quantitative Magnetic Resonance Imaging*, pp.819-838.
[2] Ma D, et al., 2013. *Nature* 495: 7440.
[3] Jain A, 1989, *Fundamentals of Digital Image Processing*, p.439.
[4] Bilgic B, et al., 2024. *Magn. Reson. Med.* 91(5): 1834-1862
[5] Zhang Y, et al., 2001. *IEEE Trans. Med. Imag.* 20(1): 45-57
[6] Pei M, et al., 2015. *Magn. Reson. Med.* 73(2): 843-850.
[7] Liu T, et al., 2013, *Magn. Reson. Med.* 69(2): 467-476.
[8] Ghodasara S, et al., 2020. *Sci. Rep.* 10(1): 10210.
[9] Katscher U, et al., 2017. *NMR Biomed.* 30(8): 3729.

Regional Neurometabolic Responses to Intermittent Hypoxia

Ferrida Ponce[1], Richard Edden[2], Yulu Song[2], Jamie Macdonald[1], Sam Oliver[1], Paul Mullins[1]
[1] Institute of Applied Health Physiology & Bangor Imaging Unit, Bangor University, UK.
[2] Division of Neuroradiology, The Johns Hopkins University School of Medicine, USA.

Introduction: Harnessing intermittent hypoxia (IH) for its potential therapeutic benefits has gained increasing attention in the past decade, as it has shown to facilitate neural plasticity [1, 2] and improve both cardiovascular [3] and cognitive function [4]. Although the acute cerebrovascular and cardiovascular responses to IH have been extensively studied, the regional effects of IH on the underlying concentrations of excitatory and inhibitory neurometabolites remains unknown. To further understand the mechanisms of therapeutic potential of IH, we aimed to assess the brains neurometabolic responses to IH in the posterior cingulate cortex (PCC) and occipital cortex (OC), brain regions known to have differential cerebrovascular responses to chronic hypoxia. From literature in chronic hypoxia, we hypothesised that glutamate would increase in the visual cortex but not the posterior cingulate cortex. We also hypothesised thar GABA would decrease during hypoxia in the visual cortex but increase in the posterior cingulate cortex and that lactate would increase in both regions [5][6][7].

Methods: To do this, we employed a counterbalanced, crossover design, healthy participants completed two experimental trials separated by at least 6 days. Trials involved 40 minutes of isocapnic normobaric intermittent hypoxia [4 cycles, 5 minutes of normoxia followed by 5 minutes of hypoxia (target $P_{ET}O_2$ = 50mmHg)]. A functional magnetic resonance spectroscopy (fMRS) experiment utilising an edited MRS sequence (HERCULES) to measure glutamate, γ-amino butyric acid (GABA), and lactate data in 4 minute 32 second blocks was employed. An MRI-compatible end-tidal targeting system (RespirAct, Thornhill Medical) allowed for the simultaneous supply of the IH stimulus and collection of breath-by-breath end-tidal gases.
Statistical Analysis: Neurometabolic concentration estimations were calculated with Osprey and be presented as ratio quantities referenced to Tissue Corrected Water (TC_{water}). A repeated measures three-way analysis of variance was performed to assess differences between neurometabolites across Brain Area (OC/PCC) vs Condition (Normoxia/Hypoxia) vs Time (cycle 1,2,3,4).

Results: Data was calculated from 10 participants (5 female, 26.2 ± 2.3 years). For glutamate, there was a main effect of region ($F(1,8)=12.255$, $p=.008$) and of condition ($F(1,8)=17.849$, $p=.003$). There was not a main effect of time/block ($p>.05$). There were no significant main effects of region, condition, or time for GABA and lactate. No significant interactions were present for GABA or lactate.

Discussion: The findings of this study provide new insights into the regional neurometabolic responses to intermittent hypoxia, particularly within the posterior cingulate cortex and occipital cortex. Contrary to our initial hypothesis, there was no significant difference in how the two brain regions responded to hypoxic bouts with glutamate decreasing in both regions during intermittent hypoxia. Our hypoxic exposure was 5 minutes, previous literature that had reported changes in in neurometabolites were at least 20 minutes [4][5][6]. Notably, the

shortest reported duration to show a measurable change, specifically, an increase in lactate—was 6 minutes into hypoxia [4]. This difference in exposure time may account for the absence of GABA or lactate changes in the present study.

Conclusions: We conclude that intermittent hypoxia, delivered in 5-minute bouts, elicits a distinct neurometabolic response compared with chronic exposures. Specifically, glutamate levels decreased during hypoxia in both the occipital cortex and posterior cingulate cortex, with no changes observed in GABA or lactate. These findings suggest an early, transient reduction of glutamatergic activity, preceding the region-specific adaptations report with prolonged hypoxic exposure.

Acknowledgements: We would also like to thank Sam Leaney, Irina Giguera and Nia Gwyn-Williams for their help with data acquisition; and Kevin Williams, and Andrew Fisher for thei technical help with MRI acquisition and hypoxia protocols.

References

1. Trumbower, R. D., Hayes, H. B., Mitchell, G. S., Wolf, S. L., & Stahl, V. A. (2017). Effects of acute intermittent hypoxia on hand use after spinal cord trauma: A preliminary study. Neurology.
2. Trumbower, R. D., Jayaraman, A., Mitchell, G. S., & Rymer, W. Z. (2012). Exposure to Acute Intermittent Hypoxia Augments Somatic Motor Function in Humans With Incomplete Spinal Cord Injury. Neurorehabilitation & Neural Repair.
3. Lyamina, N. P., Lyamina, S. V., Senchiknin, V. N., Mallet, R. T., Downey, H. F., & Manukhina, E. B. (2011). Normobaric hypoxia conditioning reduces blood pressure and normalizes nitric oxide synthesis in patients with arterial hypertension. Journal o Hypertension.
4. Wang, H., Shi, X., Schenck, H., Hall, J. R., Ross, S. E., Kline, G. P., Chen, S., Mallet, R. T., & Chen, P. (2020). Intermittent Hypoxia Training for Treating Mild Cognitive Impairment: A Pilot Study. American Journal of Alzheimer's Disease and Other Dementias.
5. Vestergaard, M. B., Ghanizada, H., Lindberg, U., Arngrim, N., Paulson, O. B., Gjedde, A., Ashina, M., & Larsson, H. B. W. (2022). Human Cerebral Perfusion, Oxygen Consumption, and Lactate Production in Response to Hypoxic Exposure. Cerebral Cortex.
6. Rogan, M., Friend, A. T., Rossetti, G. M., Edden, R., Mikkelsen, M., Oliver, S. J., Macdonald, J. H., & Mullins, P. G. (2022). Hypoxia alters posterior cingulate cortex metabolism during a memory task: A 1H fMRS study. NeuroImage.
7. Harris, A. D., Roberton, V. H., Huckle, D. L., Saxena, N., Evans, C. J., Murphy, K., Hall, J. E., Bailey, D. M., Mitsis, G., Edden, R. A. E., & Wise, R. G. (2013). Temporal dynamics of lactate concentration in the human brain during acute inspiratory hypoxia. Journal of Magnetic Resonance Imaging.

Enhancing temporal resolution of fMRI data through multi-modal data fusion with paired MEG measurements using machine learning.

Jiri Benacek[1], Krish Singh[1], Derek Jones[1], David Marshall[2,3], Simon Rushton[1], Marco Palombo[1,2]

[1] School of Psychology, Cardiff University, Cardiff, UK

[2] School of Computer Science and Informatics, Cardiff University, Cardiff, UK

[3] School of Engineering, Cardiff University, Cardiff, UK

Introduction: Functional magnetic resonance imaging (fMRI) and magnetoencephalography (MEG) offer complementary advantages. MEG captures neuronal activity with millisecond temporal resolution and directly measures neural dynamics, but with lower spatial resolution and reduced sensitivity to subcortical sources [1]. fMRI provides higher spatial resolution and maps subcortical activity, albeit indirectly via the blood-oxygen-level-dependent (BOLD) signal [2,3]. Combining these modalities could harness their respective strengths, though inherent differences in signal properties present integration challenges [4,5,2]. This study represents an initial step toward linking these modalities within a unified framework, extending previous work on multimodal spatial quality transfer [6].

Methods: Sixteen volunteers underwent MEG and fMRI while viewing a 20-minute film [7] sequence encompassing diverse stimuli. BOLD data were acquired on a 3T scanner (EPI, 3 mm^3 resolution) and aligned to MNI space. High-resolution (1 mm^3) anatomical images were collected via a fast-spoiled gradient echo sequence. MEG was recorded with a 275-channel system, bandpass filtered into delta (δ; 1–4 Hz), theta (θ; 4–8 Hz), alpha (α; 8–13 Hz), beta (β; 13–30 Hz), and low gamma (low-γ; 40–60 Hz). Frequency-specific MEG data were source-localized using synthetic-aperture magnetometry onto an MNI template at 6 mm^3. MEG time-series were de-spiked, high-pass filtered, and convolved with a canonical haemodynamic response function to match the slower BOLD profile.

Group-level Tensorial Independent Component Analysis (TICA) [8] yielded 25 MEG and 30 fMRI independent components (ICs) with temporal profiles. We developed a supervised framework to predict low-temporal-resolution fMRI signals (2 s TR) at 0.5 s resolution from MEG timecourses across all frequency bands. Each model was trained per fMRI component using temporally aligned MEG components as features. A sliding window (±3 TRs; 28 MEG samples) captured local temporal dynamics around each target fMRI timepoint. Benchmarked models included a multilayer perceptron (MLP), XGBoost [9], and linear regression. As a baseline, we applied linear interpolation to the downsampled fMRI data. Models were evaluated on (1) training subset, (2) held-out test subset, and (3) upsampling of the training subset to 0.5 s resolution. Performance was quantified using the coefficient of determination (R^2), and absolute temporal error profiles were computed.

Results: For fMRI Component 4 (r = 0.65 with early visual areas [12], Figure 1), the Transformer and MLP achieved near-perfect fits on the training subset (R^2 = 0.991 and 0.980), with similar performance in true upsampling. On the held-out test subset, performance declined sharply (Transformer = –0.176, MLP = –0.126), falling below the interpolation baseline (R^2 = 0.948). XGBoost and linear regression produced negative R^2 values across contexts, while interpolation remained consistently high (≈0.95–0.97). Importantly, despite training on only 25% of modelled timepoints present in upsampled series, the Transformer and MLP outperformed interpolation when predicting ground-truth fMRI points from the same subset, showing that the learned mappings captured cross-modal relationships beyond simple smoothing. Upsampling results for all models as compared to the linear interpolation can be seen in Figure 2.

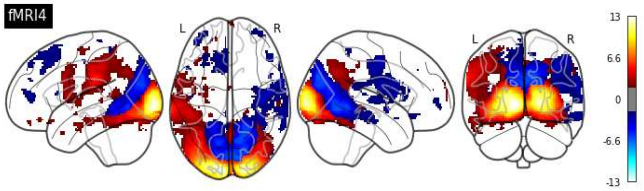

Fig. 1. *Visualisation of the modelled fMRI component 4, strongly correlated with early visual networks*

Discussion: The strong training and upsampling performance of the Transformer and MLP models demonstrates that MEG-derived features contain sufficient information to reconstruct fMRI temporal dynamics at higher sampling rates when evaluated in-sample. Notably, even with reduced training data, both models outperformed interpolation for predicting held-out fMRI points from the same subset, indicating that the learned mappings reflect meaningful aspects of the underlying electro-haemodynamic relationship. This suggests that the temporal structure of MEG activity can be mapped onto slower BOLD dynamics, offering a new means to investigate neurovascular coupling. Beyond physiological insight, these capabilities could be integrated with previous spatial MEG upsampling work [6] to produce

fused multimodal representations combining MEG's temporal resolution with fMRI's spatial resolution.

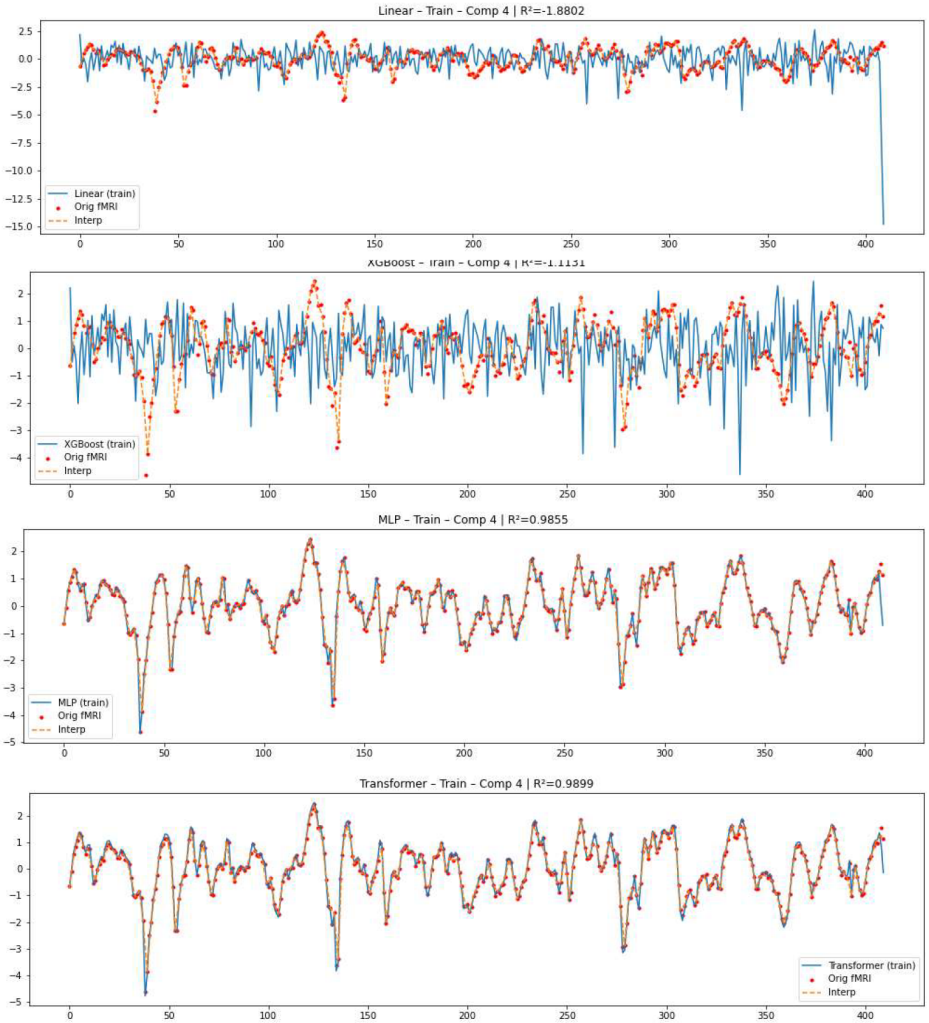

Fig. 2. *Visualisation of up-sampling time series of modelled fMRI component 4, with orange dots marking ground truth fMRI measurements, orange dotted line marking interpolation baseline, and blue solid line marking individual models' performance from top: Multiple linear regression model, XGBoost model, MLP model, Transformer model*

Conclusions: Cross-modal temporal upsampling using MEG and fMRI can outperform interpolation and reveal rich, mappable correspondences between electrophysiological and haemodynamic signals. While improving generalisability remains a challenge, these findings support the feasibility of multimodal fusion pipelines that leverage the complementary strengths of these imaging modalities.

References

[1] A. Hillebrand and G. R. Barnes, "A quantitative assessment of the sensitivity of whole-head meg to activity in the adult human cortex," Neuroimage, vol. 16, no. 3, pp. 638–650, 2002.
[2] Z.-Q. Liu, G. Shafiei, S. Baillet, and B. Misic, "Spatially heterogeneous structure-function coupling in haemodynamic and electromagnetic brain networks," NeuroImage, vol. 278, p. 120276, 2023.
[3] D. Rangaprakash, R. L. Barry, and G. Deshpande, "The confound of hemodynamic response function variability in human resting-state functional mri studies," Frontiers in Neuroscience, vol. 17, p. 934138,2023.
[4] K. D. Singh, "Which "neural activity" do you mean? fmri, meg, oscillations and neurotransmitters," Neuroimage, vol. 62, no. 2, pp. 1121–1130, 2012.
[5] J. Daunizeau, H. Laufs, and K. J. Friston, "Eeg–fmri information fusion: biophysics and data analysis," EEG-fMRI: Physiological Basis, Technique, and Applications, pp. 511–526, 2010.
[6] Benacek et al. "Enhancing brain activity mapping through BOLD-fMRI and MEG data fusion using explainable machine learning." ISMRM 2025 Abstract. 2025.
[6] M. G. Wilson, B. Broccoli, N. Purvis, R. Wade, and J. Logan, Skyfall. Sony Pictures Entertainment, 2012.
[7] C. F. Beckmann and S. M. Smith, "Tensorial extensions of independent component analysis for multi- subject fmri analysis," Neuroimage, vol. 25, no. 1, pp. 294–311, 2005.
[8] T. Chen and C. Guestrin, "Xgboost. a scalable tree boosting system. arxiv. 2016; 1603.02754 v3," 2023.
[9] S. M. Smith, P. T. Fox, K. L. Miller, D. C. Glahn, P. M. Fox, C. E. Mackay, N. Filippini, K. E. Watkins, R. Toro, A. R. Laird, et al., "Correspondence of the brain's functional architecture during activation and rest," Proceedings of the national academy of sciences, vol. 106, no. 31, pp. 13040–13045, 2009.

Deep Spatiotemporal Neural Networks and tSNR-Guided Frame Retention for Frame Quality Classification in Infant Awake fMRI

Param Ahir[1], Áine T. Dineen[1], Chen Qin[2], Rhodri Cusack[1]

[1]Trinity College Institute of Neuroscience, Trinity College Dublin, Ireland

[2]Biomedical Image Analysis Group, Department of Computing, Imperial College London, London, United Kingdom

Introduction: Functional MRI of infants often suffers from motion and physiological noise, leading to frames that degrade data quality and reduce sensitivity for the detection of brain activity. Traditional pipelines remove frames using fixed thresholds on metrics like framewise displacement (FD) and data variance statistic (DVARS). However, these thresholds can miss subtle abnormalities in the data or conversely remove volumes that are not too noisy. This study explored whether a deep learning (DL) model can better identify low-quality frames and improve the temporal signal-to-noise ratio (tSNR).

Methods: Awake fMRI comprising 310 runs from 165 infants was acquired using multiband EPI (510 volumes/run 64*64*36voxels; $(3mm)^3$; TE=32ms; FA=40; multiband slice acceleration=4) during a picture-viewing task from foundation of cognition (FOUNDCOG) project. The dataset was split at the subject level to ensure generalisation to new subjects across training, validation, and test sets. Ground-truth frame quality labels were derived using two approaches: FD/DVARS thresholding (FD < 1.69 mm, DVARS < 28.8) and a machine learning model trained on 19 framewise features including motion, signal, and intensity metrics, all calibrated to optimize tSNR[1]. A deep spatiotemporal neural network was trained to classify poor-quality frames using eight-frame input windows with four derived channels per volume. Features were extracted via 3D convolutional layers followed by a gated recurrent unit (GRU) to capture temporal changes, and final frame scores were produced using sigmoid-activated linear layer [2][3]. Frame retention thresholds were applied to ensure that 70–90% of frames were retained per run, balancing denoising with temporal continuity [4].

Results: On validation runs, the model achieved an AUC of approximately 0.74. Across methods, ΔtSNR was computed as the change in mean tSNR within the brain mask after removing frames marked as low quality. The DL-based approach produced the highest mean ΔtSNR across the cohort, outperforming both FD/DVARS and the ML-based frame quality classifier. However, FD/DVARS generated the most runs (131/310) with improved tSNR, followed closely by DL (129), and ML (50). Further analysis of frames marked “good” by FD/DVARS but “bad” by the DL model showed that removing them improved tSNR in 154 runs. These additional frames have other abnormal features beyond FD and DVARS, suggesting that the DL model captures more subtle spatiotemporal anomalies.

Discussion: The deep learning model captured quality issues beyond motion-related artifacts measured by FD/DVARS, though FD/DVARS still improved tSNR in slightly more runs overall. These results suggest

that deep learning and traditional metrics identify overlapping yet distinct sources of noise. However, relying on tSNR as a benchmark has limitations, since it cannot capture task-specific deviations in neural signals [5].

Conclusions: Deep spatiotemporal neural networks can be a scalable and effective approach for automated frame-level quality control in infant fMRI. While FD/DVARS thresholds remain effective in many cases, the DL approach showed distinct advantages in improving tSNR in numerous runs. tSNR is a useful preliminary metric for assessing denoising, as it reflects improved temporal stability. However, it may increase by reducing the data retention rate and removing the task-related signals. Future work will explore using GLM performance and inter-subject correlation for defining ground truth and evaluating model impact.

Acknowledgement: We acknowledge the FOUNDCOG team for the dataset used in this study.

References

[1] Power, J. D., Barnes, K. A., Snyder, A. Z., Schlaggar, B. L., & Petersen, S. E. (2012). Spurious but systematic correlations in functional connectivity MRI networks arise from subject motion. Neuroimage, 59(3), 2142-2154.

[2] Tran, D., Bourdev, L., Fergus, R., Torresani, L., & Paluri, M. (2015). Learning spatiotemporal features with 3d convolutional networks. In Proceedings of the IEEE international conference on computer vision (pp. 4489-4497).

[3] Jiang, X., Yan, J., Zhao, Y., Jiang, M., Chen, Y., Zhou, J., ... & Liu, T. (2023). Characterizing functional brain networks via spatio-temporal attention 4D convolutional neural networks (STA-4DCNNs). Neural Networks, 158, 99-110.

[4] Phạm, D. Đ., McDonald, D. J., Ding, L., Nebel, M. B., & Mejia, A. F. (2023). Less is more: balancing noise reduction and data retention in fMRI with data-driven scrubbing. NeuroImage, 270, 119972.

[5] Parkes, L., Fulcher, B., Yücel, M., & Fornito, A. (2018). An evaluation of the efficacy, reliability, and sensitivity of motion correction strategies for resting-state functional MRI. Neuroimage, 171, 415-436.

Impact of Bayesian-inference vs least squares fitting on the repeatability of ASL perfusion estimates.

Aisling E Fothergill[1,2], David Higgins[3], Owen Thomas[1,4], David Coope[1,4], Ibrahim Djoukhadar[1,4], and Laura M Parkes[1,2]

[1]School of Health Sciences, Faculty of Biology Medicine and Health, The University of Manchester, [2]Geoffery Jefferson Brain Research Centre, Manchester Academic Health Science Centre, Manchester, [3]Philips, Farnborough, United Kingdom [4]Salford Royal Hospital, Northern Care Alliance, NHS Foundation Trust, Manchester Academic Health Science Centre, Manchester.

Corresponding email address: aisling.fothergill@manchester.ac.uk

Introduction: Quantification of arterial spin labelling (ASL) MRI remains challenging due to low signal to noise ratio (SNR). There are multiple methods proposed to quantify ASL signal including least-squares and Bayesian-inference based methods. Additionally multi-delay ASL (MD-ASL) has increased prevalence in recent years [1] however information on the repeatability compared to single-delay (SD-ASL) is limited. The goal of this study was to determine the repeatability of SD-ASL and MD-ASL using both Bayesian-inference and least-squares fitting pipelines.

Methods: 9 healthy volunteers (age 23-53, 7F/2M) were recruited and scanned 14 days apart on a 3T Philips Elition X scanner. Both single and multi-delay 3D GraSE ASL sequences were acquired for all participants with MD-ASL using the Spin Labeling ASL Research patch. SD-ASL acquisition: TE/TR (same for M0 and label/control)=12ms/4280ms, 30 slices, acquired voxel size=3.75x4.00x5mm^3, label duration=1800ms, post label delay(PLD)=2000ms, 6 repeats per PLD, scan duration=7mins 16secs. MD-ASL acquisition: M0 TE/TR= 20ms/6000ms, label/control TE/TR=20ms/2675ms, 30 slices, acquired voxel size=2.5x2.5x5.0mm^3, label duration=2000ms, PLDs=500, 1000, 1500, 2000, 2500, 3000ms, 2 repeats per PLD, scan duration = 8mins 20secs. The ASL acquisitions were positioned with the acquisition field of view at the bottom of the cerebellum with the labelling plane 30mm below to ensure consistent labelling between sessions.

The SD-ASL and MD-ASL acquisitions were quantified with both least-squares and Bayesian-inference methods to determine the whole brain, grey matter (GM) and white matter (WM) , and relative GM/WM CBF and ATT. Least-squares analysis used in-house Python scripts and Bayesian-inference analysis used the BASIL FSL toolbox [2]. Both analysis techniques used GM M0 calibration, SD-ASL was analysed as described in the SD-ASL consensus paper[4]. MD-ASL BASIL analysis used a bolus arrival time prior of 1.3secs with a standard deviation of 3secs to ensure repeatability was not driven by the width or confidence of the prior [3]. A T1-weighted image was used to segment GM and WM regions using FSL FAST[5]. The within-subject Coefficients of variation (CoVs) were used to assess repeatability of SD-ASL and MD-ASL estimates [4].

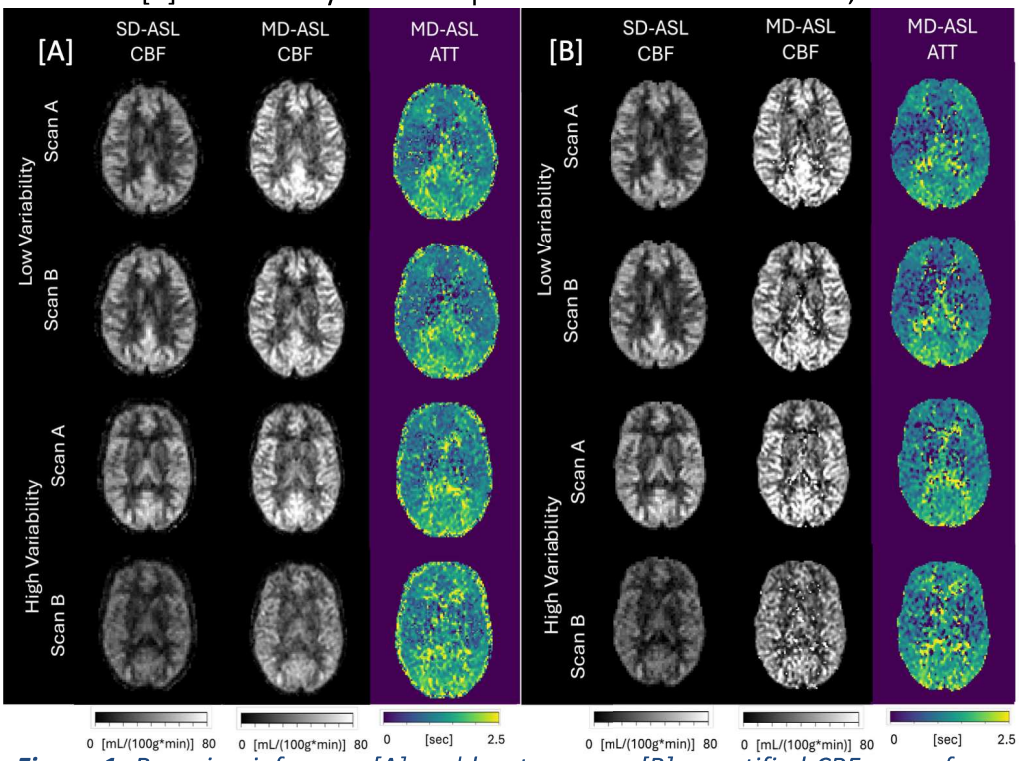

Figure 1: *Bayesian inference [A] and least squares [B] quantified CBF maps from the SD-ASL and MD-ASL acquisitions and ATT map from the MD-ASL acquisition for one participant with low between-session variability (top) and with high between-session variability (bottom).*

Results and Discussion: Visually, both Bayesian-inference and least-squares fitting showed similar variability between sessions (Figure 1), however least-squares had more erroneous fitting voxels particularly in white matter (Figure 1[B]). Mean values for least-squares and Bayesian-inference fitting of the SD-ASL and MD-ASL acquisitions are reported in Table 1. Figure 2 summarises the repeatability when quantified using the Bayesian-inference based BASIL toolbox and Figure 3 for least-squares. For both BASIL and least-squares, ATT was more repeatable than CBF (4-7% CoVs for ATT and 11-23% for CBF in WB, GM, and WM). However, relative CBF repeatability was 3-4 times better than absolute CBF, with CoVs similar to ATT which is likely to indicate relative CBF and ATT are less dependent on global factors such as labelling efficiency that may vary between scans. The repeatability of least-squares and Bayesian-inference was comparable with 1-4% difference in CoVs (see Table 1). MD-ASL CBF was slightly more repeatable than SD-ASL with 4-6% lower CoVs using Bayesian-inference fitting or 8-12% lower when quantified with least-squares, however this may be due to the increased scan time.

Conclusion: This study suggests that for longitudinal perfusion studies, relative CBF measures may be more useful given the higher repeatability. BASIL and least-squares quantification methods had comparable repeatability. MD-ASL was more repeatable than SD-ASL in all measures and provides additional ATT information with high repeatability.

	SD-ASL CBF [mL/100g*min] & (COV)		MD-ASL CBF [mL/100g*min] & (COV)		MD-ASL ATT [secs] & (COV)	
	Bayesian-inference	**Least-Squares**	**Bayesian-inference**	**Least-Squares**	**Bayesian-inference**	**Least-Squares**
Whole Brain	23.2 (19%)	23.4 (21%)	32.1 (15%)	39.3 (11%)	1.58 (5.8%)	1.50 (6.9%)
Grey Matter	28.6 (19%)	29.1 (20%)	37.7 (15%)	46.8 (12%)	1.51 (6.5%)	1.50 (7.3%)
White Matter	13.6 (21%)	13.0 (23%)	22.8 (15%)	28.5 (11%)	1.72 (4.5%)	1.52 (5.7%)
Relative GM/WM	2.12 [a.u.] (5.9%)	2.25[a.u.] (5.9%)	1.65[a.u.] (3.7%)	1.64[a.u.] (7.8%)	0.87[a.u.] (3.1%)	0.98[a.u.] (2.9%)

Table 1: *Summary of mean perfusion estimates and CoVs*

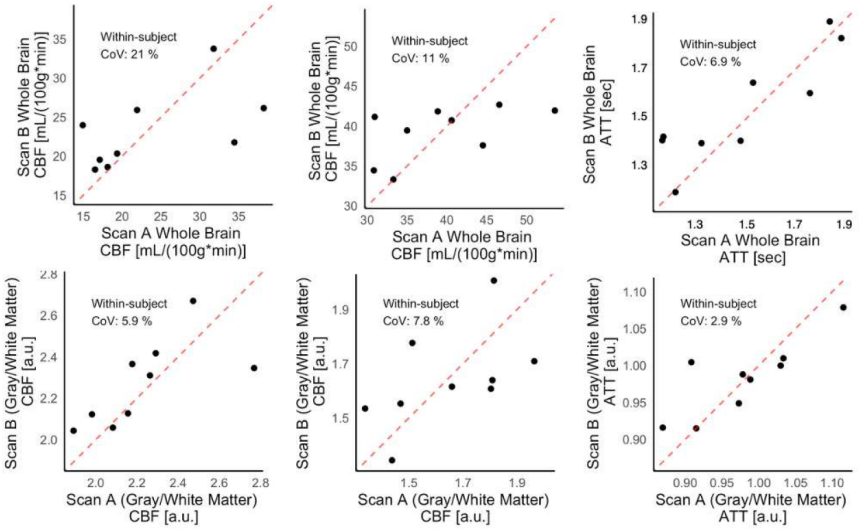

Figure 2: *Bayesian-inference parameter estimation and CoVs for SD-ASL and MD-ASL CBF and ATT. Top row shows values in the whole brain, and bottom row shows relative GM/WM values.*

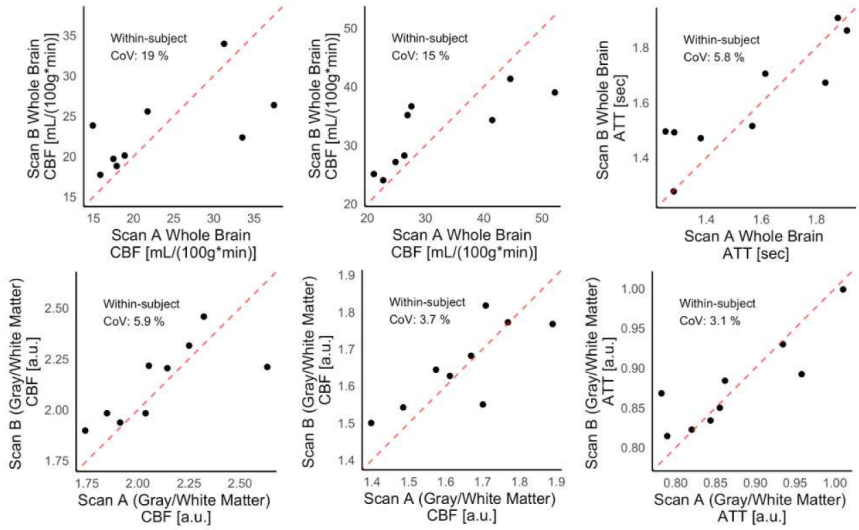

Figure 3: *Least-squares parameter estimation and CoVs for SD-ASL and MD-ASL CBF and ATT. Top row shows values in the whole brain, and bottom row shows relative GM/WM values.*

References: **[1]** Woods JG, et al. Magn Reson Med. 2024;92(2):469–95. **[2]** Chappell MA, Groves AR, Whitcher B, Woolrich MW. IEEE Trans Signal Process. 2009 Jan 1;57(1):223–36. **[3]** Fothergill A, et al. Impact of Bayesian-Inference vs Least-Squares Fitting on Multi-Delay Arterial Spin Labelling Parameter Estimation. In: Proc Intl Soc Mag Reson Med 32 (2024:2016). Singapore; 2024. **[4]** Bland JM, Altman DG. BMJ. 1996;313(7059):744–744.

Dual Output Modes of 4DFlowNet Highlight Super-Resolution Advantages for Hemodynamic Profiling in Bicuspid Aortic Valve

Houriehsadat Jamalidinan[1], Caryl Richards[3], Anvesha Singh[3], Gerry P McCann[3], Julio Garcia[1,2]
[1]Department of Biomedical Engineering, University of Calgary, Calgary, AB, Canada,
[2]Department of Radiology, University of Calgary, Calgary, AB, Canada
[3] Leicester British Heart Foundation Centre of Research Excellence, and National Institute for Health and Care Research Biomedical Research Centre, Department of Cardiovascular Sciences, University of Leicester, Leicester, UK

Introduction: Four-dimensional Flow Magnetic Resonance Imaging (4D Flow MRI) offers unparalleled insight into cardiovascular hemodynamics. However, in the context of bicuspid aortic valve (BAV) disease, its diagnostic power is often compromised by technical artifacts, including low spatial resolution and significant noise. Such data degradation undermines the reliable measurement of key hemodynamic markers implicated in the progression of BAV-related aortopathy, limiting the clinical utility of 4D Flow MRI for early risk stratification. In this study, we sought to overcome these limitations by developing and validating two deep learning models based on the 4DFlowNet architecture [1]: a post-processing (PP) model for data refinement and a super-resolution (SR) model that also increases spatial resolution. The central hypothesis was that the SR model would provide superior correction of velocity fields and improve the estimation of hemodynamic metrics—including peak velocity, wall shear stress, and flow displacement—than the PP model.

Methods: Two deep learning models based on the 4DFlowNet architecture [1] were trained on 4D Flow MRI data from 70 patients with BAV disease. Both models performed PP, including denoising and artifact correction, while the second model additionally applied a two-fold spatial SR enhancement. Training was performed using over 36,000 image patches, employing a combined loss function that incorporated perceptual loss, eddy current correction, and mean squared error. For SR training, inputs were synthetically degraded through k-space downsampling and noise injection. Both models showed consistent improvements over baseline in Peak Signal-to-Noise Ratio (PSNR), Structural Similarity Index Measure (SSIM), Root Mean Square Error (RMSE), and Bland-Altman metrics. The models were internally validated on 20 cases from the University of Calgary and externally tested on five independent BAV cases from the University of Leicester, where hemodynamic parameters including peak systolic velocity, wall shear stress (WSS), normalized flow displacement (NFD), and vortex shedding, were extracted for evaluation.

Aortic Segmentation and Plane Extraction:

The entire aorta was manually segmented in each dataset. For our analysis, we focused on a specific region of interest (ROI) within the ascending aorta. This ROI was defined as the section extending from the aortic valve to the last cross-sectional slice just proximal to the aortic arch where the ascending and descending lumens appeared distinct. Within this ROI, an aortic centerline was automatically generated, and 25 equidistant planes perpendicular to this centerline were extracted for hemodynamic analysis.

Peak Velocity Calculation: Global peak velocity was identified by locating the maximum velocity magnitude across the 4D volume for each time frame, with the highest value defining peak systole. Within the ROI, voxel-level peak velocity was extracted using a Maximum Intensity Projection (MIP), and the peak voxel's velocity was tracked across all phases [3]. To reduce noise and improve robustness, a spatially averaged peak velocity was then computed using a 3×3×3 kernel.

WSS: WSS was computed from the spatial gradients of the velocity field at the vessel wall. This calculation assumed blood is a Newtonian fluid with a dynamic viscosity (μ) of 3.5 mPa·s. We subsequently calculated the mean and maximum WSS, axial WSS, and WSS angle for each plane.

NFD: NFD was calculated to quantify flow eccentricity. It was defined as the displacement of the velocity-weighted flow centroid from the geometric center of the vessel, normalized by the local aortic diameter [2].

Results: Across five BAV cases, the SR model outperformed the PP model in capturing key hemodynamic features. As shown in Figure 1, SR yielded up to 98% higher global peak velocities, 2–10× higher WSS, and up to 83% higher NFD, indicating greater sensitivity to high-velocity jets, eccentric flow, and diastolic shifts. It also preserved late-phase vortex shedding and exhibited broader spatial NFD distributions (Figure 2) that were suppressed in PP due to temporal smoothing. Visual assessment confirmed SR's clearer flow patterns and sharper vessel boundaries (Figure 3), supporting its potential for early risk stratification in BAV aortopathy.

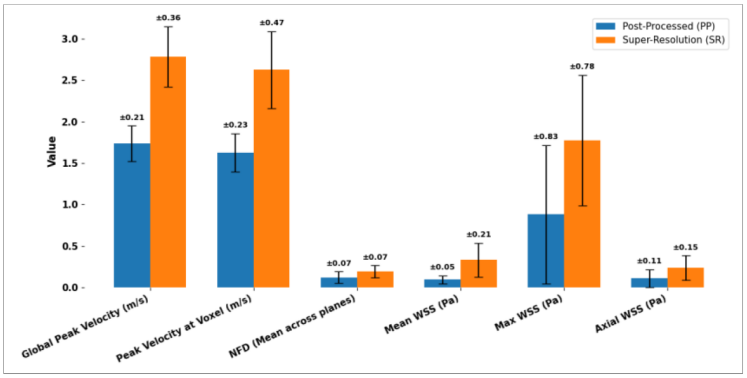

Fig. 1. Quantitative Comparison of Hemodynamic Metrics from Super-Resolution (SR) and Post-Processed (PP) Models.

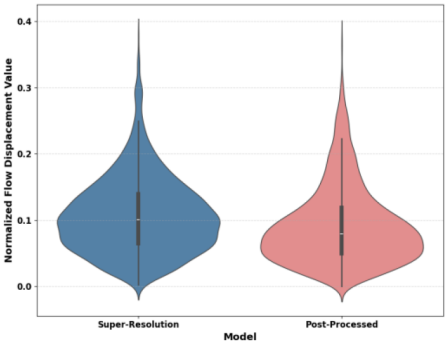

Fig. 2. Violin plots comparing Normalized Flow Displacement (NFD), a metric for flow eccentricity. The broader distribution for the Super-Resolution (SR) model demonstrates its enhanced sensitivity to complex, eccentric flow patterns compared to the Post-Processed (PP) model.

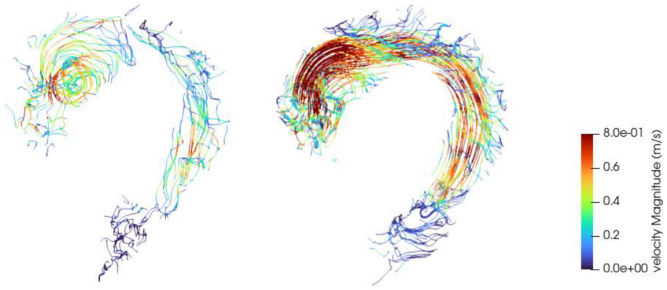

Fig. 3. Streamline Comparison Between Super-Resolution(right) and post-processed (left) 4D Flow MRI at peak systole (Same Seeding and Velocity Range).

Discussion: The SR model outperformed standard post-processing by capturing sharper velocity peaks, higher WSS, and more eccentric flow. It preserved late-phase vortex shedding and revealed broader NFD patterns, highlighting its ability to detect subtle flow abnormalities in BAV.

Conclusions: SR enhances 4D Flow MRI by improving sensitivity to key hemodynamic markers in BAV. It shows promise as a non-invasive tool for early diagnosis and risk assessment. In the future, SR could enable more precise monitoring of disease progression and help guide treatment decisions in BAV-related aortopathy.

References

[1] Ferdian E, Suinesiaputra A, Dubowitz DJ, Zhao D, Wang A, Cowan B, Young AA. 4DFlowNet: super-resolution 4D flow MRI using deep learning and computational fluid dynamics. Frontiers in Physics. 2020 May 4;8:138.

[2] Richards C, Alfuhied A, Parker A, Aslam S, Debiec R, Mccann GP, Singh A. The effect of aortic valve replacement on 4D flow-measured flow displacement in patients with bicuspid and tri-leaflet aortic valves with severe aortic stenosis. European Heart Journal. 2023 Nov;44(Supplement_2):ehad655-027.

[3] Rose MJ, Jarvis K, Chowdhary V, Barker AJ, Allen BD, Robinson JD, Markl M, Rigsby CK, Schnell S. Efficient method for volumetric assessment of peak blood flow velocity using 4D flow MRI. Journal of Magnetic Resonance Imaging. 2016 Dec;44(6):1673-82.

Addressing bias in FreeSurfer imaging-derived phenotypes arising from T2-FLAIR scan omission in UK Biobank using harmonization approaches

Jacob Turnbull[1], Gaurav Bhalerao[1,2], Fidel Alfaro-Almagro[1], Ludovica Griffanti[1,2], Stephen M. Smith[1]
[1] Centre for Integrative Neuroimaging, FMRIB, Nuffield Department of Clinical Neurosciences, University of Oxford - Oxford - United Kingdom
[1] Oxford Centre for Human Brain Activity, Department of Psychiatry, University of Oxford - Oxford - United Kingdom

Introduction: The UK Biobank has recently completed multimodal MRI scans of 100,000 participants using the same acquisition protocol on identical scanners and extracting image derived phenotypes (IDPs) with a standardised pipeline [1,2]. However, confound effects are still present and need to be carefully addressed. In previous work [3], it has been shown that when T2-FLAIR is not used as an additional input for FreeSurfer (FS) processing [4,5], IDPs are affected. This batch variable, hereon referred to as FST2, only affects ~2% of participants in UKB, but accounts for up to 14% of variance explained in some IDPs. In this work we investigate the prevalence and magnitude of the FST2 batch variable across IDPs and assessed strategies for mitigating it. We used established harmonization methods and compared their ability to remove this batch effect through analysis of the mean and variance differences. We then compared the impact of different strategies on the correlations between affected IDPs and non-imaging variables (nIDPs).
Methods: We used Cohen's d and the ratio of variance between the groups with and without the T2 FLAIR across 1432 structural IDPs. We created age nomograms for IDPs with known age changes to show how missing T2-FLAIR can bias models and downstream analysis. We then compared standard confound correction of age, sex, head position and head size scaling and four harmonization methods for mitigating the FST2 batch effect along with these confounding variables. 1) multiple linear regression of just confounds; 2) multiple linear regression of confounds and binary FST2 vector indicating batch; 3). A modified form of ComBat [6,7] which skips the step at which the least squares estimate for covariate effects are added back in, effectively regressing them out, 4) Method 3 but omitting the scaling correction on the variance; 5) ComBat pooling only across similar IDP classes (e.g. cortical thickness or surface areas) and not all FS IDPs together. We validated these approaches against each other using Cohens d between the groups with and without T2-FLAIR to show the mean effect and the ratio of within group variances to show the variance differences. Finally, we compared potential downstream impact of each of our methods through measuring the correlations between FS IDPs and over 18,000 nIDPs, showing the results as Bland Altmann plots.
Results: We found a strong negative effect size between the group with and without the T2-FLAIR in over 250 FS IDPs, particularly those related to cortical volume and thickness. In the most affected IDPs, the ratio of variance between the two groups was as high as 2.8 (fig 1A). All harmonization methods reduced Cohen's d effect size (mean shift bias) below 0.1 for all IDPs, however, linear regression was unable to correct variance differences between batches, whereas ComBat methods 3 and 5 were able to (fig 1B). When looking at correlations with nIDPs, there were minor differences between methods 2-5, but larger differences compared to method 1 when looking at weaker correlations, suggesting the FST2 effect may be causing spurious but weak correlations.

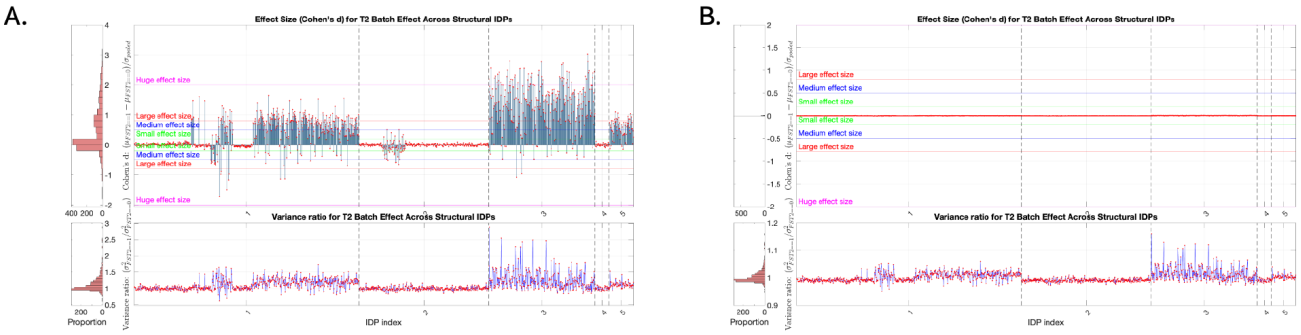

Figure 1: Cohens d (top) and variance ratio (bottom) between group with (FST2==1) and without (FST2==0) T2-FLAIR before applying harmonization (A) and after applying ComBat harmonization using method 4 (B).

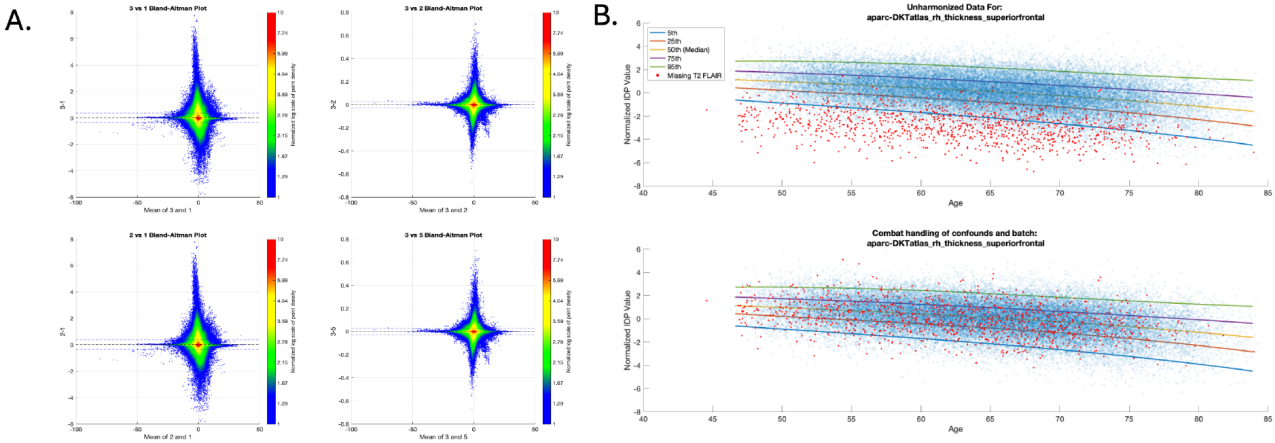

Figure 2: Panel A: Bland Altmann plots showing the Fischer transformed Z-statistics of the correlations between the FS IDPs and nIDPs using different methods of harmonization and confound removal. Here methods 1-5 are matched to those described in the methods section. Panel B: Age Nomogram showing the batch effect (blue dots FST2==1, used to derive the percentiles; red dots FST2==0) on a cortical thickness IDP with a known age effect before harmonisation (top) and after applying method 3 (bottom nomogram) with age preserved by ComBat.

Discussion: The FST2 confound causes a strong bias in the mean and variance in over 250 IDPs. We have shown ComBat's advantage over simple regression in its ability to correct for variance differences between batches. Comparing correlations with nIDPs, we have shown that using ComBat to handle both confound and batch correction is comparable to simple regression but offers no significant advantage.

Conclusions: Addressing the FST2 batch effect using regression sufficiently corrects the mean shift bias, but not the inter-batch variance differences. Researchers using their own FS derived IDPs or using UKB FS IDPs should be aware of these effects and consider using this modified ComBat approach to handle both the FST2 effect and other confound correction.

References

[1] Miller, K. L. et al. (2016). Multimodal population brain imaging in the UK Biobank prospective epidemiological study. Nature neuroscience, 19(11), 1523–1536.
[2] Fidel, A., et al. (2018). Image processing and Quality Control for the first 10,000 brain imaging datasets from UK Biobank. NeuroImage,166, 400-424.
[3] Fidel, A., et al. (2021). Confound modelling in UK Biobank brain imaging. NeuroImage, 224, 117002
[4] Fischl B. (2012). FreeSurfer. NeuroImage, 62(2), 774–781.
[5] Iglesias, J. E., et al. (2018). A probabilistic atlas of the human thalamic nuclei combining ex vivo MRI and histology. NeuroImage, 183, 314–326.
[6] Jean-Philippe, Fortin, et al. (2018). Harmonization of cortical thickness measurements across scanners and sites. NeuroImage, 167, 104-120.
[7] W. Evan Johnson and Cheng Li. (2007). Adjusting batch effects in microarray expression data using empirical Bayes methods. Biostatistics, 8(1):118-127.

RWKV-MoEst: An RWKV-based 4D fMRI Motion Estimation Model

Zi Ye[1], Áine T. Dineen[1], Chen Qin[2], Rhodri Cusack[1]
[1]Trinity College Institute of Neuroscience, Trinity College Dublin, Dublin, Ireland
[2]Imperial College London, White City Campus, London, United Kingdom

Introduction: Functional MRI (fMRI) is highly sensitive to head movement, which corrupts the images. This is particularly challenging in populations such as awake infants [1]. Several strategies have been developed to address motion-corrupted fMRI images, including volume censoring, subject-level exclusion, and motion estimation and correction tools such as SPM and FSL [2]. However, up to 50% of experimental runs may still be excluded due to motion in awake infant fMRI studies. Recently, deep neural networks (DNNs) have been increasingly applied to medical imaging, demonstrating promising performance in MRI registration. Therefore, we hypothesize that DNNs hold considerable potential for motion correction in fMRI data because of their ability to capture rich prior information and correct nonlinear artifacts. In this study, we introduce an RWKV-based 4D fMRI motion estimation model (RWKV-MoEst), where the RWKV-6 model, commonly used in natural language processing, is adapted to solve fMRI tasks [3]. We aim to demonstrate that DNNs can effectively estimate head motion in fMRI by predicting six motion parameters, i.e., three translations and three rotations, and highlight the potential of deep learning technology for accurate motion estimation.

Methods: The architecture of our model is depicted in Figure 1. The RWKV-MoEst architecture consists of four stages, where the input is two successive fMRI volumes and the objective is to predict the difference between their corresponding positions (i.e., time *t* minus *t-1*). Each stage was constructed through the implementation of patch merging, with patch embedding employed in the case of Stage 1. The multiple 4DfMRI-Global-RWKV were applied repeatedly within the stages, and in each layer, tokens are fed into the VRWKV-SpatialMix-V6 module, which served as a global attention mechanism. Specifically, the VRWKV-SpatialMix-V6 module drew inspiration from the Eagle time-mixing module in the RWKV-6 network, maintaining a balance between performance and computational cost when handling high-dimensional datasets, such as fMRI, due to its attention-free mechanism. The temporal difference between feature maps was calculated after four encoder stages, followed by an MLP to predict the differences in motion parameters.

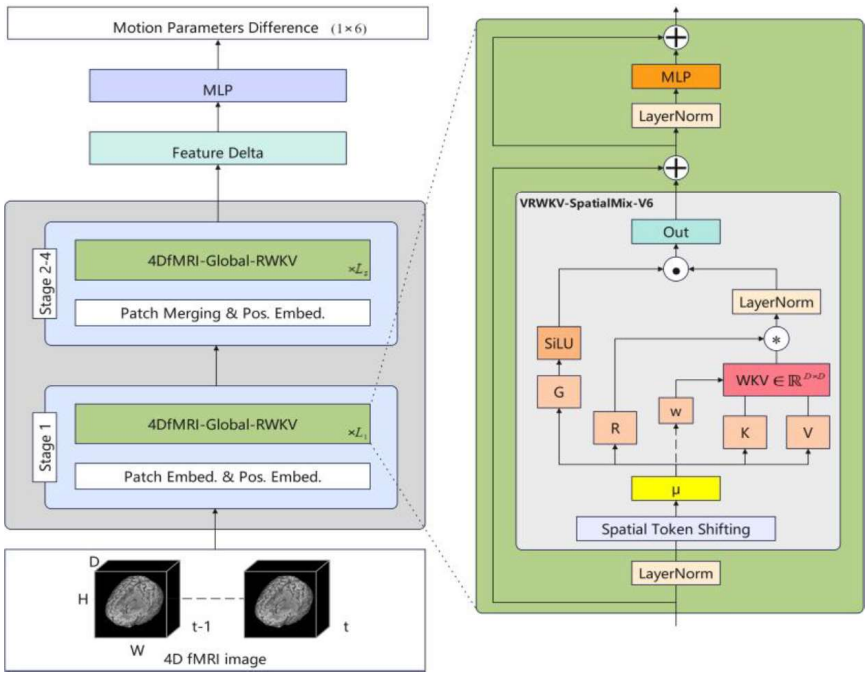

Fig. 1. The overview architecture of the RWKV-MoEst model

We evaluated this model on a longitudinal neuroimaging dataset from awake infants scanned a 2-months-old (n = 130) and again at 9 months old (n = 65), resulting in a total of 903 fMRI acquisitions using multiband EPI (acceleration factor 4) [4]. We then split the dataset into training, validation, and test sets in an 8:1:1 ratio at the subject level.

Results: A frame-wise displacement loss was used for training. To reduce learning of subject-specific brain anatomy, we randomly cropped to 32*32 in the x-y plane, hypothesizing this would improve generalisation to new subjects. However, given the rich temporal structure of the slices in the z-

direction, due to the interleaved slice order and multiband acquisition, we hypothesized that random crops in this dimension would negatively impact motion estimation. To evaluate these hypotheses we therefore compared three cropping regimes. Table 1 presents the numerical results, including the Mean Absolute Error (MAE), the adjusted MAE after denormalizing to the original scale, and the Pearson Correlation Coefficient (PCC) for each motion parameter. Moreover, the respective scatter plots of each of the six motion parameters are shown in Figure 2.

Tab. 1. Quantitative results on test dataset

Method	Loss	PCC-Tx	PCC-Ty	PCC-Tz	PCC-Pitch	PCC-Yaw	PCC-Roll	MAE	Adjust_MAE
RWKV-MoEst (crop x,y&z)	0.68	**0.90**	0.65	0.64	0.43	0.84	0.90	0.27	0.033
RWKV-MoEst (crop x&y)	**0.63**	0.89	**0.74**	**0.68**	0.34	**0.90**	**0.92**	**0.25**	**0.028**
RWKV-MoEst (no crop)	0.67	0.88	0.65	0.64	**0.51**	0.87	0.88	0.27	0.032

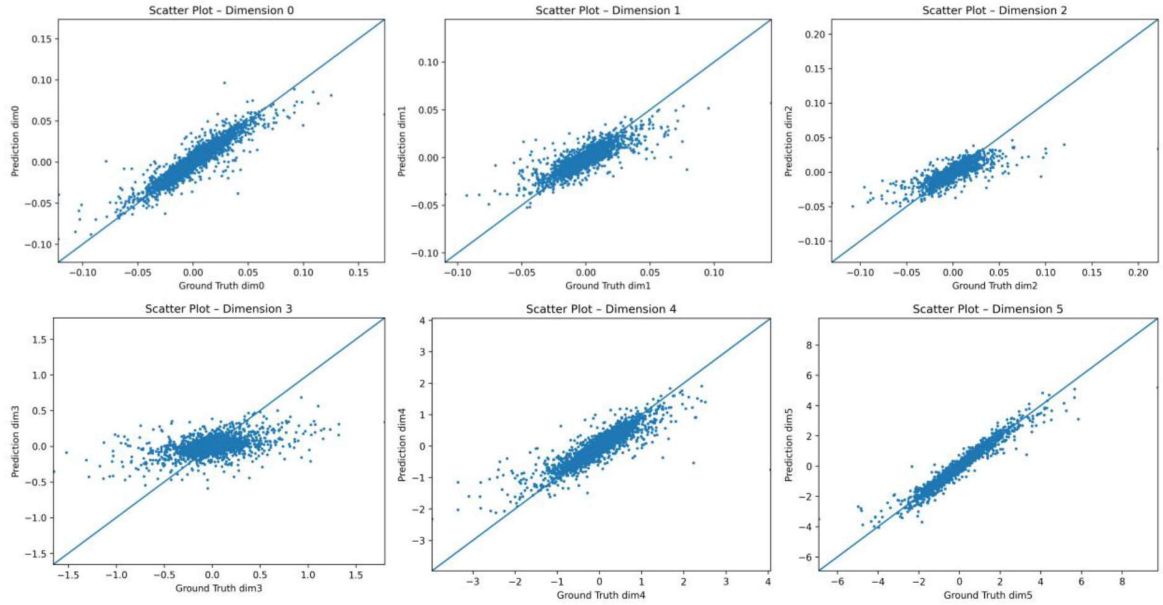

Fig. 2. Scatter plots of each of the six motion parameters

Discussion: The RWKV-MoEst model with random cropping on x and y outperformed other regimes, this suggests that restriction augmentation along the z-axis helps the model avoid cropping out supporting the hypotheses that preserving the z dimension is important but removing subject-specific anatomy aids generalisation. It is also noticeable from Figure 2 that the pitch rotation is most challenging to predict for the awake infant fMRI data, likely due to their frequent and irregular nodding movement.

Conclusions: This study presents RWKV-MoEst, an RWKV-based model designed for 4D fMRI Motion Estimation, highlighting the feasibility of using DNNs to predict motion parameters from raw fMRI.

References

[1].C. T. Ellis, L. J. Skalaban, T. S. Yates, V. R. Bejjanki, N. I. Córdova, and N. B. Turk-Browne Nat. Commun. **11**, 4523 (2020).

[2].J. F. Soares, R. Abreu, A. C. Lima, L. Sousa, S. Batista, M. Castelo-Branco, and J. V. Duarte Front. Neurosci. **16**, 1017211 (2022).

[3].B. Peng, D. Goldstein, Q. G. Anthony, A. Albalak, E. Alcaide, S. Biderman, E. Cheah, T. Ferdinan, K. K. GV, H. Hou, S. Krishna, R. McClelland Jr., N. Muennighoff, F. Obeid, A. Saito, G. Song, H. Tu, R. Zhang, B. Zhao, Q. Zhao et al. Eagle and Finch: RWKV with Matrix-Valued States and Dynamic Recurrence. Proc. COLM, 2024.

[4].C. O'Doherty, Á. T. Dineen, A. Truzzi, G. King, L. Zaadnoordijk, E. L. D'Arcy, J. White, K. Harrison, R. Cusack et al. Deep neural network models of infant visual cortex. CCN, 2024.

Microstructural imaging of Glioblastoma using ultra-strong gradient diffusion MRI

Michael Law[1], Jennifer Golten[1,2,3], Elise Gwyther[1], Najmus Sahar Iqbal[2], George Eralil[2], Harpreet Hyare[4], Kathy Seddon[5], Florien Siebzehnrubl[1], James Powell[2,3,5], Derek Jones[1], Marco Palombo[1].

1. Cardiff University, CF10 3AT, 2. Velindre cancer centre, Cardiff CF14 2TL, 3. University Hospital Wales, Cardiff CF14 4XW, 4. University College London, WC1E 6BT 5. Wales Cancer research Centre

Aims

Glioblastoma (GBM) is the most common and aggressive CNS tumour in adults. Treatment involves maximum resection followed by radiotherapy and Temozolomide chemotherapy. However, recurrence almost always occurs, and median survival is 12-18 months. Additionally, repeat biopsies of brain tumours are challenging, and there is a need for sensitive non-invasive tools to monitor disease progression and treatment efficacy. Standard MRI imaging is a non-invasive, non-ionising tool but lacks the resolution to detect microstructural changes characteristic of early stage GBM recurrence. Diffusion MRI (dMRI) is sensitive to water movement in tissues at a much higher resolution than standard MRI imaging. By using a range of b values the signal can be sensitised to different compartments in the tissue, then model assumptions can be applied to link these to changes in microstructure[1]. By modelling changes in the microstructure using high quality diffusion data at multiple timepoints, it could be possible to define biomarkers of treatment response and progression. Here we present two rich dMRI datasets at baseline and aim to collect 40 datasets at three timepoints using a state-of-the-art ultra-strong gradient dMRI scanner[2] to assess treatment response and disease progression.

Method

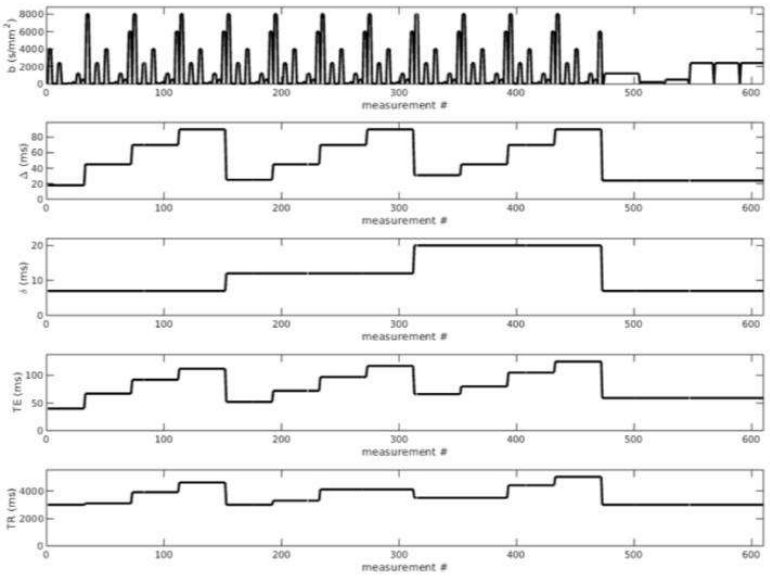

Figure 1 *Acquisition parameters of the MIMOSA study and how the parameters change in relation to each other over the duration of the scan. Total acquisition time = 1h:10m.*

dMRI datasets of suspected glioblastoma patients were acquired with a 3T Siemens Connectom scanner equipped with an ultra-strong gradient system (300 mT/m), using a pulsed-gradient spin-echo echo-planar imaging (PGSE-EPI) sequence with voxel resolution 2 mm² isotropic and full brain coverage; SENSE=2; b-values: [100, 200 500, 1200, 2400, 4000, 6000, 8000]s/mm²) in three orthogonal directions; TE=[40-125] ms and TR=[3000-5000] ms. For each b-value and TE/TR combination, three diffusion encoding schemes were employed: Δ=[18–90] ms, δ=7 ms; Δ=[25–90] ms, δ=12 ms; and Δ=[31–90] ms, δ=20 ms (**Fig.1**).

Processing included denoising, Gibbs ringing, eddy current, motion and gradient non-uniformity corrections. Whole-brain parametric maps of overall *T1* relaxation time, compartmental T2 relaxation times (intracellular $T2_{ic}$, extracellular $T2_e$, intra-neurite $T2_{in}$) and diffusion properties (extracellular, cellular and neurite signal fractions f_e, f_{ic} and f_{in}=1-f_e-f_{ic}, cell radius R and intra-neurite diffusivity D_{in}) were obtained by fitting a modified Relaxation-VERDICT model[3] to the data at b values > 100 s/mm²:

$$S(b,\Delta,\delta,TE,TR) = S_0(1-e^{-\frac{TR}{T_1}})(f_e e^{-\frac{TE}{T2_e}} S_{ball}(b,D_e) + f_{ic} e^{-\frac{TE}{T2_{ic}}} S_{sph}(b,\Delta,\delta,R) + f_{in} e^{-\frac{TE}{T2_{in}}} S_{stk}(b,D_{in}))$$

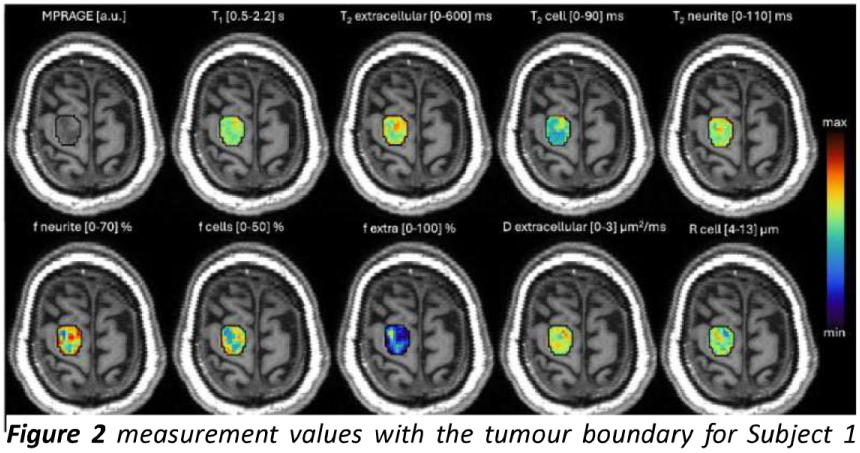

Figure 2 *measurement values with the tumour boundary for Subject 1 diagnosed with Meningioma, for T1, T2 extracellular component, T2 cell, T2 neurite, f neurite, f cell, f extra, D extracellular, and R cell. Region of low cellularity in the central tumour region corresponding to an area of necrosis in f cells and R cell.*

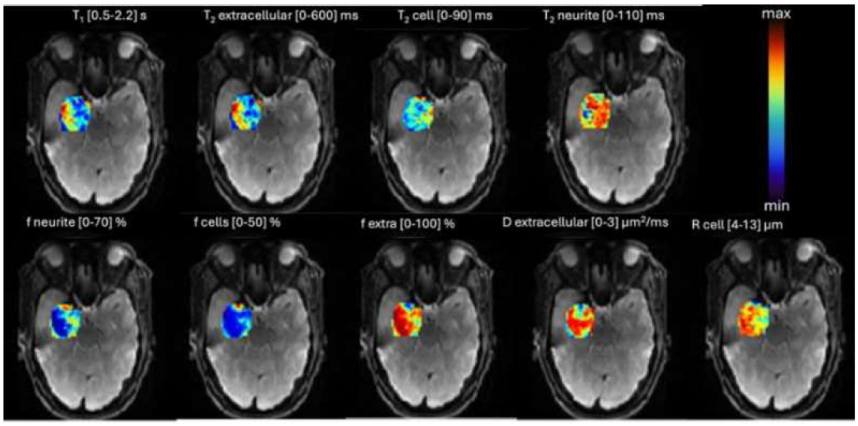

Figure 3 *Tumour parametric map of T1, T2 extracellular, T2 cell, T2 neurite, neurite fraction, cellular fraction, extracellular fraction, extracellular diffusivity, and cell radius in a grade 4 glioblastoma patient.*

Results

We show unique dMRI measurements with ultra-high diffusion weighting and multiple (b,TE,TR,Δ,δ) combinations enabling unprecedented characterisation of the GBM microenvironment. Excellent data quality (SNR>35) has enabled the estimation of whole-brain parametric maps, showing higher cell radii, cellular fraction (f cells and R cell) around two edges of patient 1 (**Fig.2**) with a central area of lower cellularity which corresponded to findings of a necrotic core upon resection, and more uniform T2 measurements corresponding to a more homogeneous tumour. For subject 2 (**Fig.3**) the T2 measurements were highly diffuse while diffusion compartments defined shaped boundaries with higher cell radii towards the lateral side of the tumour.

Discussion

Analysis of data produced high quality subject-specific tumour parametric maps. Participant 1 was diagnosed histologically with a grade 2 atypical meningioma. F cells, and f extra parameter maps (**Fig.2**) exhibited a low overall cellularity in a section running through the anterior-posterior direction corresponding to histologically confirmed central necrosis. Overall cellularity (R cell, f cell) and diffusion parameters (D extra) were more uniform as expected from a lower grade tumour.

The parametric maps of glioblastoma patient 2 (**Fig.3**) were far more diffuse on T2 measures, characteristic of glioblastoma heterogeneity and had areas of high R-cell and f-cell at the edges likely indicating areas of high proliferation. Extracellular diffusion and cell radii were higher and more varied in this subject again fitting with the higher histological grade.

Conclusion

The ultra-strong gradient scanner (b-value up to 8000 s/mm^2) and novel dMRI acquisition (varying TE, TR, Δ, and δ) shows promise for monitoring the GBM microenvironment. We showed high resolution maps of diffusion and relaxation properties (e.g., T2 in extra, intra and cellular compartments, and cell radius) which identify tumour grade specific characteristics and could potentially further assist in diagnosis and boundary identification for surgical intervention. We aim to predict treatment response with follow-up scans at three and six months.

References: [1]Alexander D.C. et al. NMR Biomed. 2017 [2]Jones D.K. et al. Neuroimage 2018; [3]Palombo M. et al. Nature Sci. Rep. 2023

^{1}H MR spectroscopy and IVIM-DWI to evaluate the effects of lonidamine and temozolomide treatment in a mouse model of glioblastoma

Tareq Alrashidi[a], Sourav Bhaduri[b], Elisabeth Non Gash[a], Mohesh Moothanchery[a], Christopher Ball[a], Sultan Aljuraysi[c], Stephen Pickup[d], Mahon L Maguire[a], Harish Poptani[a]

[a] Centre for Pre-Clinical Imaging Depart. University of Liverpool, Crown Street, Liverpool, L69 3BX

[b] Institute for Advancing Intelligence (IAI), TCG CREST, Kolkata, India

[c] Department of Physiology, King Saud University, Riyadh, Saudi Arabia

[d] Department of Radiology, University of Pennsylvania, Philadelphia, USA

Introduction: Enhanced glycolysis is a distinctive hallmark of cancer (Warburg effect) [1]. Lonidamine (LND) is an inhibitor of aerobic glycolysis and mitochondrial respiration, but only has a modest antineoplastic impact when used as a single agent [2]. However, when combined with temozolomide (TMZ), it results in a dramatic effect in melanomas [3]. TMZ is the standard of care for GBM and has led to an increased median overall survival in about 50% of patients [4]. Lonidamine induces intracellular acidification and reduction in ATP production by inhibiting various metabolic pathways, thereby sensitising tumour cells to conventional therapies like TMZ [3,5,6]. TMZ is subject to an energy-dependent multi-drug resistance that pumps the cytotoxic effect out of the tumour cell, which is potentially diminished by LND-mediated tumour denergization [3,5], so it is rational to combine TMZ with LND to enhance the therapeutic outcome. As LND causes intracellular acidification through the inhibition of lactate export, it was expected that LND would increase the TMZ stability within tumors; however, this has enhanced both short-term and long-term tumour response to TMZ, as shown in studies on melanoma xenografts [7]. The combination of LND+TMZ has been reported in human melanoma xenografts assessed by ^{31}P MRS and ^{1}H lactate [7]; however, it hasn't been reported in GBMs. The current study was thus performed to evaluate the synergistic effect of LND and TMZ using longitudinal MRS.

Methods: C57BL6 mice were injected intracranially with $2.5x10^5$ GL261 GBM cells in the right cortex. When tumours exceeded 2 mm on T2-weighted MRI, animals received daily treatment for five days: saline (control, i.p.), LND (100 mg/kg, i.p.), TMZ (50 mg/kg, oral gavage), or LND+TMZ (both as above). MRI was performed on days 0, 3, and 6. Single-voxel (2×2×2 mm³) PRESS spectra (TR = 2000 ms, TE1 = 9.13 ms, TE2 = 7.37 ms, 200 averages, 2048 points, 4401 Hz) were acquired from the tumour, and metabolite ratios (tCho/NAA, Lip+Lac/tCr) quantified using QUEST in jMRUI. Lactate was assessed with ISIS-SelMQC (TR = 2000 ms, 32 averages, 2048 points, 8012 Hz) using the same voxel placement of PRESS. IVIM-DWI (13 b-values, spin-echo EPI) was analysed with in-house software to derive D, D*, and f.

Results: Representative ^1H ISIS-SelMQC spectra for LND (red), TMZ (blue), LND+TMZ (green), and saline control (black) groups are shown in Fig. 1B–E at days 0, 3, and 6. At baseline, lactate resonance was detectable in all groups. Post-treatment, lactate became undetectable in LND and LND+TMZ groups, indicating marked suppression of glycolytic activity; TMZ produced a gradual decline, while saline controls maintained detectable lactate throughout, consistent with sustained glycolytic metabolism in untreated tumours. Quantitative analysis of the % change (relative to baseline) in lactate signal intensity at day 3 and day 6 in all the groups (Fig. 1F).

No significant difference in tumour volume was observed between any group. The tCho/NAA ratio decreased steadily in TMZ and LND+TMZ animals but increased in controls, yielding significant differences at day 6 ($p=0.04$ and $p=0.01$, respectively; Fig. 2A). Both treated groups also showed a non-significant declining trend in Lip+Lac/tCr (Fig. 2B) relative to saline. True-diffusion coefficient (D) values

did not differ significantly between groups (Fig. 2C). A representative PRESS spectrum from the tumour (Fig. 2D) shows characteristic resonances including Lip+Lac, NAA, Glx, tCr, tCho, and mI.

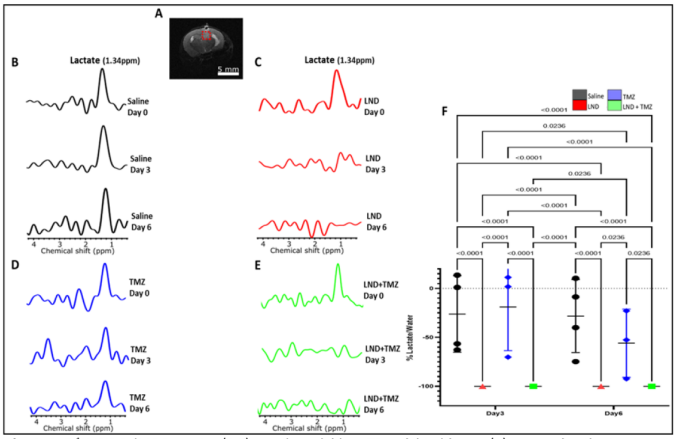

Fig. 1. A_F. ^{1}H ISIS-SelMQC spectra (B-E), voxel overlaid on T2 weighted image (A), comparing the treatment response on day 0, day 3, and day 6 in LND group (C, red spectra), TMZ (D, blue spectra) and LND+TMZ group (E, green spectra) compared to saline control group (B, black spectra). Fig. 1F shows quantitative analysis of % changes (relative to baseline) in Lactate/Water ratios between all treated groups and the control saline one.

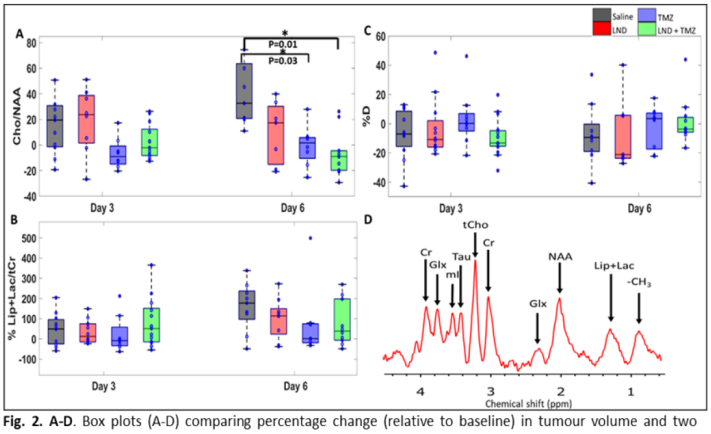

Fig. 2. A-D. Box plots (A-D) comparing percentage change (relative to baseline) in tumour volume and two amplitude ratios (tCho/NAA, Lip+Lac/tCr) between saline and LND+TMZ groups. Box plots illustrating the percent change in the IVIM-DWI parameter, D, with time relative to day 0 for all groups. A representative 1H MR spectra showing Lip + Lac, NAA, Glx, tCr, tCho and mI peaks from the tumour region (D). Asterisks indicate that the difference between groups reached a significance level of ≤ 0.05.

Discussion: We observed a significant metabolic change in tumours treated with LND, TMZ and LND+TMZ despite no differences in the tumour growth or survival between treated and control animals. The disappearance of the lactate signal indicates inhibition of lactic acid production and may subsequent depletion of ATP, resulting in reduced tumour cell proliferation due to the combined effects of LND and TMZ [7]. A significant reduction in the tCho/NAA ratio may reflect decreased cellular proliferation, given choline's role as a marker of membrane turnover, and the effect of temozolomide (TMZ) in halting DNA replication, thereby limiting tumour cell growth [3]. The notable reduction of Lip+Lac/tCr is probably due to a decrease in tumour lactate as evidenced by the ^{1}H ISIS-SelMQC. However, as the tumours kept growing at a similar rate to controls, and IVIM-DWI parameters, particularly D, did not show any significant changes among cohorts. Further studies are needed in a larger cohort as well as longer study points to evaluate whether these metabolic changes are only acute in nature or whether the therapeutic effect (reduction in volume) of the combined treatment with LND+TMZ happens much later, which would further indicate that metabolic changes are earlier marker of treatment response.

Conclusion: Tumour selectivity and low toxicity to normal tissues are critical characteristics that make LND an attractive agent for the treatment of cancer by potentiating the activity of other agents such as TMZ. MRS has been shown to detect metabolic-induced changes, offering the potential for monitoring early post-treatment changes.

References

[1] Vander Heiden MG, Cantley LC, Thompson CB. Understanding the Warburg effect: the metabolic requirements of cell proliferation. *Science*. 2009;324(5930):1029-1033.

[2] Forster R, Campana A, D'Onofrio E, Henderson L, Mosesso P, Scorza Barcellona P. Lonidamine: a non-mutagenic antitumor agent. *Carcinogenesis*. 1990;11(9):1509-1515.

[3] Huang Y, Sun G, Sun X, et al. The Potential of Lonidamine in Combination with Chemotherapy and Physical Therapy in Cancer Treatment. *Cancers (Basel)*. 2020;12(11):3332.

[4] Ortiz R, Perazzoli G, Cabeza L, et al. Temozolomide: An Updated Overview of Resistance Mechanisms, Nanotechnology Advances and Clinical Applications. *Curr Neuropharmacol*. 2021;19(4):513-537. doi:10.2174.

[5] Nath K, Guo L, Nancolas B, et al. Mechanism of antineoplastic activity of lonidamine. *Biochim Biophys Acta*. 2016;1866(2):151-162. doi:10.1016.

[6] Cervantes-Madrid D, Romero Y, Dueñas-González A. Reviving Lonidamine and 6-Diazo-5-oxo-L-norleucine to Be Used in Combination for Metabolic Cancer Therapy. *Biomed Res Int*.2015:690492. doi:10.1155.

[7] Nath K, Nelson DS, Roman J, et al. Effect of Lonidamine on Systemic Therapy of DB-1 Human Melanoma Xenografts with Temozolomide. *Anticancer Res*. 2017;37(7).

Combining single and double diffusion encoding for improved dendritic spine density estimation with magnetic resonance spectroscopy

Maëliss Jallais[1,2], Sophie Malaquin[3], Kadir Simsek[1,2], Julien Valette[3], Marco Palombo[1,2]
[1]CUBRIC, Cardiff University, Cardiff, United Kingdom; [2]School of Computer Science and Informatics, Cardiff University, Cardiff, United Kingdom; [3]Université Paris-Saclay, CEA, CNRS, Molecular Imaging Research Center (MIRCen), Fontenay aux Roses, France.

Introduction: Diffusion-weighted MR spectroscopy (dMRS) probes brain microstructure by examining cell-specific metabolite diffusion, such as N-acetylaspartate (NAA), predominantly found in neurons. Recent works investigated the sensitivity of Single Diffusion Encoding (SDE) [1-3] and Double Diffusion Encoding (DDE) [4-6] to fine cellular structures, such as dendritic spines. Here, we consider two acquisition sequences: SDE with high b-values and DDE in the long mixing time regime, where sensitivity to soma size, branching and dendritic length is minimal [4]. Our goal is to evaluate the robustness of spine density estimates in realistic scenarios using those two acquisitions, and how combining them can help reducing the estimates bias, uncertainty and degeneracies. Using a gray matter (GM) model of spiny dendrites and somas, we simulate SDE/DDE signals, estimate spine density posterior distributions, and compare with in-vivo dMRS mouse data.

Methods: Acquisition sequences (matched for simulations and in-vivo data):

- SDE: b-values=[0.02,0.5,1.5,3,6,10,15,20] ms/µm2, 16 diffusion encoding directions uniformly distributed per b-shell, diffusion time Δ=54.2 ms, gradient duration δ=3.1 ms, TE=58.4 ms.
- DDE: Δ=30 ms, δ=4.5 ms, mixing time=29.5 ms, b-values=[1, 7.5] ms/µm² per diffusion block, TE=144 ms, 32 gradient directions isotropically distributed on a half-sphere for the first block and second block's orientation w.r.t. the first block θ varying from 0° to 180° in 45° steps. Reported signals are averaged across the 32 directions.

Numerical Simulations (Fig.1):

- Model 1: Isotropically distributed spiny dendrites were modeled with the Trees-Toolbox [7] for skeleton building and meshed in Blender. We simulated the SDE/DDE signals using the Monte-Carlo simulator DisimPy [8], applying 16 isotropic rotations to minimize macroscopic anisotropy bias. Spine densities σ ranged from 0 to 3.5 spines/µm and diffusivities D from 0.25 to 0.45 µm²/ms.
- Model 2: Adds a non-exchanging spherical compartment (radius=5µm, same diffusivity as spiny dendrites) to Model 1 to represent somas in GM[9], whose signals were generated analytically using MISST [10], with soma signal fractions $fs \in [0.05;0.34]$.

In-vivo data**:** Seven C57BL/6J mice (4 overexpressing amyloid precursor protein, APP+; 3 wild-type, APP-) were scanned on a 11.7T scanner using a cryoprobe. The MRS acquisitions were performed in a 15 µL voxel positioned in the cortex, using the protocols in [11] (SDE) and [5] (DDE). Water signal was suppressed using a VAPOR module. Signal post-processing was performed as described in [12].

Inference: We estimated posterior distributions of σ, D and fs using µGUIDE [13], a Bayesian inference framework, using the SDE and DDE signals separately or combining them. We extracted three quantities from the posterior distributions: the maximum-a-posteriori (MAP), an uncertainty value, based on the interquartile range, and assessed degeneracies, that is multimodality in the distributions. We trained it on $2x10^5$ simulations with random combinations of the models parameters uniformly sampled from biologically plausible ranges, with added Gaussian noise with SNR$\sim$N(135,13.5) to match the noise in the acquired tNAA group-averaged (APP– and APP+) signals.

Results: Fig1d-e show examples of SDE and DDE normalized signals for varying spine densities. SDE signals attenuate less with increasing spine density, while DDE θ-modulation decreases, suggesting both sequences are sensitive to spine density. Fig.2 presents the estimated MAPs versus ground truth values used for simulating the signals, uncertainty values distribution, and the percentage of degenerate posterior distributions when considering SDE and DDE signals separately or jointly. Finally, µGUIDE was applied to group-averaged mice in-vivo signals (Fig.3). Fig.3b (Model 1) shows distinct posterior distributions between the two groups, suggesting measurable differences in microstructure.

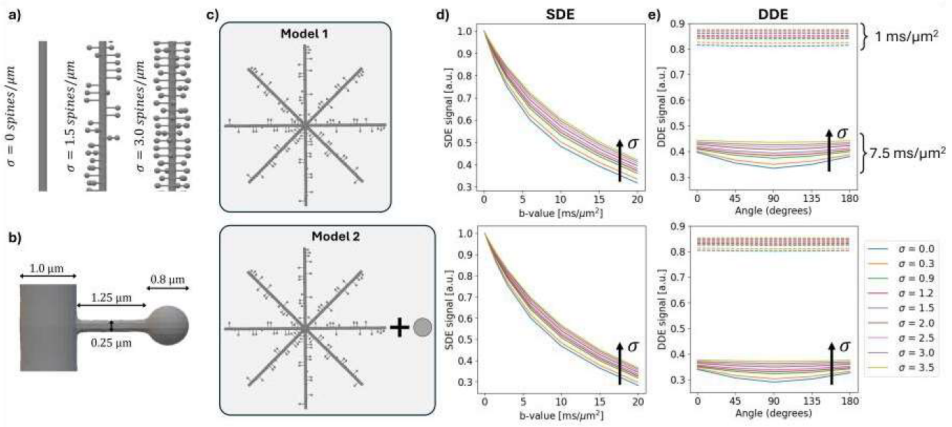

Fig.1: a) Spiny dendrites with varying spine density. **b)** Spine characteristics. **c)** Two numerical models. **d-e)** Examples of normalized SDE and DDE signals respectively for varying spine densities with fixed diffusivity (D = 0.35µm2/ms) and soma fraction (fs = 0.2).

Discussion: Combining SDE/DDE acquisitions allows to reduce uncertainty and remove almost all degeneracies. The APP mouse model is known to lead up to 50% decrease in spine density and plaque-associated dystrophic neurites with disrupted trajectories[14], which agrees with our estimates of σ and D from the neuronal tNAA.

Conclusions: Using simulations, in-vivo mouse data and AI-based Bayesian inference, we show that combining SDE and DDE-MRS enables accurate and precise estimation of dendritic spine density, providing a new avenue for in-vivo studies of brain GM microstructure.

References: [1]Simsek and Palombo, *ISMRM 2024*. Program number 0933 [2]Simsek and Palombo, *ISMRM 2024*. Program number 3456 [3]Chakwizira et al., *ISMRM 2024*. Program number 3463 [4]Ianus et al., *NeuroImage* (2021) [5]Vincent et al., *NeuroImage* (2020) [6]Jallais et al., *ISMRM 2025*. Program number 3898 [7]Cuntz et al., *PLoS Comput Biol.* (2010) [8]Kerkeläet al., *J Open Source Softw.* (2020) [9]Palomboet al., *Neuroimage* (2020) [10]Ianuş et al., *SASHIMI 2016* [11]Mougel et al., *Journal of Magnetic Resonance* (2022) [12]Ligneul et al., *MRM* (2017) [13]Jallais and Palombo, *eLife* (2024) [14]Spireset al., *Journal of Neuroscience* (2005).

Acknowledgements: This work, MJ, KS and MP are supported by UKRI Future Leaders Fellowship (MR/T020296/2). This project has received funding from the European Research Council under the European Union's Horizon 2020 research and innovation programmes (grant agreement No 818266).

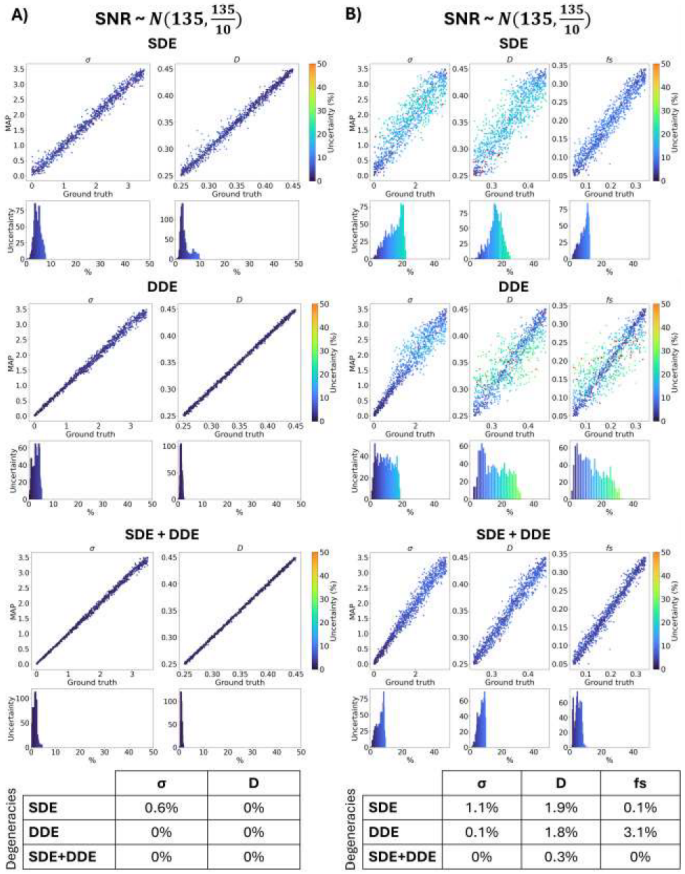

A)	σ	D
SDE	0.6%	0%
DDE	0%	0%
SDE+DDE	0%	0%

B)	σ	D	fs
SDE	1.1%	1.9%	0.1%
DDE	0.1%	1.8%	3.1%
SDE+DDE	0%	0.3%	0%

Fig.2: Estimations of Model 1 (**A**) and Model 2 (**B**) parameters with µGUIDE, using the SDE (first row) and DDE (second row) signals separately, or combining the two (third row). We report the estimated MAPs vs ground truth values used for generating the simulations, the uncertainty distribution, and the percentage of degenerate posterior distributions.

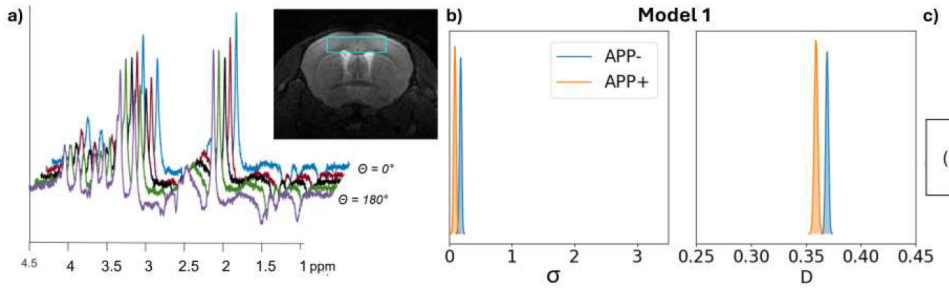

		σ [spines/µm]	D [µm²/ms]
tNAA (Neuronal marker)	APP-	0.22	0.37
	APP+	0.11	0.36

Fig. 3: a) dMRS spectra and positioning of the voxel in the cortex. **b)** Posterior distributions obtained using Model 1 on the tNAA signal using the mean mice signal per group. **c)** MAP estimates.

Investigation of Gradient-Induced Artefacts in Simultaneous Graphene-Array Electrophysiology-fMRI in 7T Preclinical MRI

Suchit Kumar[1], Boyuan Song[1], Samuel M. Flaherty[2], Alejandro Labastida-Ramírez[2], Nerea Alvarez de Eulate Llano[3,4], Anton Guimerà Brunet[3,4], Ben Dickie[4], Rob C. Wykes[1,2], Kostas Kostarelos[2], Louis Lemieux[1*]

[1]University College London Queen Square Institute of Neurology, London, UK

[2]Centre for Nanotechnology in Medicine & Division Neuroscience, University of Manchester, UK

[3]Institut de Microelectrònica de Barcelona (IMB-CNM, CSIC), Universitat Autònoma de Barcelona, Barcelona, Spain

[4]Centro de Investigación Biomédica en Red en Bioingeniería, Biomateriales y Nanomedicina (CIBER-BBN), Madrid, Spain

[5]Division of Informatics, Imaging and Data Sciences, University of Manchester, Manchester, UK

Introduction: Concurrent electrophysiology (EP) and functional magnetic resonance imaging (fMRI) is a powerful technique for investigating brain activity, offering insights into both electrical and hemodynamic processes. However, a significant challenge in simultaneous EP-fMRI acquisitions is the contamination of electrophysiological data by artifacts, primarily the gradient artifact (GA), which is induced by the rapidly switching magnetic gradients of the MRI scanner. Traditional artifact correction methods, such as Average Artefact Subtraction (AAS), are commonly employed to mitigate these artefact [1]. New graphene-based electrophysiological recording technology, specifically Graphene Solution-Gated Field-Effect Transistors (gSGFETs) [2], offers distinct advantages over conventional electrodes, including a significantly reduced amount of metallic content that can interfere with MRI signals and the capability for high-fidelity DC-coupled brain signal recording [3]. Given these benefits, there is considerable interest in performing simultaneous MRI acquisitions in animals with implanted gSGFET probes. This pilot study aims to investigate the performance of these novel probes during concurrent MRI acquisition in rodents within the MRI environment, with the specific goal of understanding and effectively removing the gradient artifacts induced during MRI scanning.

Methods: Electrophysiology data were acquired using 16-channel graphene arrays of gSGFETs, identical to the Computer-Aided Design (CAD) model presented in Fig. 1A. Magnetic Resonance Imaging was performed on an Agilent 7-Tesla, 16 cm horizontal-bore magnet interfaced with a Bruker Biospec Avance III console. A custom-built 25 mm diameter loop surface coil was designed for both RF transmission and reception (Fig. 1B), specifically due to the unavailability of space to effectively accommodate the arrays and PCB in commercial volume RF coil. This RF coil was positioned above the rodent's head, with the graphene arrays cemented and their PCB located inside the loop coil. The arrays were connected via a long MRI-compatible cable to a recording amplifier, which was situated outside the MRI's safety line.

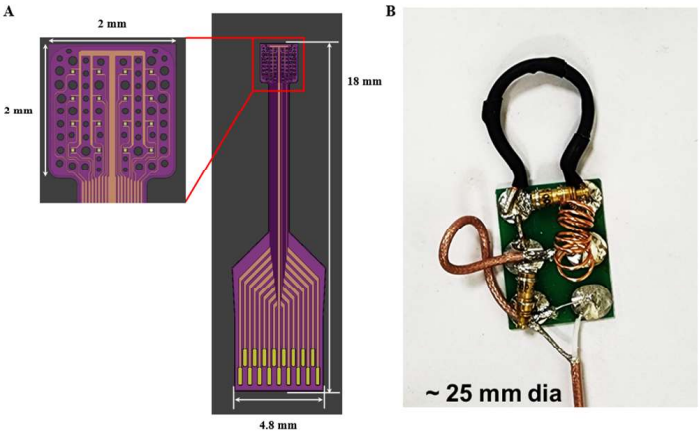

Fig. 1. *(A) Schematic CAD diagrams and dimensions of the epicortical probe (for a detailed description, see [4]); (B) Custom-built transmit–receive loop RF coil.*

Electrophysiological data were recorded on a healthy rodent at a sampling rate of 50 kHz using a 32-channel recorder system configured for 16-channel active recording (Multichannel Systems). The raw data were subsequently exported to the EDF for inspection and gradient artifact correction using either BrainVision Analyzer or EEGLAB software. Due to the absence of direct synchronization

between the MRI scanner clock and the MCS amplifier, automated artifact correction features within these tools were not effective. Consequently, manual marker detection was performed for each slice repetition time (TR) before applying the AAS correction algorithm to the raw electrophysiology data.

Results: Prior to data acquisition, the custom-built RF coil underwent rigorous tuning and matching procedures inside the MRI scanner, utilizing a uniform saline phantom loading. This process ensured optimal resonance at 300 MHz, as verified by a Vector Network Analyzer (VNA). Figure 2 illustrates the comprehensive workflow implemented for GA correction, alongside a representative single slice of the generated artifact template. Figure 3 visually shows the electrophysiological raw data following the crucial manual marker detection step, clearly demonstrating the substantial reduction in gradient artifacts after the application of the AAS correction algorithm.

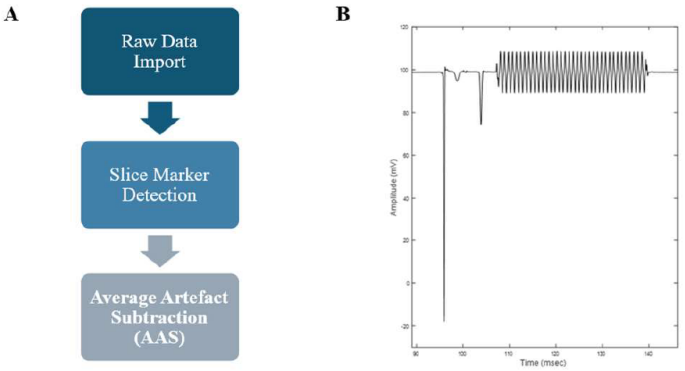

***Fig. 2**. (A) Workflow for unmarked GA correction; (B) Single-slice artefact template.*

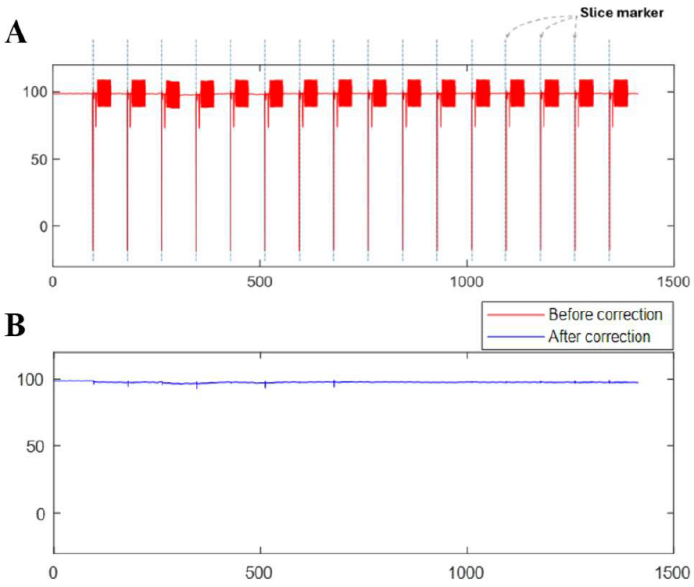

***Fig. 2.** (A) Raw data after the marker detection; (B) Electrophysiology data after the GA correction.*

Discussion: This work shows an progressive effort in utilizing graphene-based technology for the acquisition of electrophysiology data in a healthy anesthetized rat during an active fMRI session. As anticipated, the simultaneously recorded electrophysiological data were significantly contaminated by MRI-induced events, particularly the gradient artifact. Our findings clearly demonstrate that while the AAS method effectively corrects a substantial portion of these artifacts, some residual artifacts persist in the corrected data. This highlights the efficacy of AAS as a primary correction strategy but also underscores the complexity of completely eliminating all MRI-related interference, suggesting avenues for further refinement in artifact removal techniques for future concurrent EP-fMRI studies with these novel probes.

Conclusions: This pilot study successfully demonstrated the feasibility of acquiring electrophysiology data using novel graphene-based probes concurrently with fMRI in a rodent model. The AAS method proved effective in substantially removing these artefacts. While some residual artifacts remain, this research validates the potential of gSGFET technology for simultaneous EP-fMRI. Future studies will focus on further optimizing artifact correction strategies, crucially involving the clock synchronization between the two modalities, and advancing studies on diseased animal models to unlock the full potential of these advanced probes for high-fidelity brain signal recording in the MRI environment.

Acknowledgements: This project is funded by the EPSRC under grant no. EP/X013669/1. The authors are grateful for the support from Sim4life, ZMT for providing the science license.

References: [1] Allen et al. Neuroimage 12 (2000): 230. [2] Bonaccini Calia, Andrea, et al. Nature Nanotechnology 17.3 (2022): 301-309. [3] Wykes, Rob C., et al. Clinical and Translational Medicine 12.7 (2022): 1-4. [4] Cancino-Fuentes, Nathalia, et al. Nanoscale 16.2 (2024): 664-677.

High-resolution T_1-weighted magnetic resonance imaging of myelinated fibre tracts in the caudate putamen of an *ex vivo* murine model at 9.4T

Stephanie Gardner [1, 2], Kate Connor [3], Jeffrey Glennon [4], Friedrich Wetterling [1,2]
[1]Medical Circuits and Systems Lab, Electronic and Electrical Engineering, Trinity College Dublin
[2]Trinity Centre for Biomedical Engineering, Trinity College Dublin
[3]Discipline of Physiology, School of Medicine, Trinity College Dublin
[4]Conway Institute for Biomolecular and Biomedical Research, School of Medicine, University College Dublin, Belfield, Ireland

Introduction: *Ex vivo* brain MRI provides an opportunity to non-invasively explore murine cerebral tissue with histological-level resolution, without destructive tissue sectioning. However, achieving high spatial resolution even at high field strengths, such as 9.4T, comes at the cost of prolonged acquisition times, often requiring over 6 hours or more to achieve isotropic voxels smaller than 100 μm^3 [1], [2], [3], [4]. The aim of this work was to optimise the radiofrequency (RF) receiver exploiting within loop detection for explanted brain tissue and to capture high resolution structural images to explore their potential to track myelinated fibre tracts without the need to conduct diffusion tensor imaging.

Methods: Three coils were used for this study: a) a 2x2 phased array for mouse head imaging, b) a single-loop receive-only detector with 10 mm diameter, and c) a home-built inductively coupled transceiver coil with 15 mm diameter (1 mm thick silver wire, fixed value tuning capacitor, one trimmer capacitor for variable tuning, and a linear translational mechanisms for matching inside the bore of the magnet all mounted to a 3D-printed polylactic acid (PLA) housing, Q unloaded/loaded=380/200). The coil performance was evaluated using two *in vitro* murine brains (10% formalin fixation for approximately 12 months). While coil (a) was assessed on the first brain, coils (b) and (c) were assessed on the second brain. T_2-weighted images were acquired using a 2D RARE sequence (coil a: TR=2500 ms, TE=8.25 ms, TA=2.67 min, coil b: TR=2200 ms, TE=8.75 ms, TA=12.32 min, coil c: TR=2500 ms, TE=8.33 ms, TA=12.0 min) at 9.4T (Bruker BioSpec 94/20). Coil geometries were assessed for Signal to Noise Ratio (SNR) efficiency and homogeneity using MATLAB (Natick, MA, USA). For comparison SNR was normalised to a voxel size of 78 µm × 55 µm × 700 µm, and a total acquisition time of 2.67 minutes (**Fig. 1**). The highest performing coil b was selected for the final ultra-high resolution *in vitro* brain scan at 25 µm isotropic resolution using T_1-weighted 3D FLASH sequence with a total acquisition time of 21.2 hours (TR=50 ms, TE=15.94 ms, flip angle=20°) (**Fig. 2**). Images were processed in Matlab.

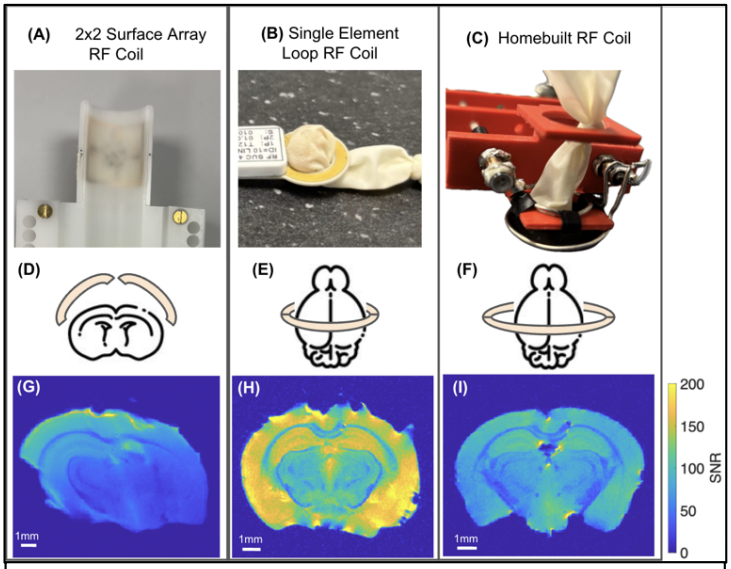

Fig. 1. *Top row: Photos of the three RF coils used (A. 2x2 surface array, B. Single element loop, C. Homebuilt). Middle row: Illustration of configuration between RF coil and ex vivo murine brain sample. Bottom row: SNR maps of three different MRI scans of an ex vivo murine brain. All SNR maps range from zero (dark blue), to 200 (bright yellow). Scale bars on the bottom-left are 1 mm in length. SNR was normalised to a voxel size of 78 µm × 55 µm × 700 µm, and a total acquisition time of 2.67 minutes*

Results: As expected, the SNR in regions closer to the receiver array gained higher SNR for coil a. However, SNR dropped considerably for sub cortical regions. The equivalent SNR was highest for the single-receive

only coil b. Yet, the proximity of the brain tissue to the coil conductor posed challenges in terms of field homogeneity set-up — resulting in considerable susceptibility related distortions in the cortex. Excellent results were found with the slightly larger diameter home-built coil. Coil b provided maximum SNR in caudate putamen and was therefore used for super high-resolution imaging achieving 25 µm isotropic resolution. Such high resolution enabled visualising the myelinated fibre tracts. Fibre tracts were segmented in each image and 3D volume segmentation of the binary maps enabled a first representative computation of myelinated fibre tracts in the caudate putamen.

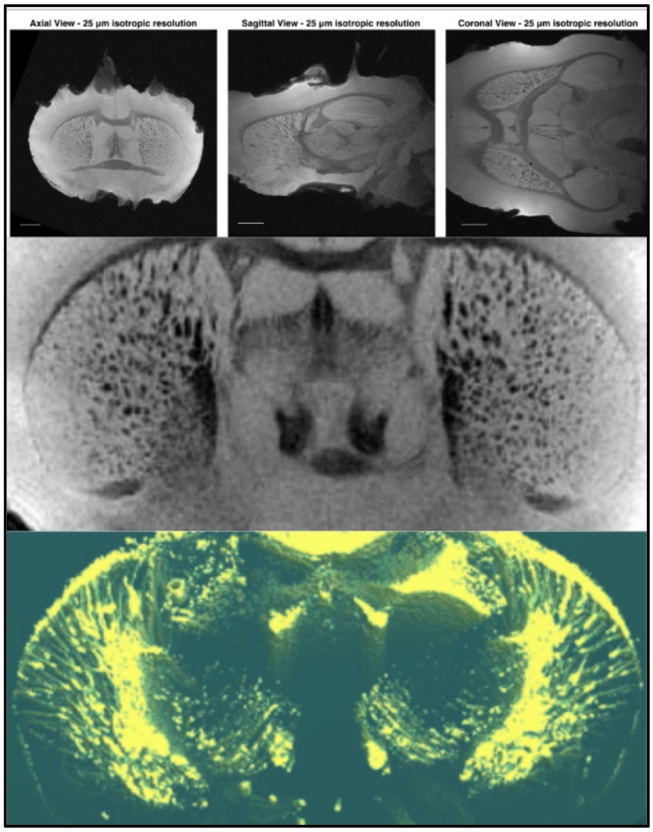

Fig. 2. *T1-weighted, ultra-high resolution 3D FLASH scans of ex vivo murine brain, with a voxel size of 25 µm x 25 µm x 25 µm (TR=50 ms, TE=15.94 ms, flip angle=20°, TA = 21.2 hours). Top row: axial, sagittal, and coronal views, scale bars are 1 mm in length. Middle row: zoomed in T1-weighted image highlighting myelinated fibre tracts as signal voids in caudate putamen. Bottom row: reconstructed fibre tracts in caudate putamen.*

Discussion: The gold standard can be considered to be small angle neutron scattering (SANS) that for a 60 µm thick brain slice offered fibre tract resolution in the range of 1.3 µm [5]. The resulting images in this whole brain study exhibited exceptional anatomical detail, with clear visualisation of myelinated fibre tracts traversing the caudate putamen, as well as distinct contrast between white and grey matter regions, such as the corpus callosum and cortex. Diffusion Tensor Imaging (DTI) requires repetition of data acquisition for many diffusion directions limiting higher spatial resolution and facing uncertainty related to crossing fibres (isotropic voxel resolution is approximately 100 µm in 2 hours) [6]. Direct anatomical resolution of fibre tracts using MRI may offer a means to validate existing DTI reconstruction approaches.

Conclusions: These results highlight the importance of tailored RF coil selection in balancing SNR and spatial coverage for ex vivo specimen. Reconstruction of myelinated fibre tracts may become a viable method to explore ex vivo brain structures in the future.

References

[1] H. Mansour *et al.*, "The Duke Mouse Brain Atlas: MRI and light sheet microscopy stereotaxic atlas of the mouse brain," *Sci. Adv.*, vol. 11, no. 18, p. eadq8089, Apr. 2025

[2] S. Boretius, L. Kasper, R. Tammer, T. Michaelis, and J. Frahm, "MRI of cellular layers in mouse brain in vivo," *Neuroimage*, vol. 47, no. 4, pp. 1252–1260, Oct. 2009.

[3] O. von Bohlen Und Halbach, M. Lotze, and J. P. Pfannmöller, "Post-mortem magnetic resonance microscopy (MRM) of the murine brain at 7 Tesla results in a gain of resolution as compared to in vivo MRM," *Front Neuroanat*, vol. 8, p. 47, June 2014.

[4] R. L. C. Barrett *et al.*, "Tissue optimization strategies for high-quality ex vivo diffusion imaging," *NMR Biomed.*, vol. 36, no. 3, p. e4866, Mar. 2023

[5] S. Maiti, H. Frielinghaus, D. Gräßel, M. Dulle, M. Axer, and S. Förster, "Distribution and orientation of nerve fibers and myelin assembly in a brain section retrieved by small-angle neutron scattering," *Sci. Rep.*, vol. 11, no. 1, p. 17306, Aug. 2021

[6] M. Yon, Q. Bao, O. J. Chitrit, R. N. Henriques, N. Shemesh, and L. Frydman, "High-Resolution 3D in vivo Brain Diffusion Tensor Imaging at Ultrahigh Fields: Following Maturation on Juvenile and Adult Mice," *Front. Neurosci.*, vol. 14, Nov. 2020

[7] M. Sack, F. Wetterling, A. Sartorius, G. Ende, and W. Weber-Fahr, "Signal-to-noise ratio of a mouse brain 13C CryoProbe™ system in comparison with room temperature coils: spectroscopic phantom and in vivo results," *NMR Biomed*, 2014.

Neural correlates of negative autobiographical memory and rumination: a personalised fMRI and pCASL study in healthy volunteers

Laith Alexander[1,2], Edie Charles[1,3], Vasileia Kotoula[1], Mitul Mehta[1]

[1]Centre for Neuroimaging Sciences, King's College London, UK.
[2]South London and Maudsley NHS Foundation Trust, London, United Kingdom
[3]University of Cardiff, Cardiff, UK.

Introduction: The recall of emotionally-valenced memories is relevant to rumination, defined as dwelling on negative thoughts, their causes and their consequences. Rumination is a transdiagnostic vulnerability factor for mood and anxiety disorders, yet its neural correlates are poorly understood. We used a personalised autobiographical memory task during fMRI to understand the neural substrates of negative *vs.* positive autobiographical recall, and how this relates to differences in rumination.

Methods: 20 healthy volunteers (12 females, 8 males) completed the Rumination Response Scale (RRS) questionnaire (Nolen-Hoeksema et al., 1999), and took part in a semi-structured interview to elicit statements and images regarding a positive and negative memory (Life Events and Difficulties schedule; (Brown & Harris, 1978)). Participants then underwent a single fMRI session. The fMRI task comprised echoplanar imaging (EPI) and pseudo-continuous arterial spin labelling (pCASL) components, to understand short-term changes in activation *vs.* intermediate-term changes in blood flow, respectively. During EPI, statements extracted from the positive or negative memory were presented (with block order pseudorandomised), interspersed with a counting task as an explicit baseline. We determined recall-specific (recall minus counting) activation during negative and positive memory statements (one-sample t-tests), together with negative *vs.* positive recall-specific activation (paired t-test). We additionally explored whether activation in identified significant clusters were correlated with trait RRS scores. During pCASL, two images (relating to the same positive or negative memory) were presented for three minutes each following EPI blocks. The contrast of interest was [Negative Images] *vs.* [Positive Images] (paired *t*-test).

Results: Recall-specific activation was observed within the default mode network (DMN) and medial temporal lobe for both positive and negative memory statements, supporting the task's construct validity for eliciting autobiographical memory processes. Recall-specific activation during negative statements *vs.* positive statements was greater in the right anterior insula and dACC (**Figure 1**), and the degree of activation within the right anterior insula correlated with baseline RRS scores.

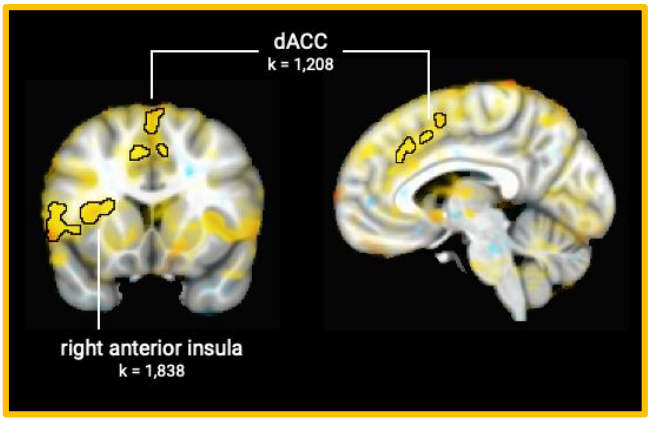

Fig. 1. Increased recall-specific (recall minus counting) activation of the right anterior insula (k = 1,838 voxels) and dACC (k = 1,208 voxels) during negative *vs.* positive memory statements. Cluster-extent corrected, voxelwise $p < 0.005$, $\alpha < 0.05$.

Whole brain pCASL analysis revealed increased right amygdala blood flow during negative memory

recall *vs.* positive memory recall (**Figure 2**).

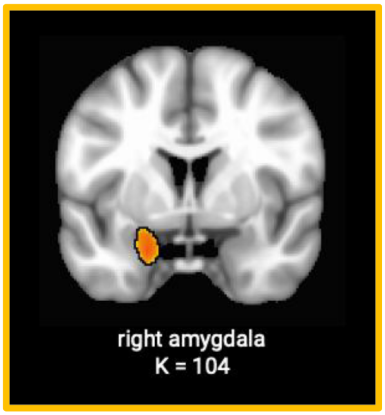

Fig. 2. Increased regional cerebral blood flow to the right amygdala, as measured by pseudo-continuous arterial spin labelling (pCASL), during negative *vs.* positive image viewing. $p < 0.005$, uncorrected.

Conclusions: Our novel, personalised autobiographical memory task robustly elicits circuits involved in autobiographical recall. EPI reveals nodes of the salience network – including dACC and right anterior insula – show increased activation during the short-term recall of negative *vs.* positive autobiographical information. pCASL highlights that over intermediate time courses, blood flow to the right amygdala is increased during negative *vs.* positive recall. These findings provide insight into the limbic network underpinning emotional autobiographical memory and rumination. It informs novel targets for neuromodulation interventions in mood and anxiety disorders.

Acknowledgements: NIHR Academic Clinical Fellowship to LA (ACF-2022-17-016). Royal College of Psychiatrists Academic Trainee Small Grant award to LA.

References:

Brown, G. W., & Harris, T. (Eds.). (1978). *Social Origins of Depression: A study of psychiatric disorder in women*. Routledge. https://doi.org/10.4324/9780203714911

Nolen-Hoeksema, S., Larson, J., & Grayson, C. (1999). Explaining the gender difference in depressive symptoms. *Journal of Personality and Social Psychology*, *77*(5), 1061–1072. https://doi.org/10.1037//0022-3514.77.5.1061

Altered Brain Energy Metabolism in Multiple Sclerosis: Elevated Lactate and Impaired Creatine Response in the Anterior Cingulate Cortex Following Exercise-Induced Fatigue

Gemma Brownbill[1,2], Jeanne Dekerle[3], Mara Cercignani[1,4], Itamar Ronen[1], James Stone[1]

[1]Brighton and Sussex Medical School, University of Sussex, Brighton BN1 9PX, United Kingdom

[2]School of Sport, Exercise and Health Sciences, Loughborough University, Loughborough LE11 3TU, United Kingdom

[3]School of Sport and Health Sciences, University of Brighton, Falmer BN1 9PH, United Kingdom

[4]Cardiff University Brain Research Imaging Centre (CUBRIC), School of Psychology, Cardiff University, Cardiff CF24 4HQ, United Kingdom

Background: Fatigue is a prominent symptom in multiple sclerosis (MS), affecting up to 75% of individuals [1]. Altered brain metabolite concentrations have been related to MS fatigue [2], but the relationship between brain metabolite changes and fatigue in MS, particularly following exertional fatigue, remains unclear. This study aimed to investigate the acute effects of fatiguing isometric wrist extension contractions in people with MS (pwMS) compared to healthy controls on brain metabolite concentrations in the anterior cingulate cortex (ACC), a key brain region in the perception of fatigue in MS [3].

Methods: Twenty-two pwMS (EDSS <3.5, relapsing-remitting, 3 male) and 22 age and gendered matched healthy controls underwent Magnetic Resonance Spectroscopy (1H-MRS) before and after performing fatiguing wrist extension exercises. 1H-MRS data were acquired from the dorsal ACC using a semi-localisation by adiabatic selective refocusing (sLASER) sequence [4]. Wrist extensor contractions were performed inside the scanner with the aid of an MRI compatible wrist ergometer (Fig. 1). Participants' ratings of fatigue and perception of effort were measured prior and post the fatiguing wrist extensions. Concentrations of glutamate + glutamine (Glx), lactate, and total creatine (tCr) were measured in the ACC, a key brain region in the perception of fatigue in MS [4]. Linear mixed models were used to analyse group differences and exercise-induced changes in metabolite concentrations.

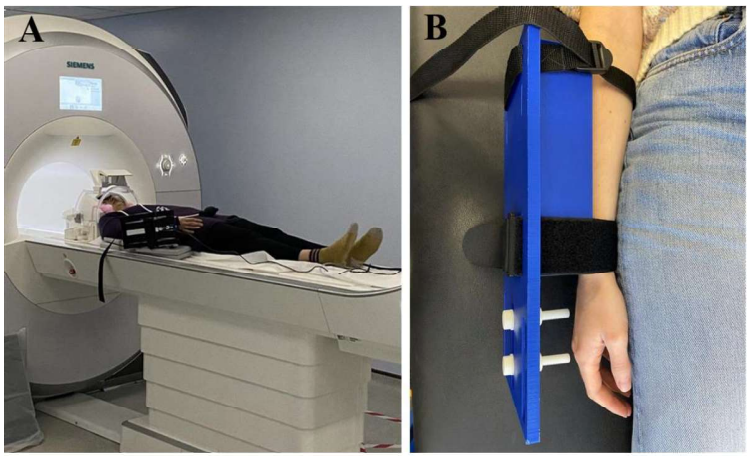

Figure 1. Experimental set-up and participant positioning for the MRI-compatible wrist extension ergometer. Panel A depicts the experimental set-up of the positioning of the participants in the MRI scanner with the MRI-compatible ergometer attached to their right forearm. Panel B shows a close-up of the positioning of the MRI-compatible wrist extension ergometer on the forearm.

Results: PwMS exhibited significantly higher lactate concentrations in the ACC compared to controls

($F_{(1, 42.3)}$ = 7.08, p = 0.011, η_p^2 = 0.14) (Fig. 2; B). No significant differences were observed in Glx concentrations between groups or following exercise (Fig. 2; A). A significant interaction effect was found for tCr ($F_{(1, 41.3)}$ = 4.63, p = 0.037, η_p^2 = 0.10), with tCr significantly decreasing after exercise-induced fatigue by 0.29 mmol/kg post-exercise in controls ($t_{(43)}$ = 3.09, p = 0.02) but remaining stable in pwMS (Fig.2; C). A moderate significant association was observed between changes in lactate and perception of effort in pwMS (r = 0.51, p = 0.04).

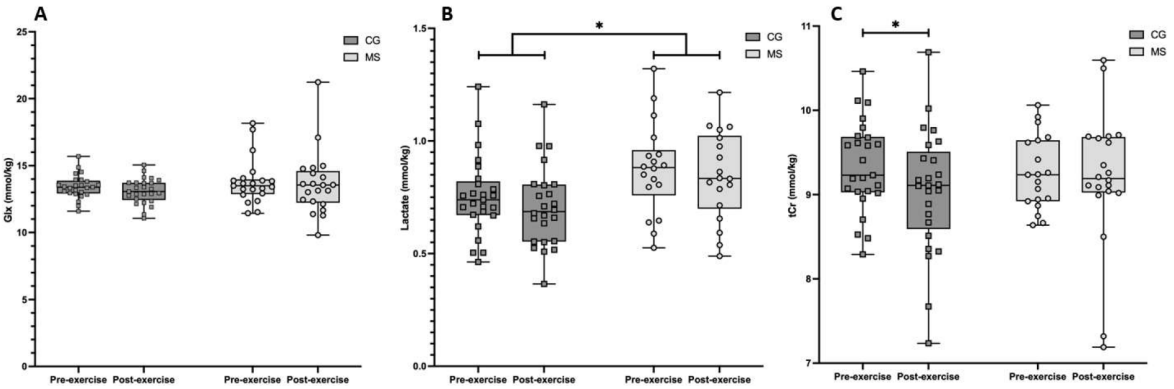

Figure 2. Comparison of glutamate + glutamine concentrations (A), lactate (B) and total creatine (C) in control and multiple sclerosis groups before and after exercise. Glx: glutamate + glutamine; tCr: total creatine; CG: control group; MS: multiple sclerosis; *: $p < 0.05$.

Conclusions: This study provides novel evidence of metabolic differences in the ACC of pwMS, characterised by elevated lactate levels and stable tCr concentrations post-exercise. These findings suggest altered energy metabolism in MS, potentially linked to mitochondrial dysfunction and impaired oxidative phosphorylation. These metabolic alterations in a key fatigue-processing brain region offer new insights into the neurobiological mechanisms underlying MS-related fatigue and may inform future therapeutic strategies.

References

[1] Krupp, L.B., 2003. Fatigue in multiple sclerosis: definition, pathophysiology and treatment. *CNS drugs*, *17*(4), pp.225-234.

[2] Markianos, M., Koutsis, G., Evangelopoulos, M.E., Mandellos, D., Karahalios, G. and Sfagos, C., 2009. Relationship of CSF neurotransmitter metabolite levels to disease severity and disability in multiple sclerosis. *Journal of neurochemistry*, *108*(1), pp.158-164.

[3] Manjaly, Z.M., Harrison, N.A., Critchley, H.D., Do, C.T., Stefanics, G., Wenderoth, N., Lutterotti, A., Müller, A. and Stephan, K.E., 2019. Pathophysiological and cognitive mechanisms of fatigue in multiple sclerosis. *Journal of Neurology, Neurosurgery & Psychiatry*, *90*(6), pp.642-651.

[4] Genovese, G., Marjańska, M., Auerbach, E.J., Cherif, L.Y., Ronen, I., Lehéricy, S. and Branzoli, F., 2021. In vivo diffusion-weighted MRS using semi-LASER in the human brain at 3 T: Methodological aspects and clinical feasibility. *NMR in Biomedicine*, *34*(5), p.e4206.

Time-Resolved Glutamate Responses During Working Memory via a Mixed Block/Event-Related ^{1}H MRS Design

Daniel Cocking[1], Ryan Elson[2], Katherine Dyke[2], Mohammad Zia Ul Haq Katshu[3,4], Claudia Danielmeier[2], Adam Berrington[1]

[1]Sir Peter Mansfield Imaging Centre, School of Physics and Astronomy, University of Nottingham, UK. [2]School of Psychology, University of Nottingham, UK. [3]School of Medicine, University of Nottingham, UK. [4]Nottinghamshire Healthcare NHS Foundation Trust, Nottingham, UK.

Introduction

Functional MRS (fMRS) offers considerable potential for probing neurochemical dynamics during task-related brain activation[1]. Conventionally, fMRS is performed using block designs with spectra averaged across sustained task and rest periods[1-4], but event-related designs may better resolve fast glutamate (Glu) responses[6,7]. A mixed block/event-related approach may offer analytical flexibility, though considerations of sensitivity and timing are essential. Here, we measured Glu dynamics using sLASER (TE=80 ms) during a mixed-design working memory (WM) task in healthy volunteers.

Methods

20 healthy volunteers aged 20-37 years (mean: 29 years, SD: 5 years), eleven female and nine male, were scanned at 7T (Philips Achieva) using a 32-channel receiver coil (Nova Medical). Single-voxel MRS was performed using semi-LASER localisation[8] (TR= 5s, 20x20x20 mm^3, N=2048, BW=6 kHz, TE=80 ms).

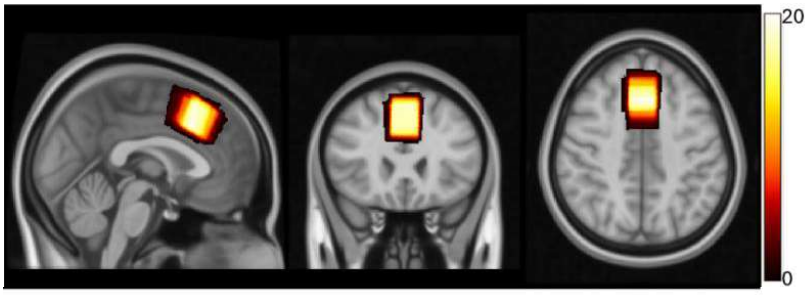

Fig.1*: Subject-averaged MRS voxel position on MNI-152 image showing consistent placement in medial prefrontal cortex. With the colourbar representing number of overlapping ROI's.*

During fMRS acquisition, participants performed an associative visuospatial WM task. Each memory trial began with the *Encoding* phase (2500ms) in which participants memorised the colours, shapes and locations of four stimuli. In the subsequent *Recall* phase (2500 ms), which followed a variable maintenance phase (0.83-5s), a specific shape or location was probed, and participants responded by selecting the associated colour. In *Control* trials (without WM load), participants were presented with only one coloured shape and asked to indicate the colour while the stimulus was still on the screen. The fMRS experiment was performed over blocks of 16 trials of either WM Task or *Control*, separated by 30 s rest periods (see Fig. 2). To obtain time course data, trial onsets were jittered across each block using 16 evenly spaced inter-stimulus intervals (ISIs) (0–2500 ms). A total of four runs were acquired in a counterbalanced design. An initial rest period served as a baseline for each run.

Spectra were processed using FSL-MRS[9] and fit using a truncated-Newton algorithm (no baseline, with macromolecules at 0.9 and 2.1 ppm). Event analysis grouped spectra across trials by phase (encoding, recall and control NSA=32/run/phase), while time course analysis further split spectra into bins according to mean measurement time [0.083, 0.417, 0.75, 1.083, 1.417, 1.750, 2.083, 2.417 s] (NSA=4/run/time group). Glu was normalised to total Creatine (tCr) and reported as percentage (%) change

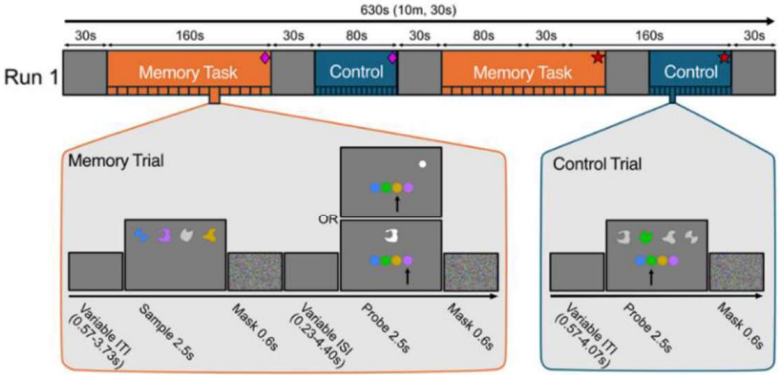

Fig.2*: Schematic of a single run, indicating control and task onset times and an example of the WM task below. Grey blocks indicate rest periods.*

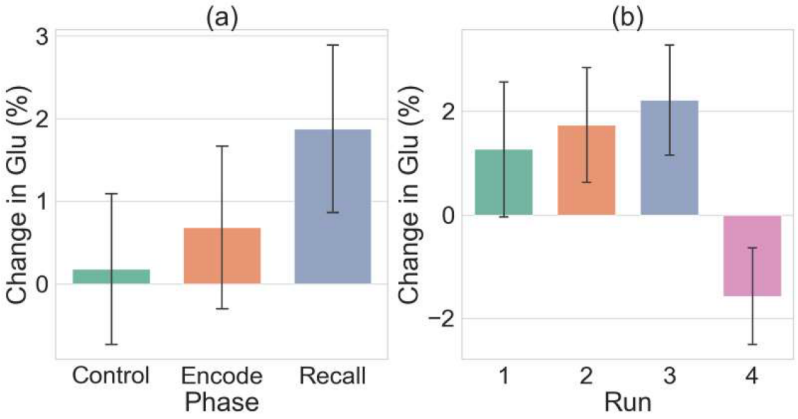

***Fig.3**: Average Glu concentrations over runs and subjects for the different trial types (i.e. phases) (a) and across different runs (b). With errorbars representing standard errors.*

from the initial rest period. A statistical linear model (intercept = 0) was applied to determine effect of phase and run on the blocked data. A timepoint × phase interaction model was used for time course analysis.

Results

The averaged event analysis revealed non-significant increases in all phases (Control, Encoding and Rest) with Glu relative to initial rest spectra (Fig. 3). Overall non-significant increases in Glu were seen in Runs 1, 2 and 3 and a decrease in Run 4. Reaction Times for the control task were 0.9 ± 0.2 s and for the memory task 1.4 ± 0.1 s.

Time course analysis (Fig. 4) showed significant Glu increases occurring during *Recall* at 0.75, 1.083 and 1.417 s following probe, and in Control at 2.417s. This supports distinct temporal Glu profiles for each phase.

Discussion

The medial frontal cortex is implicated in WM maintenance[10], and Glu fluctuations in the dorsolateral prefrontal cortex (DLPFC) during WM tasks are documented[11], consistent with its role in WM[12]. Glu modulation is most pronounced during recall[13], aligning with our findings of non-significant Glu increase during the recall phase.

In the time course analysis the first *in vivo* evidence of statistically significant Glu peaks at ~1.5 s post-stimulus is shown following a WM task, at a temporal resolution of ~300 ms. These dynamics extend beyond previous work which identified peaks in the 300–1000 ms range[6]. Event-related fMRS has been previously used to investigate excitatory/inhibitory balance[7], but longer measurement period post stimulus was needed to resolve later dynamics shown here[14]. Prominent peaks are observed in the control phase at time points corresponding to reaction times, while the largest peak in the recall phase occurs at a similar time to that of the memory task reaction times.

Conclusion

We detect Glu non-significant increases relative to baseline during retrieval in a WM task. We report the first time-resolved Glu responses for encoding, recall, and control with ~300 ms resolution, identifying a peak at ~1.5 s.

Acknowledgements

This study was supported by Wellcome grant 226715/Z/22/Z. AB would like to acknowledge the Royal Academy of Engineering.

References

1. Mangia et al. (2007), 2. Chen et al. (2017), 3. Bell et al. (2021), 4. Stanley & Raz (2018), 5. Jelen et al. (2019), 6. Mullins (2018), 7. Koolschijn et al. (2021), 8. Finkelman et al. +(2022), 9. Clarke et al. (2024), 10. Kaminski et al. (2017), 11. Woodcock et al. (2018), 12. Goldman-Rakic (1995), 13. Stanley et al. (2017), 14. Craven et al. (2024).

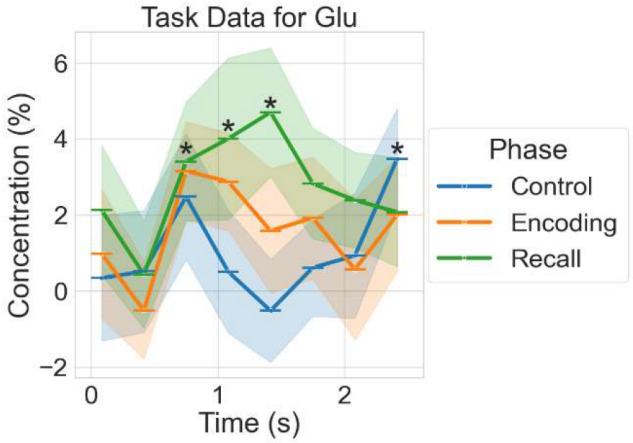

***Fig.4**: Glu response for control (blue), encoding (orange) and recall (green) phase. Concentrations are percentage increases from initial rest spectra. Errorbars are standard error across runs and subjects. Significant points indicated by '*'. Horizontal bars represent the timepoints averaged.*

Regional ATT, but not CBF, Correlates with Amyloid Burden in Early Dementia: Insights from a Multimodal Imaging Exploration

Elizabeth J. Davies[1], Yasmin Tyrrell[1], Olivia N. Murray[2], Aisling Fothergill[1], Hamied Haroon[1], Karl Herholz[1], Jullian Matthews[1], Laura Parkes[1]

[1]Division of Psychology, Communication and Human Neuroscience, School of Health Sciences, Faculty of Biology, Medicine, and Health, University of Manchester, UK [2]Division of Cardiovascular Sciences, School of Medical Sciences, Faculty of Biology, Medicine, and Health, University of Manchester, UK

Email: Elizabeth.davies-7@student.manchester.ac.uk

Introduction: A hallmark of Alzheimer's disease (AD) is the presence of fibrillar amyloid-β (Aβ) plaques. The use of standardised uptake value ratios (SUVRs) in amyloid-PET enables quantification of plaque burden. PET SUVRs have enabled early detection of Aβ pathology[1], however, PET is costly, involves exposure to ionising radiation, and is limited by radiotracer availability. Multi-delay arterial spin labelling (ASL) allows for the quantification of cerebral blood flow (CBF) and arterial transit time (ATT) non-invasively. Perfusion changes may emerge during early AD-Aβ pathology via multiple mechanisms; reduced flow may impair glymphatic clearance of soluble Aβ, while Aβ induced microvascular damage may decrease perfusion. Importantly, recent studies have reported inverse associations between regional CBF and Aβ burden, particularly in early AD and MCI, suggesting that vascular and amyloid changes may interact in these stages of the disease[2].

Global reductions in CBF have been consistently observed in patients with mild cognitive impairment (MCI; a state seen preclinically but not exclusively in AD) and AD, especially in early amyloid-affected regions such as the precuneus[2; 3]. Meta-analyses of voxel-wise ASL studies confirm regional patterns of reduced CBF in AD, yet few compare directly to amyloid PET in the same participants or utilise ATT measures[4]. These analyses assess whether regional hypoperfusion and Aβ plaques co-localise in early AD, using CBF and ATT metrics to better characterise the spatial and temporal dynamics of pathology. This approach could enable alternative sensitive, localised, and biologically meaningful MRI perfusion biomarkers, informing amyloid pathology detection and the proximal aetiology of AD.

Methods: Thirty-four adults (60–80 yrs; mean 70.0 ± 4.8 yrs, 10 amyloid-positive) with Montreal Cognitive Assessment >17 were recruited from community and clinical sources, resulting in a group ranging from normal cognition to MCI. All participants underwent simultaneous MRI and PET on a 3T GE SIGNA PET/MR scanner. Twenty-six received [^{18}F]Flutemetamol and eight [^{18}F]Florbetaben PET. Full methodological details are described in McFadden et al. (2025)[5].

MRI: We acquired a 3D T1 MPRAGE and multi-delay ASL data using pseudo-continuous ASL labelling and 3D spiral FSE read-out, with six label durations of 0.573, 0.885, 2.042, 0.573, 0.885, 2.042 secs and six paired post-label delay times of 0.700, 1.273, 2.158, 1.000, 1.573, 2.458 secs. Calibrated CBF and ATT maps were generated using FSL BASIL with a 1.5 sec BAT prior, and voxel wise M0 calibration [6].

PET: Static time-of-flight reconstructions used the VPFX protocol (4i, 28s, full corrections, ZTE-derived attenuation correction) averaged over 90–110-minute post-injection. Binary amyloid status was classified by an experienced clinical neurologist.

Quantification: CBF, ATT and PET were co-registered to participants T1w native space using FSL FLIRT and SPM12 MATLAB respectively. T1w images processed in FreeSurfer[7] using the Destrieux[8] atlas generated 105 subject-specific cortical and subcortical parcellations. Segmentations were used for PET partial volume corrections (Labbé and region-based-voxel-wise correction in PETPVC[9]). Nine composite ROIs and a control region (Table 1) were defined a priori, informed by consensus literature on regions of early Aβ accumulation in AD[10]. We extracted regional volumes and median values for CBF and ATT and calculated Aβ-PET mean SUVRs normalised to the cerebellum.

Statistical Analysis: Welch's t-tests were used to assess group differences in mean SUVRs across 10 regions (Table 1), ($\alpha < 0.005$ for multiple comparisons). Associations between CBF, ATT and SUVR were assessed via multiple linear regressions (MATLAB) for each ROI and the control region.

Results: Mean SUVR was markedly higher in amyloid-positive across all ROIs, with statistically significant differences ($p < .0001$) observed in most regions (Table 1).

Table 1. *Mean regional SUVRs differences for amyloid + and – participants, normalised to cerebellum. Compared via Welch's t-tests ($\alpha < .005$). ACC includes rostral & caudal subregions. Medial temporal region includes hippocampus & entorhinal cortex.*

Anatomical Region	*% Difference of +ve & -ve SUVRs*	*t-stat*	*p-value*
Medial Temporal	27	3.09	0.0108
Anterior Cingulate	186	11.02	<.0001
Medial Orbitofrontal	167	12.52	<.0001
Precuneus	229	9.71	<.0001
Posterior Cingulate	225	9.35	<.0001
Inferior Parietal	191	7.43	<.0001
Middle Temporal	163	9.20	<.0001
Inferior Temporal	130	7.44	<.0001
Superior Temporal	134	9.50	<.0001
Cuneus (control)	45	2.12	0.0596

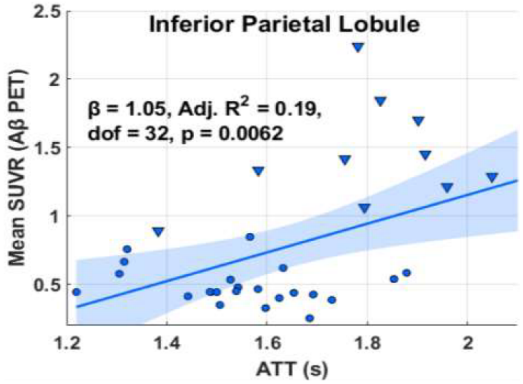

Fig 1. *Scatterplots of SUVR versus ATT in the inferior parietal lobule (above) and anterior cingulate* ***cortex*** *(below; including regression line and 95 % CI)*

Table 2. Linear regression results for regional SUVR regressions with arterial transit time (ATT) and cerebral blood flow (CBF). β coefficients, 95 % CI and p-values for each region.

	ATT		CBF	
Region	***β [95 % CI]***	***p-Value***	***β [95 % CI]***	***p-value***
Medial Temporal	0.173 [–0.100, 0.445]	.207	–0.001 {–0.006, 0.005]	.844
Anterior Cingulate	0.871 [0.476, 1.267]	<.001	–0.008 [–0.015, –0.001]	.025
Medial Orbitofrontal	0.934 [0.433, 1.434]	<.001	–0.011 [–0.021, –0.001]	.028
Precuneus	0.949 [0.403, 1.494]	<.001	–0.012 [–0.025, 0.001]	.065
Posterior Cingulate	0.894 [0.343, 1.444]	.002	–0.008 [–0.019, 0.004]	.184
Inferior Parietal	1.026 [0.532, 1.520]	<.001	–0.010 [–0.021, 0.001]	.080
Middle Temporal	0.708 [0.007, 1.409]	.048	–0.007 [–0.025, 0.009]	.302
Inferior Temporal	0.890 [–0.009, 1.790]	.052	–0.003 [–0.019, 0.013]	.693
Superior Temporal	0.635 [0.235, 1.035]	.002	–0.005 [–0.014, 0.004]	.258
Cuneus (control)	0.358 [–0.012, 0.728]	.057	–0.004 [–0.013, 0.005]	.345

Regressions with $\alpha = 0.005$ revealed no significant CBF–SUVR associations in any ROI and ATT–SUVR showed positive relationships in early-affected regions (Table 2) below $p < .05$ but fell short of the strict $p < .005$ threshold. The strongest relationships are shown in Fig 1. In the cuneus, metrics showed the weakest relationships to SUVR, supporting this as an amyloid control region and the specificity of these exploratory ATT findings.

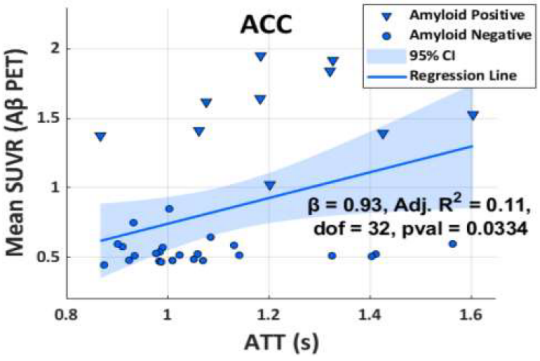

Discussion: These findings suggest that ATT, but not CBF, may correlate with amyloid plaque burden across multiple early affected regions, with the cuneus control region remaining unlinked. While associations did not survive strict Bonferroni correction, initial trends underscore potential biologically plausibility. Our findings support regional specific changes and suggest that altered ATT may reflect early Aβ–vascular interactions. However, CBF changes were possibly masked by a mixed pathology cohort, and effects of age and atrophy on ATT and SUVR warrant covariate adjustment in future studies. While limited sample size may have reduced capacity to produce robust relationships, findings suggest regional microvascular dysfunction is reflected in ATT changes, rather than global CBF.

Acknowledgements: GE Healthcare and EPSRC grant EP/M005909/1

References: **[1]** V. L. Villemagne et al., *The Lancet Neurology*, vol. 12, no. 4, pp. 357–367, 2013. **[2]** N. Mattsson et al. *Brain*, vol. 137, no. 5, pp. 1550-1561, 2014. **[3]** A. Sierra-Marcos, *International Journal of Alzheimer's Disease*, vol. 2017, p. 5479597, 2017. **[4]** H. R. Ma et al., *Oncotarget*, vol. 8, no. 54, pp. 93196–93208, 2017. **[5] J**] J.adden et al., *NeuroImage: Clinical*, vol. 45, p. 103746, 2025. **[6]** M. A. Chappell et al., *Imaging Neuroscience*, vol. 1, pp. 1–16, 2023. doi: 10.1162/imag_a_00041 **[7]** B. Fischl, *NeuroImage*, vol. 62, no. 2, pp. 774–781, 2012**. [8]** C. Destrieux, B. Fischl, A. Dale, and E. Halgren, *NeuroImage*, vol. 53, no. 1, pp. 1–15, 2010. **[9]** B. A. Thomaset et al., *Physics in Medicine & Biology*, vol. 61, no. 22, pp. 7975–7993, 2016. **[10]** S. Palmqvist et al., *Nature communications*. 2017 Oct 31;8(1):1214.

Investigating Microstructural Determinants of Propagation Delays: a Multimodal MEG-MRI study

Svetla Manolova[1], Carolyn McNabb[1], Eirini Messaritaki[1], Marco Palombo[1], Krish Singh[1], Derek Jones[1], Mara Cercignani[1], Matteo Mancini[2]
[1] Cardiff University, Cardiff, Wales, United Kingdom,
[2] Centro Ricerche Enrico Fermi, Rome, Italy

Introduction: Timing in region-to-region propagation is fundamental for brain function, and its characterisation is key to better brain modelling and to understand changes in pathologies. Segregated neuronal populations in grey matter (GM) interact through white matter (WM), and resulting delays are constrained by both WM and GM properties. Tract length, axonal radius and myelination directly influence conduction, but their role in macroscopic propagation is less clear [5]. To shed more light on the determinants of these end-to-end propagation phenomena, we combined MEG with MRI, respectively estimating propagation delays (PropD) with neuronal avalanches [9], and computing WM and GM properties.

Methods: 60 healthy participants (mean age [SD]:20.97[1.65]; F/M=36/24) had MRI (Siemens Connectom 3T) and MEG (275-channel CTF radial gradiometer) [6]. MRI included an anatomical (T1w) scan, 2 diffusion-weighted imaging (DWI) protocols (multi-shell DWI and AxCaliber) [1], and multi-component relaxometry (McDESPOT) [4]. MEG data (sampling:1.2kHz) were acquired at rest for 10 minutes with eyes open and fixated on a cross. T1w data were processed with FreeSurfer for atlas parcellation and cortical thickness (CT) extraction. DWI underwent denoising, artifact corrections and registration to the T1-weightwed images. Tractograms obtained with multi-tissue spherical deconvolution and anatomically constrained tractography were filtered using COMMIT (stick-zeppelin-ball model) [4]. We also fitted two microstructural models: NODDI - for neurite density (NDI) and isotropic fraction (ISO) - and SANDI - for myelinated neurite (FN), soma fraction (FS) and soma radius (RS) [7]. AxCaliber data were fitted with COMMIT-AxSize, to estimate bundle-specific axon radii [2].

McDESPOT data were processed using QUIT to estimate myelin water fraction (MWF). We combined MWF, ISO and NDI to compute the g-ratio (i.e. inner/outer axon diameter ratio) [10]. Structural connectivity matrices (streamline count, length, g-ratio, radius) were computed and thresholded using a >4 streamline cutoff and a 60% group-consensus mask. Using the Rushton model [8], we derived a conduction delay-weighted (CD) matrix by integrating radius, g-ratio and length. For each pair of regions and each GM metric (CT, FS, FN, RS), we also summed their values to quantify their end-to-end contribution. MEG data were filtered (1-150Hz), epoched (2s) and downsampled (512Hz) before beamformer source-localisation and computing mean timeseries for each DK region. Neuronal avalanches were defined as periods of continuous z-scored activity >3 SDs, binned using a time window size calculated based on previous literature [9]. Duration (PropD) was averaged per avalanche to generate PropD connectivity matrices (see Figure 1 for reference). Comparisons were made on group-averaged matrices.

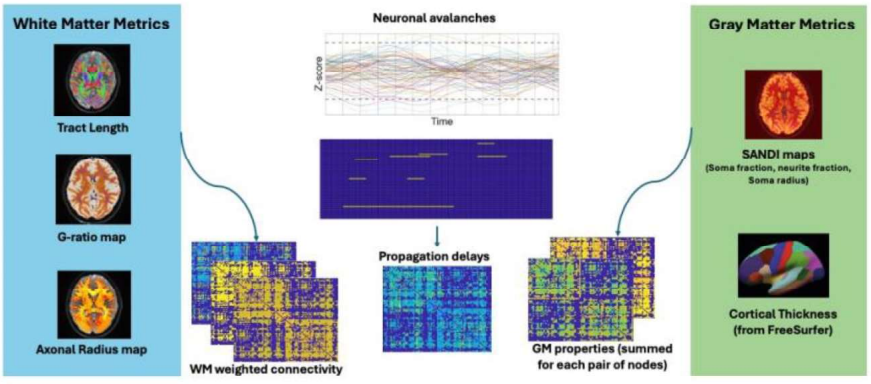

Figure 1. Summary of analysis: the overthreshold MEG signals are used to estimated neuronal avalanches and those are combined into a propagation delays (PropD) matrix; the white matter (WM) properties are assessed along the connections and used to build the related connectivity matrices; the grey matter (GM) properties are

computed for each node and combined pairwise; the resulting matrices are then compared to study how PropD changes with WM and GM.

Results: Figure 2. shows the relationships between the PropD and the WM-GM metrics. For WM, longer tracts are associated with longer PropD. PropD also increases with CD, but as CD is estimated dividing by length by conduction velocity, this trend is likely due to length as well. PropD shows little variation with axonal radius and with g-ratio - suggesting a different role compared to simple conduction and likely affected by the bias towards larger axons. For GM, PropD increases with CT and FS, and decreases with FN, so thicker layers (higher CT) could increase PropD, while myelinated neurites (higher FN) could shorten them. FS- PropD trend requires further study but, together with flat RS, suggests that more somas would increase PropD.

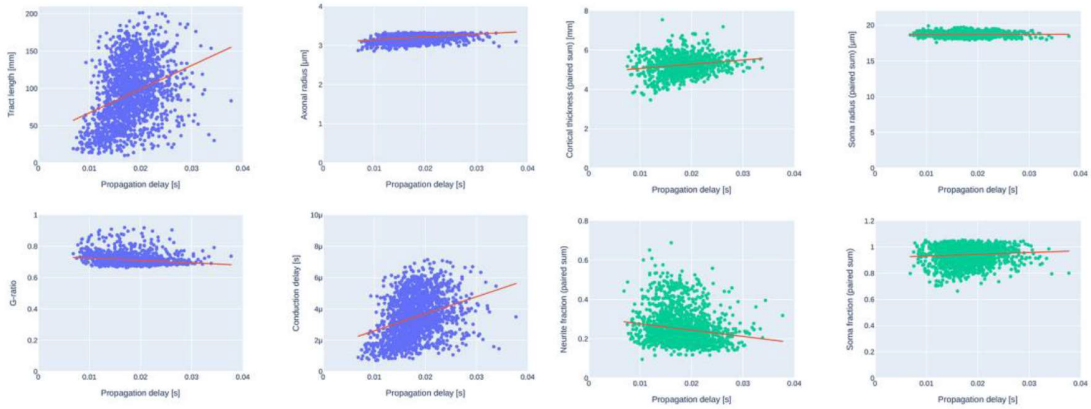

Figure 2. Relationship between propagation delays from MEG and WM metrics (in blue) as well as GM metrics (in green) from MRI, with each point representing a connection in the group connectivity matrix. The red lines are obtained through linear regression (ordinary least squares).

Conclusions: Our results show that GM-WM microstructure provides additional insights into propagation delays and can potentially aid their prediction.

Acknowledgements: The WAND data were funded by the EPSRC (grant EP/M029778/1), Wellcome Trust Investigator Award (096646/Z/11/Z) and Wellcome Trust Strategic Award (104943/Z/14/Z).

References

[1] Assaf, Y., Blumenfeld-Katzir, T., Yovel, Y., et al. (2008). AxCaliber: a method for measuring axon diameter distribution from diffusion MRI. Magnetic Resonance in Medicine: An Official Journal of the International Society for Magnetic Resonance in Medicine, 59(6), 1347-1354.

[2] Barakovic, M., Girard, G., Schiavi, S., et al. (2021). Bundle-specific axon diameter index as a new contrast to differentiate white matter tracts. Frontiers in neuroscience, 15, 646034

[3] Daducci, A., Dal Palù, A., Lemkaddem, A., et al. (2014). COMMIT: convex optimization modeling for microstructure informed tractography. IEEE transactions on medical imaging, 34(1), 246-257.

[4] Deoni, S. C., Matthews, L., Kolind, S. H. (2013). One component? Two components? Three? The effect of including a nonexchanging “free” water component in multicomponent driven equilibrium single pulse observation of T1 and T2. Magnetic resonance in medicine, 70(1), 147-154.

[5] Mancini, M., Tian, Q., Fan, Q., et al. (2021). Dissecting whole-brain conduction delays through MRI microstructural measures. Brain Structure and Function, 226(8), 2651-2663.

[6] McNabb, C. B., Driver, I. D., Hyde, V., et al. (2024). The Welsh Advanced Neuroimaging Database: an opensource state-of-the-art resource for brain research. In Proceedings of the ISMRM & ISMRT Annual Meeting & Exhibition, Singapore.

[7] Palombo, M., Ianus, A., Guerreri, et al. (2020). SANDI: a compartment-based model for non-invasive apparent soma and neurite imaging by diffusion MRI. Neuroimage, 215, 116835.

[8] Rushton, W. A. H. (1951). A theory of the effects of fibre size in medullated nerve. The Journal of physiology, 115(1), 101.

[9] Sorrentino, P., Petkoski, S., Sparaco, M., et al. (2022). Whole-brain propagation delays in multiplesclerosis, a combined tractography-magnetoencephalography study. Journal of Neuroscience, 42(47), 8807-8816.

[10] Stikov, N., Campbell, J. S., Stroh, T., et al. (2015). In vivo histology of the myelin g-ratio with magnetic resonance imaging. Neuroimage, 118, 397-405.

Non-invasive ^{2}H-MRS reveals increased liver fat from de novo lipogenesis in South Asians compared with Europeans

Mueed Azhar[1], Amy Barrett[2], Jieniean Worsley[3], Elspeth Johnson[2], Mandour O. Mandour[4], Emanuella De-Lucia Rolfe[4], Katherine Carr[3], Michele Ferraro[1], Ranalie De Jesus[3], Samuel King[3], Sherly Jose[3], Simon R. White[5], Peter Barker[4], Graham J. Kemp[6], Kevin M. Brindle[7], Nita G. Forouhi[4], Michelle Venables[4], Laura Watson[3,4], Leanne Hodson[2], David B. Savage[4], Alison Sleigh[1,3,4]

[1]Clinical Neurosciences, [4] Institute of Metabolic Science, [5] MRC Biostatistics Unit, [7] CRUK CI & Dept of Biochemistry, University of Cambridge, Cambridge Biomedical Campus, Cambridge, UK.
[2]OCDEM, Radcliffe Department of Medicine, University of Oxford, Oxford, UK.
[3]NIHR Cambridge Clinical Research Facility, Cambridge University Hospitals NHS Foundation Trust, Cambridge Biomedical Campus, Cambridge, UK.
[6] Department of Musculoskeletal & Ageing Science, University of Liverpool, Liverpool, UK

Introduction: South Asians (SA) have a higher risk of developing type 2 diabetes and cardiovascular disease compared to their European-origin (E) counterparts with the same body mass index (BMI). One proposed mechanism underlying this disparity is increased hepatic de novo lipogenesis (DNL) [1]. Biopsy is invasive, and traditionally DNL in humans is quantified using tracer studies with blood sampling [2], offering only indirect estimates of the impact of DNL on liver fat. In this study, we use non-invasive deuterium magnetic resonance spectroscopy (^{2}H-MRS) to quantify the storage of lipids in human liver derived from DNL, comparing individuals of SA and E ancestry.

Methods: Thirteen healthy adult males (7 SA, 6 E), group-matched for age and BMI, and free from chronic conditions, made two visits five days apart to the Cambridge Biomedical Campus. Visit 1: ^{1}H-MRS to assess liver fat (IHL) and composition [3] at 3T, and ^{2}H-MRS to measure pre-dose fat and water signals at 7T using a RAPID Biomedical ^{2}H/^{1}H TxRx surface coil. For ^{2}H-MRS, chemical shift imaging (CSI_fid) with weighted acquisition (FOV 260 x 280 x 240 mm; grid 13 x 14 x 12, interpolated to 16 x 16 x 16) enabled spatially localised spectra covering the right abdomen. Reference voltage was established and 4 datasets acquired with scan time of 6.37, 12.88 and 25.97 min with TR 330ms, and 13.52 mins with TR 700ms. Following an energy-balanced evening meal, participants consumed a priming dose of ^2H_2O (8pm & 10pm) to reach body water enrichments of ~0.3%, followed by maintenance water to maintain a stable body water enrichment until their return visit, where the same relocalised 7T scan was performed to quantify DNL-derived liver lipids using ^{2}H-MRS. Liver spectra were analysed using jMRUI [4] and OXSA (MATLAB) [5]. The TR 700ms scan was used for ^{2}H water signal, and an SNR-optimised combination of all 4 datasets for fat signal. 1.5 Hz line broadening was applied and spectra baseline-corrected prior to integration. An external phantom within the coil housing was used for normalisation between visits. Both fractional DNL (% of existing liver fat made by DNL over the 5 days), as well as absolute DNL (absolute amount of liver fat made by DNL over the 5 days), were calculated. ^{2}H fat signal reproducibility was assessed by comparison of ^{2}H fat from 25.97 min scan with the optimally-combined other 3 scans. Studies were ethically approved and all participants provided written informed consent. Statistics were performed in SPSS v28: Mann U Whitney test, between-group comparison; absolute intraclass correlation coefficient (ICC), ^{2}H fat reproducibility; Spearman's correlation coefficient, associations with other variables.

Results:

Table 1. Participant characteristics, expressed as median (Q1 – Q3)

	SA	E	P value
Age, (years)	40.0 (28.0 – 42.0)	32.0 (25.8 – 44.8)	0.731
BMI, (kg/m^2)	28.6 (26.5 – 31.6)	29.9 (27.8 – 33.7)	0.534
Liver fat (CH_2/[CH_2 + water]), (%)	6.2 (2.4 – 16.7)	1.5 (0.8 – 2.6)	**0.035**
Saturated liver fat, (%)	37.7 (32.1 – 52.1)	32.5 (24.9 – 34.9)	0.181

One SA withdrew after Visit 1. Reproducibility of ^{2}H-liver fat: ICC = 0.99 (pre-dose), 0.96 (post-dose).

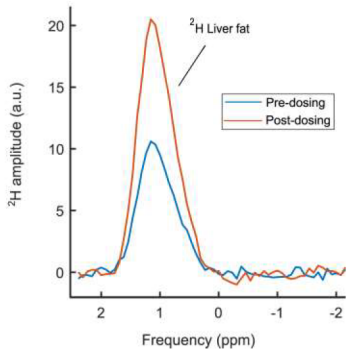

Fig. 1. ^{2}H liver fat before (red) and after (blue) dosing with ^2H_2O.

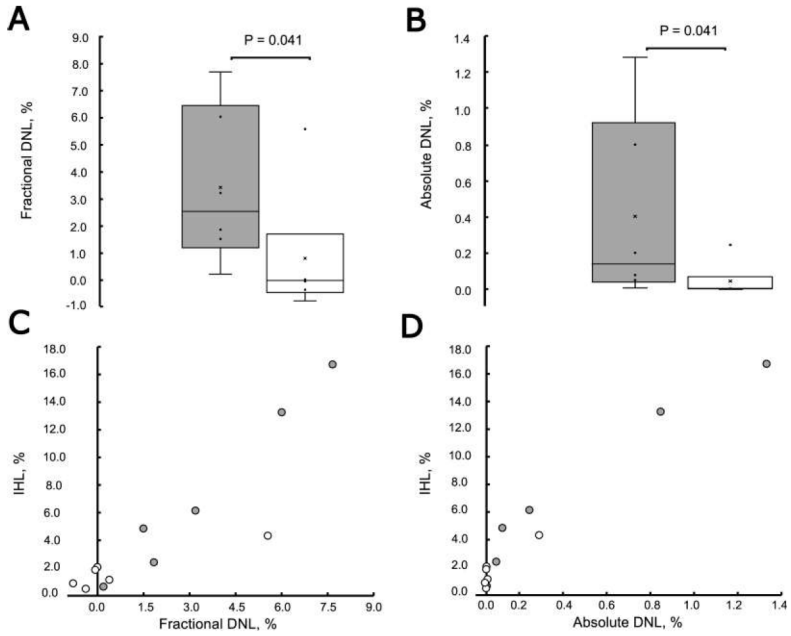

Fig. 2. Fractional (A) and Absolute (B) DNL, and their associations with ^{1}H MRS liver fat (IHL) (C-D) in South Asian (grey bars & circles) and Europeans (white bars & circles).

Fig. 1 illustrates the liver fat signal pre- and post-dose in a SA individual with 16.7% liver fat. IHL was higher in SA *vs* E participants (Table 1). Both fractional and absolute DNL (%) were higher in SA (p = 0.041, Figs. 2A & B). They strongly correlated with IHL (fractional DNL r_s=0.874, p=0.001, Fig. 2C; absolute DNL r_s=0.888, p=0.001, Fig. 2D). Absolute DNL positively correlated with IHL saturation but fell short of statistical significance (r_s=0.503, p=0.095).

Discussion and Conclusion: We have established a non-invasive method of measuring ^{2}H fat and water pre- and post-dosing with ^2H_2O, and used this to quantify the storage of liver lipids derived from DNL *in vivo* in humans. The higher liver fat in SA aligns with findings from a meta-analysis [6], and the higher fractional DNL suggests that a higher proportion of liver fat in SA is derived from DNL. This, together with the associations of DNL and liver fat, suggests that DNL could play a pivotal role in driving the increased liver fat in SA. This is consistent with Hudgins *et al.* [1] who showed increased lipogenic sensitivity in healthy young SA, and as this was despite normal indices of insulin sensitivity in [1], this suggests an early gene–nutrient interaction may contribute to this population's high prevalence of type 2 diabetes and coronary disease. Our findings highlight the value of ^{2}H-MRS as a powerful non-invasive tool for investigating human fat metabolism.

Acknowledgements: We thank the participants. This work was funded by the Medical Research Council (MR/V011758/1). AS gratefully acknowledges salary support from the NIHR Cambridge Clinical Research Facility.

References

[1] L. C. Hudgins, J. L. Hugo, S. Enayat et al. *Clin Endocrinol (Oxf)*. **86(3)**, 361-366 (2017).
[2] C. Pramfalk, M. Pavlides, R. Banerjee et al. *Diabetes*. **65(7)**, 1858–1867 (2016).
[3] K. H. M. Roumans, L. Lindeboom, P. Veeraiah et al. *Nat Commun*. **11(1)**, 1891 (2020).
[4] A. Naressi, C. Couturier, J. M. Devos et al. *MAGMA*. **12(2-3)**, 141-152 (2001).
[5] L. A. B. Purvis, W. T. Clarke, L. Biasiolli et al. *PLOS ONE*. **12(9)**, e0185356 (2017).
[6] S. Iliodromiti, J. McLaren, N. Ghouri et al. *Diabetologia*. **66**, 44–56 (2023).

Development of high-resolution ^{19}F-MRI of inhaled perfluoropropane using a 6-channel receive array coil with compressed sensing-parallel imaging.

Dominic Harrison[1,2,3], Mary Neal[1,2], Ben Pippard[1,2], Kieren G. Hollingsworth[1,2], Pete Thelwall[1,2]

[1]Translational and Clinical Research Institute, Newcastle University, Newcastle upon Tyne;[2]Newcastle Magnetic Resonance Centre, Newcastle University, Newcastle upon Tyne;[3]Northern Medical Physics and Clinical Engineering, Newcastle upon Tyne NHS Foundation Trust, Newcastle upon Tyne, United Kingdom

Introduction: This study evaluated the ability of compressed sensing-parallel imaging (CS-PI), and a custom 6-channel ^{19}F receiver array (Rapid Biomedical, Germany) to accelerate ^{19}F-MRI of inhaled perfluoropropane gas for measurement of lung ventilation properties. ^{19}F-MRI exhibits significant signal limitations due to the low ^{19}F spin density in a gaseous phase, thermal polarisation and the restrictions on total scan duration (and thus the amount of signal averaging) necessitated by achievable breath hold durations. Phased receive arrays have shown 2-5x SNR gains over single-channel setups in sodium phantoms[1]. Combined with CS-PI, we anticipate these gains will enable improvement of ^{19}F-MRI scan resolution beyond the 10mm isotropic resolution employed in our current respiratory research studies, and with potential to also reduce breath-hold duration requirements.

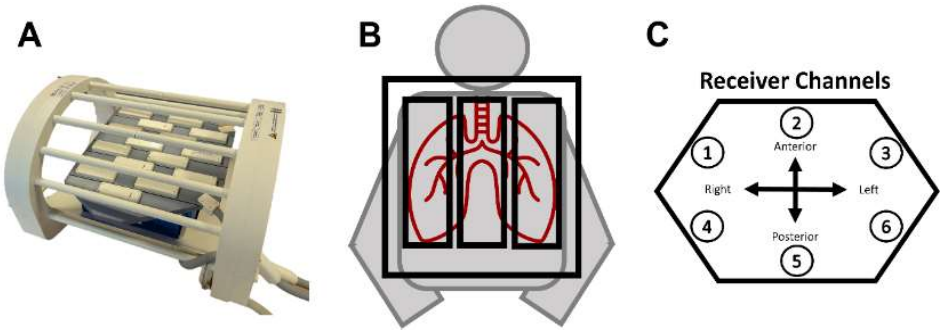

***Fig. 1**: Photo of the upgraded ^{19}F receiver array inserts & birdcage coil (A). Illustration of channel dimension sizes w.r.t participant (B). Schematic of receive channels and position within the array (C).*

The receive coil array consists of a rigid posterior and flexible anterior resonators fitting within a transmit birdcage coil, maximising proximity of the receive coils to lung (Figure 1). Six elements were positioned in a 2×3 layout (3 anterior, 3 posterior), each with dimensions 35×40cm (H-F × L-R). This orientation supports acceleration along the two phase-encoding directions (H-F and A-P) of the 3D gradient echo scan used for ^{19}F-MRI.

Methods: Five healthy volunteers were recruited under Newcastle University ethical approval. Participants performed three deep inhalations of a 79% perfluoropropane, 21% oxygen gas mixture immediately prior to ^{19}F-MRI scan acquisition on inspiratory breathhold. Prospectively accelerated 3D ^{19}F-SPGR scans were acquired at multiple scan resolutions and CS-PI acceleration factors (Table 1) for a total of n=5 healthy volunteers. We acquired scans at 25% of the voxel volume used in previous in-house studies and compared them to 10mm isotropic scans. The change in image quality across acquisition resolution and acceleration factor was assessed visually. Scan duration was maintained at approximately 15 seconds for all ^{19}F-MRI scans by adjusting the number of signal averages (NSA) as matrix size and acceleration factor (AF) changed. All scans had the following common acquisition parameters: TE=1.7ms, TR=7.5ms, FA=45°, FOV=400x320x250 and bandwidth=500Hz/pixel. Differences in image quality were evaluated qualitatively,

Parameters	^{19}F 3D SPGR Acquisition sequence					
	10 mm isotropic 1.8x	10 mm isotropic 6x	7 mm isotropic 6x	6 mm isotropic 6x	7 mm isotropic 4x	5x5x10 mm 4x
Acquisition Resolution / mm	10 x 10 x 10	10 x 10 x 10	7 x 7 x 7	6 x 6 x 6	7 x 7 x 7	5 x 5 x 10
Optimal λ	0.05	0.05	0.005	0.005	0.005	0.005
Reconstruction matrix size	160 x 128 x 25	160 x 128 x 25	168 x 132 x 36	204 x 156 x 42	168 x 132 x 36	240 x 192 x 25
CS-PI acceleration	1.8x	6.0x	6.0x	6.0x	4.0x	4.0x
NSA	6	19	10	7	7	7
Acquisition duration / s	15.2	15.3	15.7	15.3	16.5	16.3
Number of participants	n=5	n=4	n=2	n=2	n=5	n=5

***Table 1**: ^{19}F-MRI scan acquisition parameters for the range of acceleration factors and acquisition resolutions studied.*

comparing how clearly signal boundaries of the pulmonary volume are visibly defined and if known structures such as the bifurcation of the trachea and pulmonary vasculature are visible. Image reconstructions were repeated using only NSA = 1 of each dataset for scans acquired with prospective 6x CS-PI acceleration to test the feasibility of high temporal resolution imaging, where the duration of NSA=1 scans would be 0.8, 1.6, and 2.2s for isotropic resolutions of 10, 7 and 6mm respectively.

Results: Figures 2 show central slices of the pulmonary volume at each acquisition resolution for a representative participant. Figure 2E shows substantially lower image quality compared to other resolutions, with poor visibility of the bifurcation of the trachea and blurring at signal boundaries. SNR is 11 or higher for all scans.

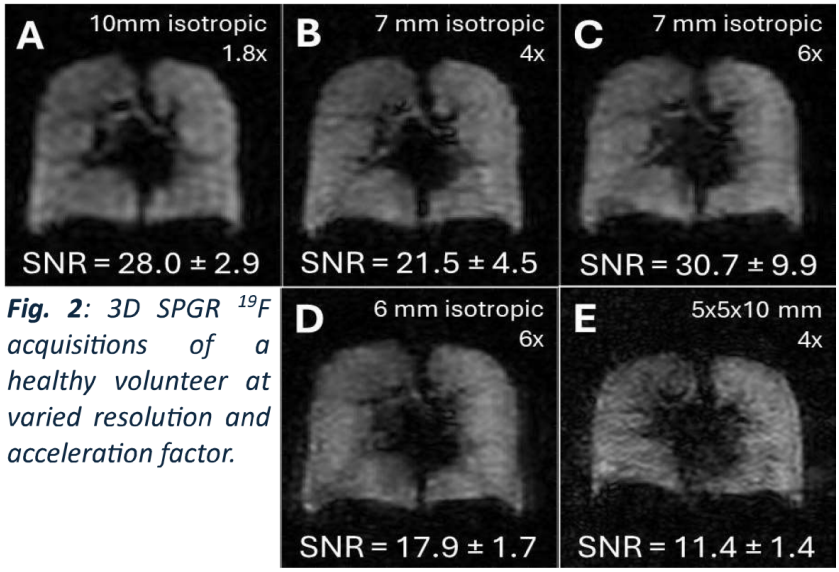

***Fig. 2**: 3D SPGR ^{19}F acquisitions of a healthy volunteer at varied resolution and acceleration factor.*

Figure 3 shows reconstructions using a single average (NSA = 1) extracted from raw MR data used to generate the images in Figure 2. These images show 6x accelerated scans with 10mm, 7mm and 6mm isotropic resolution, where the scan duration for NSA=1 data would be 0.8, 1.6 and 2.2 seconds respectively. Calculated SNRs of each resolution are annotated. Images exhibit blurring and lower SNR compared to the data shown in Figure 2.

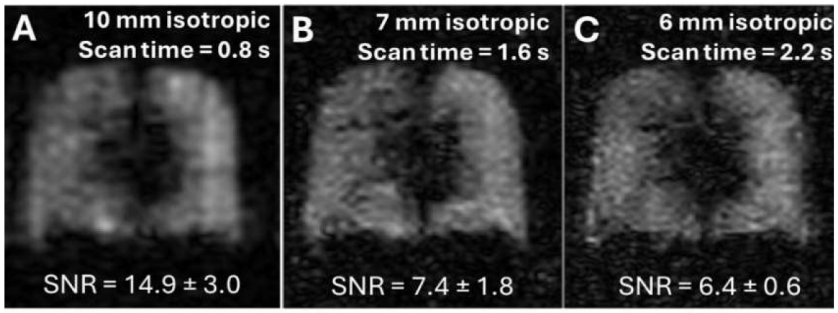

***Fig. 3**: Reconstructed images from NSA=1 3D ^{19}F SPGR scan data with varied 6x accelerated isotropic resolutions.*

Discussion: This study presents the first documented *in vivo* human 3D ^{19}F lung MRI acquisitions of inhaled PFP with voxel volumes below 0.25mL. The reduction in signal amplitude per voxel with decreasing voxel volume was mitigated by the gains delivered by CS-PI acceleration and incorporation of a receive coil array into the ^{19}F birdcage RF coil. Comparisons of image detail based on qualitative visual assessment of the reconstructions show that anatomical detail varied with image resolution. Scans with 7mm isotropic resolution acquired with 4x acceleration show greater anatomical clarity than scans with 6mm isotropic and 5x5x10mm resolution. This qualitative improvement is likely due to higher SNR achieved from the larger voxel volume in the 7mm isotropic scans. Poorer image detail and lower SNR were shown for scanned resolutions of 5x5x10mm when compared to 6mm isotropic acquisitions. This is likely due to the larger k_y and k_z matrix sizes allowing for improved incoherent sampling resulting in better suppression of image artefacts.

NSA = 1 reconstructions of highly accelerated 10, 7 and 6mm isotropic acquisitions were performed with scan durations of 0.8, 1.6, 2.2 seconds, respectively. The data shows surprisingly effective imaging of lung structure for such short acquisition times in comparison to previous non-accelerated scans with an approximate 15s duration reported by our group (SNR = 11.7 ± 4.1)[2].

Conclusions: We have assessed the capability of CS-PI to increase ^{19}F-MRI scan resolution and reduce scan duration. These findings are directly applicable to future ^{19}F-MRI studies of patients with respiratory disease.

1. Amin Nazaran, J.D.K., Meredith Taylor, Daniel J Park, Grayson Tarbox, Rexford D Newbould, Neal Bangerter, and Glen Morrell, *An SNR Comparison Between a Sodium Phased Array Coil and a Single Channel Coil.* Proc 23rd Annual Meeting ISMRM Toronto 2015, 2015.
2. Neal, M.A., et al., *Optimized and accelerated 19 F-MRI of inhaled perfluoropropane to assess regional pulmonary ventilation.* Magnetic Resonance in Medicine, 2019. **82**(4): p. 1301-1311.

Sequence-Specific Geometric Distortions in Breast MRI at 3T: A Phantom-Based Analysis

Klara Mišak [1,2,3], Agnieszka Sierhej [2,3], Chris A Clark [2], Kelley Ferreira [3], Simon Walker-Samuel [1], and Matt T Cashmore [3]

[1] Centre for Computational Medicine, Division of Medicine, University College London, London, UK

[2] UCL Great Ormond Street Institute of Child Health, London, UK [3] National Physical Laboratory, Teddington, UK

Introduction: Accurate spatial localization and characterization of lesion shape and size are essential for breast cancer detection and MRI-guided interventions [1]. This is particularly critical for small lesions such as ductal carcinoma in situ (DCIS), which require sub-millimetre precision and show reported detection sensitivities of 77–96% [2, 3]. However, geometric distortions in breast MRI can impair lesion localization and morphology assessment, potentially affecting clinical decision-making [4]. We developed a dedicated breast phantom with tissue-mimicking gels targeting the relaxation properties of fibroglandular (FGT) and adipose tissue [5, 6], enabling assessment of geometric distortion and shape fidelity. By comparing MRI-derived centroid metrics to co-registered CT (distortion–free reference), we quantified geometric distortion in 3T T_1- and T_2-weighted breast MRI. We further compared manual and automated registration strategies to assess their influence on distortion magnitude and measurement reproducibility.

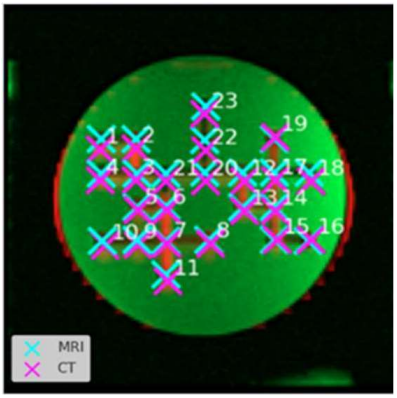

Fig. 1: MRI T_1-weighted scan (green) overlaid on CT (magenta)

Methods: A custom 3D-printed breast phantom was designed to simulate FGT and adipose compartments using relaxation-matched gels [5]. Twenty-three spherical fiducial markers and a branching internal structure were embedded to introduce spatial complexity. Imaging was performed on a 3T Siemens MAGNETOM Prisma using T_1- and T_2-weighted spin-echo sequences (T_1w: TR = 500–3500 ms, TE = 7 ms; T_2w: TR = 500 ms, TE = 7–350 ms). A 5 mm-slice CT scan served as the distortion-free reference. MRI-to-CT rigid registration was performed using Fiji (ImageJ) (Fig. 1). Two strategies were evaluated: ten repeated manual registrations by a single operator (to assess intra-operator variability), and automated rigid-body registration using the StackReg plugin. For each registration, geometric distortion was quantified as the Euclidean distance between corresponding fiducial centroids, extracted via thresholding and particle analysis. For each region of interest (ROI), mean distortion and standard deviation were calculated. Paired t-tests were used at each control point to assess distortion differences between T_1w and T_2w. Registration precision and reproducibility were compared between the two pipelines using standard deviation across repetitions.

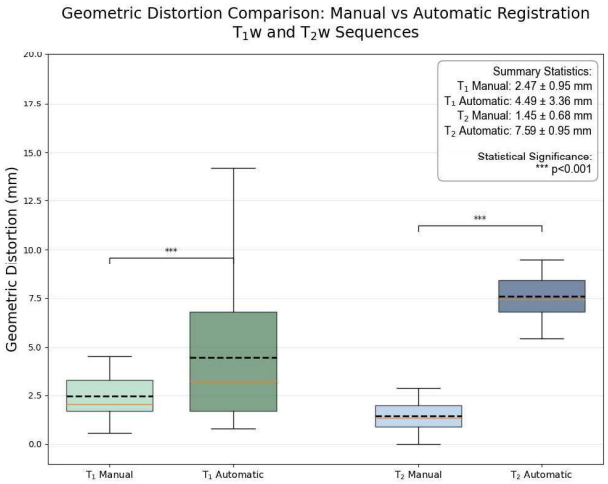

Fig 2: Comparison of geometric distortion between manual and automatic registration methods for T_1w and T_2w MRI sequences

Results: T_1w images yielded a mean distortion of 2.47 ± 0.95 mm with manual registration and 4.49 ± 3.36 mm with automatic registration. For T_2w, distortion was 1.45 ± 0.68 mm manually and 7.59 ± 0.95 mm automatically (Fig. 2). Distortion was significantly lower in T_2w than T_1w for both registration methods ($p < 0.001$). Manual registration consistently outperformed automated registration in reducing distortion across all sequences. Intra-operator variability (standard deviation across 10 registrations) was lower with manual alignment, confirming its greater precision (Fig. 3). American College of Radiology (ACR) geometric accuracy threshold exceedance (±2 mm) [7] occurred

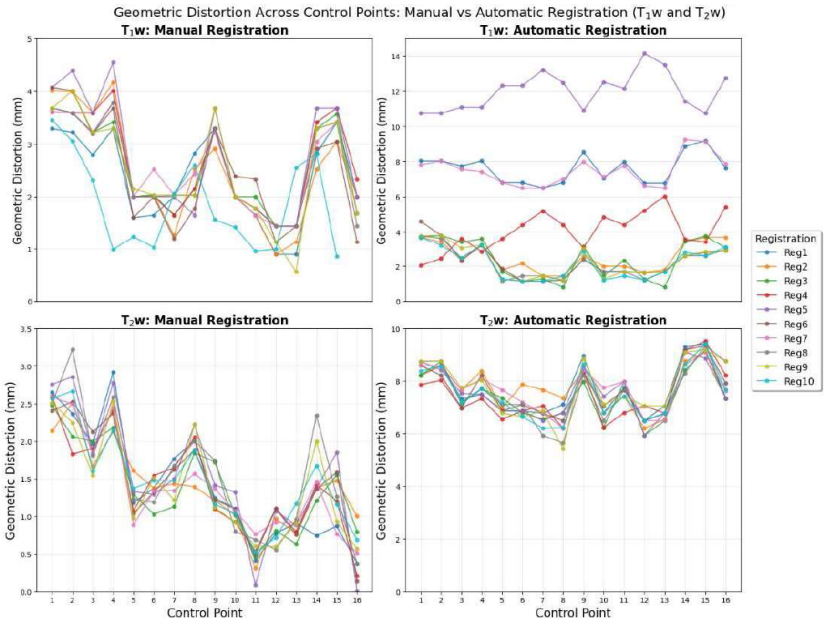

Fig. 3: Point-wise geometric distortion across control points for T_1-weighted (top row) and T_2-weighted (bottom row) sequences, comparing manual (left) and automatic (right) registration methods

in 44% (T_1w) and 27% (T_2w) of control points under manual registration, increasing to 69% (T_1w) and 94% (T_2w) under automatic registration.

Discussion: Geometric distortion was significantly lower in T_2w images compared to T_1w across both registration methods. T_2w sequences exhibited reduced mean distortion and lower variability, consistent with prior findings that T_2-weighted spin-echo imaging is less susceptible to B_0 inhomogeneities and gradient nonlinearities than T_1w acquisitions, especially those using gradient-echo components [8]. Despite distortion-minimizing sequences, many measurements, particularly under automated registration, exceeded ACR thresholds, highlighting the persistent risk of distortion from field inhomogeneities and tissue susceptibility differences [8]. Manual registration produced significantly lower distortion than StackReg-based automated alignment, though at the cost of slightly higher intra-operator variability. These findings demonstrate the trade-off between manual precision and automated consistency. Limitations include the absence of DCIS-mimicking lesions and computational phantom validation with known distortion fields to verify measurement accuracy.

Conclusions: T_2w imaging demonstrated superior geometric accuracy with fewer ACR threshold violations than T_1w imaging, supporting its preferential use for sub-millimeter lesion localization critical for DCIS detection and MRI-guided interventions. These findings emphasize the importance of sequence-specific QA and optimal registration strategies to minimize geometric distortion.

References

[1] Bick U, et al. (2020). Image-guided breast biopsy and localisation: Recommendations for information to women and referring physicians by the European Society of Breast Imaging. *Insights into Imaging*, 11(1), 1–11.
[2] Mann R, et al. (2008). Breast MRI: Guidelines from the European Society of Breast Imaging. *European Radiology*, 18(7), 1307–1318.
[3] Le Bihan D, Camps-Herrero J. (2023). The road to breast cancer screening with diffusion MRI. *Frontiers in Oncology*, 13, 993540.
[4] Kim K, et al. (2013). MRI-guided intervention for breast lesions using freehand technique. *Korean Journal of Radiology*, 14(2), 171–176.
[5] Rakow-Penner R, et al. (2016). Design of a breast phantom for quantitative magnetic resonance imaging. *PLoS ONE*, 11(8), e0160663.
[6] Sindi S, et al. (2020). Quantitative measurement of breast density using personalized 3D-printed models. *Journal of Imaging*, 6(10), 94.
[7] American College of Radiology. (2021). *Phantom Test Guidance for the ACR MRI Accreditation Program*. ACR Committee on MR Accreditation.
[8] Kavaluus H, et al. (2021). Determination of acceptance criteria for geometric accuracy of magnetic resonance imaging scanners used in radiotherapy planning. *Physics and Imaging in Radiation Oncology*, 17, 58–64.

Repeatability metrics for automatically derived quantitative pancreatic MRI measures

Eve S. Shalom[1], George Ralli[1], Yuchen Ma[1], Paul Aljabar[1], Edward Jackson[1], Michael Brady[1]
[1]Perspectum Ltd, Oxford, United Kingdom

Introduction: With rising incidence of pathologies affecting the pancreas [1], methods for assessment and monitoring are increasingly important. Quantitative pancreatic MRI enables non-invasive assessment of pancreas volume, scanner reference T1 (srT1) [2-4], Proton Density Fat Fraction (PDFF) [5], and Signal Fat Fraction (SFF) [6]. Such measures can be used to grade disease severity and could assist in early detection, diagnosis or treatment response monitoring [7]. Manual assessment of pancreatic MRI requires time and expertise, typically involving Regions-of-Interest (ROIs) placement in homogenous regions [8], so automation is essential for scalability. However, pathology is often heterogeneous, and there is increasing focus on the pancreas head, body, and tail. We present repeatability metrics for automatically segmented pancreatic MRI acquisitions.

Methods: The scan-rescan cohort (46 subjects) were collected across three imaging sites with Siemens scanners (1.5T, 20 subjects; 3T, 26 subjects). Both scan and rescan acquisitions were obtained within one imaging session, each subject exited then re-entered the scanner. The MRI protocol for each scan comprised three sequence types: a 3D breath-hold, 2-point Dixon T1-weighted scan covering abdominal region; 2D breath-hold MOLLI; and 2D breath-hold IDEAL. 2D Maps of srT1 and PDFF were reconstructed using methods outlined in [2] from MOLLI and IDEAL scan data. 3D SFF maps were derived directly from Dixon fat and water images.

An automated method [4] assesses the Dixon water volume image and generates a 3D pancreas segmentation. Pancreas volume and SFF measures were derived using this 3D mask. Segmentation of the mask into the head, body and tail was done [9]. The 2D srT1 and PDFF maps were aligned with the 3D mask. This allows propagation of the 3D mask to a 2D pancreas segmentation within the srT1 and PDFF maps to extract percentile-based measures. Median percentile values were reported in all measures, as well as lower percentiles for srT1, PDFF and SFF that have previously been shown as useful [4]. Repeatability metrics (Bland-Altman bias and Limits-of-Agreement (LoA), repeatability (RC) and intra-class-correlation (ICC) coefficients) were obtained for all measurements. Manual ROI based scan-rescan assessment was also done across the same cohort, for srT1 and PDFF, enabling comparison against the automated method.

Results: Full 3D pancreas volume segmentation, with resampled 2D segmentation masks for srT1 and PDFF slices, were returned for the whole scan-rescan cohort (Figure 1a-d). Repeatability metrics (bias, LOAs, RC, ICC) were reported (Table 1) with the cohort considered as split by field strength (1.5T or 3T) or combined (both 1.5/3T). Scan-rescan repeatability reported for the manual ROI method of srT1 (combined field strengths: bias=-8.2ms, LoA=[-66.0, 49.7]ms, RC=59.4ms, ICC=0.85) and PDFF (combined field strengths: bias=0.3%, LoA=[-2.1, 2.7]%, RC=2.4%, ICC=0.92) measurement, are comparable with the corresponding automated values (Table 1).

Discussion: ICC values for all automated outputs were good (0.75-0.9) or excellent (>0.9) and are comparable or better than the respective manual measurements. Repeatability metrics of 32.5th percentile srT1 (Table 1) are in line with previous reported values [4]. The metrics represent the repeatability performance of the pipeline without *any* manual or automated quality control to confirm that the pancreas area is adequately captured. Future work should include assessment of cross-vendor repeatability, as the cohort acquisitions were obtained using only Siemens scanners.

Conclusions: Quantitative pancreatic MRI measures derived from automatic segmentation show good or excellent repeatability. The repeatability metrics of automatically derived measures align well with manual ROI-based derived measures where comparative data is available.

References: **[1]** Smits and Van Geenen. 2011. *The clinical significance of pancreatic steatosis.* Nat Rev Gastroenterol Hepatol. 8(3):169-177. **[2]** Dennis A, et al. 2023. *Multi-organ impairment and long COVID: a 1-year prospective, longitudinal cohort study.* J R Soc Med. 116(3):97-112. **[3]** CoverScan v1 510(k) Premarket Notification **[4]** Bagur, et al. 2025. *Standardized pancreatic MRI-T1 measurement methods: comparison between*

manual measurement and a semi-automated pipeline with automatic quality control. BJR. 98(1170):965-973. **[5]** Reeder, et al. (2012). *Proton density fat-fraction: a standardized MR-based biomarker of tissue fat concentration.* JMRI. 36(5):1011–1014. **[6]** Bray, et al. 2018. *Fat fraction mapping using magnetic resonance imaging: insight into pathophysiology.* BJR. 91(1089):20170344. **[7]** Wang, et al. 2018. *Magnetic resonance elastography and T1 mapping for early diagnosis and classification of chronic pancreatitis.* JMRI. 48(3):837-845. **[8]** Al-Mrabeh, et al. 2017. *Quantification of intrapancreatic fat in type 2 diabetes by MRI.* PloS one. 12(4):e0174660. **[9]** Bagur, et al. 2022. *Pancreas MRI Segmentation Into Head, Body, and Tail Enables Regional Quantitative Analysis of Heterogeneous Disease.* JMRI. 56(4):997-1008.

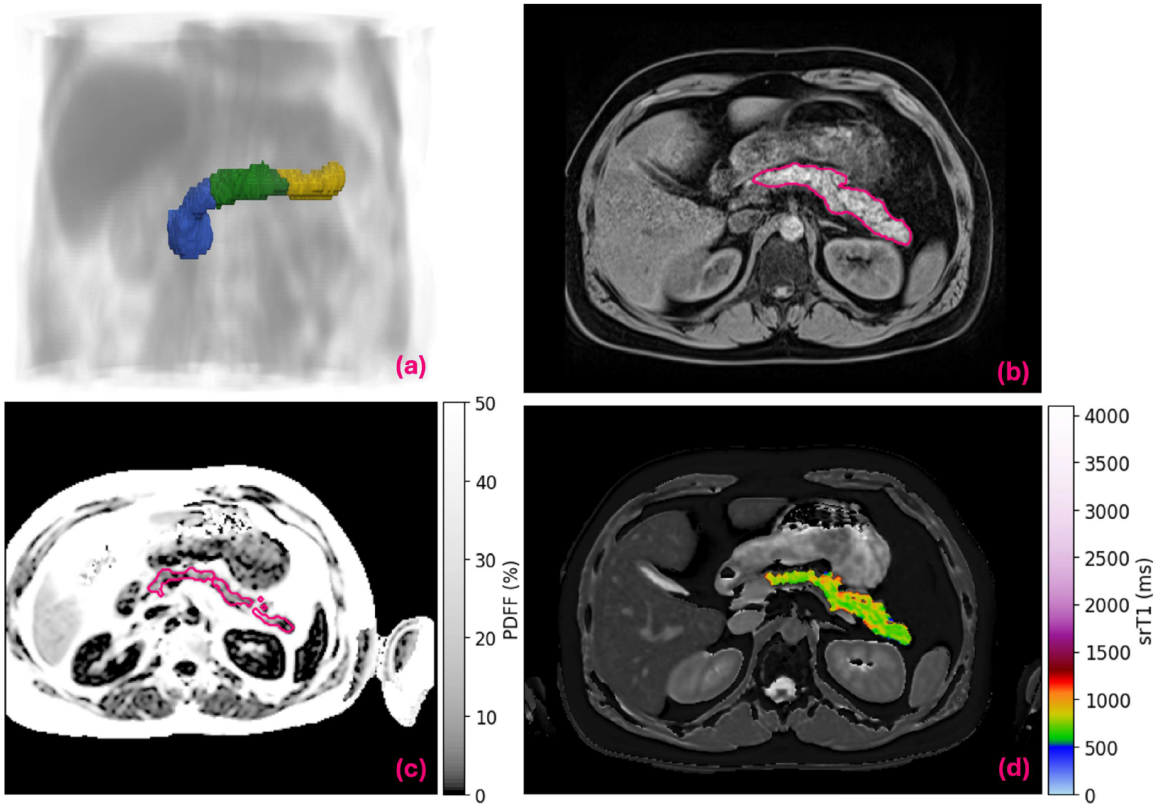

Figure 1: Example segmentation output: **(a)** 3D pancreas segmentation rendered in place showing head/body/tail (blue/green/yellow) with the Dixon water volume, **(b)** resampled Dixon water slice with corresponding 2D mask overlaid as a pink outline, **(c)** PDFF map with 2D mask overlaid as a pink outline, and **(d)** srT1 map with 2D mask area overlaid as a colourmap.

Table 1: Repeatability metrics for outputs derived from the automated pancreas pipeline. Outputs are grouped by acquisition type. ICC reliability metrics are shown as *good (0.75-0.9)* in italics or **excellent (>0.9)** in bold.

	Output	Percentile	1.5T (N=20)			3T (N=26)			Combined (N=46)		
			Bias [LOA_l, LOA_u]	ICC	RC	Bias [LOA_l, LOA_u]	ICC	RC	Bias [LOA_l, LOA_u]	ICC	RC
2D IDEAL	PDFF (%)	50	-0.5 [-3.5, 2.6]	**0.90**	3.1	-0.0 [-5.9, 5.8]	**0.92**	5.7	-0.2 [-5.0, 4.6]	**0.92**	4.8
	PDFF (%)	25	-0.1 [-1.3, 1.1]	**0.94**	1.2	0.1 [-2.6, 2.9]	**0.96**	2.7	0.0 [-2.2, 2.2]	**0.96**	2.2
2D MOLLI	srT1 (ms)	50	-11.8 [-63.9, 40.3]	*0.76*	55.8	-2.0 [-100.6, 96.7]	*0.75*	96.8	-6.2 [-87.7, 75.3]	*0.78*	81.5
	srT1 (ms)	32.5	-11.6 [-45.0, 21.7]	*0.85*	39.7	-4.2 [-70.8, 62.5]	*0.84*	65.8	-7.4 [-62.1, 47.3]	*0.86*	56
3D DIXON	SFF (%)	50	0.1 [-2.0, 2.2]	**0.95**	2.1	0.2 [-1.9, 2.2]	**0.99**	2	0.2 [-1.9, 2.2]	**0.99**	2
	SFF (%)	25	0.1 [-1.3, 1.5]	**0.92**	1.4	0.2 [-1.6, 1.9]	**0.98**	1.8	0.1 [-1.5, 1.7]	**0.98**	1.6
	volume (mL)	-	-2.2 [-10.5, 6.1]	**0.91**	9.2	3.6 [-19.0, 26.2]	*0.82*	23.3	1.1 [-17.5, 19.7]	*0.84*	18.5
3D DIXON PARTS	Head SFF (%)	50	0.1 [-3.2, 3.3]	*0.86*	3.2	0.0 [-4.2, 4.2]	**0.96**	4.1	0.0 [-3.7, 3.8]	**0.95**	3.7
	Body SFF (%)	50	0.2 [-2.8, 3.2]	**0.95**	2.9	0.5 [-2.3, 3.3]	**0.99**	2.9	0.3 [-2.5, 3.2]	**0.98**	2.9
	Tail SFF (%)	50	0.4 [-2.4, 3.1]	**0.93**	2.8	-0.4 [-3.9, 3.2]	**0.98**	3.5	-0.0 [-3.3, 3.2]	**0.97**	3.2

What is the effect of a breath-hold on renal BOLD MRI scans?

Anna Griffith[1], Eve Shalom[1], Kanishka Sharma[2], Kywe Soe[1], Ho-Fung Chan[3], Guilhem Collier[1], Neil Stewart[1], Steven Sourbron[1], Joao Periquito[1]

[1]School of Medicine & Population Health, The University of Sheffield, Sheffield, United Kingdom

[2]Antaros Medical AB, Entreprenörsstråket 10, 431 53 Mölndal, Sweden

[3]Auckland Bioengineering Institute, University of Auckland, New Zealand

Introduction: Renal hypoxia is a key factor preceding renal tissue damage, arising from a mismatch between increased oxygen demand due to hyperfiltration and reduced oxygen supply from impaired perfusion [1]. Blood Oxygenation Level–Dependent (BOLD) MRI can detect changes in tissue oxygenation by reflecting the oxy-/deoxy-hemoglobin ratio [2]. It promise as a non-invasive biomarker for early detection of renal hypoxia and monitoring chronic kidney disease (CKD) progression [3]. Conventional renal BOLD MRI (T2* mapping) protocols often employ breath-holding to reduce respiratory motion and imaging artifacts. However, breath-holding induces hypercapnia and may trigger renal autoregulatory mechanisms, potentially confounding T2* measurements [4]. This study aimed to investigate the impact of medium (up to 40 s) and long (up to 90 s) breath-holds on renal BOLD MRI.

Methods: Data acquisition: Ten healthy volunteers were scanned using a GE 3T PET-MRI scanner with a fast BOLD protocol. A multi-gradient echo sequence with 16 echo times (3.0–24 ms), TR = 55 ms, flip angle = 25°, and matrix size = 256 × 256 was used. Two coronal slices were acquired, with a total scan time of 6 s (Fig. 1). Participants were instructed to hold their breath as long as possible. For nine volunteers, T2*-weighted data were acquired every 6 s for 1 min, repeated three times with 120 s rest intervals. In one volunteer, a 90s breath-hold was tested (Fig. 3). Respiratory data were monitored via a bellows system. Image processing: Pixelwise T2* maps were generated using an in-house Python fitting script (mono-exponential function). Whole-kidney, cortex, and medulla ROIs were drawn on both kidneys, and mean T2* values were extracted. Image analysis: Percentage change was calculated relative to the first breath-hold scan. Changes across the three trials were averaged, and linear regression assessed T2* decline over time.

Results: One volunteer was excluded due to severe susceptibility artifact. All others managed at least one 36s breath-hold. For nine subjects, whole-kidney T2* values declined during breath-hold in 8/9 participants. After 36s, average T2* reductions across repeated trials ranged from +1.36% to –7.8%. Medullary responses were less consistent than those in cortex and whole kidney. Linear regression revealed negative slopes in T2* across all ROIs, indicating decline. On average, whole-kidney T2* decreased by 3.0% at 36s (Fig. 2). In the single subject performing 90 s breath-holds, all three trials were successful. T2* values showed a sharp 27% reduction between ~36–90s, markedly greater than in shorter protocols.

Discussion: Our findings confirm that renal T2* declines during breath-hold, reflecting progressive deoxygenation. The linear reduction suggests breath-hold duration is a possible confounder for renal BOLD MRI protocols using 30–40s acquisitions. The subject sustaining 90s breath-holds exhibited continued T2* decline beyond one minute. This suggests activation of parasympathetic autoregulation, potentially involving vasoconstriction and reduced renal blood flow/volume, both important confounders in BOLD interpretation [5]. Thus, while breath-holding minimizes motion artifacts, it also introduces physiological changes that complicate data interpretation. Protocols must account for these factors to avoid overestimating renal oxygenation deficits.

Conclusions: Breath-holding significantly influences renal T2* during BOLD MRI. Longer holds (>60 s) cause greater reductions, likely due to renal autoregulatory responses. Identifying the timing of this activation may provide insights into impaired renal vasoreactivity, common in early diabetic kidney disease. Since microvascular and macrovascular dysfunction occur early, these changes could serve as early biomarkers for disease detection and monitoring.

References

[1] - Pruijm M, Milani B, Pivin E, et al. "Reduced cortical oxygenation predicts a progressive decline of renal function in patients with chronic kidney disease." Kidney Int. 2018;93(4):932–940. doi:10.1016/j.kint.2017.10.023
[2] - Prasad PV. "Functional MRI of the kidney: tools for translational studies of pathophysiology of renal disease." Am J Physiol Renal Physiol. 2006;290(5):F958–F974. doi:10.1152/ajprenal.00349.2005
[3] - Pruijm M, Milani B, Pivin E, et al. "Reduced cortical oxygenation predicts a progressive decline of renal function in patients with chronic kidney disease." Kidney Int. 2018;93(4):932–940. doi:10.1016/j.kint.2017.10.023
[4] - Ebrahimi B, et al. "Temporal analysis of renal oxygenation using BOLD MRI: Impact of breathing patterns and data acquisition techniques." J Magn Reson Imaging. 2013;38(5):1191–1196. doi:10.1002/jmri.24099
[5] - Niendorf T, Pohlmann A, et al. "How BOLD is blood oxygenation level-dependent (BOLD) magnetic resonance imaging of the kidney?" Acta Physiol (Oxf). 2015;213(1):19–38. doi:10.1111/apha.12321

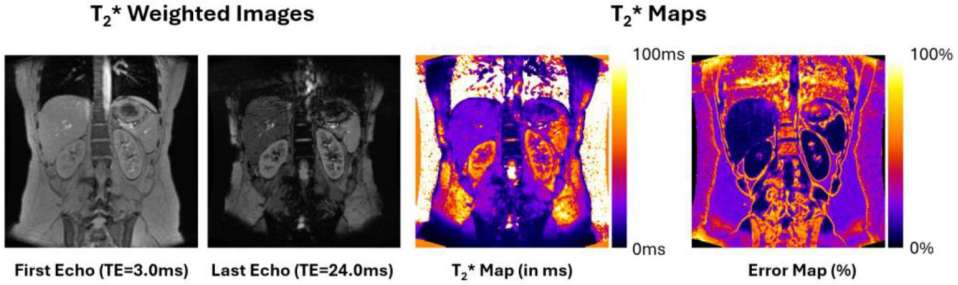

Fig. 1. Left: Example of the first and last echoes from the T2*-weighted image series. Right: Example

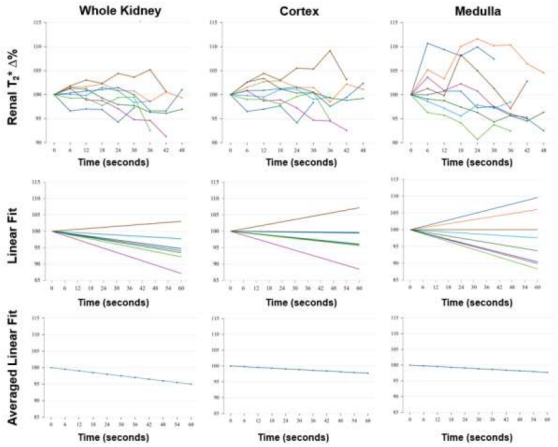

Fig. 2. Top: Averaged percentage change in renal T2* across three breath-holds for each volunteer, using the first detected scan as the reference for each ROI. Middle: Linear regression curves for each ROI. Bottom: Average slope from the linear fits

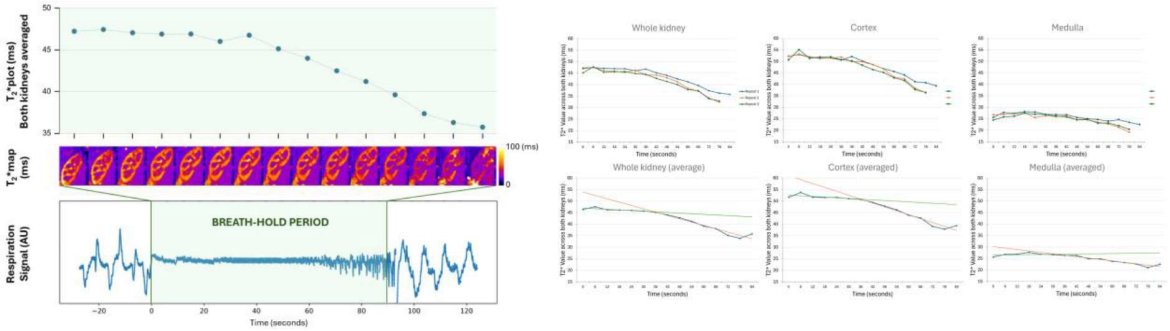

Fig. 3. Left: Top: averaged T2* values from whole-kidney ROIs in both kidneys using long breath-hold protocol. Middle: calculated T2* map (every 6 seconds). Bottom: respiration signal recorded during the experiment using respiratory bellows. Right: Top: absolute renal T2* values over the three repeats using the long breath-hold protocol. Bottom: Average signal from the three repeats, along with linear fits for the intervals [0–36] seconds and [36–90] seconds.

Feasibility of Dissolved-Phase Hyperpolarised ^{129}Xe MRI at 0.5 T

***Benjamin LB Wilson*[1], *Graham Norquay*[1], *Jan Wolber*[2] *and Jim M Wild*[1]**
[1] POLARIS, Division of Clinical Medicine, School of Medicine & Population Health, University of Sheffield, Sheffield, UK. [2] GE Healthcare, Amersham, UK.

Introduction Hyperpolarised (HP) ^{129}Xe MRI is a powerful tool for assessing pulmonary function, and implementing it at lower magnetic field strengths could improve accessibility and affordability. Low-field imaging offers several technical advantages, including longer transverse relaxation times and a relatively field-independent signal-to-noise ratio [1,2], making it an attractive option for wider clinical deployment. Dissolved-phase ^{129}Xe MRI offers valuable metrics for pulmonary gas exchange but has not been explored between 0.2 T and 1.5 T. At lower fields, chemical exchange broadening of the red blood cell (RBC) and membrane (M) peaks may hinder separation of their signals, and relaxation times remain uncharacterised. We have simulated spectra at 0.5 T to assess peak broadening of RBC and M resonances at 0.5 T and performed experiments to examine the field-dependence of the relaxation and exchange of dissolved ^{129}Xe, and search for a solution which models the exchange dynamics of ^{129}Xe dissolved in blood.

Methods The NMR spectrum of HP ^{129}Xe dissolved in human blood at 0.5 T was simulated by applying a two-compartment model of the Bloch-McConnell equations [3] using relaxation and exchange rate constants measured at 1.5 T in previous experiments [4,5]. Spectroscopy measurements were performed at 1.5 T and 3 T on samples of HP ^{129}Xe dissolved individually in olive oil, ethanol, chloroform and saline. Measurements were also taken at 1.5 T and 3 T of ^{129}Xe dissolved in mixtures of two of these solvents. T_1, T_2*, and δ_{gas} (chemical shift relative to ^{129}Xe gas resonance) were calculated by fitting Lorentzian functions to the data.

Results and Discussion The simulated and experimental spectra of ^{129}Xe dissolved in blood at 1.5 T (shown in **Fig. 1A**) had a root mean square error of 0.009, indicating close agreement between the two. This implies the validity of applying Bloch-McConnell theory to this scenario, and therefore of the simulated 0.5 T spectrum (for which there is no experimental data to provide a comparison). **Fig. 1B** shows the simulated spectrum of ^{129}Xe dissolved in blood at 0.5 T, with Lorentzian fitting applied to each resonance. This suggests that distinguishing RBC and M signals should be possible at 0.5 T. T_2* relaxation times were shortened from 2.75 ms to 2.57 ms in RBC and from 1.95 ms to 1.78 ms in M due to chemical exchange broadening. It is worth noting that simulations did not account for the field-dependence of T_2*, so these values may be underestimations.

Measurements of T_1, T_2, and δ_{gas} for HP ^{129}Xe dissolved in each of the solvents at 1.5 T and 3 T are shown in **Table 1**. As expected, T_1 increased with field strength while T_2* decreased in each case. T_2* was consistently 2-3 times shorter at 3 T than at 1.5 T. Measured chemical shifts were 3-5 ppm lower than the expected values [6]. The olive oil chemical shift was observed to decrease by 5 ppm when mixed with ethanol, compared to on its own. T_1 and T_2* were both generally longer for olive oil and ethanol in the mixed solvent, compared to as single solvents. The olive oil and chloroform mixture exhibited a single ^{129}Xe resonance, consistent with rapid chemical exchange due to the high miscibility of the two solvents. This contrasts with the distinct resonances observed in the mixture of olive oil and ethanol.

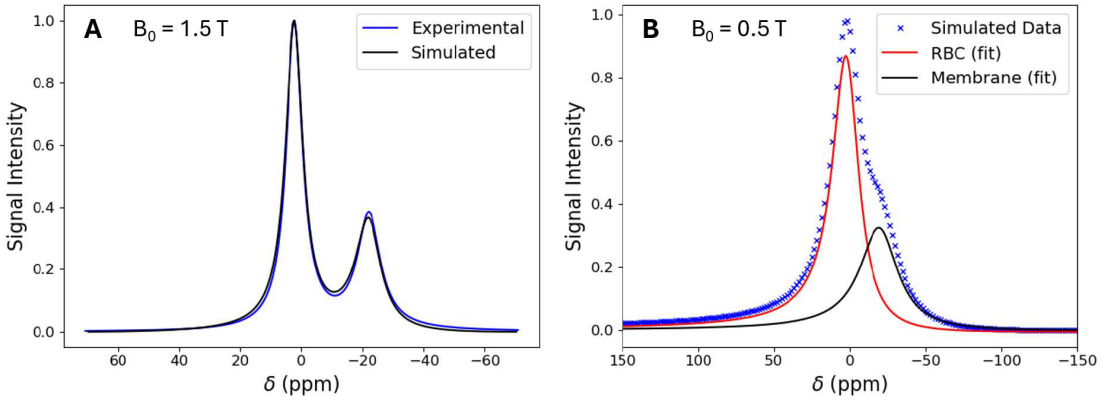

Fig. 1: (**A**) *Comparison of the experimental and simulated absorption spectrum of HP ^{129}Xe dissolved in blood at B_0 = 1.5 T.* (**B**) *Simulation of the same frequency spectrum at B_0 = 0.5 T, with Lorentzian functions fitted to the RBC and Membrane resonances.*

Solvent (peak)	B_0 = 1.5 T			B_0 = 3 T		
	T_1 (s)	T_2* (ms)	δ_{gas} (ppm)	T_1 (s)	T_2* (ms)	δ_{gas} (ppm)
Olive Oil	14.5	39.0	192	28.1	16.6	193
Ethanol	13.8	53.9	162	43.2	18.3	162
Saline	117	84.9	192	-	-	191
Chloroform	13.4	60.0	211	15.2	22.0	213
OO + Eth (Olive Oil)	12.0	45.7	187	35.0	19.4	187
OO + Eth (Ethanol)	15.9	61.9	162	128	21.4	162
OO + Chl (Olive Oil)	-	-	-	25.1	17.7	204
OO + Chl (Chloroform)	-	-	-	25.1	17.7	204

Table 1. *Measured relaxation times for ^{129}Xe dissolved in single or mixed solvents at 1.5 T and 3 T. 'OO + Eth' is a mixed solvent of olive oil and ethanol. 'OO + Chl is a mixed solvent of olive oil and chloroform. '-' indicates that this data was not collected.*

Conclusion & Future Work Simulations of the Bloch-McConnell equations indicate that dissolved-phase ^{129}Xe MRI at 0.5 T can resolve distinct RBC and M signals, enabling quantification of pulmonary gas exchange metrics such as the RBC:M ratio. However, experimental validation of the simulations is necessary. Measurements of dissolved ^{129}Xe relaxation times in different solvents demonstrate a strong dependence on magnetic field strength. Our future in vitro blood experiments will aim to measure ^{129}Xe relaxation times and exchange rates at 0.5 T to evaluate the feasibility of low-field gas-exchange imaging.

References [1] Parra-Robles et al. Med. Phys 2005;32:221-229. [2] Durand et al. Magn. Reson. Med. 2002;47(1):75-81. [3] McConnell J. Chem. Phys. 1958;28(3):430-431. [4] Norquay et al. Magn. Reson. Med. 2015;74:303-311. [5] Bifone et al. Proc. Natl. Acad. Sci. USA 1996;93(23):12932-12936. [6] Miller et al. Proc. Natl. Acad. Sci. USA 1981;78(8):4946-4949.

Accelerated Bloch-Siegert B_1^+ Mapping using Concentric Ring ^{31}P-MRSI at 7T.

Alice Conner[1], Ferenc E. Mózes[1], Jabrane Karkouri[2], Aaron Axford[1], Fabian Niess[3], Christopher T. Rodgers[2], Wolfgang Bogner[3], Damian Tyler[1], Ladislav Valkovič[1,4].
[1]OCMR, University of Oxford. [2]WBIC, University of Cambridge. [3]High-field MR Centre, Medical University of Vienna. [4]Department of Imaging Methods, Institute of Measurement Science, Slovak Academy of Sciences.

Introduction: Non-invasive quantification of energy metabolism using ^{31}P Magnetic Resonance Spectroscopy (^{31}P-MRS) has high clinical potential. However, absolute quantification of phosphorus metabolites requires saturation correction (as data are often acquired with short TR), which in turn requires accurate B_1^+ knowledge. The Bloch-Siegert method of B_1^+ mapping has been successfully applied in the human heart using 3D Cartesian-sampling of k-space (3D-CSI)[1]. However, long acquisition times (e.g. 21 min for cardiac imaging)[2] prevent this method from being routinely used in larger organs, or alongside already long ^{31}P-MRS experiments. Instead, accelerated k-space sampling may facilitate significantly shorter scan times[3]. This work aimed to optimize Bloch-Siegert B_1^+ mapping using a 3D-concentric ring k-space trajectory (3D-CRT). As acceleration impacts SNR, the effect of apodization-induced line broadening (applied to improve spectral fitting) and k-space sampling density on B_1^+ maps was investigated.

Methods: A uniform KH_2PO_4 30mM phantom (30 L jerrycan, 43x26.5x26.5 mm^3) was scanned in a 7T scanner (Magnetom Plus, Siemens Healthineers) equipped with a ^{31}P whole-body birdcage transmit and 16-channel receive array coil (Rapid Biomedical). B_1^+ mapping utilized a Bloch-Siegert Fermi pulse (T_p= 8 ms, T_0= 4 ms, α= 0.1 ms, offsets= ±1000Hz) for 2D-CSI and 3D-CRT acquisitions, with variations to the scan time/SNR. 'Short' and 'long' scans were acquired for 2D-CSI (10 or 60 averages, 9:56 min or 48:48 min respectively) and 3D-CRT (17 or 39 rings, 8:48 min or 48:28 min respectively). Additional 2D-CSI acquisition parameters included T_R= 1 s, T_E= 2.3 ms, matrix= 12x12x1, FOV= 300x300x30 mm^3, spectral samples= 2048, bandwidth= 8000 Hz. Additional 3D-CRT acquisition parameters included T_R= 1 s, T_E= 2 ms, matrix= 12x12x12, FOV= 300x300x170 (or 300x300x30 mm^3 for apodization linewidth comparisons), spectral samples= 756, bandwidth= 2778 Hz. 3D-CRT data were reconstructed offline using the non-uniform fast-Fourier transform toolbox with min-max Kaiser-Bessel kernel interpolation and two-fold oversampling. Individual coil data were combined using WSVD[4], and apodized in the time domain before spectral fitting using OXSA[5] (MATLAB R2024b, MathWorks). Apodization linewidths of 0Hz, 10Hz, 20Hz, 30Hz and 40Hz were applied to 'short' scans when investigating the effect of apodization-induced line broadening. All other comparisons used spectra apodized by 10Hz. Voxels were excluded from analysis if they were outside the ROI, or had a voxelwise CoV >0.4, baseline fitted linewidth >2000Hz (indicating failed spectral fitting), or SNR-weighted Cramér–Rao lower bound (CRLB) >10°. Matched voxels were compared using a two-tailed paired *t*-test or repeated measures ANOVA with Tukey's multiple comparisons (>2 groups). Bias between 2D-CSI and 3D-CRT was evaluated using Bland-Altman analysis (GraphPad Prism v10.2.2). Results are presented as mean±SD.

Results: Apodization-induced line broadening did not significantly alter B_1^+, producing stable 2D-CSI values for apodization linewidths of 0Hz (3.8±1.3 μT), 10Hz (3.9±1.2 μT), 20Hz (3.8±1.3 μT), 30Hz (3.8±1. 2 μT) and 40Hz (3.8±1.2 μT) (all p>0.05, Fig 1). Similarly, 3D-CRT B_1^+ values were stable for 0Hz (4.1±1.3 μT), 10Hz (4.1±1.3 μT), 20Hz (4.1±1.2 μT), 30Hz (4.1±1.3 μT), and 40Hz (4.1±1.3 μT) (all p>0.05, Fig. 1). Importantly, all apodization linewidths significantly improved the CRLB of phase fitting for both 2D-CSI and 3D-CRT (all p<0.0001). Mean B_1^+ of 'short' 2D-CSI (3.6±1.2 μT) and 'short' 3D-CRT (4.1±2.0 μT) did not significantly differ (p>0.05), with a bias of 0.4 μT (LoA -3.6 to 4.5 μT). However, a significant difference was observed between 'long' 2D-CSI (3.6±0.9 μT) and 'long' 3D-CRT (3.0±1.3 μT) (p=0.0006), with a bias of -0.6 μT (LoA -3.4 to 2.2 μT) (Fig. 2). Notably, no significant difference was seen between 'long' 2D-CSI (3.6±0.9 μT) and 'short' 3D-CRT (4.1±2.0 μT) (p<0.05), with a bias of 0.5 μT (LoA -3.4 to 4.4).

Discussion: Bloch-Siegert B_1^+ mapping is feasible using 3D-CRT, and can facilitate accelerated scanning. This work demonstrates that apodization-induced line broadening can improve fitting confidence, while not significantly altering B_1^+ quantification in phantoms- data that supports its use in spectral fitting and post-processing of B_1^+ maps. Notably, 'short' 3D-CRT B_1^+ values were comparable to 'short' and 'long' 2D-CSI scans, despite indicating a small bias to overestimate B_1^+. The observed difference between 'long' 2D-CSI and 'long' 3D-CRT may be due to higher voxel variability (and associated lower SNR) from 3D-CRT measurements, despite both methods producing visually homogenous results. Future work aims to further optimise 3D-CRT SNR within clinically feasible scan times, and to explore the relationship between 2D-CSI and 3D-CRT in vivo.

Conclusion: 3D-CRT Bloch-Siegert B_1^+ mapping provides greater image coverage in scan times comparable to single slice 2D-CSI. Future work aims to integrate this method into the Bloch-Siegert Four Angle Saturation Transfer method, and for absolute quantification of phosphorus metabolites in vivo.

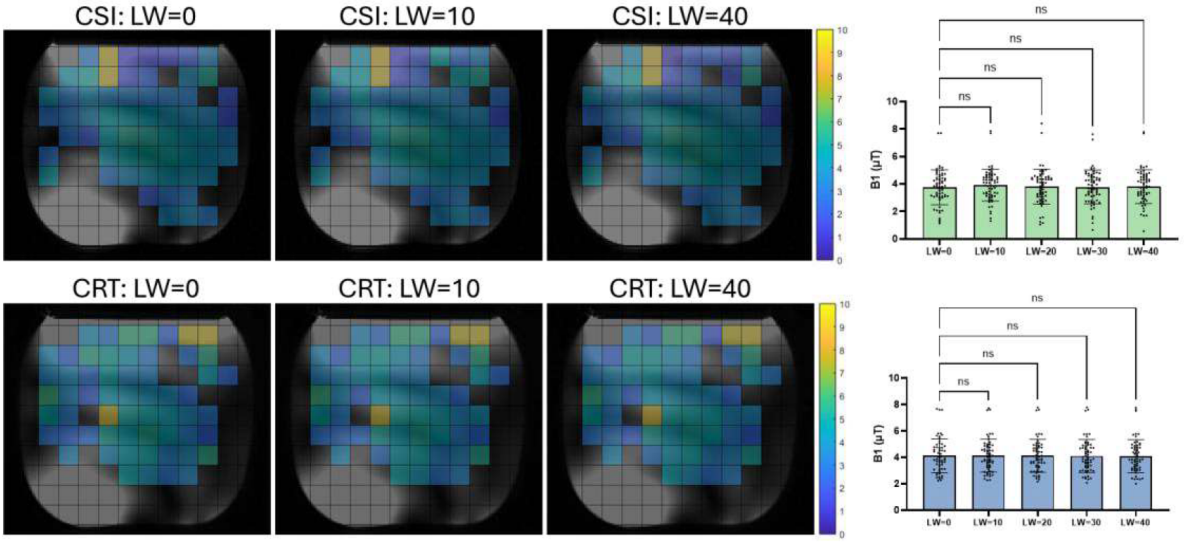

Fig 1. *B_1^+ maps of matched voxels with different levels of apodization (0-40Hz) for 2D-CSI and 3D-CRT acquisitions.*

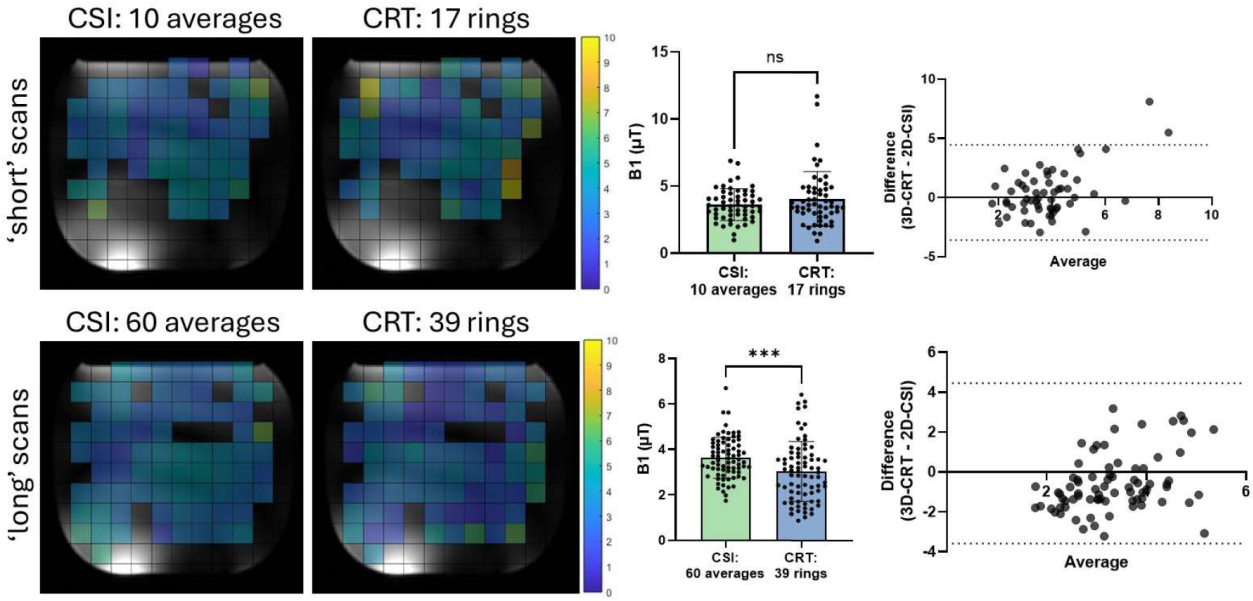

Fig 2. *B_1^+ maps of matched voxels across* conditions of 'short' (10 averages vs 17 rings) and 'long' scans (60 averages vs 39 rings) using *2D-CSI and 3D-CRT. Bland-Altman plots depict a small bias between B_1^+ mapping techniques.*

References: [1] Clarke WT et al., *NMR Biomed*, 2016; **[2]** Clarke WT et al., *Magn Reson Med*, 2017; **[3]** Clarke WT et al., *NMR in Biomed,* 2022; **[4]** Rodgers CT et al., *Magn Reson Med,* 2010; **[5]** Purvis LB et al., *PLoS One,* 2017.

Generating a Novel Digital Phantom for Simultaneous QSM and EPT

Philippa Sha[1], Jierong Luo[1], Patrick Fuchs[2], Karin Shmueli[1]
[1]Department of Medical Physics and Biomedical Engineering, University College London, London, United Kingdom.
[2] imec-Visionlab, Department of Physics, University of Antwerp, Antwerp, Belgium.

Introduction:

Quantitative susceptibility mapping (QSM) and electrical properties tomography (EPT) are two emerging MRI techniques to non-invasively measure tissue electromagnetic properties. QSM uses the phase of the MRI signal to reconstruct the underlying distribution of magnetic susceptibility (χ) [1]. Phase-based EPT uses the transceive phase (ϕ_0) to estimate tissue electrical conductivity (σ) [2].

QSM and EPT have each shown promise for various clinical applications [2-5]. Although typically performed separately, simultaneous QSM and EPT has been shown to be feasible and beneficial, due to the complementary information they provide [6,7]. While digital phantoms have been developed separately for QSM [8] and EPT [9], none currently support the evaluation of both techniques. Therefore, we developed a novel digital brain phantom, designed for the simultaneous application of QSM and EPT.

Methods:

Phantom construction: Multi-echo GRE magnitude and phase data were obtained from the QSM Challenge 2.0 [8], with sequence parameters: 4 echoes, TE_1 = ΔTE = 4 ms, resolution = 0.64 mm isotropic, FOV = 205 x 205 x 164 mm^3. Because phase extrapolation to TE=0 did not yield a meaningful transceive phase, we simulated ϕ_0 by non-linear registration of the ϕ_0 data from the EPT Challenge phantom (Sim4Life; resolution = 1 mm isotropic, FOV = 256 x 256 x 160 mm^3 [9]) into the QSM Challenge anatomical space, using FLIRT [10,11] and FNIRT [12]. The registered ϕ_0 was added to the GRE phase in the complex domain according to $\varphi(t) = \gamma \Delta B\, TE + \varphi_0$.

Segmentations of 10 regions of interest (ROIs) were obtained from the QSM Challenge phantom, and a corresponding tissue segmentation was generated by grouping ROIs into cerebrospinal fluid (CSF), grey matter (GM) and white matter (WM). Ground truth susceptibility was taken directly from the QSM Challenge. Ground truth conductivity was generated by assigning literature values to each tissue type (CSF = 2.22 S/m, GM = 0.69 S/m, WM = 0.41 S/m) [13].

Validation: QSM reconstruction was performed based on consensus recommendations [14]: SEGUE was used for phase unwrapping [15], PDF for background field removal [16], and FSL BET for masking [17] with additional noise-based thresholding [18]. Four of the most popular and robust dipole inversion methods were assessed: iteratively regularised Tikhonov (iterTik) [19], FANSI nonlinear TGV (nlTGV) [20], weak harmonics (WH-QSM) [21], and automatically regularised nonlinear dipole inversion (autoNDI) [22].

EPT was performed using an optimised in-house pipeline [23]. Conductivity was reconstructed via the surface integral of the ϕ_0 gradient, using 3D spherical kernels to perform differentiation and integration, each with optimised radii. Magnitude- and segmentation-based kernel weighting was applied for noise suppression and edge preservation [23].

QSM and EPT reconstructions were assessed by calculating the mean absolute error (MAE) relative to the ground truth. QSM accuracy was evaluated using the mean susceptibility per ROI. EPT accuracy was assessed using the median conductivity per tissue type, as well as percentage of non-physical values (<0 S/m and >10 S/m), which were considered erroneous.

Results:

Fig. 1 shows the complete phantom, including multi-echo magnitude and phase, segmentations, and ground truth maps.

QSM reconstructions using all four dipole inversion methods are shown in Fig. 2, alongside MAE values. Table 1 lists mean ROI χ values for all methods vs the ground truth. IterTik yielded the lowest overall MAE and produced χ values closest to the ground truth in 6 of 10 ROIs.

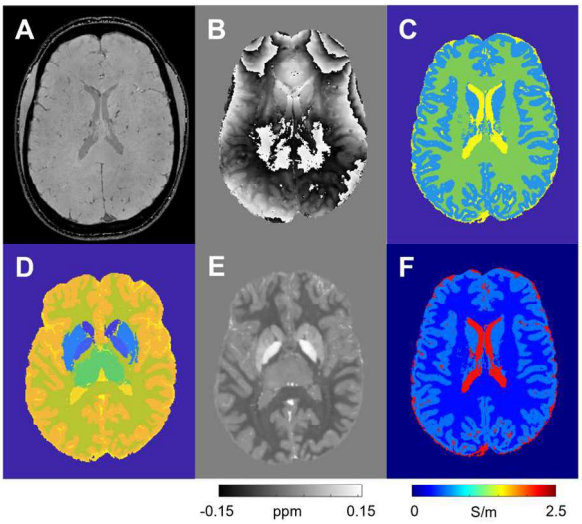

Fig. 1: Complete phantom dataset. (A) Final echo of multi-echo magnitude. (B) Final echo of multi-echo phase (wrapped). (C) Tissue segmentation. (D) ROI segmentation. (E) Ground truth susceptibility map. (F) Ground truth conductivity map.

Fig. 3 compares conductivity maps reconstructed from ϕ_0 extrapolated from the QSM Challenge data, vs our simulated ϕ_0, using identical parameters and optimal kernel radii (15 mm for both differentiation and integration). Our simulation produced median σ values closely matching those in the literature: 2.16 S/m (CSF), 0.69 S/m (GM), and 0.50 S/m (WM).

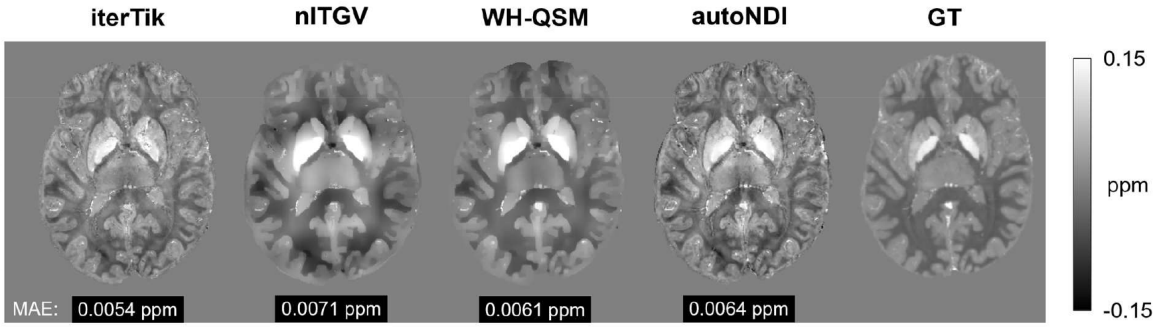

Fig. 2: QSMs reconstructed using four dipole inversion methods, with susceptibility ground truth (GT).

ROI	Mean χ (ppm)				
	iterTik	nlTGV	WH-QSM	autoNDI	GT
Caudate	0.049	0.059	0.075	0.057	0.044
Globus Pallidus	0.134	0.228	0.201	0.152	0.131
Putamen	0.036	0.057	0.051	0.038	0.038
Red Nucleus	0.129	0.157	0.166	0.154	0.100
Dentate Nucleus	0.099	0.216	0.232	0.115	0.152
Substantia Nigra & Sub-Thalamic Nucleus	0.111	0.145	0.146	0.121	0.111
Thalamus	0.023	0.039	0.009	0.031	0.020
WM	-0.025	-0.032	-0.027	-0.028	-0.030
GM	0.015	0.014	0.012	0.014	0.020
CSF	0.012	0.017	0.022	0.013	0.019

Table 1: Mean χ values per ROI using each QSM reconstruction method on phantom, compared to GT.

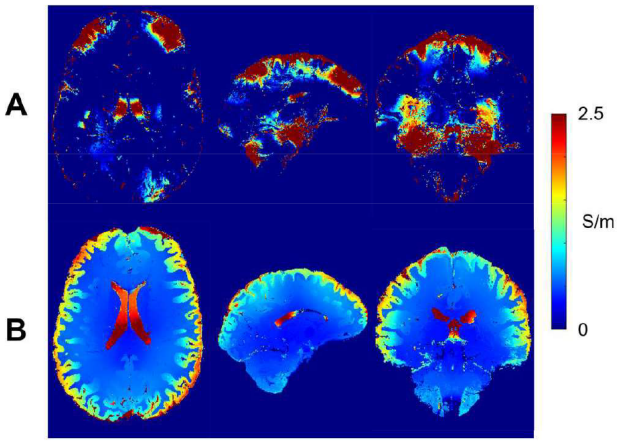

Fig. 3: Conductivity maps generating using (A) original QSM Challenge data vs (B) our simulation.

Discussion: Our simulated phantom produced high-quality susceptibility and conductivity maps, with minimal errors. A major limitation in the original QSM Challenge data was its inability to provide a meaningful ϕ_0, rendering it unsuitable for EPT, as highlighted in Fig. 3A. Our simulation approach overcomes this issue, while maintaining QSM compatibility. One limitation, however, is that although our ϕ_0 simulation is noiseless, the multi-echo QSM Challenge data has an SNR of approximately 160, meaning a totally noiseless version of the phantom is not currently available. Future work may expand the phantom to include artefacts or pathology such as calcifications, to enable optimisation of QSM and EPT for clinical applications.

Conclusions: We generated a dual-purpose QSM+EPT digital phantom, enabling optimisation of both techniques in a unified framework. This will facilitate joint investigation of simultaneous susceptibility and conductivity mapping in future clinical studies.

References:

[1] Shmueli, K. *Advances in MR Technology & Applications.* 2020; 819-38. **[2]** Katscher, U. et al. *NMR Biomed.* 2017; 30(8):e3729. **[3]** Liu, C. et al. *Tomography*. 2015; 1(1):3-17. **[4]** Ruetten, P.P.R. et al. *Br. J. Radiology.* 2019; 92(1101). **[5]** Hancu, I. et al. *MRM*. 2019; 81(2):803-10. **[6]** Kim, D-H. et al. *MRM*. 2013; 71(3):1144-50. **[7]** Kiersnowski, O.C. et al. *Proc. Ann. Meeting ISMRM*. 2024; 0188. **[8]** Marques, J.P. et al. *MRM*. 2021; 86(1):526-42. **[9]** Mandija, S. et al. *Proc. Ann. Meeting ISMRM*. 2022; 0704. **[10]** Jenkinson, M. et al. *Med. Image Analysis.* 2001; 5(2):143-56. **[11]** Jenkinson, M. et al. *NeuroImage*. 2002; 17(2):825-41. **[12]** Andersson, J.L.R. et al. *FRMIB Technical Report TR07JA2*. 2010. **[13]** Gabriel, S. et al. *Phys. Med. Biol.* 1996; 41(11):2251-69. **[14]** QSM Consensus Org. Comm. et al. *MRM*. 2024; 91(5):1834-62. **[15]** Karsa, A. et al. *IEEE Trans. Med. Imag*. 2019; 38(6):1347-57. **[16]** Liu, T. et al. *NMR Biomed.* 2011; 24(9):1129-39. **[17]** Smith, S.M. *Human Brain Mapping*. 2002; 17(3):143-55. **[18]** Karsa, A. et al. *Proc. Ann. Meeting ISMRM*. 2022; 2462. **[19]** Karsa, A. et al. *MRM*. 2020; 84(6):3206-22. **[20]** Milovic, C. et al. *MRM*. 2018; 80(2):814-21. **[21]** Milovic, C. et al. *MRM*. 2019; 81(2):1399-1411. **[22]** Milovic, C. et al. *Proc. Ann. Meeting ISMRM*. 2021; 3982. **[23]** Karsa, A. et al. *Proc. Ann. Meeting ISMRM.* 2021; 2774.

TAsk-DRiven Experimental Design for Protocol Optimization of Ultra-high Gradient Strength Diffusion-weighted MRI Measurements

Kadir Şimşek[1,2], Marco Palombo[1,2], Muhammed Barakovic[3], Stefano Mango[3], Jens Wuerfel[3], Derek K. Jones[1] and Paddy Slator[1,2]

1-Cardiff University Brain Research Imaging Centre (CUBRIC), School of Psychology, Cardiff University, Cardiff, United Kingdom; 2-School of Computer Science and Informatics, Cardiff University, Cardiff, United Kingdom; 3-Hoffmann-La Roche AG, Basel, Switzerland

Introduction

This study focuses on optimizing diffusion MRI (dMRI) acquisition protocols to improve image quality, reduce scan time, and enhance sensitivity to tissue microstructure. Traditional methods achieve this by minimizing the Cramer-Rao Lower Bound (CRLB) [1], optimizing angular coverage of b-shells [2], or applying data interpolation [3]. More recent machine learning approaches, such as TADRED (Task-Driven Experimental Design) [4] and physics-informed networks [5], offer greater flexibility across different dMRI models. TADRED combines a subsampling network, which selects the most informative measurements, with a task network to perform the desired analysis, thereby improving acquisition efficiency. This study evaluates the TADRED-based subsampling method against a naïve approach that focuses solely on maximizing angular coverage within each shell.

Methods

Data Acquisition, Processing and Fitting

Multi-shell dMRI data [6] were acquired on an ultra-strong gradient system with seven b-shells (up to b = 6 ms/μm²), 266 directions (including 13 b=0), and acquisition parameters TE = 80 ms, TR = 5 s, 1.8 mm slice thickness, and 120 × 120 mm² FOV. Direction counts scaled with b-values, and b=0 images were interleaved for correction purposes. Data preprocessing included MP-PCA denoising [7–10], correction for drift and outliers using SOLID [11], distortion correction with FSL's topup [12,13] and eddy [14], gradient non-linearity correction in MATLAB, and Gibbs ringing removal via MRtrix3 [15]. For TADRED, SANDI model parameter maps were generated from the full dataset using a random forest regression via the SANDI MATLAB Toolbox [16].

Data Subsampling and Analysis

Two subsampling methods were used to reduce dMRI data: uniform subsampling and the TADRED framework [4]. Uniform subsampling reduced data by 10%, 30%, and 50% per b-shell while maintaining uniform angular distribution. In contrast, TADRED used the full dMRI data, SANDI maps, and acquisition parameters as input to train subsampling and task networks (84% training, 8% validation, 8% testing). TADRED then generated optimized subsampled datasets without relying on the original sampling pattern. SANDI parameter maps were computed for both subsampled datasets and compared to full-data maps to assess accuracy and effectiveness.

Results

Fig. 1 shows the subsampled diffusion directions across several b-shells for both uniform and TADRED approaches. Notably, TADRED removed more directions at the intermediate b-shell (b = 2.4 ms/μm²). **Fig. 2** compares SANDI model parameter maps derived from the uniform and TADRED-subsampled datasets, illustrating variations between the two approaches.

Discussion

TADRED showed less than 20% error in brain tissue, with higher errors mainly in CSF regions. Across all subsampling rates, it outperformed uniform subsampling in SANDI parameter accuracy (Fig. 3). At 50% subsampling, TADRED showed slightly higher errors in $f_{neurite}$ and R_{soma} compared to uniform subsampling, but these errors were largely confined to CSF voxels. This study focused solely on TADRED's subsampling network for protocol optimization, using the same model fitting for both methods. Future work will incorporate the task network to directly estimate SANDI parameters.

Conclusion

TADRED outperformed uniform subsampling in estimating SANDI parameters, showing lower error rates and promising potential for efficient dMRI protocol optimization in future clinical and research applications.

Acknowledgements

- This project is funded by Hoffmann-La Roche AG
- KŞ works as a leading researcher in the project funded by Hoffmann-La Roche AG and it is also funded by UKRI FLF MR/T020296/2.
- MP and DKJ are the principal co-investigators in the project funded by Hoffmann-La Roche AG. MP is also funded by UKRI FLF MR/T020296/2.

References

[1] D. C. Alexander, *et al., MRM*, 2008 [2] E. Caruyer, *et al., MRM*, 2013 [3] T. B. Dyrby *et al., Neuroimage,* 2014 [4] S. B. Blumberg, *et al.*, arxiv, 2022 [5] Á. Planchuelo-Gómez, *et al., Med Image Anal*, 2024.[6] Y. Assaf, *et al., Neuroimage*, 2005 [7] J. Veraart, *et al., MRM*, 2016 [8] J. Veraart, *et al., Neuroimage,*.2016 [9] L. Cordero-Grande, *et al., Neuroimage*, 2019 [10] J. D. Tournier *et al., Neuroimage*, 2019 [11] V. Sairanen, *et al., Neuroimage,* 2018 [12] J. L. R. Andersson, *et al., Neuroimage*, 2003 [13] S. M. Smith *et al., Neuroimage*, 2004 [14] J. L. R. Andersson, *et al., Neuroimage*, 2016 [15] E. Kellner *et al., MRM*, 2016 [16] M. Palombo *et al.*, 2020

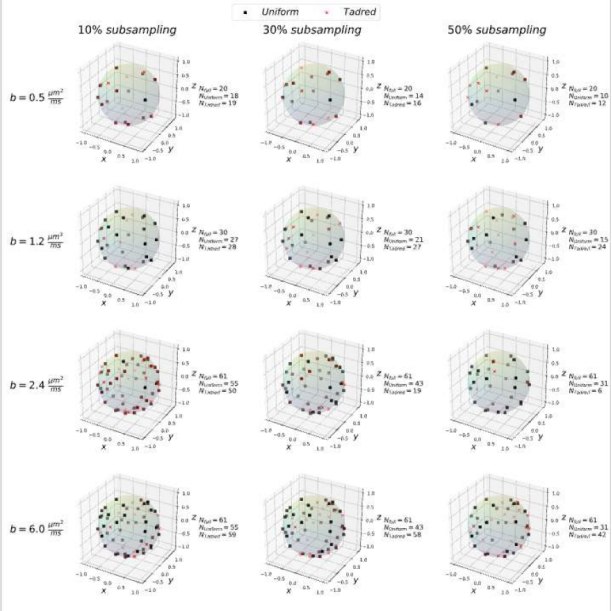

Figure 1: Diffusion directions shown for selected b-shells after subsampling using manual uniform sampling (black squares) and TADRED (red crosses) at different subsampling levels.

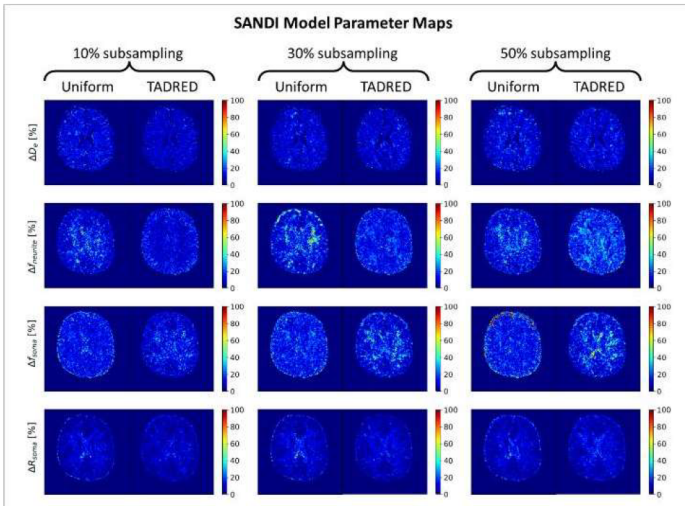

Figure 2: Difference maps of SANDI model parameters are shown for all subsampling ratios and both subsampling approaches. These maps were generated by comparing the SANDI fits from the subsampled datasets to the ground truth maps. Overall, the TADRED-based subsampling yields lower errors in the difference maps compared to uniform subsampling.

Improving transmit magnetic field homogeneity using a neurovascular head and neck coil with tailored parallel transmission pulses

Chia-Yin Wu[1], Divya Baskaran[1], Keith Muir[1], Natasha E. Fullerton[1,2], Shajan Gunamony[1,3], David A. Porter[1]

[1]Imaging Centre of Excellence, University of Glasgow, Glasgow, UK

[2]Department of Neuroradiology, Institute of Neuroscience, NHS Greater Glasgow and Clyde, Glasgow, UK

[3]MR CoilTech Limited, Glasgow, UK

Introduction: A 7T neurovascular head-and-neck coil (NVHN)[1] provides coverage of the brain and cervical spine regions enabling various neurovascular imaging techniques at ultra-high field (UHF). UHF systems significantly improve SNR and parallel-imaging but capabilities are challenged by non-uniform transmit magnetic fields (B_1^+). Parallel transmission (pTx) can be used to mitigate the B_1^+ problem[2]. With a single dedicated NVHN coil (Fig. 1), tailored pTx pulse designs can remain more streamlined without the need of coordinating multiple coils imaging different anatomical regions. Here we demonstrate an initial evaluation using a NVHN coil with tailored pTx pulses to improve signal uniformity across the brain and neck region in vivo.

Methods: All data were collected on a 7T Terra system (Siemens Healthineers, Germany) using a custom-built 8TxRx56Rx NVHN coil. Prior to the scan, the healthy volunteer provided written informed consent of the project ethics approved by the local ethics committee. Absolute (SA2RAGE[5]) and relative B_1^+ maps (resolution 4x4x4mm^3) were acquired to design tailored pTx pulses. Non-selective tailored pTx pulses (8 k_T-points[2], duration=1.66ms) were designed using the MLS spatial-domain-method[3,4]. 3D GRE datasets were acquired with 5° and 10° flip-angle pulses. Acquisitions were made using the standard non-selective excitation pulse in the circularly polarised (CP) mode and with pTx pulses. Combined with the SA2RAGE[5] maps, the ratio between the CP and pTx images was used to construct flip-angle maps produced by each pulse.

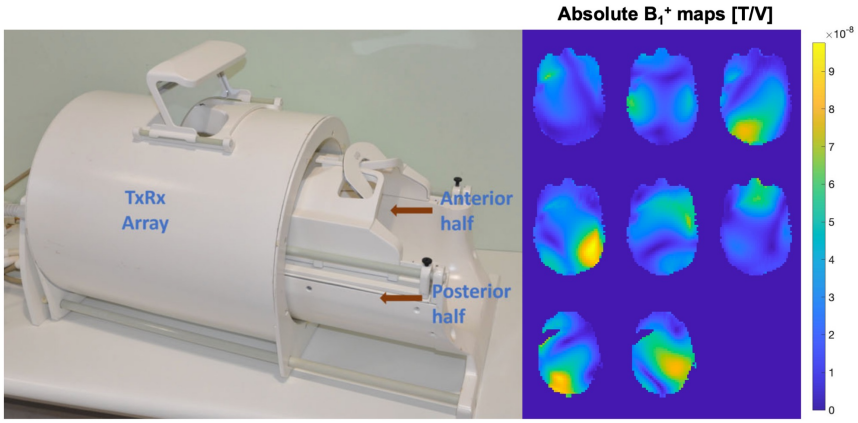

Fig. 1. Left: 8TxRx56Rx Neurovascular Head-and-Neck (NVHN) coil (Image from [1]). Right: Transmit sensitivity maps measured for each of the 8Tx-channels.

Results and Discussion: Significant improvements in excitation fidelity was achieved in the peripheral regions of the head extending down to the upper neck region in pTx-mode compared to CP-mode. The pTx pulses produced superior excitation uniformity with a NRMSE of 0.23 in comparison to 0.45 in the brain using CP-mode for 5° flip-angle. Similarly, a NRMSE of 0.26 was achieved for 10° flip-angle using pTx.

To put this into perspective 3D T_2^*-weighted images were collected to visually assess uniformity. Figure 3 show areas of improved signal uniformity in cerebellum, peripheral regions of the brain and central neck region when using pTx pulses compared to standard non-selective pulses.

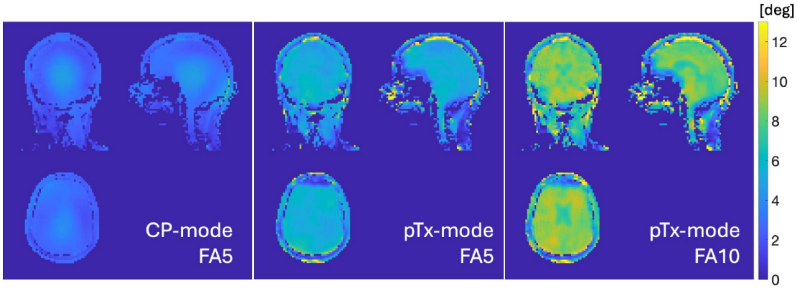

Fig. 2. Comparison of flip-angle maps for the use of 5° pulse in CP-mode, 5° and 10° k_T-points pulse in pTx-mode.

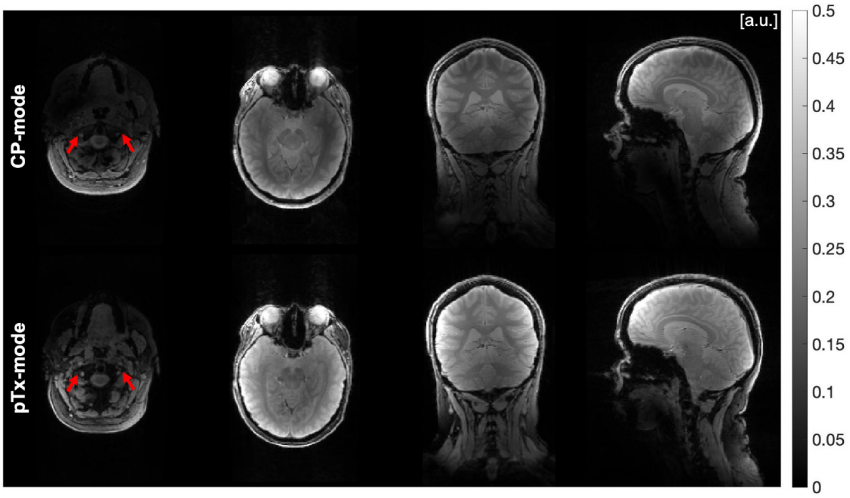

Fig. 3. T_2*-weighted images acquired in CP-mode (top) and pTx-mode (bottom). Note: measured images have the receive sensitivity bias superimposed.

Conclusions: Conventional tailored pTx pulses can improve excitation fidelity across both brain and neck regions. This shows promising potential in incorporating pTx pulses in more advanced MRI techniques with targeted interest in both the brain and neck regions.

Acknowledgements: This project is funded by Scottish Funding Council, grant H07012/242700324, the Christine Rodgers endowment fund, the Neuroscience Foundation, the Strength in Places fund, and Innovate UK through The Living Laboratory: driving economic growth in Glasgow through real world implementation of precision medicine (award Ref: 107140). The authors also thank Robin Sayer and Iain Hendry from the NHS Medical Devices Unit for providing the mechanical design for this coil.

References

[1] D. Baskaran, B. Ding, S. Chu et al. Magn Res Med. 70(1): 386-400 (2024).
[2] M. A. Cloos et al. Magn Res Med. 67(1): 72-80 (2012).
[3] W. Grissom, C.-Y. Yip, Z. Zhang et al. Magn Res Med. 56(3): 620-629 (2006).
[4] K. Setsompop, L. L. Wald, V. Alagappan et al. Magn Res Med. 59(4): 908-915 (2008).
[5] F. Eggenschwiler, T. Kober, A. W. Magill et al. Magn Res Med. 67(6): 1609-1619 (2012).

Contact: chia-yin.wu@glasgow.ac.uk

POSTER ABSTRACTS

In order of programme

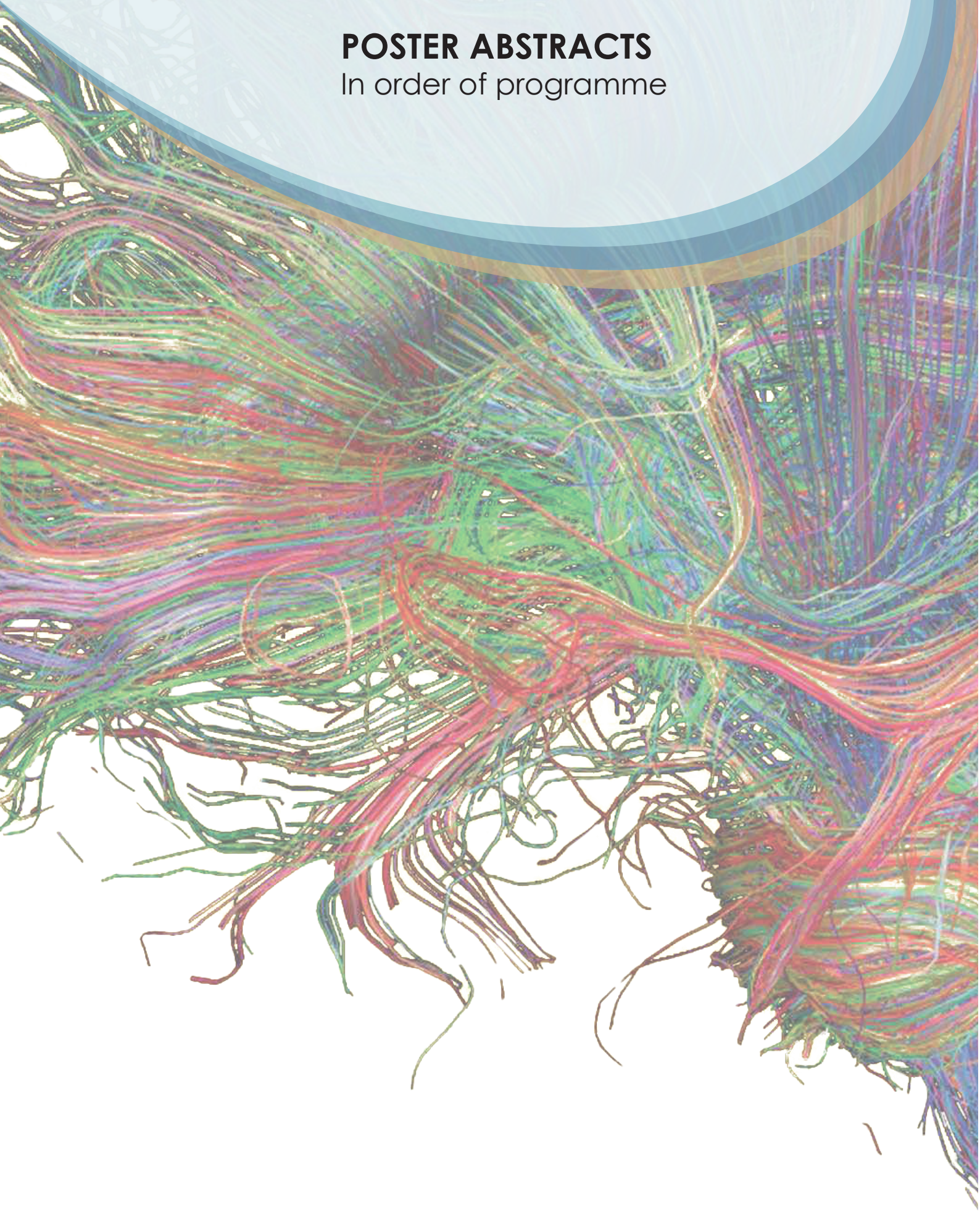

Altered Resting State Ventrolateral Periaqueductal Grey Functional Connectivity in Sickle Cell Anaemia

Mitchel Lee[1], Fenella Kirkham[2], Karin Shmueli[1]
[1]Medical Physics and Biomedical Engineering, University College London, London, UK
[2]Developmental Neurosciences, Institute of Child Health, University College London, London, UK

Introduction: Sickle cell anaemia (SCA) is a genetic blood disorder associated with episodes of acute pain and a substantial burden of chronic pain, potentially relating to neurological dysfunction [1]. Abnormal brain activity and functional connectivity have been widely reported [1]. Here, we investigated SCA-related changes to the connectivity patterns of a major pain-processing brainstem structure, the periaqueductal grey (PAG). The PAG comprises several functionally distinct subdivisions, with the lateral (lPAG) and dorsolateral (dlPAG) regions associated with active coping and non-opioid analgesia, and the ventrolateral PAG (vlPAG) linked to passive coping and opioid-mediated pain control [2]. The relationship between connectivity changes in these regions and self-reported pain scores was also considered.

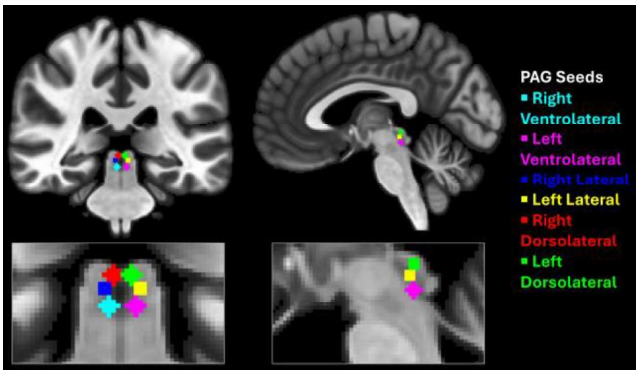

Figure 1: PAG seeds shown overlaid on coronal and sagittal slices of the MNI space T1w template, with zoomed views below each slice.

Methods: 36 SCA patients (aged 8-64 years, mean age 23 years, 15 male) and 16 healthy controls (HCs, aged 10-64 years, mean age 18 years, 12 male), recruited for the Prevention of Morbidity in Sickle Cell Anaemia (POMS) study [3], were imaged at 3T with a 6.2 minute single-echo EPI resting-state MRI scan with parameters: TR = 1.24 s, TE = 26 ms, 2.5 x 2.5 x 3 mm resolution, matrix 80 x 80 x 40, and a T1-weighted structural MPRAGE acquisition with 1 mm isotropic resolution. Functional and structural data were pre-processed with a standard pipeline including geometric distortion correction, slice timing correction, outlier detection, SPM12 unified segmentation and MNI-space normalisation, 8-mm FWHM Gaussian smoothing, and denoising, all implemented in the CONN toolbox using default parameters [4]. PAG seeds were created as 2-mm radius spherical seeds on the MNI space structural template as per previous literature [5]. These defined the lPAG, dlPAG and vlPAG for both hemispheres (Fig. 1). The bilateral lPAG, dlPAG and vlPAG seeds were used to compute whole-brain connectivity maps (Fisher-transformed correlation of each seed's time series with every voxel signal timecourse). Group differences between SCA patients and controls were determined at the cluster level (voxel threshold $p < 0.001$, cluster p-FDR < 0.05) using Random Field Theory [4] with age and sex regressed out as nuisance covariates. Clusters showing significant changes relative to controls were then regressed against pain scores derived from a two-week pain diary completed before scanning, which were available for 18 of the SCA patients [6].

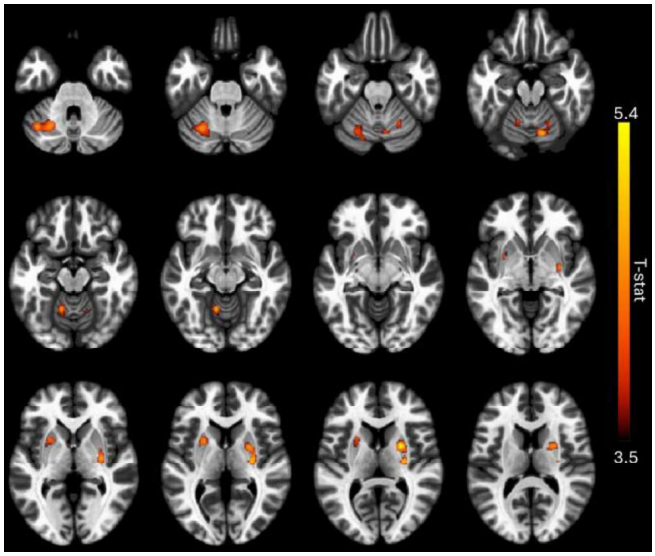

Figure 2: Clusters showing significantly higher functional connectivity with the bilateral vlPAG in SCA patients compared to controls.

Results: PAG seeds are shown in Figure 1. The lPAG and dlPAG did not show any significant connectivity differences between SCA patients and controls. The vlPAG showed 4 clusters of significantly increased connectivity in SCA patients, located primarily in the bilateral cerebellum and

putamen (Figure 2 and Table 1). No relationship was found between pain scores and connectivity in any of these clusters (Figure 3).

Cluster	Extent (voxels)	p-FDR	Region(s)
1	448	0.00014	Cerebellum VI L (44%), Crus I L (36%)
2	356	0.00039	Putamen R (73%)
3	148	0.02107	Putamen L (98%)
4	148	0.02107	Cerebellum VI R (85%)

Table 1: Cluster extent, FDR-corrected p-value and main regions (with % of cluster within that region) for the significant vlPAG connectivity clusters.

Discussion: Our results show some consistency with a previous PAG connectivity study in SCA, which also found elevated connectivity to the cerebellum in SCA patients with chronic pain compared to patients without chronic pain and healthy controls [7]. Increased putamen connectivity to other brain regions has also been observed in SCA [8]. We previously reported widespread increases in connectivity in this cohort between several large-scale brain networks [9], and these results may be linked to that hyperconnectivity pattern. The putamen is widely implicated in pain disorders [10]. Interactions between the vlPAG and putamen have been linked to the transmission of pain-expectancy signals, with the putamen relaying expected pain-relief signals to the PAG, and the PAG issuing an ascending prediction-error signal whenever incoming nociceptive input violates those expectations [11]. In SCA, increased vlPAG-putamen connectivity may therefore reflect a maladaptive loop of pain anticipation reinforcement - a mechanism that may drive central sensitisation [12]. Increased connectivity between the cerebellum and vlPAG may reflect similar processes. The PAG, particularly the vlPAG, is highly connected to the cerebellum [13], including to cerebellar nuclei such as the fastigial nucleus, and this specific pathway may be involved in conditioning fear and defensive states (e.g. anxiety) [14]. This is again highly related to chronic pain mechanisms [15]. The lack of relation to pain scores likely reflects insufficient power and challenges in identifying neural correlates of self-reported pain, rather than implying the pain-irrelevance of these connectivity changes. SCA can lead to pain due to a diverse range of causes, with potentially distinct neural correlates. Stratifying patients by pain subtype or specific conditions, e.g. pain secondary to hip necrosis [16], could reveal specific abnormalities.

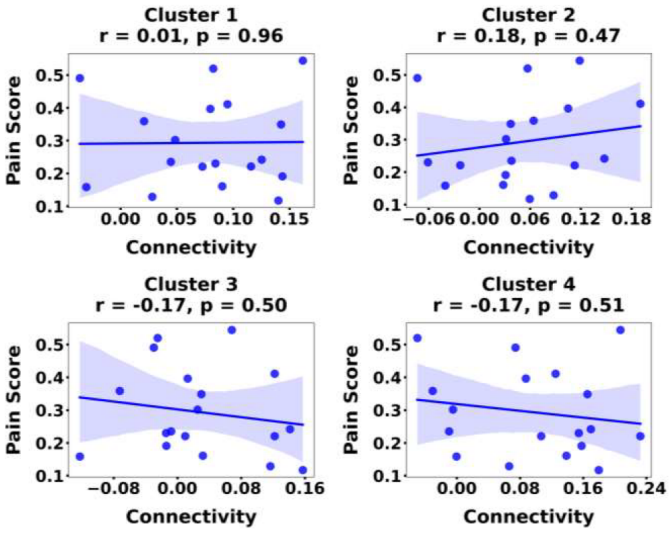

Figure 3: Linear regressions of vlPAG connectivity clusters against pain scores. Correlation coefficient (r) and p-values are shown above each regression plot.

Conclusions: Sickle cell anaemia patients showed increased ventrolateral periaqueductal grey connectivity to the putamen and cerebellum, consistent with abnormal pain and emotion-related processing. These changes may reflect mechanisms of pain anticipation or sensitisation, though no associations with pain scores were found, highlighting the need for further investigation.

References

[1] Da Silva, Joyce T., et al. *Pain* 160.9 (2019): 1933-1945. **[2]** Linnman, Clas, et al. *Neuroimage* 60.1 (2012): 505-522. **[3]** Howard, Jo, et al. Trials 19 (2018): 1-10. **[4]** Nieto-Castanon, Alfonso. Hilbert Press, 2020. **[5]** Coulombe, Marie-Andree, et al. *Human brain mapping* 37.4 (2016): 1514-1530. **[6]** Kawadler, Jamie M., et al. *British Journal of Haematology* (2019). **[7]** Karafin, Matthew, et al. *PLoS One* 14.5 (2019): e0216994. **[8]** Case, Michelle, et al. *NeuroImage: Clinical* 14 (2017): 1-17. **[9]** Lee, Mitchel, et al. *ISMRM* (2025): 2859. **[10]** Starr, Christopher J., et al. *Brain* 134.7 (2011): 1987-2004. **[11]** Roy, Mathieu, et al. *Nature neuroscience* 17.11 (2014): 1607-1612. **[12]** Crombez, Geert et al. *Pain* 116.1-2 (2005): 4-7. **[13]** Cacciola, Alberto, et al. *Brain Structure and Function* 224.6 (2019): 2153-2165. **[14]** Da Silva, Gabriela N. et al. *Frontiers in Systems Neuroscience* 17 (2023): 1160083. **[15]** Meulders, Ann. *Behaviour research and therapy* 131 (2020): 103635. **[16]** Santana, Jamille Evelyn RS, et al. *Clinical EEG and neuroscience* 54.3 (2023): 333-342.

Title: Comparison and validation of Two automated lesion segmentation tools.

Authors: Zaeema Fatima[1], Lewis Kitchingman[1], Svetla Manolova[1], Emma Tallantyre[2], Marco Palombo[1], Mara Cercignani[1]

[1] Cardiff University Brain Imaging Research Centre and [2]Division of Psychological Medicine and Clinical Neuroscience, Cardiff University, Wales

Introduction: Accurate segmentation of white matter lesions in multiple sclerosis (MS) is critical for both clinical trials and research. Lesion counts and volumes derived from MRI scans serve as surrogate markers of disease burden [1] and are essential for evaluating treatment efficacy and tracking disease progression [2]. Manual segmentation remains the gold standard but is time consuming, prone to human error, and poorly scalable for large datasets. These challenges have motivated the development of automated methods, many of which leverage AI to improve speed and consistency [3]. However, few of these tools have been systematically validated against expert segmentations in MS populations. In this study we compare two tools available in FreeSurfer: Samseg [4] and WMH-SynthSeg [5], to evaluate their performance relative to manual lesion outlines, in order to assess their reliability for broader use in both research and clinical applications. We hypothesized that significant correlations would be observed between manual and each automated segmentation method, reflecting their ability to approximate expert annotations.

Methods: Thirteen patients with clinically diagnosed multiple sclerosis (mean age: 39.5 ± 8.5 years; 8 females, 5 males) have been included so far in the study. All participants had an Expanded Disability Status Scale (EDSS) less than 4, indicating mild to moderate disability. Functional performance was assessed via the MS Functional Composite (MSFC) score incorporating the 25 foot walk test, 9 Hole Peg Test, and Symbol Digit Modality Test across participants, reflecting average performance on motor and cognitive tests. All participants underwent scanning on a 3T Siemens Connectom system, with 3D T2w images and T1w MPRAGE sequences acquired as part of the acquisition protocol. Manual lesion segmentation was performed on the T2w images using 3D Slicer [8] referencing MPRAGE scans to improve boundary confidence. Two automated segmentation tools within FreeSurfer were evaluated: (1) Samseg (as implemented in Freesurfer v7.4.1), applied to T2-weighted inputs with hyperintensity constraints relative to CSF[4] and (2) WMH-SynthSeg (Freesurfer development version), applied to T2w images with the -save_lesion_probabilities option [5]. Manual and automated binary lesion masks were used to compute lesion volumes in mm^3 using FSL [6] and analysed using a custom script in MATLAB. Agreement between segmentation methods was assessed using Pearson's correlation, repeated-measures ANOVA, and Bland-Altman plots.

Results: The mean lesion volume was, respectively, 3121.68mm^3 (SD = 4911.81), 4286.57mm^3 (SD = 6390.22) and 5887.8 mm^3 (SD = 3354.47) for manual, Samseg, and WMH-Synthseg. Samseg showed a strong correlation with manual segmentation ($r = 0.88$, $p < 0.001$), while WMH-SynthSeg showed a statistically significant correlation with Samseg ($r = 0.65$, $p = 0.015$), but was not correlated with manual segmentation $r = 0.40$, $p = 0.18$) (Figure 1). Two participants displayed outlying values with high lesion volumes on both manual and automated tools. After their exclusion, the correlations decreased substantially (e.g., Samseg–Manual $r = 0.27$, $p = 0.42$), indicating these cases strongly influenced the observed associations. Bland-Altman plots (Figure 2) revealed good visual agreement between manual and Samseg, and wider variability for WMH-SynthSeg. A consistent positive bias was observed between Samseg and WMH-SynthSeg, suggesting systematic overestimation of lesion volume by WMH-SynthSeg. In contrast, repeated measures ANOVA comparing lesion volumes across the three methods did not reveal significant differences ($F(2,24) = 2.67$, $p = 0.089$), indicating no statistically confirmed agreement at the group level.

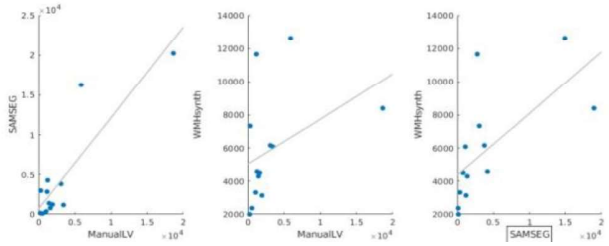

Figure 1. Scatterplots showing Pearson correlations between manual, Samseg, and WMH-SynthSeg lesion.
Each panel demonstrates the relationship between three of the segmentation methods. Gray line represents the correlation line.

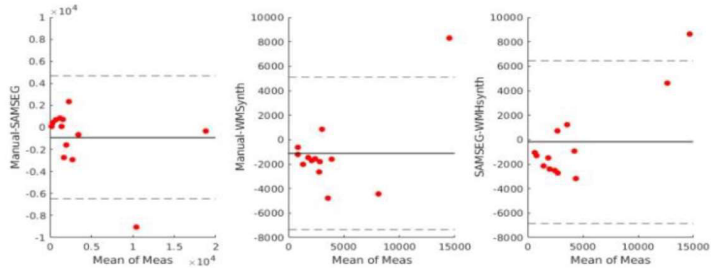

Figure 2. Bland-Altman plots comparing lesion volume agreement between manual, Samseg, and WMH-SynthSeg segmentations.
Each panel demonstrates the agreement between a pair of the three segmentation methods. The solid line represents the mean difference; dashed lines indicate the 95% limits of agreement.

Discussion: This study assessed the agreement between manual lesion segmentation and two fully automated FreeSurfer pipelines Samseg [4] and WMH-SynthSeg [5]when applied to T2-weighted images. Both tools initially showed moderate to strong correlations with manual volumes, but this was heavily influenced by two participants with substantially higher lesion loads. These cases reflected true biological variability rather than segmentation error. Once excluded, correlation values dropped indicating that the observed correlations were not statistically significant (e.g., Samseg–Manual: r = 0.27, p = 0.42). These findings were mirrored in the Bland-Altman analysis, which showed relatively narrow limits of agreement between Samseg and manual methods, and wider variability for WMH-SynthSeg. A clear positive bias was observed between Samseg and WMH-SynthSeg, indicating a tendency for WMH-SynthSeg to overestimate lesion volumes. Notably, direct comparison of lesion volumes revealed large absolute differences in several cases. For example, in one participant, Samseg estimated 805 mm^3 of lesion volume, whereas WMH-SynthSeg returned 4511 mm^3 a more than fivefold difference. This pattern was observed across multiple patients, particularly in those with low lesion burden, and helps explain the observed bias and weakened agreement statistics. Visual review suggests that in a few cases this was explained by non-lesion structures likely ventricular spaces or periventricular regions being misclassified as lesions, particularly by WMH-SynthSeg. This results is consistent with findings from low field and clinical imaging studies that highlight inconsistencies in WMH quantification by automated tools across heterogeneous datasets [7]. The main limitation of this study is its small sample size (N = 13), which restricts generalizability and limits the statistical power of agreement metrics. Future studies should incorporate larger cohorts with a broader range of lesion loads, and consider integrating additional contrasts to support more robust multi-modal segmentation. Manual quality control and consensus ground truths will remain essential for validating segmentation performance in both clinical and research contexts. The lesion probability maps provided by WMH-Synthseg could also be used to further refine the lesion maps.

Acknowledgment: This work was supported by the UKRI Future Leaders Fellowship (MR/T020296/2) and the Hodge Promising Leads Grant, Hodge Center for Translational Neuroscience.

References

[1] Hemond CC, Bakshi R. Magnetic Resonance Imaging in Multiple Sclerosis. Cold Spring Harb Perspect Med. 2018 May 1;8(5):a028969. doi: 10.1101/cshperspect.a028969

[2]García-Lorenzo D, Francis S, Narayanan S, Arnold DL, Collins DL. Review of automatic segmentation methods of multiple sclerosis white matter lesions on conventional magnetic resonance imaging. Med Image Anal. 2013;17(1):1–18.

[3] Lladó X, Oliver A, Cabezas M, Freixenet J, Vilanova JC, Quiles A, Valls L, Ramió-Torrentà L. Segmentation of multiple sclerosis lesions in brain MRI: A review of automated approaches. Inf Sci (Ny).

[4] 2012;186(1):164–185. MS lesions: A Contrast-Adaptive Method for Simultaneous Whole-Brain and Lesion Segmentation in Multiple Sclerosis. S. Cerri, O. Puonti, D.S. Meier, J. Wuerfel, M. Mühlau, H.R. Siebner, K. Van Leemput. NeuroImage, 225, 117471, 2021.

[5] Quantifying white matter hyperintensity and brain volumes in heterogeneous clinical and low-field portable MRI. Laso P, Cerri S, Sorby-Adams A, Guo J, Matteen F, Goebl P, Wu J, Liu P, Li H, Young SI, Billot B, Puonti O, Sze G, Payabavash S, DeHavenon A, Sheth KN, Rosen MS, Kirsch J, Strisciuglio N, Wolterink JM, Eshaghi A, Barkhof F, Kimberly WT, and Iglesias JE. Proceedings of ISBI 2024 press)

[6] S.M. Smith, M. Jenkinson, M.W. Woolrich, C.F. Beckmann, T.E.J. Behrens, H. Johansen-Berg, P.R. Bannister, M. De Luca, I. Drobnjak, D.E. Flitney, R. Niazy, J. Saunders, J. Vickers, Y. Zhang, N. De Stefano, J.M. Brady, and P.M. Matthews. Advances in functional and structural MR image analysis and implementation as FSL. NeuroImage, 23(S1):208-19, 2004

[7] P. Laso *et al.*, "Quantifying White Matter Hyperintensity and Brain Volumes in Heterogeneous Clinical and Low-Field Portable MRI," *2024 IEEE International Symposium on Biomedical Imaging (ISBI)*, Athens, Greece, 2024, pp. 1-5, https://doi.org/10.48550/arXiv.2312.05119

[8] Kikinis R, et al. 3D Slicer: a platform for subject-specific image analysis. Intraoperating Imaging and Image-Guided Therapy, Ferenc A. Jolesz, Editor 3(19). 2014:277–89.

Evolution of White Matter Hyperintensities and the impact of acute ischaemic Stroke

Claire Holland[1,2], Hamied Haroon[1,2], Sarah Al-Bachari[3], Matthew Gittins[1], Stuart M Allan[1,2], Laura Parkes[1,2], Craig J Smith[1,2,4]
[1] Faculty of Biology, Medicine and Health, University of Manchester (UoM)
[2] Geoffrey Jefferson Brain Research Centre, Northern Care Alliance NHS Trust, UoM
[3] Faculty of Brain Sciences, University College London
[4] Manchester Centre for Clinical Neurosciences, Northern Care Alliance NHS Trust
Email: Claire.holland-3@manchester.ac.uk

Introduction: White matter hyperintensities (WMH) – neuroimaging biomarkers of white matter (WM) damage and cerebral small vessel disease (cSVD) – are associated with increased risk of stroke and cognitive impairment[1]. However, longitudinal studies into the association of acute ischaemic stroke (AIS) on this relationship are limited[2][3]. This preliminary analysis investigates the evolution of WMH in cerebrovascular disease, the impact of stroke, and the association with global cognitive impairment.

Methods: Study Participants: Patients with AIS underwent cognitive assessment at 6-, 18- and 30-months post-stroke, and structural MRI (T1w and FLAIR) at 6- and 30-months post-stroke. Controls, matched for cerebrovascular risk factors but without AIS, completed parallel cognitive and MRI assessments. Automated WMH Segmentation was via the Enigma-PD-WML pipeline [4], which integrates FSL (version 6.0.7.13;[5]) and U-Net[6] to analyse co-registered T1w and FLAIR images acquired from the same scanning session. WMHs were further segmented into periventricular WMH (PVWMH) and deep WMH (DWMH) based on distance from the lateral ventricles (PVWMH: ≤ 10 mm; DWMH: > 10 mm). All available MRI scans (T1w and FLAIR at 6- and 30-months) from both cohorts were processed through this pipeline. Output images (T1w, FLAIR, and binary lesion masks) were available in both native and standard MNI152 1mm space (linear and non-linear registration). Total Brain Volume (TBV) was estimated using GM, WM, and CSF probability maps from Enigma-PD-WML. WMH volumes were calculated from binary lesion masks in native (T1) space and are presented as percentage of TBV (% TBV). Global cognitive performance was assessed using the Montreal Cognitive Assessment (MoCA). Participants were given standardised instructions and different versions were used each follow-up (6-month, v7.2; 18-month, v7.3 alternate version; 30-month, v7.2 alternate version) to avoid recollection bias. Statistical Analysis: (1) DWMH, PVWMH, and total WMH volumes were calculated for each participant at each timepoint. Mann Whitney U tests were performed to determine groupwise differences in WMH burden and spatial distribution. (2) WMH volume at 6-months and change in MoCA score from 6- to 30-months were assessed using Spearman correlation. (3) Evaluation of changes in lesion volume from 6- to 30-months was determined using Mann Whitney U and paired t-tests.

Preliminary Results and Discussion: Study participants: Presently, 58 participants with AIS (mean age 64.4 years ± 9.2) have undergone 6-month cognitive assessment and MRI; of these, 12 have completed 30-month follow-up. Sixteen Controls (mean age 65.4 years ± 8.0) have undergone cognitive assessments and MRI. Recruitment and follow-up are ongoing. WMH volume (6-months): Median total WMH volume did not differ significantly between the cohorts (p = 0.2; Stroke: 0.280% TBV; Control: 0.180% TBV) (Figure 1). However, the difference in the distribution of total WMH volumes between the cohorts was significant (p = 0.02) (Figure 2). A more even distribution across a range of WMH volumes was observed in the Stroke cohort while the majority of total WMH volumes in the Controls (62.5%) were within the $0.10 < x \leq 0.20$ range. It is possible that this difference in distribution is due to differences in lesion progression, underlying pathophysiology, or variations in the index stroke themselves. Regional WMH volume: A significant difference was found in DWMH volume between the cohorts (p = 0.04) with the median burden in Stroke being two-fold higher than in

Controls (0.030-5.640% TBV vs 0.040-2.570% TBV). A strong positive correlation was found between PVWMH and DWMH volumes within the Stroke cohort (r = 0.7604, p < 0.0001; Spearman Correlation) but not in the Controls (r = 0.042, p = 0.876). All control participants exhibited DWMH, even at low total WMH burdens. This is unexpected given the conventional model of cSVD progression, i.e., DWMH arises only in more advanced disease[7]. WMH Volume vs MoCA: Total and regional WMH volumes (6-months) did not correlate with changes in MoCA score from 6- to 30-months (Total WMH: r = 0.63, p = 0.8; PVWMH: r = 0.06 p = 0.8; DWMH: r = 0.17; p = 0.6). Future analyses will explore specific cognitive domains more closely linked to WM pathology. Evolution of WMH: WMH volume did not increase significantly from 6- to 30-months in the Stroke cohort (0.230% TBV to 0.290% TBV; p = 0.7). However, small but significant changes at an individual level were observed (p = 0.04). 3D-lesion maps show evolution and regression of specific WM lesions over time (Figure 3).

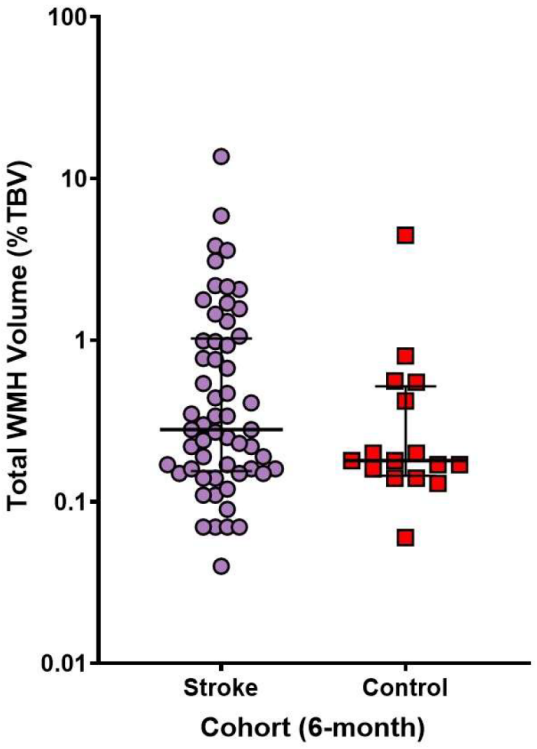

Figure 1: Total WMH Volume at 6-months. Median and IQR indicated. Total WMH given as percentage of total brain volume (% TBV) to normalise for individual differences in TBV. Y-axis plotted on $\log_{10}$ scale.

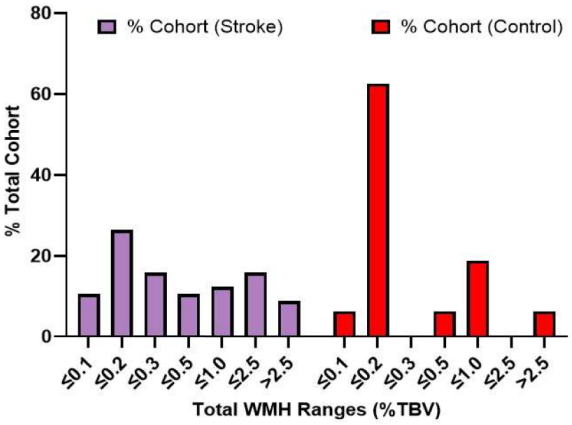

Figure 2: Distribution of Total WMH volumes at 6-months.

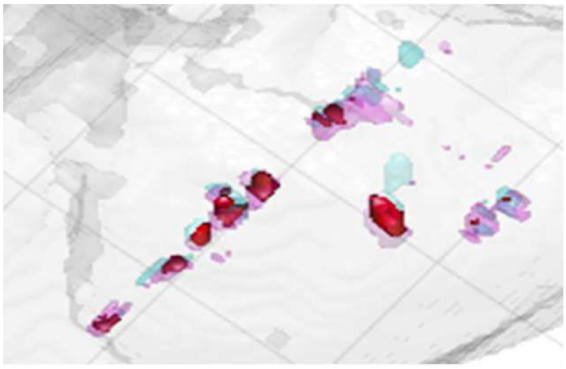

Figure 3: Section of a single participant 3D-lesion map of longitudinal WMH evolution. Cyan: 6-months. Magenta: 30-months. Red: Overlap between 6- and 30-months. Grey: Brain template. Non-linear registration to MNI152 1mm space.

Conclusions: Total WMH burden did not significantly differ between cohorts, but DWMH burden was significantly higher in Stroke patients. WMH burden post-stroke showed significant individual variation over time. 3D-lesion maps evidence progression and regression of specific lesions over time.

References

[1] Debette, S & Markus, H.S. (2010). *BMJ*. **341**: c3666.

[2] Jokinen, H., Lipsanen, J., Schmidt, R., *et al.* (2012). *Neurology*. **78:** 1785-1792.

[3] Brodtmann, A., Khlif, M.S., Egorova, N., *et al.* (2020). *Stroke*. **51**: e183-e192.

[4] Enigma-PD-WML (2025). **Retrieved from:** https://github.com/UCL-ARC/Enigma-PD-WML

[5] Jenkinson, M., Beckmann, C.F., Behrens, T.E., *et al*. (2012). *Neuroimage*. **62**: 782-790.

[6] Park, G., Hong, J., Duffy, B. A., *et al*. (2021). *Neuroimage*. **237**: 118140.

[7] Wardlaw, J.M., Valdés Hernández, M.C. & Muñoz-Maniega, S. (2015). *J. Am. Heart Association*. **4**: e001140.

DCE-MRI measurements of blood-brain barrier permeability in chronic ischaemic stroke.

Olivia A Jones[1,2], Zuzanna Biesiada[1,2], Owen M Thomas[2,3], Ben R Dickie[1,2], Stuart M Allan[1,2], Marion S Buckwalter[4], Craig J Smith[1,2], and Laura M Parkes[1,2]

[1] Faculty of Biology, Medicine and Health, University of Manchester, Manchester, UK

[2] Geoffrey Jefferson Brain Research Centre, Manchester Academic Health Science Centre, Northern Care Alliance NHS Foundation Trust, University of Manchester, Manchester, UK

[3] Department of Radiology, Salford Royal NHS Foundation Trust, Salford, UK

[4] Department of Neurology and Neurological Sciences, Stanford University, Stanford, CA, USA

Correspondence to: olivia.jones-4@manchester.ac.uk

Introduction: Blood-brain barrier (BBB) dysfunction may contribute to cognitive decline following stroke but is not well characterised chronically. Dynamic-contrast enhanced (DCE)-MRI involves tracking T_1-weighted signal changes from injected contrast agent which only extravasates where the BBB is disrupted. Mathematical modelling estimates parameters relating to blood vessel permeability, the contrast agent volume transfer constant (K^{trans}), and the volume of tracer leakage spaces, such as the blood plasma volume fraction (v_p). Post-stroke dementia risk is biphasic, with an initial steep increase ending at ~6 months, followed by more gradual but longer-term risk [1]. Here, we use DCE-MRI to characterise patterns of BBB permeability at 6 months after stroke, a time-point marking the transition to chronic post-stroke dementia risk.

Methods: *Participants* – 54 ischaemic stroke survivors and 8 age/risk matched controls underwent DCE-MRI at 6 months post-stroke (Table 1). *MRI Acquisition* – Data were acquired on a Philips Elition 3T scanner with a 32-channel head coil. A dynamic series of 157 3D-T_1-FFE images were acquired with a spiral k-space read-out (stack-of-spirals, 10 interleaves), 12° flip-angle, TR/TE = 10.6/0.8ms, spatial resolution = 1.5×1.5×2mm^3, temporal resolution = 7.6s, and an acquisition time of 20 minutes. A T_2-weighted FLAIR and structural T_1-weighted image were also acquired. *DCE-MRI Analysis* – An Extended Tofts [2], Patlak [3], and intravascular [4] model of contrast agent leakage with an input function derived from a region drawn in the sagittal sinus were fit to the data and voxel-wise tracer kinetic model selection [5] used to map K^{trans} and v_p across the brain. *Region of Interest Analysis* – The acute stroke lesion was delineated manually from clinical DWI acquired <14 days since onset. This was dilated by 1cm to define the peri-lesion tissue. FLAIR hyperintensities and normal-appearing white matter (NAWM) were delineated from the 6-month structural images. Median K^{trans} and v_p were extracted from each region. *Statistical Analysis* – Wilcoxon tests were used for paired comparisons, Mann-Whitney tests were used to test differences between groups. Spearman's rank tests were used to assess for correlations with infarct volume, stroke severity (NIHSS), and cognition (MoCA). All tests were Bonferroni corrected (P<0.008).

Table 1. Summary of the cohort.

Measure	Stroke Group (N = 54)	Control Group (N = 8)
Age (years) *Median (IQR, Range)*	63.5 (13, 47 – 84)	68.5 (10, 56 – 71)
Sex (Female) *N (%)*	10 (19%)	2 (25%)
NIHSS *Median (IQR, Range)*	3 (4, 0 – 15)	-
Infarct volume (mL) *Median (IQR, Range)*	2.4 (11.4, 0.1 – 52.5)	-
MoCA Score (at scan) *Median (IQR, Range)*	27 (3, 20 – 30)	25 (4, 19 – 29)

Results: High K^{trans} was observed in and around the old stroke lesion of some participants (Fig. 1), though spatial patterns varied across the group. K^{trans} was significantly elevated in FLAIR hyperintensities, the old infarct lesion, and peri-lesion tissue regions compared to the NAWM within individuals and compared to controls (Fig. 2). The peri-lesion region also had a significantly greater v_p

than the normal-appearing white matter of both stroke survivors and controls. K^{trans} in the peri-lesion was correlated with infarct volume (r=0.39, P=0.004), but not acute stroke severity (NIHSS) or cognition (MoCA) at the time of the DCE-MRI scan. No significant differences in K^{trans} or v_p were found when comparing the normal-appearing tissue of stroke survivors to that of controls.

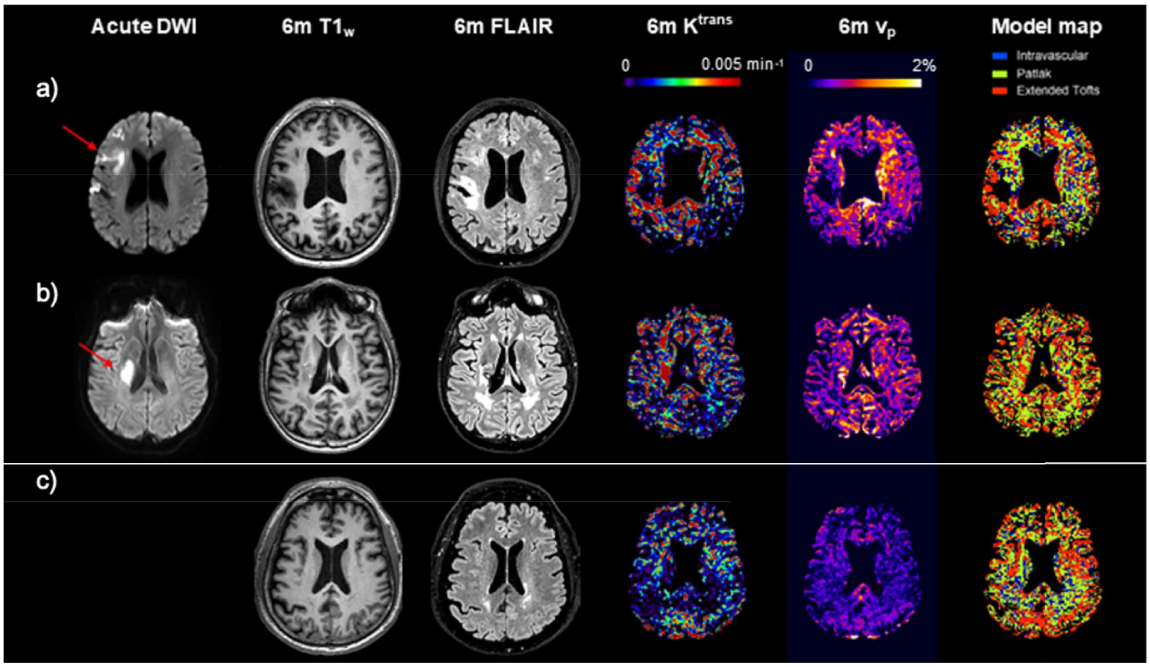

Fig. 1. Example images from two stroke survivors (a – b) and a control participant (c).

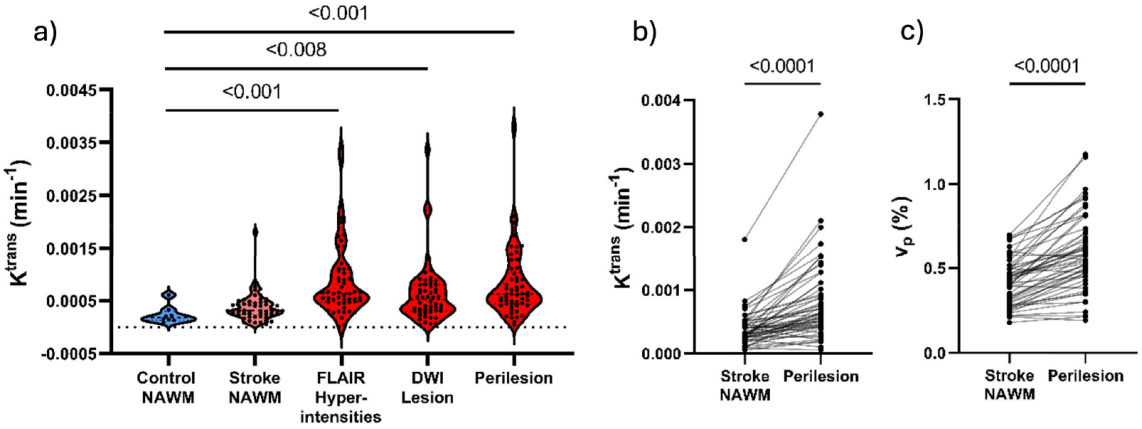

Fig. 2. (a) Violin plots of the average K^{trans} in the controls (blue) and stroke (red) groups. (b – c) Paired differences in average K^{trans} (b) and v_p (c) between the NAWM and the peri-lesion.

Discussion and conclusion: We demonstrate persistent BBB dysfunction in stroke survivors at 6 months after onset, notably immediately surrounding the old infarct. Concurrently elevated BBB permeability and blood plasma volume in this region is intriguing and could indicate ongoing vascular remodelling in tissue beyond the acute stroke lesion. The correlation between peri-lesion K^{trans} and infarct volume but not stroke severity suggests that persistent BBB permeability at this time point may relate to the spatial extent of the initial tissue injury but not the acute neurological impairment resulting from stroke. Participants underwent a 60-minute comprehensive cognitive test battery at the time of scanning [6] and testing is carried out yearly; longitudinal follow-up will determine if these patterns are related to or can predict later cognitive decline.

Acknowledgements: The StrokeCog-BBB study is funded by NIH-NINDS R01NS124927. DCE-MRI data were acquired using research sequences (spiral k-space acquisition), provided by Philips. We would like to acknowledge the Stroke-IMPaCT network, funded by the Leducq Foundation (19CVD01).

References

[1] S. T. Pendlebury and P. M. Rothwell, *Lancet Neurol.* **18**, 248-258 (2019). [2] P. S. Tofts et al., *J. Magn. Reson. Imaging* **10**, 223-232 (1999). [3] C. S. Patlak, R. G. Blasberg, and J. D. Fenstermacher, *J. Cereb. Blood Flow Metab.* **3**, 1-7 (1983). [4] S. P. Sourbron and D. L. Buckley, *NMR Biomed.* **26**, 1004-1027 (2013). [5] O. A. Jones et al., *Proc. ISMRM* **32**, abstract 3270 (2024). [6] L. L. Drag et al., *BMC Neurol.* **20**, 313 (2020).

Chemsex and the Brain: Interim Findings from a Multimodal Pilot Neuroimaging Study

Naulls S[1,3], Nagle A,[1] Ronen I[2], Stone J[1,3]

[1]*Deparment of Clinical Neurosciences, Brighton & Sussex Medical School*
[2]*Clinical Sciences and Imaging Centre, University of Sussex*
[3]*Sussex Partnership NHS Trust*

Contact: stephen.naulls5@nhs.net

Introduction: 'Chemsex' is the use of drugs such as methamphetamine, GHB/GBL, mephedrone, and ketamine in sexual contexts by gay, bisexual, and other men who have sex with men (GBMSM) [1]. Researchers have extensively characterised the individual effects of these substances. However, chemsex typically involves polysubstance use during prolonged sessions, sometimes lasting several days. The long-term neurobiological impact of this distinctive pattern of polysubstance use, combined with sexual activity, remains unclear. Chemsex is associated with mental illness, compulsive sexual behaviour, and addiction-related harms, including psychosis and death through overdose [2]. Our study is the first to use multimodal MRI to examine how chemsex affects brain structure and function.

Methods: We recruited GBMSM actively and significantly engaged in chemsex, along with age-matched GBMSM controls who do not use drugs. Participants underwent an hour-long neuroimaging session, during which we collected structural MRI, resting-state fMRI, task-based fMRI (using the Stop-Signal Task), proton magnetic resonance spectroscopy (^{1}H-MRS) from the pregenual anterior cingulate cortex (pgACC), and neuromelanin-sensitive MRI of the ventral tegmental area and substantia nigra (VTA/SNc). All participants completed validated psychometric questionnaires (PHQ-9, GAD-7, BIS-11, CSBI-13, ASSIST). Additionally, participants in the chemsex group provided detailed information about their drug use through comprehensive qualitative interviews.

Results: This abstract presents our emerging findings. BIS-11 and CSBI-13 scores were raised in the chemsex group. Preliminary analyses of NM-MRI signal intensity in the SNc and VTA in chemsex participants relative to controls along with other task and resting state data will be presented.

Discussion: This is the first multi-modal MRI study completed in people involved in chemsex. Our interim results support the feasibility of multimodal imaging in this under-researched population and reinforce the relevance of addiction neuroscience frameworks to chemsex-related harms. Our full study will integrate these data with ^{1}H-MRS (glutamate/GABA levels in the pregenual anterior cingulate cortex), resting-state and task-based fMRI, alongside clinical and behavioural measures, to understand the neurobiology of chemsex in GBMSM.

Conclusions: Our interim findings suggest that chemsex is associated with elevated impulsivity and compulsive sexual behaviour, alongside emerging differences in neuromelanin signal intensity in key dopaminergic regions. These results support the hypothesis that chemsex may affect brain systems involved in reward, inhibition, and motivation. Ongoing analyses will clarify how these neurobiological findings relate to clinical and behavioural data. This work underscores the importance of applying addiction neuroscience to understand chemsex and paves the way for better-informed interventions.

References

[1] David Stuart, (2019) "Chemsex: origins of the word, a history of the phenomenon and a respect to the culture", Drugs and Alcohol Today, Vol. 19 Issue: 1, pp.3-10, https://doi.org/10.1108/DAT-10-

2018-0058
[2] Coronado-Muñoz M, García-Cabrera E, Quintero-Flórez A, Román E, Vilches-Arenas Á. Sexualized Drug Use and Chemsex among Men Who Have Sex with Men in Europe: A Systematic Review and Meta-Analysis. J Clin Med. 2024 Mar 21;13(6):1812. doi: 10.3390/jcm13061812. PMID: 38542036; PMCID: PMC10971601.

6

Impact of infarct location on cognitive performance 6 months post-stroke

Zuzanna Biesiada[1,2], Hamied A Haroon[1,2], Michael Mlynash[5], Lauren Drag[5], Eileen Jones[2,4], George Arthur[1,2], Olivia A Jones[1,2], Stuart M Allan[2,3], Owen M Thomas[2], Marion S Buckwalter[5], Craig J Smith[2,4] and Laura M Parkes[1,2]

1) Division of Psychology, Communication and Human Neuroscience, School of Health Sciences, University of Manchester
2) Geoffrey Jefferson Brain Research Centre, Manchester Academic Health Science Centre,
3) Division of Neuroscience, School of Biological Sciences, University of Manchester
4) Division of Cardiovascular Sciences, School of Medical Sciences, University of Manchester
5) Department of Neurology and Neurological Sciences, Stanford University School of Medicine

Introduction: The risk of developing dementia is well-established to be increased in stroke survivors. The evidence suggests that the risk trajectory of cognitive impairment is biphasic: the acute impairment is associated with stroke size and location more closely than the later cognitive trajectory [1]. It has been suggested that the 6-month post-stroke timepoint can therefore be used as a baseline for studies assessing the latter, chronic phase of cognitive decline in stroke survivors [2]. Characterising the effects of infarct volume and location to the cognitive performance at this period of initial stabilisation could therefore provide additional insight into our understanding of post-stroke cognitive trajectory.

Here, we explore the relationship between acute infarct volume/location and cognition at 6 months after stroke in a multi-centre cohort of stroke survivors.

Methods: Infarct ROIs were manually delineated on acute diffusion-weighted images from 119 ischaemic stroke patients and registered to MNI152 space. Regional analysis was performed according to the DKT cortical parcellation and ASEG subcortical segmentation of the MNI152 template (Freesurfer v7.4.1). Each cortical and subcortical region was assigned a percentage of total voxels in the region that overlapped with the infarct ROI, with regions affected by an infarct in at least 18 patients chosen for further analysis. Participants underwent a 60-minute comprehensive cognitive test battery at 6 months post-stroke, and z-scores for 5 cognitive domains were calculated [3].

Linear relationship between domain-specific cognitive z-scores and the level of infarct occupation of specific regions (log10 transformed due to lognormal distribution) was assessed with Pearson's correlation coefficient (R v4.4.2). No multiple testing corrections were applied.

Results:

Table 1: Summary of brain regions analysed. Pearson's r between cognitive domain z-score and log10 transformed infarct occupation percentage. N between 28-18. *P < 0.05, **P < 0.01

	Global	Language	Processing speed	Memory	Visuospatial	Working memory
Putamen	**-0.39***	**-0.43***	**-0.38***	-0.35	-0.18	-0.06
Caudate	-0.35	-0.29	**-0.5****	-0.35	-0.11	-0.01
Precentral	-0.04	-0.08	-0.06	0.23	-0.11	-0.17
Postcentral	0	0.07	-0.04	-0.06	-0.09	0.14
Thalamus	0.04	0.01	0.08	0.11	-0.02	-0.11
Insula	-0.26	-0.16	-0.33	0.02	-0.35	-0.06
Superior parietal	-0.05	0.2	0.04	0.10	-0.21	-0.26

Contact: zuzanna.biesiada@manchester.ac.uk

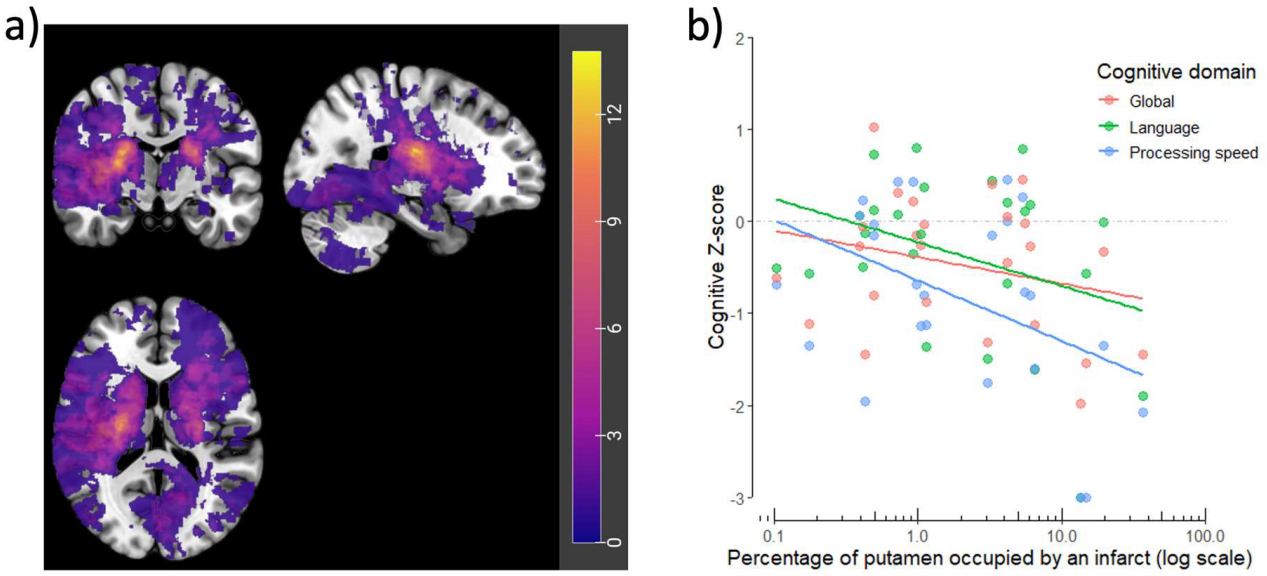

Fig. 1. a) Infarct location for 119 ischaemic stroke patients, registered to MNI152. Total infarct volume ranged from 69 mm^3 to 81561 mm^3 (median: 1876.5 mm^3, IQR: 6683 mm^3). b) Proportion of right putamen affected by an infarct (%, log scale) is negatively correlated with performance in language (R = -0.43, p = 0.02) and processing speed (R = -0.38, p = 0.04) - tasks, as well as global cognitive impairment (R = -0.39, p = 0.04). N = 28

Discussion: Previous work identified basal ganglia and thalamic infarcts as significantly associated with global cognitive impairment [5,6]. In contrast, our findings suggest no significant association of thalamic infarct with any of the cognitive domains (Table 1). The putamen was the only region identified that displayed a negative correlation with global cognitive performance, as well as impaired processing speed and language skills (Figure 1). Putamen was previously demonstrated to play a role in speech articulation and word processing, possibly thanks to its contributions to motor control [3]. Caudate nucleus infarcts were strongly associated with impairments in processing speed, which is consistent with previous findings in dementia patients [4].

This work highlights the putamen as a strategic infarct location, where stroke survivors with putamen infarcts may be at a higher risk of impaired executive function and language several months after stroke. Our findings stress the importance of controlling for infarct location in analyses examining cognitive data collected chronically after stroke.

Acknowledgements: This study is funded by an R01 grant (NIH-NINDS R01NS124927) to Prof. Buckwalter at Stanford University and by Stroke IMPaCT, funded by Leducq Foundation (19CVD01).

References

[1] Doyle KP, Buckwalter MS. Curr Opin Neurol. **33(1)**:30-36. (2020)
[2] Drag et al. BMC Neurol. **20(1)** 313 (2020)
[3] Oberhuber et al. Front Hum Neurosci. **7** 787. (2017)
[4] Botzung et al. Alzheimer's Research & Therapy **11(1)** 108 (2019)
[5] Zhao et al. J Cereb Blood Flow Metab**. 38(8)** 1299–311 (2018)
[6] Liang et al. World J Psychiatry **14(8)** 1190–8 (2024)

Detection of brain metabolites in HIV-associated tuberculous meningitis using magnetic resonance spectroscopy

James R. Barnacle[1-3], Laeeqa Allie[3], Nonzwakazi Bangani[3], Lauren Barron[3], Cari Stek[3], Petronella Samuels[4], Georg Oeltzschner[5], Itamar Ronen[6], Frances Robertson[4], Angharad G. Davis[7], Robert J. Wilkinson[1-3]

[1]The Francis Crick Institute, London, UK

[2]Department of Infectious Disease, Imperial College London, UK

[3]Centre for Infectious Diseases Research in Africa, University of Cape Town, Observatory, RSA

[4]Cape Universities Body Imaging Centre, University of Cape Town, Observatory, RSA

[5]Department of Radiology and Radiological Science, Johns Hopkins School of Medicine, Baltimore, USA

[6]Clinical Imaging Sciences Centre, University of Sussex, Falmer, UK

[7]Blizard Institute, Queen Mary University of London, UK

Introduction: Tuberculous meningitis (TBM) causes death in a quarter of cases, and a third of survivors suffer persistent neurological disability [1]. In the CSF of children with TBM, genes associated with glutamate release and GABA degradation are overexpressed, and glutamate and glutamine concentrations are significantly increased compared to non-infectious controls [2], [3]. We hypothesised that brain damage in TBM may be driven by neuroexcitotoxicity and that glutamate would be increased and GABA decreased in the basal ganglia of adults with TBM.

Methods: Adults with HIV-associated TBM provided consent for up to three MRS scans at day 7, week 4 and week 8 following enrolment. Two age and ethnicity matched control groups living with and without HIV infection were included. Targeted LC-MS metabolomics was performed on lumbar CSF from TBM patients taken +/- 48 hours of the day 7 and week 4 scan (Figure 1A). The basal ganglia, the most common region of vascular injury in TBM, was selected for voxel placement. Scans were conducted at the Cape Universities Body Imaging Centre, Cape Town using a 3T Siemens Skyra MRI scanner using a 1H 32-channel head coil. A structural T1-weighted MP-RAGE acquisition was acquired for voxel placement and tissue segmentation. This was followed by a single voxel PRESS acquisition with CHESS water suppression (2000 ms TR, 30 ms TE, 2000 Hz spectral bandwidth, 1024 vector size, 64 averages, 30x30x30 mm^3 voxel). Shimming was done using automated B_0 field mapping with manual shimming of water to <26 Hz if FWHM ≥26 Hz. MEGA-PRESS acquisitions were then obtained from the same voxel using (2000 ms TR, 80 ms TE, 320 averages, 2000 Hz acquisition bandwidth, 2048 vector size with ON editing pulse at 1.9 ppm targeting GABA). MEGA-PRESS spectra were analysed with Gannet v3.4.0 [4]. PRESS spectra were analysed with Osprey v2.9.6 outsourcing the fitting to LCModel using a custom macromolecule basis set for 3T PRESS TE30 [5], [6]. The following metabolites were combined: Glx = Glu + Gln; tNAA = NAA + NAAG; tCho = GPC + Cho + PCh; tCr = Cr + PCr. Metabolites were excluded for all scans if any scan had a CRLB >25%. Visually poor-quality spectra were excluded. For the MEGA-PRESS data, scans with a water or creatine FWHM >15 Hz were excluded.

Results: 21 HIV-associated TBM patients, and 21 HIV-negative and 22 HIV-positive controls were scanned. 18 TBM follow up scans were done at week 4 and week 8. 70/100 PRESS and 42/88 MEGA-PRESS acquisitions passed quality control. There were no significant differences between groups (Figure 1C). Over time, total choline was significantly increased at week 4 compared to day 7 (Figure 1D).

Discussion: Metabolite concentrations in the left basal ganglia, in the absence of visible lesions, did not differ from matched controls. Over time, only total choline concentrations were increased at week 4 and 8, which may suggest delayed gliosis or infarct maturation. There are several reasons why the other results were non-significant including the fact our TBM cohort had mild disease, scan quality was lower than expected, and the basal ganglia may not have been the most sensitive region to target.

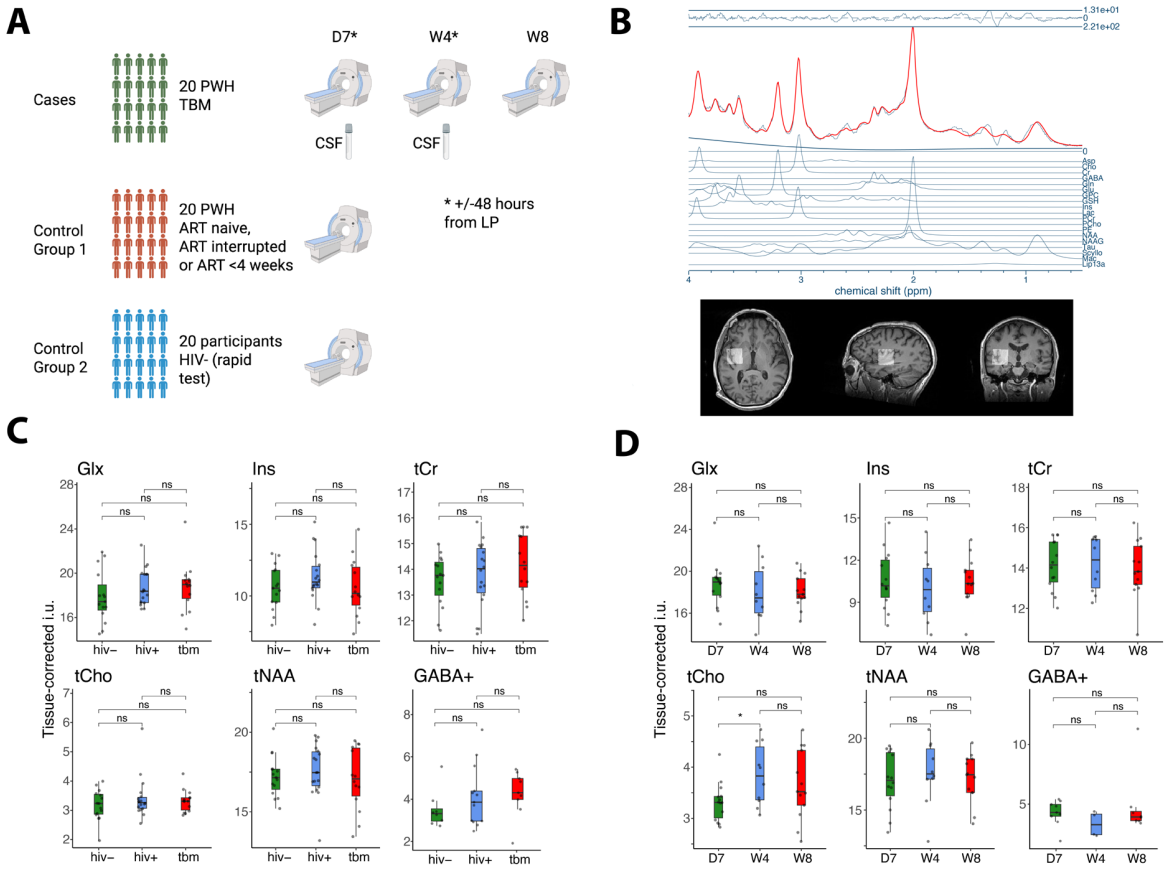

Figure 1. A) Study outline. B) Example PRESS spectrum and co-registration from Osprey with custom basis set. C) Tissue-corrected metabolite concentrations of day 7 TBM scans (n = 14), HIV-uninfected (n = 15), and HIV-positive (n = 18) controls. D) Changes in tissue-corrected metabolite concentrations between day 7 (n = 14), week 4 (n = 10) and week 8 (n = 13). GABA+ values are also alpha corrected. PWH, people living with HIV; ART, anti-retroviral therapy; LP, lumbar puncture; CSF, cerebrospinal fluid; HIV, human immunodeficiency virus.

Acknowledgements: Thank you to Bernard Siow from the Francis Crick Institute for his input.

References

[1] A. M. Stadelman *et al.*, 'Treatment Outcomes in Adult Tuberculous Meningitis: A Systematic Review and Meta-analysis', *Open Forum Infect. Dis.*, vol. 7, no. 8, p. ofaa257, Aug. 2020, doi: 10.1093/ofid/ofaa257.

[2] U. K. Rohlwink *et al.*, 'Tuberculous meningitis in children is characterized by compartmentalized immune responses and neural excitotoxicity', *Nat. Commun.*, vol. 10, no. 1, p. 3767, Aug. 2019, doi: 10.1038/s41467-019-11783-9.

[3] C. D. W. van Zyl, D. T. Loots, R. Solomons, M. van Reenen, and S. Mason, 'Metabolic characterization of tuberculous meningitis in a South African paediatric population using 1H NMR metabolomics', *J. Infect.*, vol. 81, no. 5, pp. 743–752, Nov. 2020, doi: 10.1016/j.jinf.2020.06.078.

[4] R. A. E. Edden, N. A. J. Puts, A. D. Harris, P. B. Barker, and C. J. Evans, 'Gannet: A batch-processing tool for the quantitative analysis of gamma-aminobutyric acid–edited MR spectroscopy spectra', *J. Magn. Reson. Imaging*, vol. 40, no. 6, pp. 1445–1452, Dec. 2014, doi: 10.1002/jmri.24478.

[5] G. Oeltzschner *et al.*, 'Osprey: Open-source processing, reconstruction & estimation of magnetic resonance spectroscopy data', *J. Neurosci. Methods*, vol. 343, p. 108827, Sep. 2020, doi: 10.1016/j.jneumeth.2020.108827.

[6] S. W. Provencher, 'Automatic quantitation of localized in vivo 1H spectra with LCModel', *NMR Biomed.*, vol. 14, no. 4, pp. 260–264, Jun. 2001, doi: 10.1002/nbm.698.

Age-dependent lactate responses in the anterior cingulate cortex during cognitive-emotional challenge.

Edward Caddye[1,2,*], Joel Patchitt[2], Anouk Schrantee[3], William T Clarke[4], Itamar Ronen[1], Alessandro Colasanti[2,*]

[1] Clinical Imaging Sciences Centre, University of Sussex, Falmer, BN1 9RR, England

[2] Department of Clinical Neuroscience, Brighton and Sussex Medical School, University of Sussex, Falmer, BN1 9RR, England

[3] Department of Radiology and Nuclear Medicine, Amsterdam University Medical Centre, location AMC, Amsterdam, the Netherlands

[4] Centre for Integrative Neuroimaging, FMRIB, Nuffield Department of Clinical Neurosciences, University of Oxford, Oxford, United Kingdom

Introduction: Functional magnetic resonance spectroscopy (fMRS) enables real-time tracking of neurometabolites, offering insights into brain function in health and disease. Lactate, a key molecule in metabolic psychiatry, has traditionally been studied with static MRS measures, potentially overlooking its dynamic regulation. Drawing inspiration from exercise physiology, we hypothesized that lactate production and clearance rates provide critical information about mitochondrial metabolism (1). Here, we applied lactate fMRS in the anterior cingulate cortex (ACC)—a region central to emotional regulation and characterized by high aerobic glycolysis—using a novel cognitive-emotional task. We further examined whether these responses vary with age.

Methods: Thirty-four healthy adults (aged 21–69) underwent fMRS during an emotional face-processing paradigm designed to impose escalating cognitive-emotional demands. Lactate and other neurometabolites were measured in the dorsal ACC (dACC) across baseline, task, and recovery periods. Using FSL MRS, we assessed task effects on lactate and tested for age-related differences in metabolite dynamics (2).

Results: Lactate levels in the dACC rose significantly with increasing task intensity ($p < 0.005$), peaking at 20.2% above baseline during the most demanding condition. No comparable changes were observed for glutamate/glutamine or other metabolites. Participants over 40 years showed markedly greater lactate responses (32.9%) than those under 40 (10.1%, $p = 0.003$), while baseline levels did not differ by age (Fig. 1).

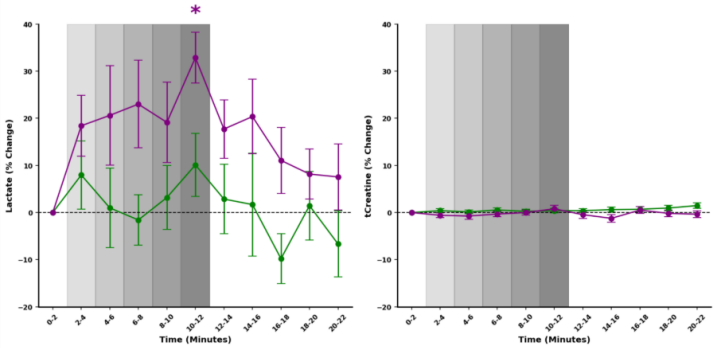

Figure 1. Lactate and tCreatine dynamics in participants over the age of 40 (purple) and under the age of 40 (green) in response to an emotion-cognitive task in the anterior cingulate cortex.

Mean ± SEM as a percentage change from the first block (0-2 min) for 19 participants under 40 and 15 participants over 40 for Lactate and total Creatine (tCreatine). A repeated measures ANOVA was carried out to determine the effect of time for lactate ($F(1, 32) = 4.77$, $p = 0.036$). For tCreatine there was no significant effect of time ($F(1, 32) = 1.81$, $p = 0.187$). Significant differences in relative lactate level changes between the 0-2 baseline block and other time blocks between the two groups are depicted with a purple asterisk ($t(32) = -5.00$, $p = 0.003$). The blocks corresponding with the task are shaded, which are progressively darker to highlight the reduction in time between face presentations and increase in intensity.

Discussion: The observed task-related lactate increases in the dACC align with fundamental neuroenergetic models, where lactate serves as an energy substrate during periods of high neural activity, paralleling exercise physiology (3). The pronounced age effect—greater lactate responses in participants over 40 despite comparable baseline levels—highlights reduced neurometabolic flexibility with ageing, likely reflecting reduced mitochondrial efficiency and altered lactate clearance (4). Importantly, lactate dynamics, rather than static levels, emerged as sensitive markers of metabolic differences. We also found a dissociation between lactate and glutamate/glutamine responses, consistent with prior pharmacological fMRS work (5), suggesting that lactate regulation during cognitive-emotional processing operates partly independently from glutamatergic neurotransmission. Together, these findings support lactate as a marker of neurometabolic state with translational relevance to disorders characterized by mitochondrial dysfunction and altered ACC metabolism (6).

Conclusions: Dynamic lactate responses in the dACC are sensitive to cognitive-emotional demand and are amplified with age, suggesting reduced neurometabolic flexibility in older adults. The dissociation between lactate and glutamate/glutamine underscores distinct regulatory mechanisms of energy metabolism. These findings position fMRS as a promising tool to probe mitochondrial efficiency and identify biomarkers relevant to affective psychopathology and related disorders.

Acknowledgements: The MRS package was developed by Gülin Öz and Dinesh Deelchand and provided by the University of Minnesota under a C2P agreement. WTC is funded by Wellcome (225924/Z/22/Z). This research was funded in whole, or in part, by the Wellcome Trust [Grant numbers 225924/Z/22/Z]. For the purpose of open access, the author has applied a CC BY public copyright licence to any Author Accepted Manuscript version arising from this submission.

References

1. San-Millán I, Brooks GA (2018): Assessment of Metabolic Flexibility by Means of Measuring Blood Lactate, Fat, and Carbohydrate Oxidation Responses to Exercise in Professional Endurance Athletes and Less-Fit Individuals. *Sports Med* 48: 467–479.
2. Clarke WT, Ligneul C, Cottaar M, Ip IB, Jbabdi S (2024): Universal dynamic fitting of magnetic resonance spectroscopy. *Magnetic Resonance in Medicine* 91: 2229–2246.
3. Pellerin L, Pellegri G, Bittar PG, Charnay Y, Bouras C, Martin JL, *et al.* (1998): Evidence supporting the existence of an activity-dependent astrocyte-neuron lactate shuttle. *Developmental Neuroscience* 20: 291–299.
4. Sondheimer N, Glatz CE, Tirone JE, Deardorff MA, Krieger AM, Hakonarson H (2011): Neutral mitochondrial heteroplasmy and the influence of aging. *Hum Mol Genet* 20: 1653–1659.
5. Boucherie DE, Reneman L, Booij J, Immink R, Hollmann MW, Schrantee A (2024, July 24): Concurrent assessment of neurometabolism and brain hemodynamics to comprehensively characterize the functional brain response to psychotropic drugs: an S-ketamine study. bioRxiv, p 2024.07.23.604721.
6. Caddye E, Pineau J, Reyniers J, Ronen I, Colasanti A (2023): Lactate: A Theranostic Biomarker for Metabolic Psychiatry? [no. 9]. *Antioxidants* 12: 1656.

Repeatability of ^{31}P CSI metabolite quantification: A voxel-wise analysis of the thalamus and the postcentral gyrus

Zoona Javed[1,2], Guilhem J Collier[1,2], Rolf Schulte[3], Nigel Hoggard[1], and Jim M Wild[1,2]
[1]Section of Medical Imaging and Technologies, Division of Clinical Medicine, School of Medicine and Population Health, Faculty of Health, University of Sheffield, Sheffield, United Kingdom.
[2]INSIGNEO institute, University of Sheffield, Sheffield, United Kingdom.
[3]GE Healthcare, Munich, Germany.
[4]Division of Neuroscience, School of Medicine and Population Health, Faculty of Health, University of Sheffield, Sheffield, United Kingdom.

Introduction: ^{31}P-MRspectroscopy offers a unique opportunity to quantify the metabolic changes occurring with age and neurodegenerative disease, to better inform therapeutic approaches [1]. The PCr/ϒ-ATP ratio is a key indicator of brain energy metabolism and changes in the PCr/ϒ-ATP ratios can be indicative of underlying neurological or psychiatric conditions [1]. These ratios are heterogeneous and are typically between 1 -2 in brain tissue [2]. However, brain spectroscopy presents challenges due to the low sensitivity of MR phosphorus signals. In this study we evaluate the voxel-wise repeatability of ^{31}P CSI in the thalamus and postcentral gyrus to support quantitative neurochemical imaging. These brain regions are particularly significant because of their role in sensory processing [3].

Methods: MR experiments were conducted using a dual-tuned 1H/31P coil on a GE 3T Signa PET/MR scanner, with four healthy volunteers scanned on two separate days to assess repeatability. A high-resolution whole-brain spectrum was first acquired with the following acquisition parameters;1024 samples; 5kHz bandwidth, flip angle= 40, averages=10, repetition time (TR)=10s. 3D CSI was then acquired using a custom radial density weighted phase encoding strategy using the following acquisition parameters; TR=210ms, echo time =0.455ms, number of points=990, FOV=25 x 25 x 25 cm, acquisition matrix=8x8x8, phase encodes = 1278, bandwidth=5kHz, flip angle= 15o and number of averages=2 acquired for a scan time of 8 minutes 57 seconds, heteronuclear decoupling was not used. The data were reconstructed using 10 Hz line broadening and zero filling to a 16x16x32 matrix. A co-registered structural axial 1H 3D T1 Bravo sequence was acquired using the same FOV as the CSI. The open-source MATLAB implementation of OXSA [4] was modified to work with GE data and used to overlay the reconstructed 3D CSI grid onto the 1H anatomical images for voxel localization and to perform the Advanced Method for Accurate, Robust and Efficient Spectral (AMARES) fitting of the spectra. The PCr/ ϒ-ATP ratios for the whole-brain spectrum in healthy volunteers were calculated using the area under the curve derived from AMARES fitting of the metabolite peaks. Intra- and inter-session repeatability were assessed by fitting voxel-wise spectral peaks in repeat scans.

Results: Fig.1 shows voxels located in (a) left thalamus, (b) right thalamus, (c) left postcentral gyrus and (d) right postcentral gyrus along with the fitted spectra from the corresponding voxels. The metabolites detected include, Phosphocreatine (PCr), Gamma-ATP (ϒ-ATP), alpha-ATP(α-ATP), beta-ATP(β-ATP), PME, PDE and Pi. Fig. 2 presents the Bland-Altman comparison of intra-session and inter-session PCr/ ϒ-ATP ratios for sub-voxels averaged across the left and right thalamus, as well as the left and right postcentral gyri (post-CG), in four healthy volunteers. The mean coefficient of variation (CV) for intra-session comparisons was 10% for the mean thalamus, 12% for the left postcentral gyrus, and 12% for the right postcentral gyrus. For inter-session comparisons, the mean CV was 15% for the mean thalamus, 21% for the left post CG, and 13% for the right post CG.

Discussion: Good quality spectra were obtained in all voxels in the chosen anatomical regions and the PCr/ϒ-ATP ratios are within the expected range. We evaluate repeatability and method agreement through Bland-Altman analysis of the voxel-wise differences. Studies have shown that PCr/ϒ-ATP ratios are higher in the cerebellum compared to the cerebrum [5]. Our results are consistent with

these higher apparent ratios in the thalamus compared to the post-central gyrus. The CV values indicate good repeatability, with intrasession CVs between 10-12%, outperforming inter-session results; only the left postcentral gyrus showed slightly higher CV inter-session likely due to partial volume effects.

Conclusion: Robust and repeatable quantification is crucial for longitudinal ^{31}P CSI studies. Reliable quantification of phosphorus metabolites in the thalamus and postcentral gyrus is feasible, supporting future metabolic studies in these brain regions.

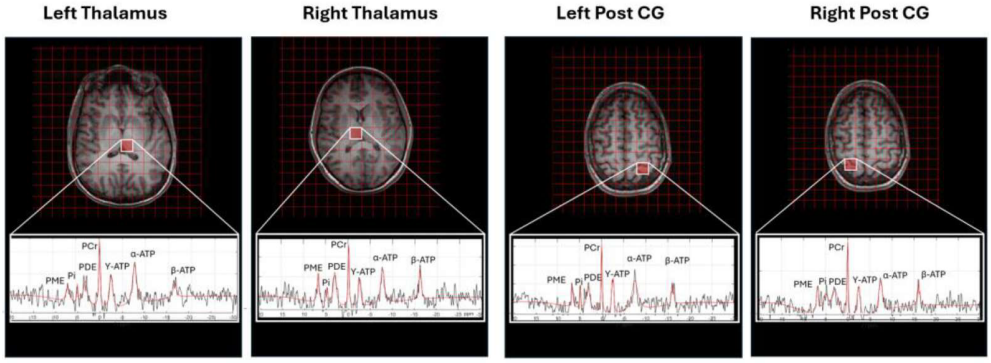

Fig.1 (a) left thalamus, (b) right thalamus and (c) left postcentral gyrus (d) right postcentral gyrus and corresponding fitted spectra.

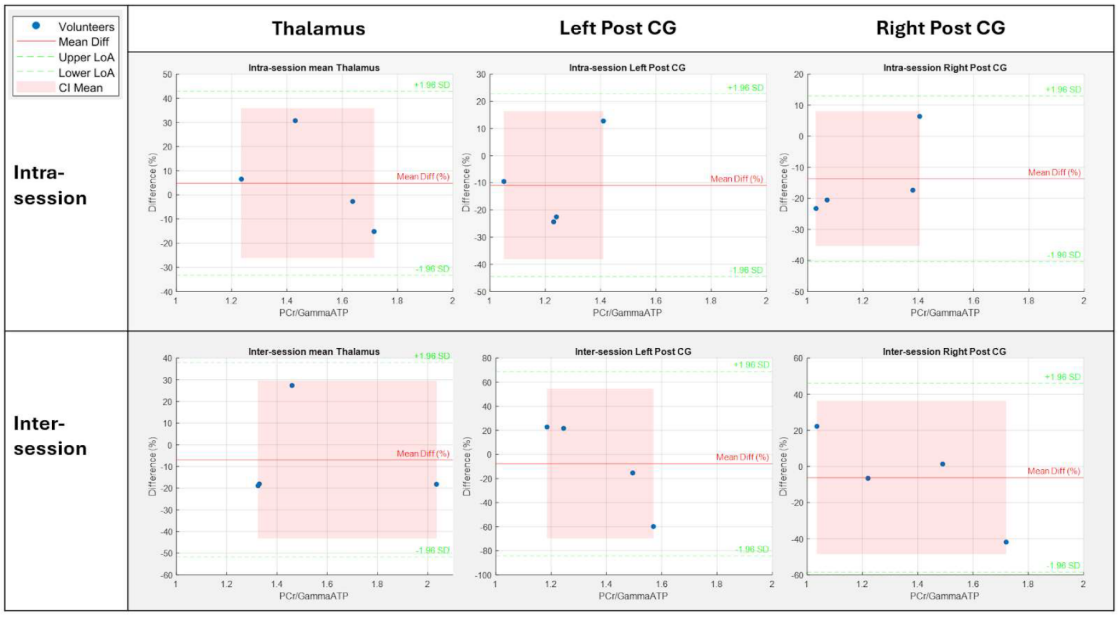

Fig. 2 Bland Altman plots comparing intra-session and inter-session mean PCr/Y-ATP ratios of sub-voxels in the mean thalamus and left and right postcentral gyrus across four healthy volunteers.

Acknowledgements: This study/research is funded by the National Institute for Health and Care Research (NIHR) Sheffield Biomedical Research Centre (NIHR203321). The views expressed are those of the author(s) and not necessarily those of the NIHR or the Department of Health and Social Care.

References: [1] Jett S, et al, doi: 10.3389/fnagi.2023.1183228. **[2]** Lu A, et al, doi: 10.1002/mrm.24281.**[3]** Croosu SS, et al. doi: 10.2337/dc22-0587**. [4]** Purvis LAB et al doi: 10.1371/journal.pone.0185356.**[5]** Hanaoka S et al.doi: 10.1016/s0887-8994(97)00201-4.

Temporal Diffusion Ratio to Map Regions of Restricted Diffusion in Human Brain Metastases

Elise Gwyther[1], Sahar Iqbal[2], James Powell[2], Jennifer Golten[2], Andrada Ianus[3], Beat Jucker[4], Derek Jones[1], Chantal M.W. Tax[1,6*], Marco Palombo[1,5*] *These authors contributed equally
[1]Cardiff University Brain Research Imaging Centre (CUBRIC), School of Psychology, Cardiff University, Cardiff, United Kingdom; [2]Velindre Cancer Center, Cardiff, United Kingdom; [3]School of Biomedical Engineering & Imaging Sciences, King's College London, London, UK; [4]Glaxosmithkline, Pennsylvania, United States; [5]School of Computer Science and Informatics, Cardiff University, Cardiff, United Kingdom; [6]University Medical Center Utrecht, Utrecht, The Netherlands.

Introduction: Diffusion weighted MRI (dMRI) has been used previously to characterise the microstructure of brain metastases, by applying models of tissue microstructure/representations of the diffusion weighted signal to estimate clinically significant parameters such as the apparent diffusion coefficient[1][2]. However, these estimates may be dependent on the acquisition protocol or subject to modelling assumptions and degeneracies[3][4]. The Temporal Diffusion Ratio (TDR)[5] is a model free approach, which does not rely on assumptions about the tissue microstructure, to characterise restricted diffusion and water exchange in the brain, where positive TDR contrast indicates restricted diffusion, and negative TDR contrast indicates water exchange. In this study, we apply TDR to dMRI scans of a cohort of 21 patients to examine the intra- and inter-metastasis heterogeneity of restricted diffusion and exchange in human brain metastases

Methods: Structural MRI scans were acquired on a 3T Siemens Prisma scanner. T1-weighted images were acquired using a T1MPRAGE sequence(TR/TE = 2.3s/2.98ms, voxel size=1×1×1mm). dMRI data was acquired on a Siemens 3T Connectome scanner using a diffusion-weighted Pulsed Gradient Spin Echo (PGSE) sequence with an echo-planar imaging (EPI) readout (TR/TE=3.5s/73.0ms, voxel size=2×2×2mm). dMRI scans were conducted with a constant diffusion gradient duration (δ = 7 ms) using multiple diffusion times (Δ=17.3,45.0ms) with b-value=4000s/mm^2,N-directions=60). TDR maps were calculated voxelwise from the dMRI scans using the following formula[5]:

$$TDR = \frac{\sum_{i=1}^{N} S_{2,i} - \sum_{i=1}^{N} S_{1,i}}{\sum_{i=1}^{N} S_{2,i}} \quad N = 60\ directions$$

$$S_{1,i} = Signal\ in\ direction\ i, \qquad \Delta = 17.3ms$$

$$S_{2,i} = Signal\ in\ direction\ i, \qquad \Delta = 45.0ms$$

Metastasis regions of interest (ROIs) were delineated by expert oncologists.

Results: In 8 patients, the metastasis ROIs were characterised by high positive TDR contrast in the metastasis periphery and negative TDR contrast in the metastasis core (**Fig.1**), and all of these metastases were surrounded by oedema. In this group, the percentage of voxels with positive TDR in the metastasis ROI had range 31.6-91.9%, with mean 64.1% and standard deviation 19.3% and the mean average TDR measured across all voxels in a single metastasis varied between -0.07 - 0.11. The mean ROI volume (measured in voxels) was 657.0 voxels with standard deviation 253.4 voxels in this group. In the remaining patients, there appeared to be no association between the TDR contrast in a voxel and the location of the voxel in the metastasis (**Fig.2**). The percentage of positive TDR contrast in these metastases had range 0-100%, with mean 49.7% and standard deviation 34%. The mean TDR contrast in these metastases had range -0.19 - 0.24 and the mean ROI volume and standard deviation was 210.1 voxels and 172.2 voxels respectively.

Discussion: Intra and inter-metastasis heterogeneity of TDR contrast was observed in the patient cohort. A distinctive TDR contrast pattern was observed in metastases surrounded by oedema in 8 patients. The mean ROI volume of the metastases in this group was higher compared to the other patients – this TDR contrast pattern is likely representative of a necrotic core encased by intact metastasis tissue with a high cellularity[6]. The clinical population characteristics of patient cohort were heterogeneous with respect to ongoing treatments (including steroids, immunotherapy, tyrosine kinase inhibitors), previous treatments, and primary cancers, to name a few examples. This population heterogeneity may explain the variability in TDR contrast characteristics across the metastases in this study.

Conclusions: TDR characterises differences in restricted diffusion across and between brain metastases. Future work will assess changes to TDR in metastases after treatment.

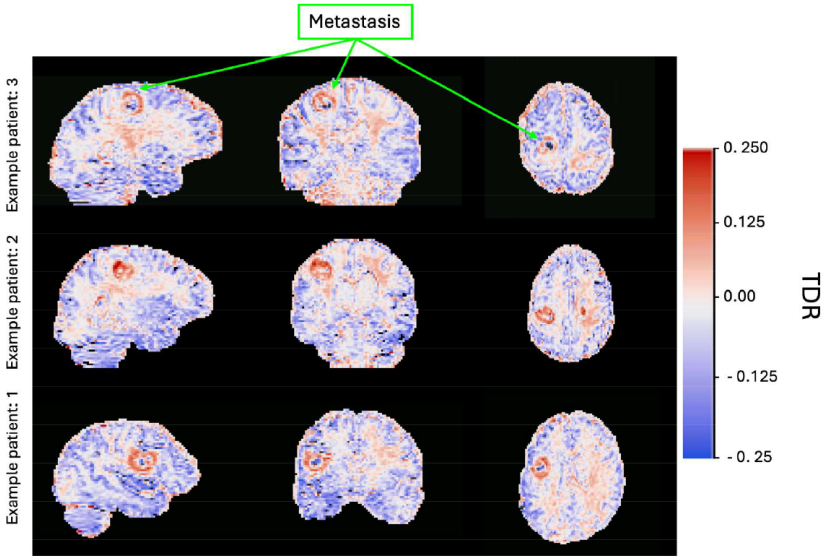

Fig. 1. Three TDR map examples of patients with brain metastases which have a high positive TDR contrast in the metastasis periphery and low negative TDR in the metastasis core, shown in the sagittal, coronal and axial planes.

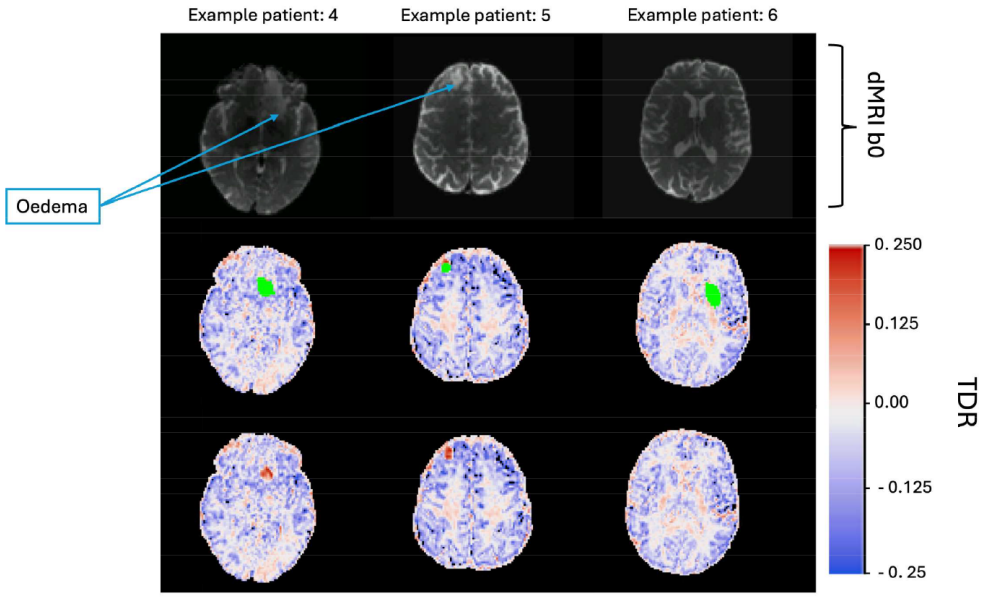

Fig. 2. Three examples of patients with brain metastases where there is no relationship between the location of the voxel in the metastasis and the TDR contrast, shown in the axial plane. In example patients 4 and 5, there is high TDR contrast across the whole metastasis; in example patient 6, the TDR contrast is negative in the majority of the metastasis.

References

[1] F. Bruzzone et al., *Exploring the Role of ADCs in Brain Metastases and Primary Brain Tumors: Insight and Future Directions*, Cancers (2025)

[2] V.Umberto et al., *Diffusion-based microstructure models in brain tumours: Fitting in presence of a model-microstructure mismatch*, NeuroImage: Clinical (2022)

[3] DS. Novikov et al., *On modeling*. Magnetic Resonance in Medicine. (2018)

[4] L. Fedeli et al., *Dependence of apparent diffusion coefficient measurement on diffusion gradient direction and spatial position – A quality assurance intercomparison study of forty-four scanners for quantitative diffusion-weighted imaging*, Physica Medica (2018)

[5] W. Warner et al., *Temporal Diffusion Ratio (TDR) for imaging restricted diffusion: Optimisation and pre-clinical demonstration*, NeuroImage (2023)

[6] WB. Pope, *Brain metastases: Neuroimaging*. Handbook of Clinical Neurology (2018)

Optimising phase-based magnetic resonance electrical properties tomography (EPT) for multi-parametric mapping (MPM) MRI acquisitions in the brain

Yirun Wang[1], Jierong Luo[1], George E. C. Thomas[2], Rimona S. Weil[2], and Karin Shmueli[1]
[1]Medical Physics and Biomedical Engineering, University College London, London, UK
[2]Dementia Research Centre, Institute of Neurology, University College London, London, UK

Introduction: Electrical properties tomography (EPT) is a rapidly developing method to non-invasively map tissue electrical conductivity by reconstructing it from the phase of the complex transmit field B_1^+ [1]. EPT has shown clinical potential to identify physiological biomarkers in the body and brain [2] Although, in principle, phase-based EPT only relies on the transceive phase available from most MRI sequences, prior studies have typically relied on dedicated EPT acquisitions for better accuracy and robustness [3]. As a quantitative MRI acquisition, multi-parametric mapping (MPM) has been widely used to investigate tissue composition and microstructure in healthy and diseased brains [4-5]. As MPM uses multi-echo gradient-echo (ME-GRE) acquisitions, if the phase data are saved, EPT reconstruction would be possible [6], providing additional tissue conductivity information "for free". In this study, we demonstrated the feasibility of EPT using MPM MRI for the first time, and optimised and evaluated our method in phantom and in-vivo data, respectively.

Methods: MRI acquisition: MPM data was acquired from one healthy subject at 3T (Siemens, Prisma, 64-channel head coil) using ME-GRE with following parameters: TR = 25ms, TE = 23ms, number of echoes = 8, FOV = 256mm, resolution = 0.8mm. High-resolution structural T1w image was acquired using MPRAGE. Construction of 3T MPM brain phantom: A realistic brain phantom was constructed to match the SNR characteristics of the in-vivo MPM data (Fig.1). Magnitude offset at TE = 0 (M_0) was first extrapolated from ME-MPM data using ARLO [7], and the SNR of M was measured within white matter. The transceive phase noise standard deviation was estimated at 1/SNR [8], and was added as Gaussian noise to the noiseless transceive phase of a 3T brain phantom obtained from the EPT challenge [9]. The corresponding magnitude of the phantom was constructed to match the SNR of the in-vivo structural T1w data.

Optimising EPT reconstruction for MPM MRI: Prior to EPT reconstruction, the transceive phase ($\boldsymbol{\phi_0}$) was extrapolated from all T1-weighted MPM echoes using a nonlinear fit [10], then unwrapped using SEGUE [11] with the coregistered *structural* T1w magnitude image used for magnitude and segmentation weighting. The MagSeg surface integral EPT method was used to minimise noise and preserve boundaries [12]. To find the optimal EPT reconstruction for MPM, we varied derivative and integration kernel radii [13] in 1-mm step between 7-10mm and 14-19mm, respectively. An optimal set of reconstruction parameters was chosen based on the mean absolute error of reconstructed EPT maps relative to the ground truth conductivity, mean conductivities in grey matter (GM), white matter (WM) and cerebrospinal fluid (CSF), the number of outliers, visual inspection and processing time. The optimised parameters for EPT reconstruction were then applied to in-vivo MPM data.

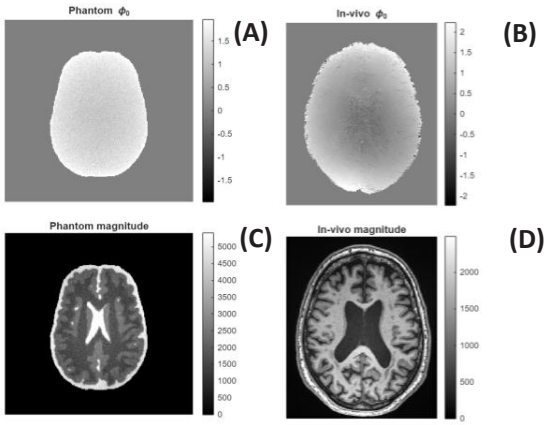

Fig. 1. (A) Phantom $\boldsymbol{\phi_0}$ with Gaussian noise (B) In vivo unwrapped $\boldsymbol{\phi_0}$ (C) Phantom magnitude with Gaussian noise (D) In vivo coregistered magnitude

k_d (mm)	k_i (mm)	STD	GM/WM ratio	CSF CV
10	19	9.153	0.618	2.954
9	19	9.152	0.603	2.990
8	19	9.138	0.588	3.060

Table. 1. Summary of top three kernel combinations (k_d: derivative radius, k_i: integration radius), ranked by higher GM/WM ratio, lower standard deviation (STD) and CSF coefficient of variance (CV)

Results and Discussion: The optimal derivative and integration kernel radii were identified as 10 mm and 19 mm, providing the best balance between tissue contrast, noise suppression, and

computational efficiency (Fig. 2A). Quantitative evaluation across GM/WM contrast ratio, whole-brain standard deviation (STD), and CSF coefficient of variation (CV) confirmed this combination as superior (Table 1).

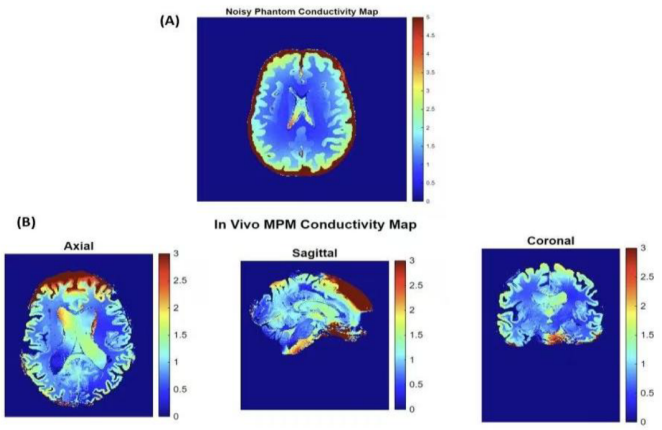

Fig. 2. Conductivity reconstructed from (A) the noisy phantom and (B) in-vivo T1w MPM data using the optimal kernel size, 10mm (derivative) and 19mm (integration).

Fig. 2B shows the EPT reconstructed from the in-vivo MPM data which exhibits clear grey-white matter contrast (~0.42 S/m). However, boundary artifacts are present at the periphery of the brain and local anomalies appear inside white and grey matter, indicating residual noise and reconstruction instability. When compared to literature values, which is approximately 0.47 S/m, 1.03 S/m and 2.14 S/m for WM, GM and CSF [14-15], respectively. In comparison, the reconstructed conductivities were higher in WM (0.729 S/m) and GM (1.18 S/m), and lower in CSF (1.40 S/m). Compared with WM and GM, CSF exhibits low conductivities at brain edges, and also a broader conductivity spread with higher standard deviation (Fig. 3), likely due to a combination of increased phase noise, low SNR in CSF regions and unreliable segmentation in fluid sections of the brain.

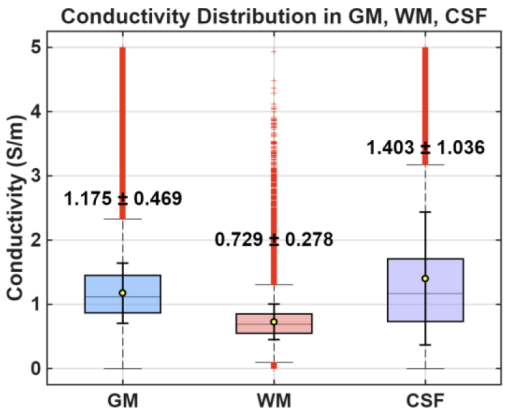

Fig. 3. Conductivity distribution in grey matter (GM), white matter (WM) and cerebrospinal fluid (CSF) for in vivo EPT. reconstruction.

Despite peripheral artifacts and residual noise, the preliminary conductivity map shows physiologically plausible values with preserved tissue contrast and anatomical consistency. Further optimisation is still required for stability, and future work should explore varying different MPM parameters, such as proton-density weighted and magnetic transfer-weighted, to increase reconstruction accuracy and robustness for EPT reconstruction to broader applications.

Conclusions: This study shows the feasibility of reconstructing conductivity maps from MPM acquisitions. These preliminary results suggest a promising future for incorporating EPT into these widely used MRI protocols, provided the signal phase is saved. With further validation, this approach could support broader clinical application of conductivity mapping without requiring dedicated sequences. Future work should also explore using the proton-density weighted and magnetisation transfer-weighted MPM acquisitions, to increase EPT reconstruction accuracy and robustness.

References

[1] Katscher U, et al. NMR Biomed. 2017. [2] van Lier AL, et al. Magn Reson Med. 2014. [3] Liu J, et al. IEEE Trans Biomed Eng. 2017. [4] Lommers E, et al. Neuroimage Clin. 2019. [5] Berg RC, et al. Neuroimage. 2022. [6] Kim DH, et al. Magn Reson Med. 2014. [7] Pei M, et al. Magn Reson Med. 2015. [8] Gudbjartsson H, et al. Magn Reson Med. 1995. [9] Meerbothe TG, et al. Magn Reson Med. 2024. [10] Liu T, et al. Magn Reson Med. 2013. [11] Karsa A, et al. IEEE Trans Med Imaging. 2019. [12] Karsa A, et al. Proc. ISMRM. 2021. Abstract 3774. [13] Karsa A, et al. Proc. ISMRM. 2021. Abstract 3775. [14] Gabriel S, et al. Phys Med Biol. 1996. [15] Kiersnowski OC, et al. Proc. ISMRM. 2024. Abstract 0188.

Comparing Standard and Tensor-based MP-PCA Complex Denoising Performance for a Highly Sampled Diffusion-Relaxometry Dataset

James Robertson[1], Jana Hutter[1,2,3], J-Donald Tournier[1,2], Joseph V. Hajnal[1,2], Andrada Ianus[1]
[1]Department of Imaging Physics and Engineering, King's College London, St. Thomas' Hospital, London, UK
[2]Department of Early Life Imaging, King's College London, St. Thomas' Hospital, London, UK
[3]Smart Imaging Lab, Radiological Institute, University Hospital Erlangen, Erlangen, Germany

Introduction: Tensor MP-PCA (tMP-PCA) is an adaptation of the Random Matrix Theory based MP-PCA denoising, which utilizes singular value decompositions (SVDs) to identify and remove noise-representative eigenvalues that follow the Marchenko-Pastur distribution[1][2]. The tensor adaptation exploits extra redundancy present in multi-dimensional MRI data (e.g. Diffusion-relaxometry) to perform multiple SVDs and thus suppress additional noise. In this work we present a comparison of denoising performances between standard MP-PCA and tMP-PCA implemented in MATLAB (https://github.com/Neurophysics-CFIN/Tensor-MP-PCA).

Methods: The data used was a fully sampled multidimensional dataset consisting of 5 b-values, 28 inversion times, and 3 echo times [3]. Denoising was performed on complex-valued data using MP-PCA and tMP-PCA scripts in MATLAB. The size of the sliding window was kept constant for both methods. The denoised data was split into subsets based on echo time, and diffusion kurtosis imaging (DKI) fitting was then performed for these subsets to compare and evaluate noise suppression in different SNR regimes, with the variance of derived DKI metrics used as a comparison.

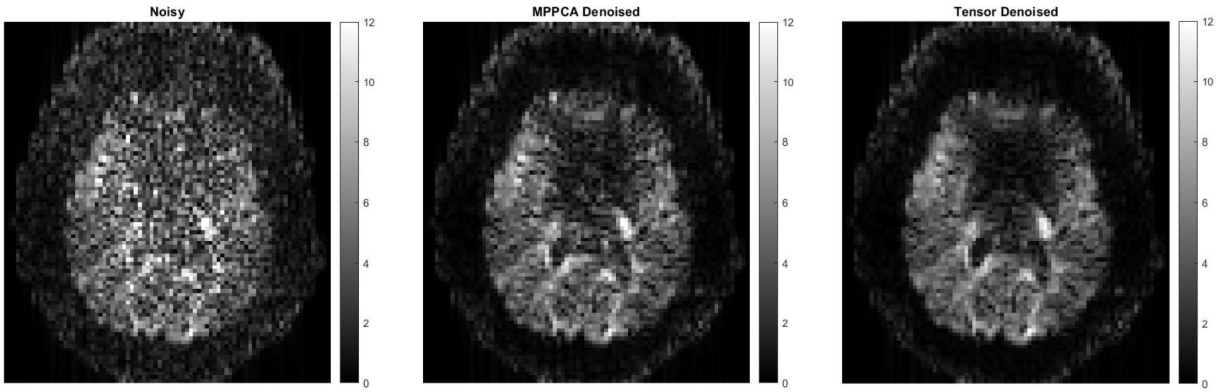

Fig 1. Three plots showing the same representative slice of the data in three forms; noisy data (left), MP-PCA denoised (middle) and tensor MP-PCA denoised (right). Images show a slice from a volume acquired with b = 2000 s/mm^2, TE = 130ms and TI = 3885ms at 2.5mm isotropic resolution.

Results: Tensor MP-PCA performed better than standard MP-PCA at denoising the complex data, evident from both visual inspection (Fig. 1) and from the reduced noise present in the mean kurtosis (MK) maps (Fig. 2) and decreased variance in the MK within a white matter region of interest (Fig. 3). The effect is more apparent when considering the 130ms TE subset of the data. Variances in the white matter region for the noisy, MP-PCA denoised, and tensor MP-PCA denoised at the two different subsets are given in Table 1.

	Noisy	MP-PCA Denoised	Tensor Denoised
80ms TE Subset	0.219	0.187	0.168
130ms TE Subset	0.493	0.349	0.256

Table 1. The variances of the mean kurtosis values within the considered white matter ROI for each TE subset for the noisy, MP-PCA denoised and tensor denoised data.

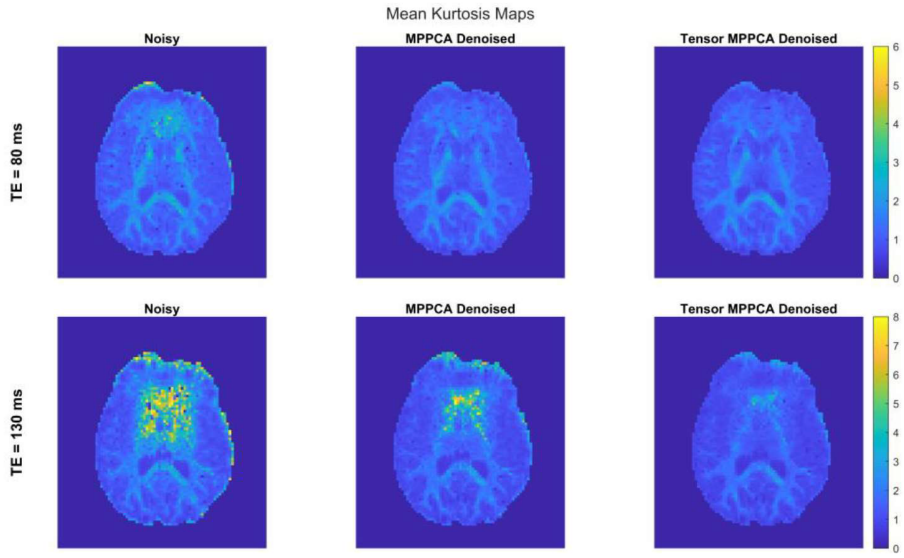

Fig. 2. Representative slice of the mean kurtosis maps for the noisy, MP-PCA denoised, and tensor MP-PCA denoised data split into two subsets of 80ms TE and 130ms TE.

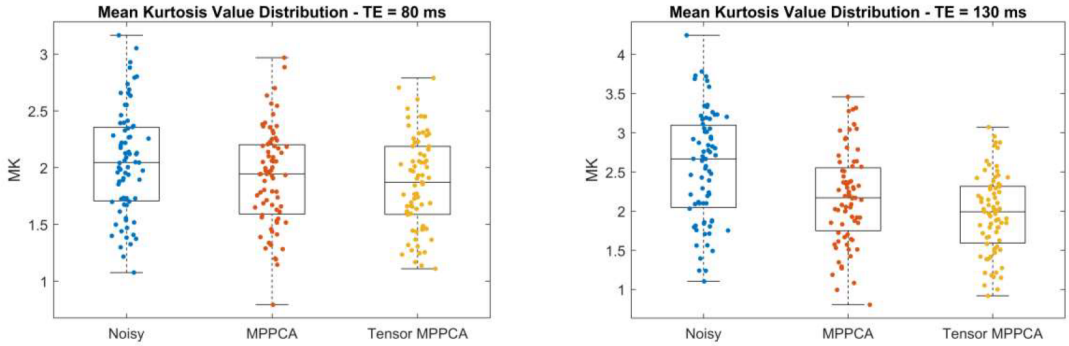

Fig. 3. Boxplots representing the mean kurtosis values within a white matter ROI for the 80 and 130ms TE subsets of the noisy, MP-PCA denoised, and tensor MP-PCA denoised data.

Discussion: At the shorter echo time of 80ms, tensor MPPCA performed similarly to standard MP-PCA, with neither significantly reducing the mean kurtosis variance in the chosen white matter ROI. At 130ms TE, both methods significantly reduced the variance of the mean kurtosis compared to the noisy data, with the tensor method yielding a notably stronger variance reduction than standard MPPCA ($p = 0.0016$ and $p = 0.0468$, respectively). This highlights the advantage of leveraging multidimensional redundancy when performing denoising.

Conclusions: This work exploited multidimensional redundancy to substantially improve the denoising performance in a complex diffusion-relaxometry MRI dataset. Using a consistent MATLAB implementation, tensor MP-PCA was more effective than standard MP-PCA. This suggests that multidimensional acquisitions may utilise the denoising technique to push towards higher resolution or lower SNR regimes while maintaining image quality, and without compromising research or clinical utility.

References

[1] J. Veraart, D. S. Novikov, D. Christiaens, B. Ades-aron, J. Sijbers, and E. Fieremans, "Denoising of diffusion MRI using random matrix theory," *Neuroimage*, vol. 142, 2016, doi: 10.1016/j.neuroimage.2016.08.016.

[2] J. L. Olesen, A. Ianus, L. Østergaard, N. Shemesh, and S. N. Jespersen, "Tensor denoising of multidimensional MRI data," *Magn Reson Med*, vol. 89, no. 3, 2023, doi: 10.1002/mrm.29478.

[3] M. Pizzolato *et al.*, "Acquiring and Predicting Multidimensional Diffusion (MUDI) Data: An Open Challenge," in *Mathematics and Visualization*, 2020. doi: 10.1007/978-3-030-52893-5_17.

Comparative Evaluation of Traditional and Deep Learning-Based Total Intracranial Volume Estimation Methods in Alzheimer's Disease and Cognitively Normal Brain MRI

Yuxin Weng[1], James Moggridge[1,2], Matthew Grech-Sollars[2,3]

[1] Institute of Neurology, University College London, UK

[2] Lysholm Department of Neuroradiology, National Hospital for Neurology and Neurosurgery, University College London Hospitals NHS Foundation Trust, London, UK

[3] Department of Computer Science, University College London, UK

Introduction: Total intracranial volume (TIV) serves as an important indicator of maximum brain capacity, playing a critical role in using quantitative MRI measures for clinical assessment of diseases such as Alzheimer's and epilepsy [1]. With the development of various deep learning–based tools and the growing acceptance and implementation of AI software in clinical practice, the performance of both traditional and AI-based methods for TIV estimation needs investigating.

Methods: We evaluated three software tools: the deep learning-based SynthSeg 2.0 (https://github.com/BBillot/SynthSeg), the conventional software SPM25 (https://github.com/spm/spm/releases/tag/25.01.02), and FreeSurfer 7.4.1 (the stable release as of June 2023). FreeSurfer was utilized with two methods: segmentation-based TIV (sbTIV, https://surfer.nmr.mgh.harvard.edu/fswiki/sbTIV) and estimated TIV (eTIV, https://surfer.nmr.mgh.harvard.edu/fswiki/eTIV). All samples were derived from T1-weighted MRI scans obtained from the ADNI database [2]. A controlled-variable design was employed to ensure comparability between groups, matched for mean age, sex ratio, and key MRI acquisition parameters, including field strength and slice thickness. This process yielded a study sample comprising 20 individuals with Alzheimer's disease (AD) and 20 cognitively normal (CN) controls. Statistical analyses included Welch's t-tests, paired-sample t-tests, and Bland–Altman plots. In addition, three segmentation-based methods (SPM25, SynthSeg, Freesurfer sbTIV) were further assessed through visual comparison, revealing several noteworthy findings.

Results: Welch's t-test revealed no statistically significant differences between the methods in estimating TIV for the AD and CN groups (Fig. 1). From the Bland–Altman percentage difference plots (Fig. 2), it was observed that SPM25, SynthSeg, and FreeSurfer sbTIV demonstrated better agreement (narrower limits of difference) compared with FreeSurfer eTIV. Qualitative visual inspection of segmentation maps for samples showing large inter-software discrepancies (Fig. 3) revealed that FreeSurfer sbTIV exhibited pronounced leakage beyond the meningeal boundaries compared to the other methods.

Discussion: It is generally accepted that TIV does not change with the progression of AD [3,4]. Although no statistically significant differences were found between the AD and CN groups across methods (Fig. 1), it can still be observed that, except for SPM25, the other three methods tended to yield slightly lower TIV values in the AD group. The lack of significance may be due to the low number of samples, and work in a larger group and diverse datasets would give more evidence to the result. From this perspective, SPM25 may provide more stable estimates for normalisation of brain volume. Considering the paired t-test results together with the Bland–Altman percentage difference plots (Fig. 2), SPM25, SynthSeg, and FreeSurfer sbTIV demonstrated narrower limits of difference and better overall consistency than FreeSurfer eTIV. Further visual inspection of segmentation maps for samples showing large inter-software discrepancies (Fig. 3) revealed that FreeSurfer sbTIV exhibited pronounced leakage beyond the meningeal boundaries, SPM25 showed evident under-segmentation of cerebrospinal fluid regions, whereas SynthSeg provided relatively stable and well-confined segmentations within the intracranial space, suggesting that SynthSeg may be the most stable method, followed by SPM25.

Conclusion: We recommend selecting the software method based on the specific needs and aims of each study, in reference to the findings above.

References:

[1] Hubbard, B. M., & Anderson, J. M. (1981). A quantitative study of cerebral atrophy in old age and senile dementia.

Journal of the Neurological Sciences, *50*(1), 135–145.

[2] Petersen, R. C., Aisen, P. S., Beckett, L. A., Donohue, M. C., Gamst, A. C., Harvey, D. J., Jack, C. R., Jagust, W. J., Shaw, L. M., Toga, A. W., Trojanowski, J. Q., & Weiner, M. W. (2010). Alzheimer's disease neuroimaging initiative (ADNI). *Neurology*, *74*(3), 201–209.

[3] Tomlinson, B. E., Blessed, G., & Roth, M. (1970). Observations on the brains of demented old people. *Journal of the Neurological Sciences*, *11*(3), 205–242.

[4] Vos, S. B., Winston, G. P., Goodkin, O., Pemberton, H. G., Barkhof, F., Prados, F., Galovic, M., Koepp, M., Ourselin, S., Cardoso, M. J., & Duncan, J. S. (2020). Hippocampal profiling: Localized magnetic resonance imaging volumetry and T2 relaxometry for hippocampal sclerosis. *Epilepsia*, *61*(2), 297–309.

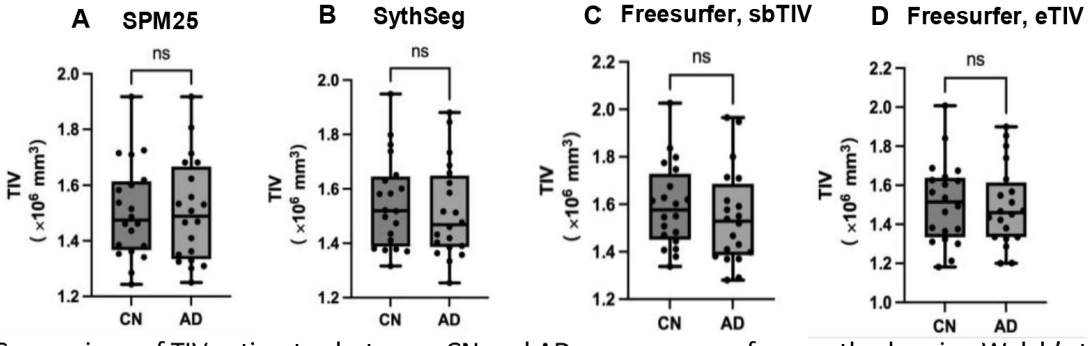

Fig. 1. Comparison of TIV estimates between CN and AD groups across four methods using Welch's t-test.

Box plots illustrate TIV estimates (×10⁶ mm³) in CN and AD groups, calculated using four different methods. "ns" denotes non-significant comparisons.

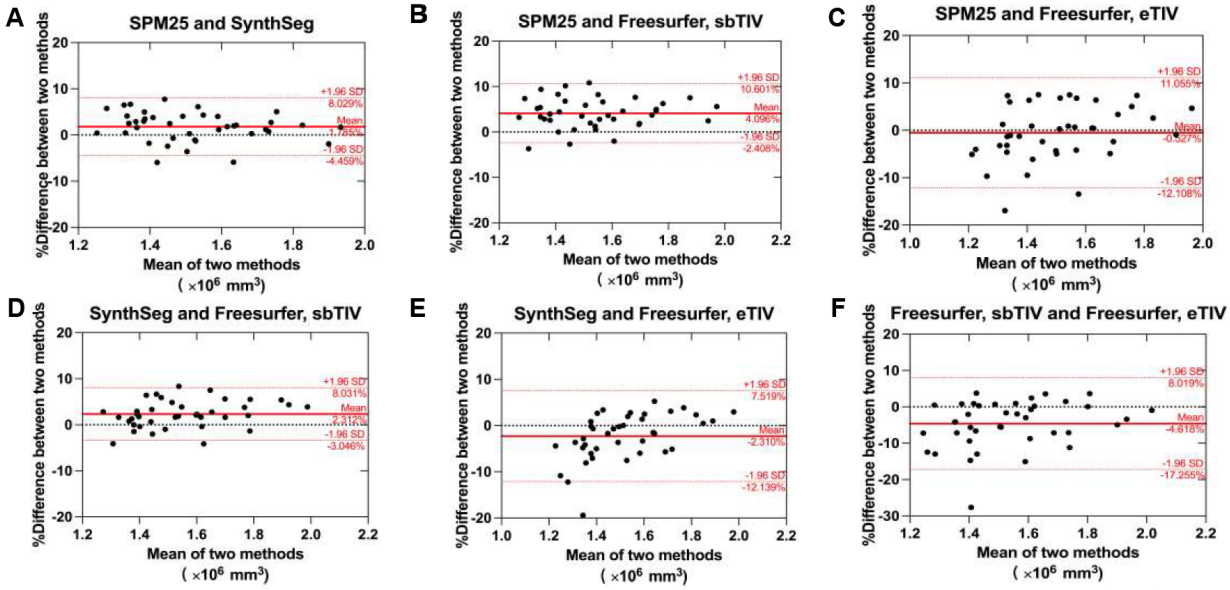

Fig. 2. The Bland–Altman plots illustrate the percentage differences in total intracranial volume (TIV) estimates between different methods in the combined CN and AD group (n = 40).

The percentage difference between the two methods calculated as: (TIV method 2 − TIV method 1) / Mean TIV of both methods × 100%.

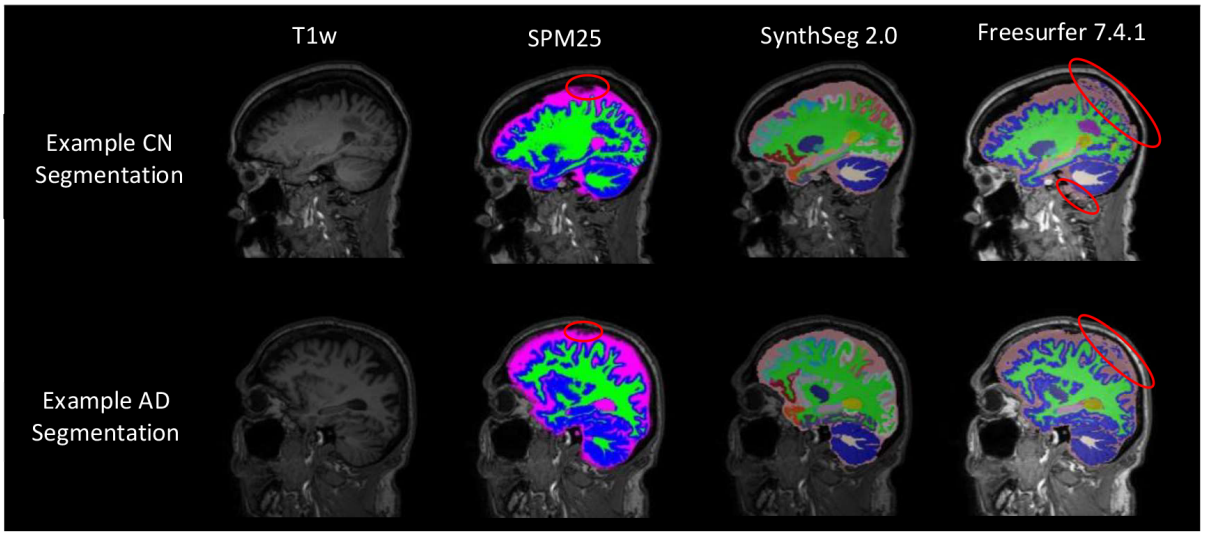

Fig. 3. Sagittal visualizations of TIV segmentation results using SPM25, SynthSeg 2.0, and FreeSurfer sbTIV in representative CN and AD subjects.

Feasibility of using convolutional neural network for automated low-contrast detectability in MRI QA

Belinda Ding[1], Lauren Fowler[1], Robert Flintham[1], Nigel Davies[1]
[1] University Hospital Birmingham NHS Foundation Trust, Birmingham, UK

Introduction

Low-contrast object detection is a critical component of MRI quality assurance (QA), particularly for evaluating scanner performance over time. The ACR MRI phantom includes a dedicated low-contrast module comprising four slices, each with ten spokes containing three low-contrast circles (Figure 1)[1]. Conventionally, the visibility of these circles is assessed manually, which is a time-consuming and subjective process poorly suited to longitudinal QA. However, due to the complexity of this module, it is often excluded from existing automated QA workflow at our site[2].

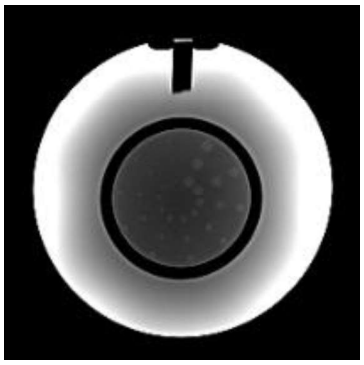

Figure 1: Low-contrast objects in the highest-contrast slice (slice 11). The low-contrast objects appear as rows of small circles, with diameters ranging from 1.5 mm to 7.0 mm, radiating like spokes from the centre of the circle (three circles/ spoke). Other slices are similarly configured, with contrast values ranging from 1.4% (slice 8) to 5.1% (slice 11).

To address this gap, we investigated the feasibility of using a convolutional neural network (CNN), trained on historical QA data, to automate assessment of this low-contrast module. Our aim was to develop a method that enhances consistency, reduces user burden, and supports scalable, longitudinal QA. The performance of the custom-trained CNN was benchmarked against LPIPS (Learned Perceptual Image Patch Similarity), a widely adopted perceptual similarity metric based on pre-trained deep neural networks.

Methods

Five T_1-weighted image volumes were randomly selected from the local MRI QA database. All images were acquired using head coils and followed the ACR-recommended phantom positioning guidelines (low-contrast module on slices 8 - 11). Four datasets were acquired on 1.5 T scanners (Siemens Sola ×2, Siemens Altea ×1, Philips Ingenia ×1) and one on a 3 T Siemens Skyra system.

All 600 circles (5 volumes × 4 slices × 10 spokes × 3 circles) were independently assessed by two raters (BD, LF) and assigned a binary visibility score: 1 (visible) or 0 (not visible). Consensus labels (defined as visible only when both raters agreed) were used to train the CNN model.

LPIPS computes perceptual similarity by comparing deep feature activations of image patches[3]. To facilitate this comparison, we generated modified images in which each circle was 'removed' by applying Telea's inpainting algorithm, which fills the circular region using information from surrounding pixels. The perceptual similarity between the original and modified images was then quantified using LPIPS, employing a VGG backbone with learned weights.

The CNN was designed to estimate the probability of each circle being visible, using both image data and contextual metadata. For each circle, a 20×20 pixel patch was extracted and paired with spatial tags (slice number, spoke number, circle index) and its LPIPS score. The CNN had two branches: a convolutional stream for image processing and a fully connected stream for encoding contextual data. These were merged and passed through further dense layers to produce a visibility probability. Data were split into training (80%) and validation (20%) sets with stratified sampling. Class imbalance (565:35) was mitigated in the training set using oversampling of the minority class and class weighting. Training was performed using binary cross-entropy loss with the Adam optimiser. Model performance

was evaluated on the fixed validation set using the area under the receiver operating characteristic curve (AUC) and sensitivity at a fixed specificity threshold of 80%.

Results and discussion

Inter-rater agreement was substantial, with a high Prevalence-Adjusted Bias-Adjusted Kappa (PABAK)[4] of 0.94. McNemar's test[5] revealed no significant asymmetry in disagreement patterns (p = 0.48), indicating consistent annotation behaviour. However, agreement on the negative class was lower, with a Negative Percent Agreement (NPA) of 0.49, highlighting difficulties in consistently identifying non-visible circles.

Figure 2 presents the sensitivity and specificity of each metric across different thresholds and the corresponding confusion matrices at the threshold where specificity reaches 80%. CNN outperformed LPIPS with higher specificity (98% vs 85%) and accuracy (97% vs 85%). Deviation of LPIPS from human raters also resulted in large differences in the final score for each phantom (Figure 3).

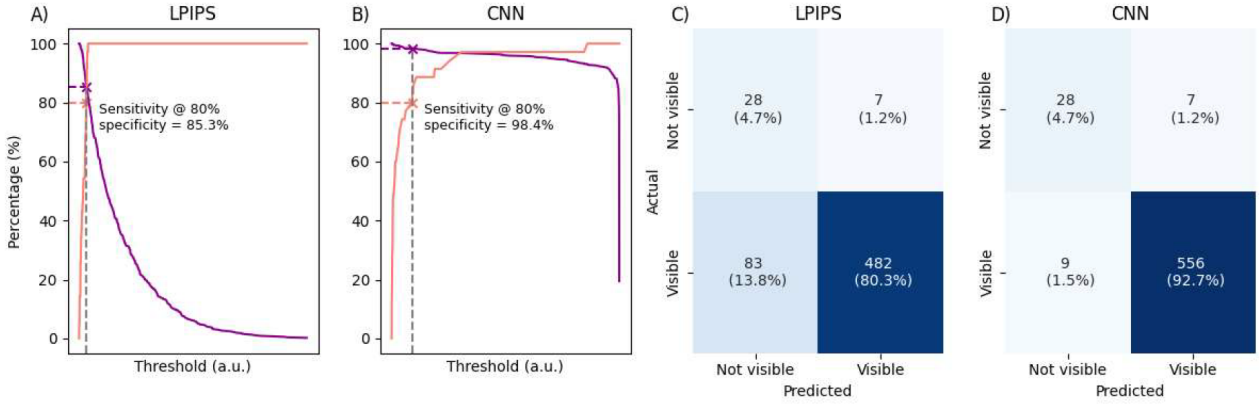

Figure 2: A, B) Sensitivity (purple) and specificity (pink) of LPIPS and CNN are plotted against different thresholds. C, D) Confusion matrix for LPIPS and CNN at the threshold where specificity reaches 80%.

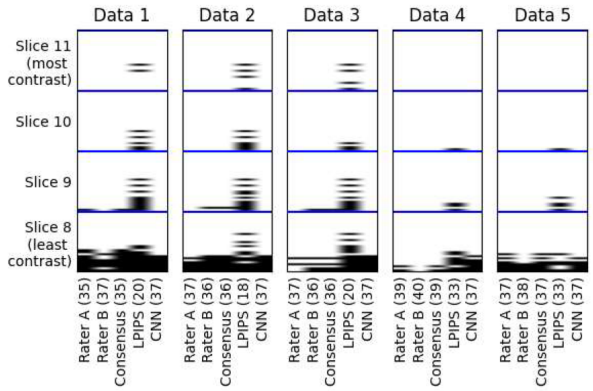

Figure 3: Plot showing how each rater, LPIPS and CNN scored each circle around the 5 data sets. The final score (defined as the sum of the number of completed spokes on each slice) is given in brackets.

It is worth noting that agreement between the CNN and the consensus rating was higher than inter-rater agreement, with a Cohen's kappa of 0.76 and PABAK of 0.95. McNemar's test (p = 0.80) indicated no significant systematic disagreement, and the CNN achieved an improved NPA of 0.64, suggesting more consistent identification of negative cases compared to human raters. However, the CNN model was trained on data from scanners that passed QA checks, so its performance on faulty systems is yet to be assessed. Also, all training data were acquired using head coils and its applicability to body coil images remains uncertain.

Conclusion

This study demonstrates that a CNN can reliably automate low-contrast detectability assessment in MRI QA, outperforming LPIPS and showing strong agreement with human raters. Further validation across diverse scanners and fault conditions is needed to confirm its robustness and broader applicability.

References: [1]Chen et al. J Digit Imaging 2004; [2]https://gitlab.com/rbf906/mippy; [3]Zhang et al. CVPR 2018; [4] Byrt et al. J Clin Epidemiol 1993; [5] Smith and Ruxton Behavioral Ecology and Sociobiology (2020);

Using functional MRI neurofeedback to modulate self-blame in major depressive disorder.

Alex Nagle[1], Alessandro Colasanti[1], Roland Zahn[2], Nick Dowell[3], Samira Bouyagoub[3], Chris Racey[4], Christina Kampoureli[4], Michael Luhrs[5], James Stone[1]

[1]Brighton and Sussex Medical School, Falmer, Brighton, UK
[2]Institute of Psychiatry, Psychology, and Neuroscience, King's College London, London, UK
[3]Clinical Imaging Sciences Centre, Falmer, Brighton, UK
[4]School of Psychology, University of Sussex, Falmer, Brighton, UK
[5]Faculty of Psychology and Neuroscience, University of Maastricht, Maastricht, Netherlands

Introduction: Major depressive disorder (MDD) is commonly framed as the result of general increases in negative emotion [1]. An alternative theory is that specific increases in self-blaming emotions, relative to other-blaming emotions, is instead what sows vulnerability to depression [2]. Though these two theories likely correspond to dissociable subsyndromes of the disorder deserving of equal attention, academic and clinical efforts have typically given primacy to the former over the latter [3]. Consequently, many current interventions do not address self-blaming biases specifically, which may result in a considerable proportion of patients responding insufficiently. fMRI neurofeedback is a novel technology well-poised to deliver self-blame-specific interventions. The subgenual cingulate cortex (SCC) is a key hub within the self-blame neural network, representing a potentially potent neurofeedback target [4]. The current study probed the feasibility of a single-session neurofeedback trial harnessing SCC BOLD activity as the sole training target.

Methods: 20 participants with current MDD were allocated to two active intervention groups, representing target activation patterns that, though opposite, have both been observed in healthy controls relative to MDD cohorts [5,6]. By pitting these interventions against each other directly, we hoped to clarify which one possesses the most therapeutic potential. In Intervention A (n=10), participants received neurofeedback to increase SCC activity during a 'guilt' task and decrease it during an 'indignation' task. In Intervention B (n=10), participants were encouraged to do the opposite. The primary outcome measure was the pre- to post-neurofeedback change in SCC BOLD activity. The secondary outcome measure was the pre- to post-neurofeedback change in clinical profile (self-esteem and symptom severity).

Results: Clinical scores improved significantly following neurofeedback, but intervention differences were not observed. Neurofeedback performance was greatest for Intervention B participants while they engaged in the indignation task, suggesting that upregulation of SCC activity for other-blame represents the most achievable training protocol. Neuroimaging analysis revealed one principal cluster of increased activation following neurofeedback (associated with the left temporoparietal region), specifically for indignation (relative to guilt) and Intervention B (relative to Intervention A; Fig. 1). Inferences from the results are limited by the small sample size, in addition to other technical issues.

Discussion: The general clinical improvements satisfy feasibility study requirements and demonstrate that engagement with negative emotions during neurofeedback is safe. The finding that modulation of the SCC is most achievable for indignation contributes to growing evidence that this region is more functionally heterogeneous for causal agency representations than previously assumed. Lastly, the functional neuroimaging observations demonstrate that self-blame-specific neurofeedback likely engages a distributed network beyond the SCC, with implications for future target selection choices.

Conclusion: In summary, the results justify more adequately powered investigations into SCC-oriented neurofeedback for depression.

Acknowledgements: Yoko Nagai, Lou-Vinh Tran, Robyn Dillon, Francis Botwe, Chris Jones, Rodrigo Basilio, George Tertikas, Will Strawson.

References

[1] Watson D., Clark L.A., Carey G. (1988). *Positive and negative affectivity and their relation to anxiety and depressive disorders.* J Abnorm Psychol, (3): 346-53

[2] Abramson L.Y., Seligman M.E., Teasdale J.D. (1978). *Learned helplessness in humans: critique and reformulation*. J Abnorm Psychol, (1): 49-74

[3] Zahn R., Weingartner J.H., Basilio R., Bado P., Mattos P., Sato J.R., de Oliveira-Souza R., Fontenelle L.F., Young A.H., Moll J. (2019). *Blame-rebalance fMRI neurofeedback in major depressive disorder: A randomised proof-of-concept trial*. Neuroimage Clin, 24:101992

[4] Zahn R., de Oliveira-Souza R., Moll J. (2020). *Moral Motivation and the Basal Forebrain*. Neurosci Biobehav Rev, 108: 207-217

[5] Lythe K.E., Gethin J.A., Workman C.I., Lambon Ralph M.A., Deakin J.F.W., Moll J., Zahn R. (2022). *Subgenual activation and the finger of blame: individual differences and depression vulnerability*. Psychol Med, 52 (8): 1560-1568

[6] Fennema D., Barker G.J., O'Daly O., Duan S., Carr E., Goldsmith K., Young A.H., Moll J., Zahn R. (2023). *Self-blame-selective hyper-connectivity between anterior temporal and subgenual cortices predicts prognosis in major depressive disorder*. Neuroimage Clin, 39: 103453

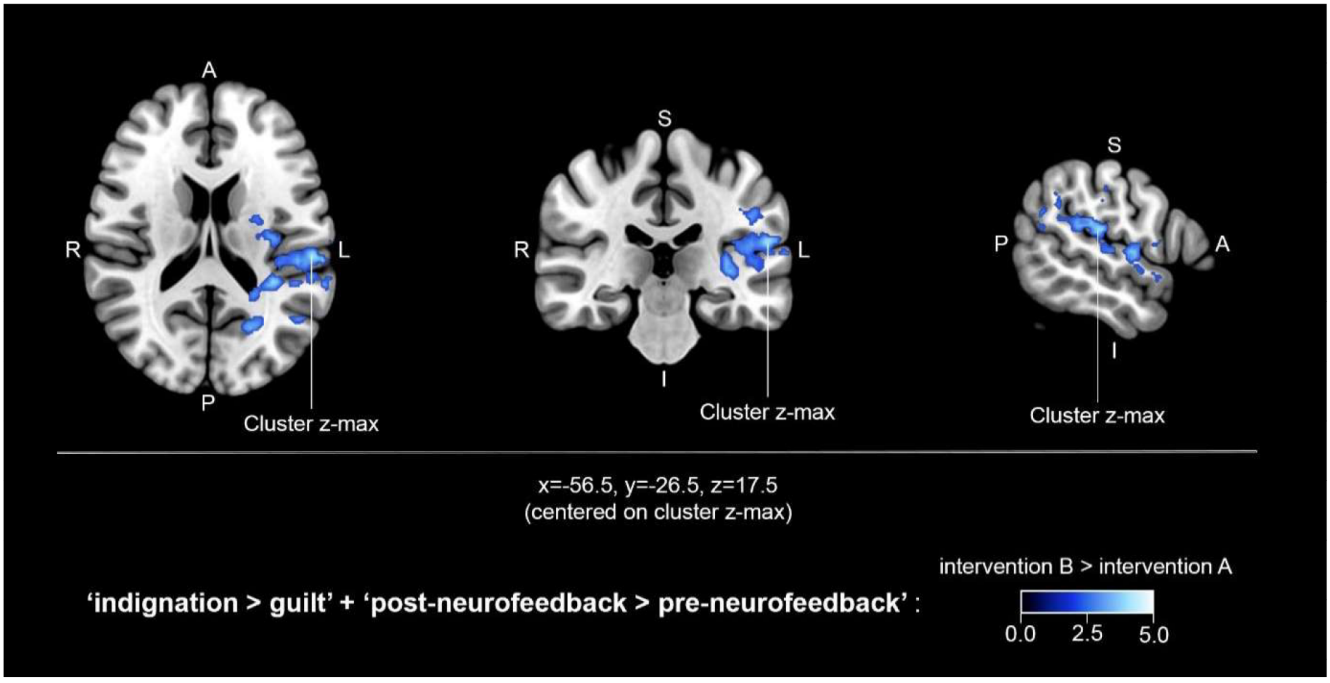

Fig. 1. Z-stat map from a whole-brain GLM investigating neural changes from pre- to post-neurofeedback. One cluster was reported for this analysis, specifically representing an increase in activation in Intervention B participants under the indignation condition, from pre- to post-neurofeedback (MNI x=-56.5, y=-26.5, z=17.5). It likely represents a moderate effect size (max z-stat=4.0, PSC=1.28%). The cluster is lateralised to the left hemisphere, in the left temporoparietal region.

Coupled grey matter BOLD-CSF oscillations measured at 7T during wake and sleep.

Qin Li[1], Ian D Driver[1], Yang yang[2], Neil A Harrison*, Mara Cercignani*

[1]Cardiff University Brain Research Imaging Centre, Cardiff, Wales, United Kingdom.

Introduction: It has been previously shown that during non-rapid eye movement (NREM) sleep, neural slow waves are coupled with low-frequency hemodynamic oscillations and accompanying oscillations in CSF flow [1]. These findings point to a coordinated pattern linking brain activity, blood flow, and CSF dynamics, suggesting a connection between sleep-related neural processes and brain waste clearance [2]. In this study, we used 7T to measure CSF dynamics and grey matter (gBOLD) signals, aiming to reproduce previous findings and compare patterns between wakefulness and sleep in healthy participants.

Methods: 9 participants (age-range: 25-33 years, 6 males) without sleep complaints, as assessed by validated questionnaires [3], underwent two MR-sessions: once during sleep following a whole-night of sleep deprivation, and once during wake following a normal night of ~8 hours sleep. All scans were conducted in the morning (6-10 o'clock). Because simultaneous recording of EEG data at 7T is not possible, we used a multimodal approach to determine sleep and wakefulness during scanning. This included real-time button press feedback, breathing patterns and post-scan subjective report.

MRI data were acquired with a Siemens 7T MAGNETOM scanner. The full protocol included sodium and proton imaging. For the purpose of this work, we used the anatomical volume (MP2RAGE) [4]and resting state function MRI (fMRI). To focus on fluid flow, all fMRIs were performed with eyes closed, with the boundary edge of the imaging volume placed below the fourth ventricle (Fig. 1), allowing detection of CSF flow into the brain [1]. Acquisitions were performed with a multiband accelerated EPI sequence [5] (TR: 1.5 s, TE: 25 ms, GRAPPA = 2, MB = 4, 400 volumes, 1.5 mm isotropic), enabling analysis of continuous low-frequency gBOLD and CSF dynamics during sleep.

MP2RAGE images were segmented using FreeSurfer to generate binary masks of the grey matter (GM) and fourth ventricle for subsequent analysis. To minimise partial volume effects at the boundaries, the fourth ventricle mask was further refined using morphological erosion. For all fMRI datasets, processing streams followed the methods in [1] and are shown in Fig.1.

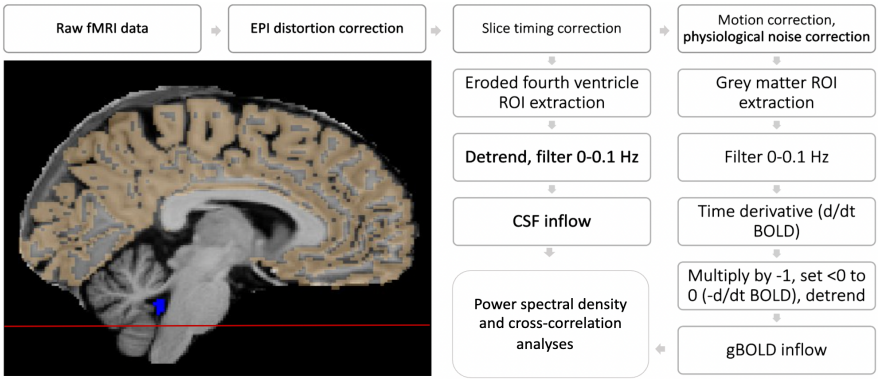

Fig. 1. First slice position (red line) GM mask (yellow), fourth ventricle mask (blue), and flowchart of preprocessing steps on each data type used in PSD and cross-correlation analyses.

Results and discussion: All participants maintained continuous button presses throughout the awake scan and no response for at least 80% of the sleep scan. Previous studies have shown that low-frequency (0 to 0.1 Hz) CSF power and gBOLD signal amplitude increase during NREM sleep [1]. 4 of our participants showed increased CSF power in the 0.03 to 0.1 Hz band, which likely reflects NREM sleep and 1 no obvious difference. As shown in the mean PSD of these 5 participants, the dominant oscillation in the CSF signal was below 0.05 Hz (Fig. 2) during sleep compared to wake state suggesting they were likely in deep NREM sleep. The other 4 participants showed lower CSF

power in this band during the sleep acquisition suggesting they were unlikely to be in deep NREM sleep. In addition, in the 5 participants likely in deep NREM sleep, the CSF signal was tightly coupled with gBOLD oscillations during the sleep (Fig. 3b) but not the wake scan (Fig. 3a). The CSF signal also strongly correlated with the negative derivative of the BOLD oscillations as previously reported (Fig. 3c). This suggests an alternation between blood flow (and accompanying increase in cerebral blood volume) causing compressive efflux of CSF from the fourth ventricle followed by compensatory CSF influx. Cross-correlation analysis further revealed that changes in the gBOLD signal preceded CSF fluctuations by approximately 3.0 seconds (Fig. 3d).

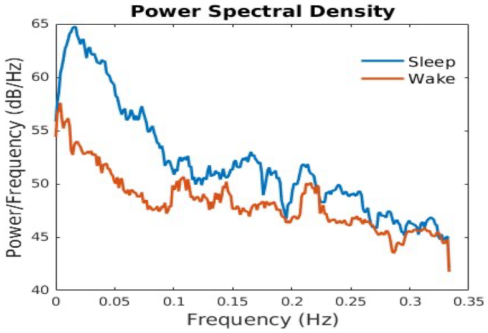

Fig. 2. Mean PSD of CSF signal (n = 5).

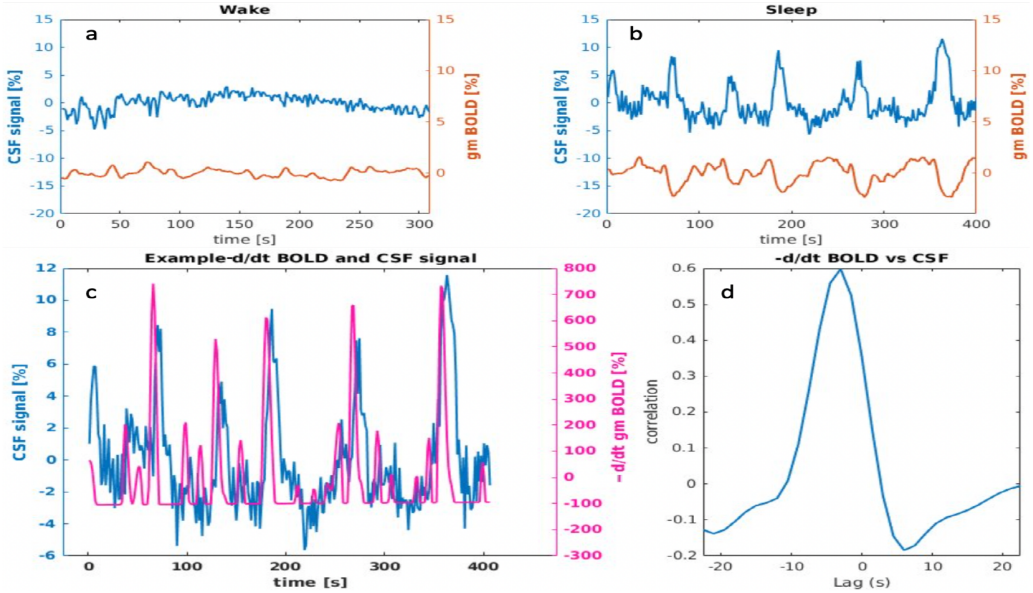

Fig. 3. (a,b) Example time series of the gBOLD and CSF signal from one participant: during sleep, signals are high amplitude. (c) CSF time series and the –d/dt BOLD signals were strongly correlated. (d) Cross-correlation of CSF and derivative of gBOLD has a max R = 0.6 at delay = –3.0 s.

Conclusions: Although we could not detect with certainty the sleep phase during scanning due to the challenge of using EEG at 7T, our results reproduced previous findings and suggest that sleep cycles may be inferred from CSF signal dynamics when EEG is not available.

References

[1] Fultz, Nina E., et al. "Coupled electrophysiological, hemodynamic, and cerebrospinal fluid oscillations in human sleep." Science 366.6465 (2019): 628-631.

[2] Xie, Lulu, et al. "Sleep drives metabolite clearance from the adult brain." science 342.6156 (2013): 373-377.

[3] Smyth, Carole. "The Pittsburgh sleep quality index." Journal of gerontological nursing 25.12 (1999): 10-10.

[4] Marques, José P., et al. "MP2RAGE, a self bias-field corrected sequence for improved segmentation and T1-mapping at high field." Neuroimage 49.2 (2010): 1271-1281.

[5] Moeller, Steen, et al. "Multiband multislice GE-EPI at 7 tesla, with 16-fold acceleration using partial parallel imaging with application to high spatial and temporal whole-brain fMRI." Magnetic resonance in medicine 63.5 (2010): 1144-1153.

Investigating the Repeatability of Phase-Based Magnetic Resonance Electrical Properties Tomography (EPT) in the Human Brain

Philippa Sha[1], Jierong Luo[1], Matthew Cherukara[1], Karin Shmueli[1]
[1]Department of Medical Physics and Biomedical Engineering, University College London, London, United Kingdom.

Introduction:

Phase-based magnetic resonance electrical properties tomography (MR-EPT) is an emerging technique to non-invasively measure tissue electrical conductivity (σ) from the MR transceive phase (ϕ_0), via the Helmholtz equation [1]. Despite technical advancements, the repeatability of EPT remains largely unstudied. In this study, we investigated and compared the repeatability of four different EPT reconstruction methods we developed [2], optimised and applied to the human brain.

Methods:

Data acquisition: Ten healthy volunteers (seven female, aged 23-30 years), recruited as part of a previous study [3], were scanned in two sessions one week apart, with three identical scans per session. Multi-echo 3D GRE images were acquired using a 3T Philips Achieva system, with sequence parameters: 4 echoes, $TE_1 = \Delta TE = 4.61$ ms, TR = 22.0 ms, resolution = 1.25 x 1.25 x 1.25 mm^3, flip angle = 12°.

EPT reconstruction: An in-house EPT pipeline [2] was applied to the denoised [4] complex GRE data. A total field map was obtained from a non-linear fit of the complex data over all TEs [5]. Residual phase wraps were removed using SEGUE [6]. The transceive phase, ϕ_0, was estimated by predicting the complex signal at TE=0 and extrapolating the phase. Conductivity was reconstructed via the surface integral of the ϕ_0 gradient, using 3D spherical kernels with four variations: (1) unmodified (*Sphere*), (2) weighted by magnitude intensity (*Mag*), (3) weighted by tissue segmentation (*Seg*), and (4) weighted by both magnitude and segmentation (*MagSeg*). Each approach was optimised, with details provided in Table 1.

Method	Magnitude-based weighting	Segmentation-based weighting	Differential kernel radius (mm)	Integral kernel radius (mm)
Sphere	✗	✗	5	6
Mag	✓ Final-echo magnitude*	✗	21	24
Seg	✗	✓ SynthSeg [7] applied to final-echo magnitude †	21	24
MagSeg	✓ Final-echo magnitude*	✓ SynthSeg [7] applied to final-echo magnitude †	21	24

Table 1: Optimised reconstruction parameters for each EPT method. *Magnitude-based weighting is adjusted automatically in each voxel based on SNR, by a free parameter δ [8]. † Segmentations consist of cerebrospinal fluid (CSF), grey matter (GM) and white matter (WM).

Repeatability analyses: For each method, repeatability was assessed both within-subject (including both intra- and inter-session) and between-subject, using some of the most popular and informative repeatability metrics [9-11]. For regional comparisons, the median conductivity was calculated within the grey matter (GM), white matter (WM) and cerebrospinal fluid (CSF), each eroded by one voxel to avoid partial volume effects. Non-physical negative conductivity values were considered erroneous and therefore excluded. To enable voxelwise comparison, each subject's conductivity maps were co-registered using FLIRT [12, 13].

Results:

Comparison of the four methods is illustrated in Fig. 1, which shows conductivity maps in a representative subject. Visually, *Sphere* performed most poorly, with the highest noise levels and reconstruction errors. *Mag*-weighting suppressed noise, while *Seg*-weighting preserved edges and tissue contrast. Combining the two (*MagSeg*) achieved optimal reconstruction.

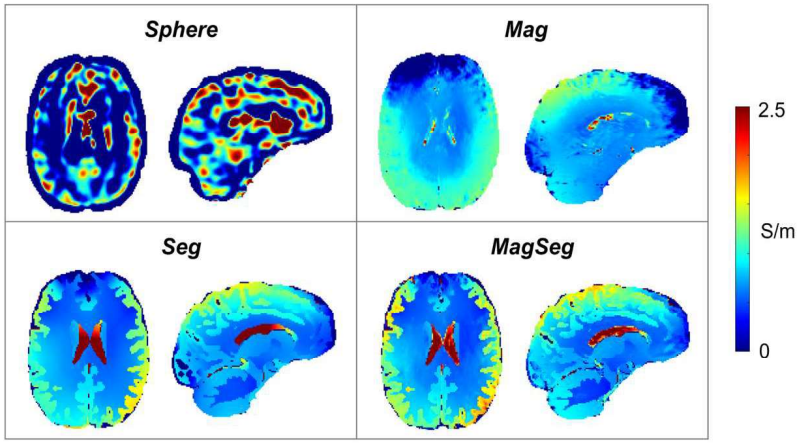

Fig. 1: Conductivity maps generated using each approach.

All repeatability metrics are shown in Fig. 2: voxel-wise normalised root mean square error (NRMSE) across repetitions, and three kinds of standard deviation (SD; within-region, within-subject, and between-subject), calculated in each tissue type. All repeatability metrics were significantly higher in the CSF, compared to GM and WM ($p<0.02$), using all four EPT methods (except NRMSE using *Sphere* and SD_w using *Mag*).

Fig. 3 further compares the performance of each method, showing the conductivity contrast-to-noise ratio (CNR) and percentage of physically implausible conductivity values, defined as those < 0 and > 10 S/m.

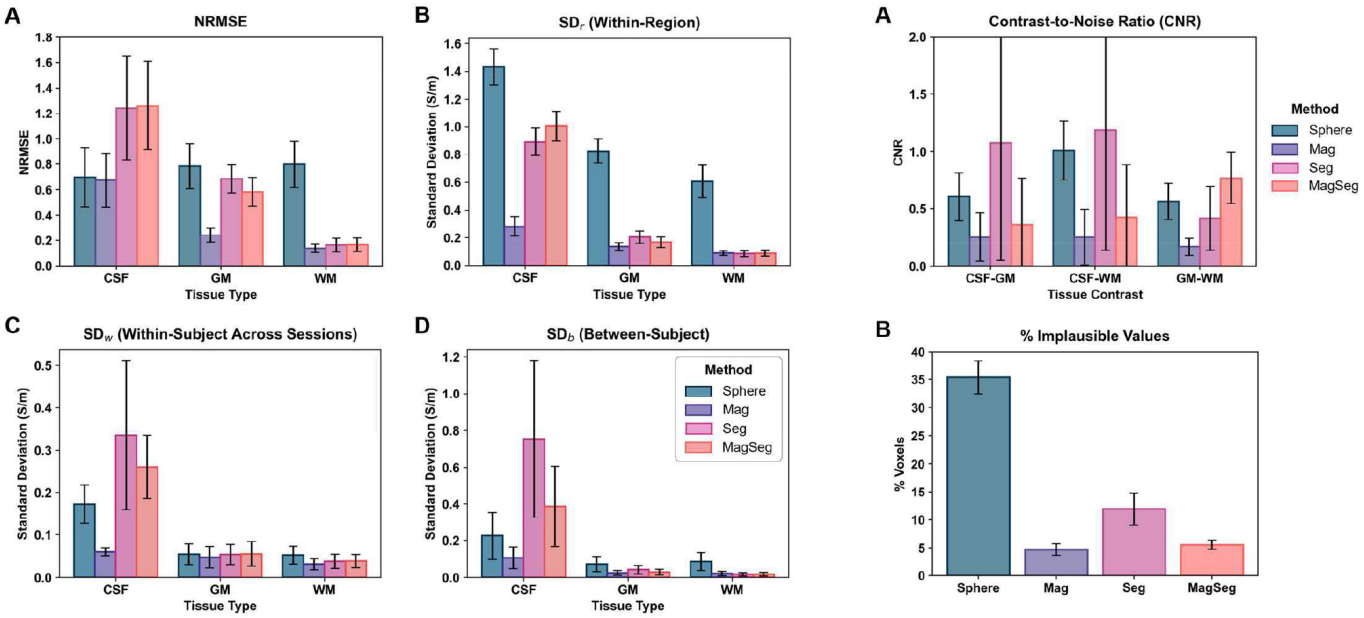

Fig. 2: Mean repeatability metrics across all subjects, calculated in each tissue type. For all metrics, a higher value indicates poorer repeatability. (A) Average NRMSE across repetitions, with error bars indicating inter-subject SD. (B)-(D) Voxel-wise SD within-region (SD_r), SD of median conductivity across repetitions (SD_w) and across subjects (SD_b), with 95% confidence intervals. Note that y-axis scales are not equal.

Fig. 3: (A) Mean CNR across all subjects and sessions, calculated between each tissue pair. (B) Mean percentage of implausible conductivity values, across all subjects and sessions. All error bars indicate inter-subject SD.

Discussion:

Repeatability varied considerably across EPT approaches. Overall, *Mag* achieved the highest repeatability, likely due to its low tissue contrast (Fig. 3A) and structural detail. *Sphere* also appeared repeatable but was dominated by noise and non-physical values (Fig. 3B). *Seg* and *MagSeg* performed similarly overall, though *MagSeg* greatly reduced the rate of reconstruction errors (5.6% vs 11.9%; Fig. 3B) and improved GM-WM CNR (Fig. 3A).

Repeatability was generally poorer in the CSF, compared to GM or WM, likely attributed to a higher rate of EPT errors in the CSF. The reason for these errors remains unclear, but may relate to pulsation effects, or increased anatomical complexity compared to more homogeneous WM areas [14]. Future work will aim to minimise such errors, as well as investigate the repeatability of alternative EPT methods, including deep learning [15].

Conclusions:

In this study, we investigated the repeatability of EPT in the human brain, using four different surface-integral-based reconstruction methods. Across all methods, repeatability varied significantly between tissue types, with the poorest repeatability in the CSF. Our *MagSeg* method was most effective in noise suppression and edge preservation. This work marks an important step towards EPT validation, and highlights minimising CSF-specific errors as a priority for future work.

References

[1] Katscher, U. et al. *NMR Biomed.* 2017; 30(8):e3729. **[2]** Karsa, A. et al. *Proc. Ann. Meeting ISMRM*. 2021; 3774. **[3]** Karsa, A. et al. *Magn. Reson. Med.* 2020; 84:3206-3222. **[4]** Doniza, L. et al. *IEEE Trans. Biomed. Eng.* 2025. **[5]** Liu, T. et al. *Magn. Reson. Med.* 2012; 69(2):467-476. **[6]** Karsa, A. et al. *IEEE Trans. Med. Imag.* 2019; 38(6):1347-1357. **[7]** Billot, B. et al. *Med. Image Analysis*. 2023; 86. **[8]** Luo, J. et al. *Proc. Ann. Meeting ISMRM.* 2024; 3682. **[9]** Barnhart, H. et al. *Trans. Oncology.* 2009; 2(4):231-235. **[10]** Raunig, D. et al. *Stat. Methods in Med. Research.* 2014; 24(1):27-67.
[11] Cherukara, M. et al. *Magn. Reson. Med.* 2025; 38:449-463. **[12]** Jenkinson, M. et al. *Med. Image Analysis.* 2001; 5(2):143-156. **[13]** Jenkinson, M. et al. *NeuroImage*. 2002; 17(2):825-841. **[14]** Mandija, S. et al. *Proc. Ann. Meeting ISMRM*. 2018; 5096. **[15]** Jung, K-J. et al. *NeuroImage*. 2025; 307:121054.

Qualitative Comparison of Harmonic and Transient Excitations in a Finite Element Brain Model for Magnetic Resonance Elastography

Mehmet N. YILDIRIM[1], Samuel Evans[2], Daneil Gallichan[1]
[1] CUBRIC / School of Engineering, Cardiff University, Cardiff, UK
[2] School of Engineering, Cardiff University, Cardiff, UK
Email: YildirimMN@cardiff.ac.uk

Introduction: Magnetic Resonance Elastography (MRE) noninvasively quantifies tissue mechanical properties by analysing induced wave propagation, crucial for diagnosing neurological disorders [1]. MRE combines mechanical excitation, motion-sensitive phase-contrast imaging, and data inversion to estimate tissue stiffness. During acquisition, acoustic vibrations are applied using a passive driver, which transmit the vibrations created by active driver located outside of the scanner room. Depending on the excitation type, the wave field is sampled differently: harmonic MRE relies on repeated cycles with varying phase offsets to capture steady-state wave motion, whereas transient MRE captures wave propagation following a brief excitation [2]. Understanding how these excitation methods influence wave propagation is important, as it directly affects the spatial distribution and the accuracy of reconstructed stiffness maps. This study directly compares harmonic and transient excitations to reveal how each method uniquely governs wave propagation characteristics and consequently shapes the spatial distribution and interpretability of mechanical properties in brain MRE. Computational models such as finite element (FE) simulations can be utilized in MRE studies to simulate wave propagation and systematically investigate how anatomy and material properties influence tissue mechanics. In this study, we used the open-source FEBio [3] software to simulate wave propagation in a 3D simplified FE model of the brain.

Methods: A 3D brain geometry was exported in STL format from a previously published finite element (FE) model [4]. This geometry was imported into MATLAB using the GIBBON toolbox [5] to generate an input file for FEBio simulations. The mesh was created with TetGen using tetrahedral (tet4) elements, consisting of 587,811 elements for the brain and 450,645 elements for the cerebrospinal fluid (CSF). Material properties used in FE simulation shown in **Table.1** were selected from published literature. Since real CSF behaves as a fluid and cannot resist shear (shear modulus G = 0), it is challenging to model it directly in standard FE simulations without advanced solvers. To avoid numerical issues and maintain a clear mechanical contrast with brain tissue, the CSF was modelled as a very soft solid.

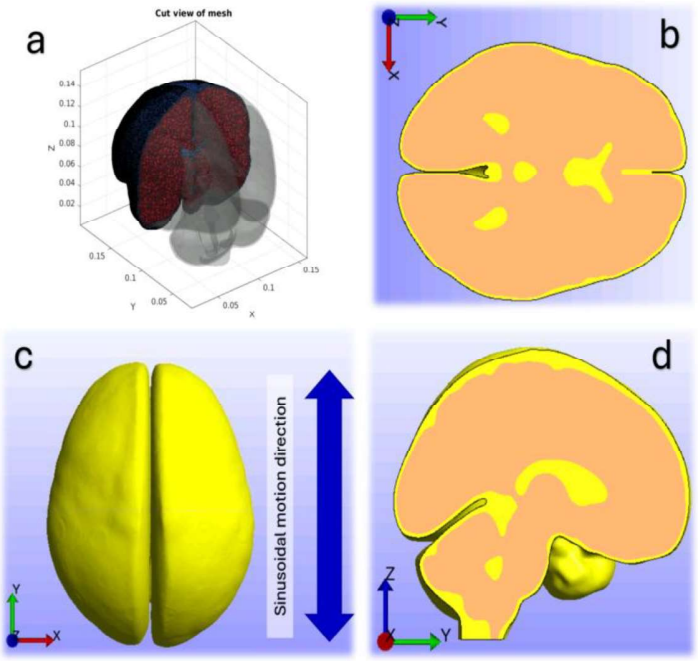

Fig. 1. Visualization of the 3D brain finite element (FE) model and anatomical structures. (a) Cut view of the meshed brain model showing tetrahedral elements representing brain tissue (red) and cerebrospinal fluid (CSF) (blue). (b) Axial cross-section of the brain model highlighting internal structures. (c) Lateral view of the brain model surface with the indicated direction of applied sinusoidal motion (Y-axis), simulating MRE excitation. (d) Midsagittal view of the brain illustrating the anatomical regions. Coordinate axes (X, Y, Z) are shown according to MR scanner coordinate system for reference in each panel.

Two types of mechanical loading were simulated: (1) Harmonic excitation at 60.1 Hz, using a continuous sinusoidal motion; and (2) Transient excitation, using a single sinusoidal impulse. To attempt to replicate experimental MRE conditions (where an inflatable pillow driver is used underneath the head), a Y-direction displacement of 150 µm was applied to all nodes on the outer CSF surface. These nodes were also fixed in

the X and Z directions to simulate the skull's restriction. Simulations ran for 200 ms with a time step of 2 ms, ensuring consistent time resolution for both loading types. Post-processing was carried out in MATLAB to extract Y-direction displacement data and compare the harmonic and transient responses using 2D image slices.

	Material Model	Parameters	Value	Unit
CSF	neo-Hookean	Young's Modulus	100	Pa
		Poisson's ratio	0.495	-
		Density	1005	kg/m^3
Brain	neo-Hookean	Young's Modulus	3000	Pa
		Poisson's ratio	0.49	-
		Density	1040	kg/m^3

Table 1. Material properties of CSF and Brain used in FE

Results: Simulations were performed using both harmonic and transient excitations to investigate differences in wave propagation within the brain model. Sagittal slices at different time-points in the simulation revealed distinct wave patterns under harmonic and transient excitations (**Fig. 2**). Harmonic excitation produced smooth, periodic wavefronts with consistent propagation across the brain, reflecting steady-state behaviour. In contrast, transient excitation generated complex but coherent wave patterns with broader spatial variation and faster attenuation. Despite the shorter excitation duration, transient loading still produced measurable wave propagation suitable for analysis.

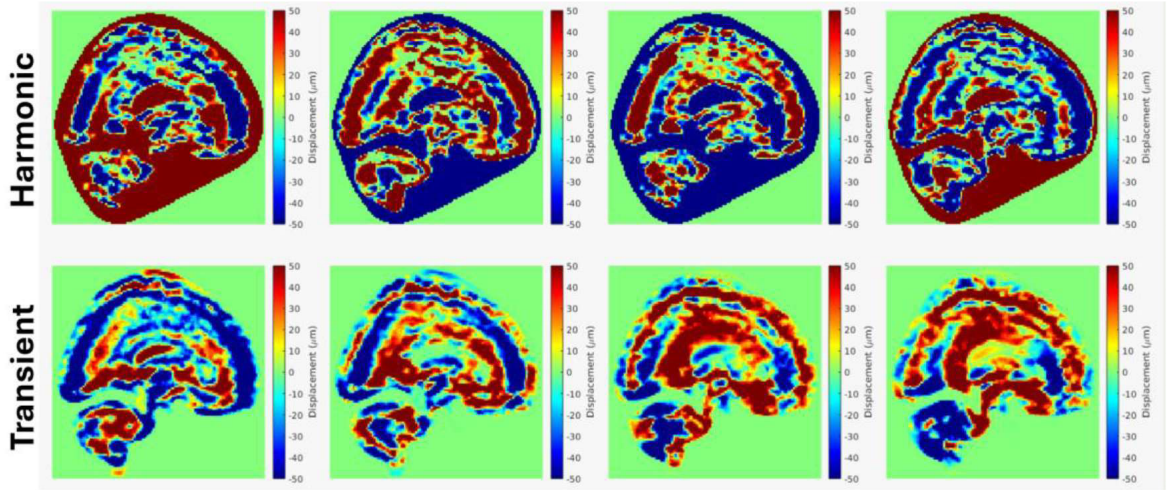

Fig.2 Shows displacement fields in the Y-direction for harmonic (top row) and transient (bottom row) excitations at different time-points in the simulation within a sagittal slice of the brain model.

Discussion: This study shows that both harmonic and transient excitations can generate usable wave patterns in the brain model. While harmonic loading produced smooth, periodic waves, transient excitation resulted in more complex but analysable waveforms. Although a simplified model was used, consisting only of homogeneous, elastic brain and CSF, the results demonstrate how excitation type affects wave behaviour.

Conclusions: This study used a simplified finite element brain model to qualitatively examine the effects of harmonic and transient excitations on wave behaviour. The simulation results revealed distinct spatiotemporal wave characteristics associated with each excitation type. The model effectively captured these differences, demonstrating its suitability for exploring excitation-dependent dynamics in MRE. Future work will focus on incorporating viscoelastic and anatomically detailed properties to enhance physiological accuracy and broaden clinical relevance.

Acknowledgements: Mehmet Nebi YILDIRIM's PhD study was funded by the Republic of Türkiye Ministry of National Education under the Study Abroad Scholarship Program.

References

[1] L. V. Hiscox et al., Phys. Med. Biol., vol. 61, no. 24, Art. no. 24, 2016, doi: 10.1088/0031-9155/61/24/R401.
[2] McCracken, P.J. et al., 2005. Mechanical transient-based magnetic resonance elastography. *Magnetic Resonance in Medicine*, 53 (3), 628–639. 10.1002/mrm.20388.
[3] Maas SA, Ellis BJ, Ateshian GA, Weiss JA: FEBio: Finite Elements for Biomechanics. Journal of Biomechanical Engineering, 134(1):011005, 2012. https://doi.org/10.1115/1.4005694
[4] N. J. Bennion et al., '*In vivo* measurement of human brain material properties under quasi-static loading', *J. R. Soc. Interface.*, vol. 19, no. 197, p. 20220557, Dec. 2022, doi: 10.1098/rsif.2022.0557.
[5] Moerman, (2018). GIBBON: *The Geometry and Image-Based Bioengineering add-On*. Journal of Open Source Software, 3(22), 506. https://doi.org/10.21105/joss.00506

Evaluating structural uncertainty in accelerated MRI: are voxelwise measures useful surrogates?

Luca L. C. Trautmann[1], Peter A. Wijeratne [1], Itamar Ronen[2] , Ivor J. A. Simpson[1]
[1] SussexAI Centre, Department of Engineering and Informatics, Brighton, UK
Brighton and Sussex Medical School, Brighton, UK,

Introduction: Magnetic Resonance Imaging (MRI) offers high-quality, non-invasive visualization but longer acquisition times limit clinical use [1,2]. Accelerated MRI using deep learning reconstruction can shorten scans but introduces ill-posedness, requiring robust and clinically relevant uncertainty quantification [2]. We stipulate, that the predominantly used voxelwise intensity-based uncertainty maps are poorly aligned with clinical needs. We argue that uncertainty quantification must be task-aware, tied to diagnostic goals.

Methods: We used the Calgary Campinas 2022 challenge dataset [5]. Three reconstruction models were ensembled: UNET, Variational Networks [6], and Recurrent Inference Machines [3], trained with identical hyper-parameters but different weight initialisations. All reconstructions were performed with 5× acceleration, preserving 1 mm isotropic voxel size at both input and output. Ensembled reconstructions were passed through SynthSeg [4] to measure morphological variability. Within-ensemble variability and bias were compared to fully sampled references. Estimated brain structure volumes were used as the primary downstream metric. Bilateral structures were aggregated by summing left and right hemisphere volumes. Ensemble variability was quantified using the coefficient of variation (CV) of predicted volumes, while bias was defined as percentage deviation from fully sampled references.

Results: All models exhibited structural variability within ensembles (0.5–3.5% volume variation), with UNET highest and RIM lowest variability. We further tested whether voxelwise intensity uncertainty could explain morphological variability. For each structure, we correlated voxel-level standard deviation maps with normalized volume variability across the ensemble. Correlations were consistently weak (R^2 values below 0.32 for all models), suggesting voxel-level uncertainty maps are not reliable predictors of ensemble variability in clinically relevant structures. Regression analyses using voxelwise uncertainty histograms confirmed this, yielding low predictive power.

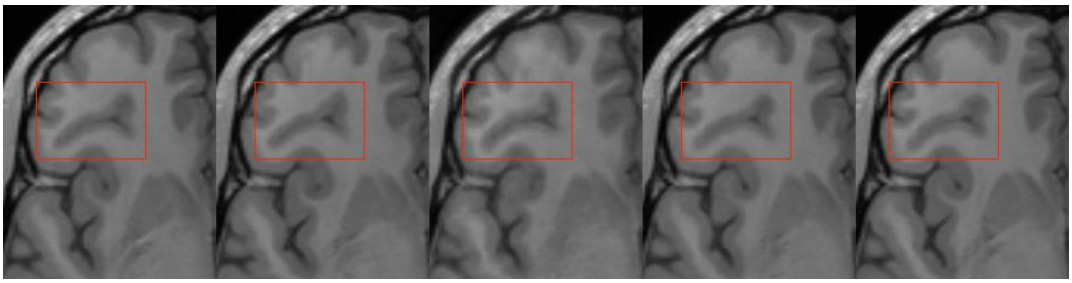

Fig. 1. Example slices from ensemble reconstructions showing subtle structural differences (white/grey matter thickness, shifted boundaries) between models trained on the same undersampled data.

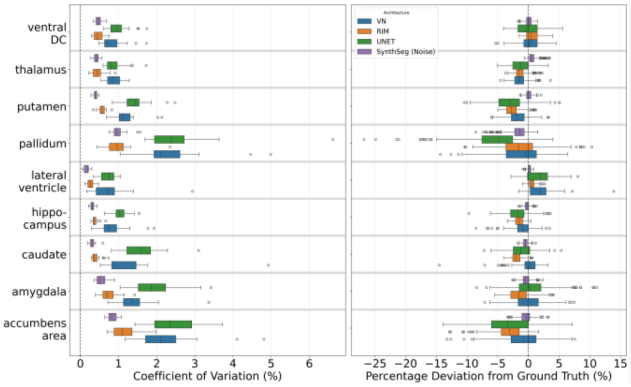

Fig. 2. Ensemble-level analysis of structure volumes. Left: within-ensemble variability across reconstructions (coefficient of variation). Right: systematic bias relative to fully sampled reference segmentation. For reference, SynthSeg (Noise) describes ensembles of fully sampled k-space with random noise added to match an SNR = 30.

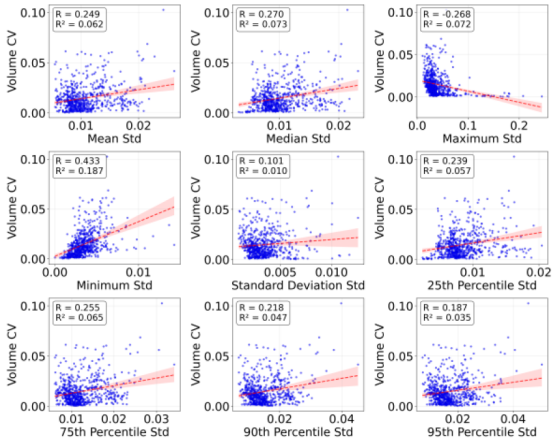

Fig. 3. Scatter plots comparing voxelwise intensity uncertainty with morphological volume variability. Low correlations show voxel-level measures fail to predict clinically relevant uncertainty.

Discussion: Voxelwise uncertainty fails to capture reconstruction bias or morphological variability. Standard image quality metrics (SSIM, PSNR) do not reflect structural uncertainty.

Conclusions: Our research suggests that voxel-level uncertainty measures are inadequate surrogates for morphological uncertainty in accelerated MRI reconstruction.

References

[1] Hammernik, K., Schlemper, J., Qin, C., Duan, J., Summers, R.M., Rueckert, D.: Systematic evaluation of iterative deep neural networks for fast parallel MRI reconstruction with sensitivity-weighted coil combination 86(4), 1859–1872. https://doi.org/10.1002/mrm.28827

[2] Heckel, R., Jacob, M., Chaudhari, A., Perlman, O., Shimron, E.: Deep learning for accelerated and robust MRI reconstruction: a review. https://doi.org/10.48550/arXiv.2404.15692, http://arxiv.org/abs/2404.15692

[3] Putzky, P., Welling, M.: Recurrent inference machines for solving inverse problems. https://doi.org/10.48550/arXiv.1706.04008, http://arxiv.org/abs/1706.04008

[4] Billot, B., Magdamo, C., Cheng, Y., Arnold, S.E., Das, S., Iglesias, J.E.: Robust machine learning segmentation for largescale analysis of heterogeneous clinical brain MRI datasets 120(9), e2216399120. https://doi.org/10.1073/pnas.2216399120, https://www.pnas.org/doi/10.1073/pnas.2216399120, publisher: Proceedings of the National Academy of Sciences

[5] Yiasemis, G., Moriakov, N., Karkalousos, D., Caan, M., Teuwen, J.: DIRECT: Deep image REConstruction toolkit 7(73), 4278. https://doi.org/10.21105/joss.04278, https://joss.theoj.org/papers/10.21105/joss.04278

[6] Hammernik, K., Klatzer, T., Kobler, E., Recht, M.P., Sodickson, D.K., Pock, T., Knoll, F.: Learning a variational network for reconstruction of accelerated MRI data, http://arxiv.org/abs/1704.00447s

Image registration for real-time deep learning-based rigid motion correction at 7T

Yiling Hu[1], David A. Porter[1], Fani Deligianni[2]
[1]Imaging Centre of Excellence, University of Glasgow, UK
[2]School of Computing Science, University of Glasgow, UK

Introduction: Magnetic resonance imaging (MRI) is highly susceptible to motion effects, due to the nature of its data acquisition in frequency space; even slight or gradual motion during scanning can compromise the entire image's quality and affect its diagnostic usefulness. This especially impacts the efficacy of 7 Tesla (7T) MRI due to its enhanced image resolution compared to clinical-strength systems. Real-time (prospective) motion correction solutions provide the clinical appeal of reducing post-processing time; deep learning-based methods have the potential to offer even faster real-time imaging volume updates to further reduce scan times. This project seeks to develop a model which outputs rigid motion parameters and replaces the image registration step in MS-PACE, a prospective motion correction method for fMRI proposed by Hoinkiss et al. [1,2]. This abstract presents early work on reproducing the image registration method and model development.

Methods:
Equipment: Jupyter Notebook, Image Calculation Environment (ICE; Siemens proprietary environment for MRI image reconstruction), SimpleITK (simplified interface for Insight Toolkit (ITK)).
Dataset: Resting-state fMRI timeseries from the Autism Brain Imaging Data Exchange (ABIDE) open-source dataset [3].
The image registration method from MS-PACE, originally developed in ICE, was replicated in Python with SimpleITK. Rigid 3D transformations were applied to echo-planar imaging (EPI) volumes and registered to the original volume; the performance was assessed using Mattes Mutual Information, the inverse of which is minimized in the registration process.
We are currently exploring avenues for fine-tuning a foundation model such as *uniGradICON*, which performs deformable medical image registration, for feature extraction and rigid registration [4]. A training dataset was built from EPI volumes with simulated rigid motion of sub-pixel translations and sub-degree rotations.

Results: The image registration method using SimpleITK did not perform as well as the gold standard, with the mutual information metric not converging during optimization and the registration output yielding inconsistent results over different runs (Fig. 1 and 2). When applied to volumes within a resting-state fMRI timeseries, the variations in translation and rotation exceed the minimal noise that was expected.
Figure 3 shows first results from applying *uniGradICON* to the ABIDE dataset, which currently only performs deformable image registration.

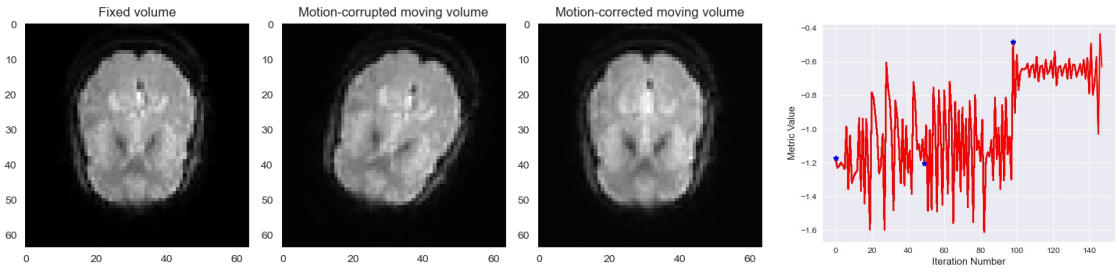

Fig. 1. Single volume registration after a 20°rotation. Although the registration method corrects accounts for the rotation, the resampled image also adds significant translation.

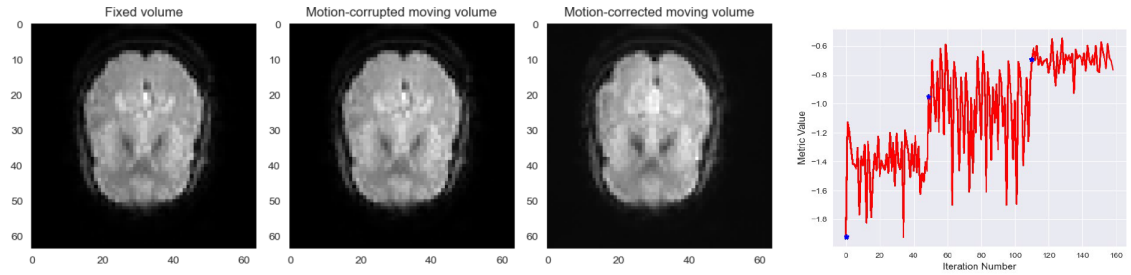

Fig. 2. Registration of consecutive volumes in a resting-state fMRI timeseries from ABIDE. It is difficult to assess the method's performance outside of the non-minimization and non-convergence of the MI metric.

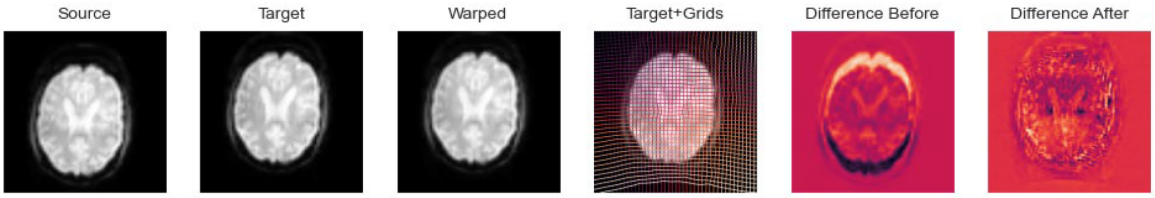

Fig. 3. Initial outputs from applying *uniGradICON* to an ABIDE EPI volume that was manually translated vertically. The difference after shows good registration performance compared to initial differences.

Discussion: The image registration method will be characterized further and improved by assessing it against the gold standard method with healthy volunteer data. Model training will begin immediately and we expect to obtain preliminary results that can be compared to the image registration method; from this we will also have a better understanding of the time benefits and further hardware requirements.

Conclusions: Real-time motion correction is an appealing direction in 7T MRI research, due to its high susceptibility to motion effects. Deep learning-based methods can offer even quicker solutions, and this project's early steps seek to tap into that potential.

Acknowledgements: This project is conducted as part of an iCASE PhD studentship funded by EPSRC and Siemens Healthineers Ltd UK.

References

[1] Hoinkiss et al., *Neuroimage*, 2009.
[2] Thesen et al., *Magn. Reson. Med.*, 2000.
[3] Di Martino et al., *Mol. Psychiatry*, 2014.
[4] Tian et al., *MICCAI*, 2024.

Temporal phase unwrapping of free-running 5D phase-contrast flow MRI by using cardiac phases reconstructed with high temporal resolution.

Jan Sedlacik[1,2], Alaine Berry[1,2], Massimo Marenzana[1,2], Jerome Yerly[3,4], Mariana BL Falcao[3], Matthias Stuber[3,4], Christopher W Roy[3], Declan P O'Regan[1,2], Ben Statton[1,2]

[1]Institute of Clinical Sciences, Imperial College, London, UK
[2]Medical Research Council, Laboratory of Medical Sciences, London, UK
[3]Department of Radiology, Lausanne University Hospital, Lausanne, Switzerland
[4]Center for Biomedical Imaging, Lausanne, Switzerland

Introduction: Low velocity-encoding (VENC) values are desired to better capture the low flow deep inside the ventricles and close to the ventricular wall. This improves, for example, the verification of computational fluid dynamics simulations which aim to better understand the hemodynamics of the heart, like the impact of trabeculae on blood flow [1]. Also, the assessment of the ventricular wall shear stress, which is a potential biomarker for ventricular remodelling [2], would benefit. Using a low VENC for the phase-contrast flow MRI measurement, causes the phase information to wrap around for faster flow velocities. An additional high VENC scan can be used to unwrap the low VENC data at the cost of additional scan time [3]. Unwrapping the low VENC data without additional high VENC data can be computationally costly [4] or fail for large wrapped regions filling almost the whole vessel [5].

The simple temporal phase unwrapping approach does not suffer from such limitations [6], but it is susceptible to noise causing false phase wraps. Also, the temporal unwrapping fails for too large jumps of the flow velocity between two consecutive cardiac phases causing phase wraps to be missed. We aim to minimise these limitations by increasing the temporal resolution of the cardiac phases, which lowers the jumps of the temporal phase, and by filtering the high temporal resolution data spatially in the complex domain, which reduces the noise due to the smaller bin size of the higher temporal resolution data. The unwrapped high temporal resolution data is then used as a primer to unwrap the phase flow data reconstructed with lower temporal resolution.

Methods: The free-running 5D flow MRI [7] was scanned with an VENC of 64cm/s and isotropic resolution of 2.5mm^2 in a healthy subject (male, 47yo). The scan was approved by the local ethics committee and the subject gave written informed consent. The image data was reconstructed with a regular (n=25) and high (n=75) number of cardiac bins resulting in bin widths of 45ms and 15ms, respectively. The real and imaginary part of the high temporal resolution data was spatially filtered using a 3x3x3 box kernel. Unwrapping was done by integrating the phase angle of the conjugate complex multiplication between two consecutive cardiac phases. Every third bin of the unwrapped high temporal resolution cardiac phase data matching the centre of the regular temporal resolution data bins was used as a primer to unwrap the latter by finding the minimum for each data point between the two data sets by adding different multiples of ±2Pi.

Results: The green crosshair in Figure 1 shows the selected voxel for exemplarily plotting the z-direction velocity encoded phase in the ascending aorta over the cardiac cycle (Fig.2). The phase wrap between the first two cardiac phases is missed when the 25 bin data was temporally unwrapped without any further information. Corresponding phase maps of the 4th cardiac phase are shown in Figs.3-5 for different unwrapping approaches.

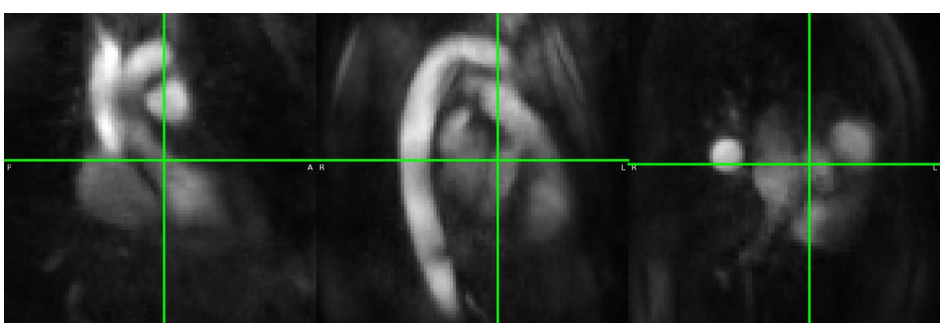

Fig. 1. Sum of flow encoded magnitude data over all flow encoding directions and cardiac phases.

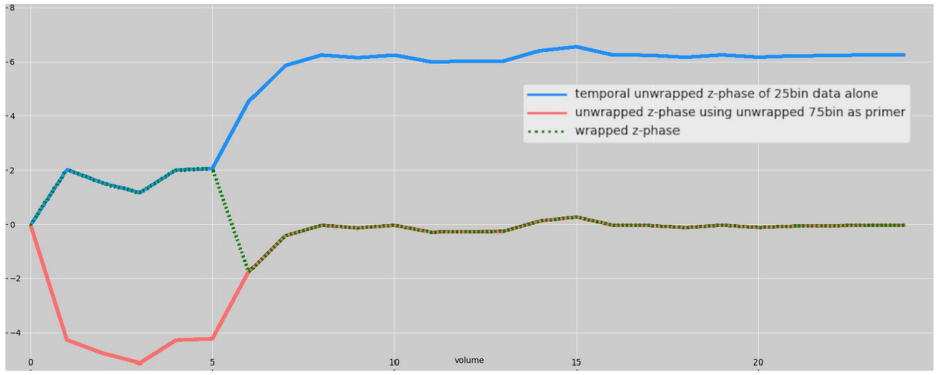

Fig.2: Time series of the regular temporal resolution phase data (25 bins) in the aorta close to the aortic valve (see crosshair in Fig.1).

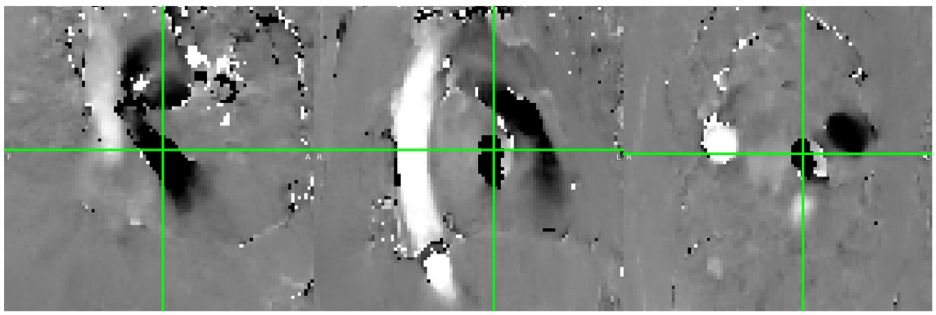

Fig.3: Unwrapped z-flow phase map of the 4th cardiac phase of the 25 binned data using the unwrapped high temporal cardiac phase data as primer. The unwrapping inside the ascending aorta is not perfect.

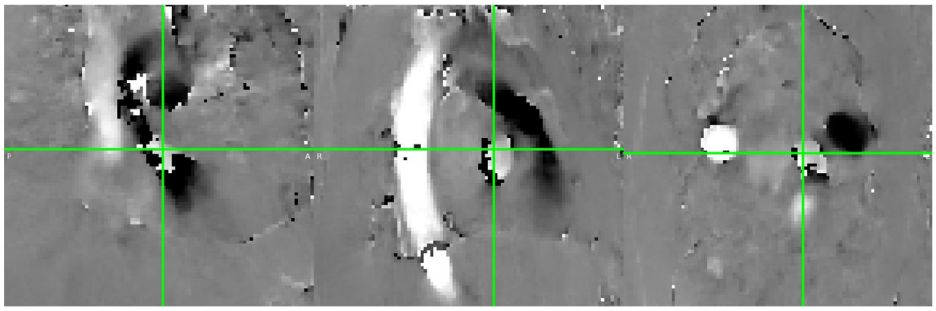

Fig.4: Same as Fig.3, but derived by temporally unwrapping the regular temporal cardiac phase data (25 bins) alone. There are more phase wraps compared to Fig.3.

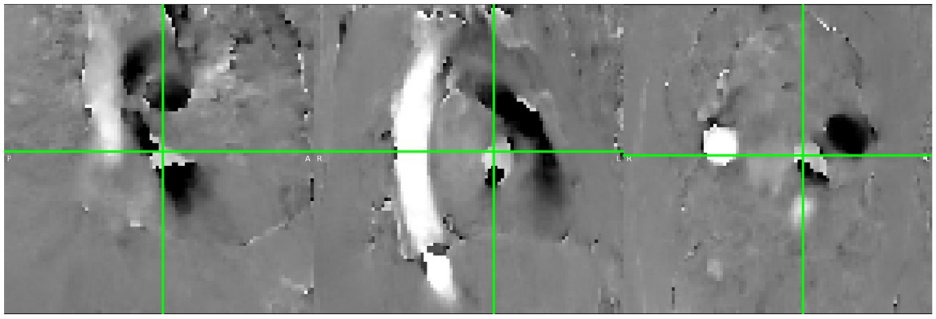

Fig.5: Same as Fig.3, but derived by 4D Laplacian unwrapping the regular temporal cardiac phase data (25 bins) alone. The phase wrap filling a large portion of the ascending aorta could not be resolved.

Discussion and Conclusions: Increasing the temporal resolution of the cardiac phases helps reducing the number of missed phase wraps using a simple temporal unwrapping approach. This performs even better than the 4D Laplacian unwrapping method of the regular temporal resolution data in the presented example. The high temporal resolution phase unwrapping approach will be further tested on more subjects and by scanning a dedicated pulsatile flow phantom with different VENC values [8]. Furthermore, other phase unwrapping methods will also be compared to the proposed method [9]. A combination of this approach with others may further improve the unwrapping performance.

References

[1] Sacco F, et al. *Front Physiol*. 2018 Apr 30;9:458. doi: 10.3389/fphys.2018.00458.
[2] Tsuda T. *J Cardiovasc Dev Dis*. 2021 Sep 29;8(10):122. doi: 10.3390/jcdd8100122.
[3] Bissell MM, et al. *J Cardiovasc Magn Reson*. 2023 Jul 20;25(1):40. doi: 10.1186/s12968-023-00942-z.
[4] Zhang J, et al. *IEEE Trans Med Imaging*. 2021 Dec;40(12):3389-3399. doi: 10.1109/TMI.2021.3086331.
[5] Loecher M, et al. *J Magn Reson Imaging*. 2016 Apr;43(4):833-42. doi: 10.1002/jmri.25045.
[6] Xiang QS. *J Magn Reson Imaging*. 1995 Sep-Oct;5(5):529-34. doi: 10.1002/jmri.1880050509.
[7] Ma LE, et al. *Radiol Cardiothorac Imaging*. 2020 Nov 12;2(6):e200219. doi: 10.1148/ryct.2020200219.
[8] https://www.elastrat.com/documents/fichiers/349_o8z3_t-s-a-007.pdf with pump Model 1423 PBP https://www.harvardapparatus.com/media/harvard/pdf/551838_Blood_Pump_Manual.pdf
[9] Pietro D, et al. *Proc. Intl. Soc. Mag. Reson. Med. 32* (2024), #4679. doi: 10.58530/2024/4679. (https://gitlab.ethz.ch/ibt-cmr-public/4dflow-unwrap/)

Comparative Performance of T_1, T_2 and Fat Fraction Mapping in Bone Marrow at 3 Tesla

Thierry M. Guihéneuf[1], Peter D. Gatehouse[1], Elizabeth M. Tunnicliffe[1], James T. Grist[1], Stefan Neubauer[1], Rupen Hargreaves[2], Adam J. Mead[2] & Damian J. Tyler[1]

[1]Oxford Centre for Clinical Magnetic Resonance Research (OCMR), Radcliffe Department of Medicine, University of Oxford, John Radcliffe Hospital, Oxford, OX3 9DU
[2]Molecular Haematology Unit, MRC Weatherall Institute of Molecular Medicine, University of Oxford, John Radcliffe Hospital, Oxford OX3 9DS

Introduction: Water T_1 and T_2 in bone marrow (BM) have shown sensitivity to pathophysiological changes induced by blood cancers such as myeloma[1] and myeloproliferative neoplasms[2]. However, despite advances in quantitative Magnetic Resonance Imaging (qMRI), the clinical assessment of BM lesions by MRI has largely relied on T_1-weighted imaging which can be prone to the background signal and heterogeneous distribution of fat in flat bones[1,3]. Quantitative T_1 mapping can overcome this limitation by accounting for fat in BM [4]. In this work, Dixon 3D-Spoiled Gradient (SPGR) MRI at Variable Flip Angle (VFA) together with Bloch-Siegert B_1^+ correction was used to separately map the T_1 of water (T_{1w}) and fat (T_{1f}) in BM at 3T. T_{1w} maps were acquired on 15 healthy adults and compared to water T_2 (T_{2w}) maps produced by fat-suppressed, multi-slice, Spin-Echo, Echo Planar Imaging (SE-EPI) together with Fat Fraction (FF) assessment by 3D Iterative Decomposition of Water and Fat with Echo Asymmetry and Least-squares estimation (IDEAL) MRI[5].

Methods: Participants: 15 healthy adults were recruited, aged 22 to 66 years (8 males, 7 females). Aside from repeatability tests conducted twice on 5 volunteers, the MRI protocol was run once on each participant. All MRI was performed on a 70cm bore, 3T GE Premier, whole-body MRI scanner using a 30-channel anterior and 60-channel posterior coil. T_1 mapping: 3D DIXON-SPGR at VFAs of 2/5/11/14/19° with a repetition time (TR) of 4.5ms. Field-Of-View (FOV): 42cm, matrix: 148x148x138, partition thickness (PTH)=2.8mm. Duration: 6min. 46s (fitting: Matlab) + B_1^+ mapping: multi-slice, gradient echo, Bloch-Siegert. Matrix: 64x64x69, slice thickness (STH)=5.6mm. Duration: 1min. 56s (B_1^+ map generated by Signa Works™, GE Healthcare). T_2 mapping: fat-suppressed, multi-slice, SE-EPI at variable echo times of 18/21/24/28/33/37/44ms with a TR of 6s and breath holds (avg=2). Matrix: 96x96x59, STH=4.4mm (fitting: Matlab). Total duration: 1min. 24s (nominal). FF mapping: IDEAL IQ, TE1/ΔTE: 0.9/0.7ms, TR=5.9ms (6 echoes, 2 shots). Matrix: 160x160x138, PTH=2.8mm (fitting: Signa Works™). Duration: 1min. 13s. Image analysis: Regions of Interest (ROI) as shown in Fig. 1.

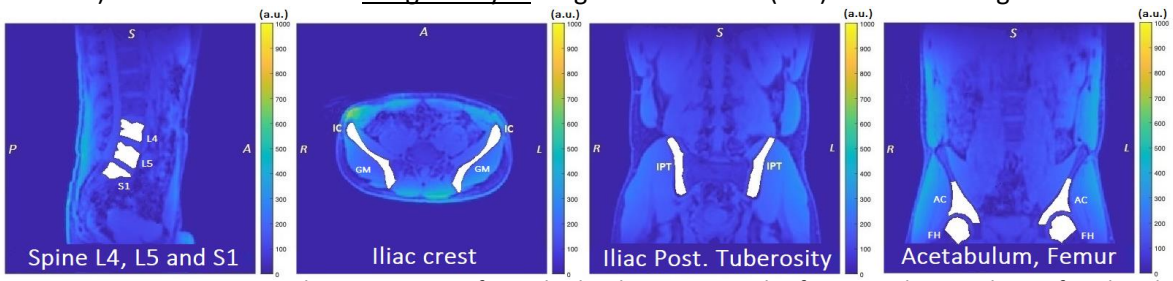

Fig. 1. Seven BM anatomical sites spanning from the lumbar spine to the femur with ROIs drawn free hand. Slices were selected from axial, sagittal and coronal orientations: Lumbar (L4, L5) and Sacrum (S1), Iliac Crest (IC) and Iliac Posterior Tuberosity (IPT), Acetabulum (AC), Femoral head (FH), Gluteal muscle (GM).

Results: The mean T_{1w} at BM anatomical sites was 1335±95ms (T_{1f}=308±17ms) for a mean T_{2w} of 26.8±3.5ms (Fig. 2). The Coefficient of Variation (CV) within ROIs reflected BM heterogeneity with a CV of 20% for T_{1w}, 14% for T_{2w} and 23% for FF, compared to Gluteal Muscle (GM, T_{1w}=1373±38ms and T_{2w}=29.9±1.2ms) with CVs of 9% and 8% and 6% respectively. FF increased from 37.5±14.3% in lumbar L4 to 85.7±7.6% in the femoral head over the cohort. Duplicate repeatability tests yielded a mean CV of 4.9% for T_{1w}, 1.2% for T_{2w} and 1.9% for FF over BM anatomical sites. A strong correlation (r^2=0.89) was observed between the mean T_{1w} and T_{2w} over BM anatomical sites (Fig. 3) whereas it was negligible in GM (r^2<0.09) and between the average fat T_{1f} and the mean T_{1w} in BM (r^2=0.03).

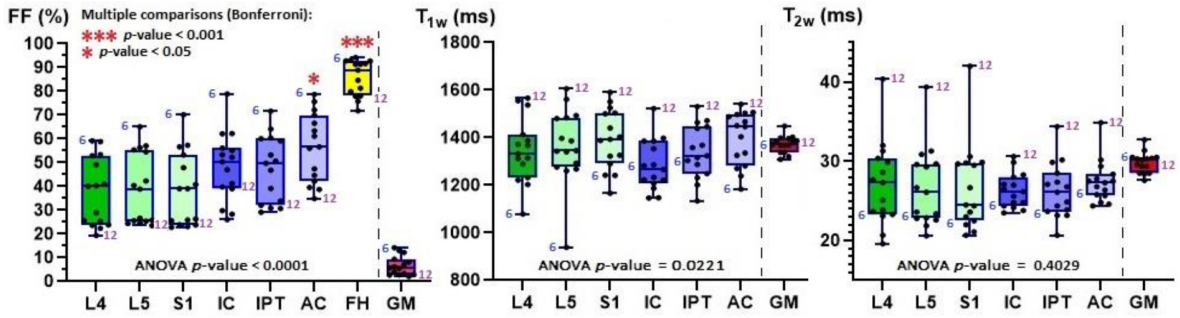

Fig. 2. Distribution of FF, T_{1w}, and T_{2w} across BM anatomical sites with each dot corresponding to each of the 15 healthy adults. FF increased gradually from the lumbar vertebrae to the femoral head with large inter-individual variability across the cohort. The mean FF correlated with age (r^2=0.70) and with body fat (assessed as FF in GM, r^2=0.67). A one-way Analysis of Variance (ANOVA) produced *p*-values between BM anatomical sites of <0.0001, 0.0221, and 0.4029 for FF, T_{1w} and T_{2w} respectively (p=0.05 at 95% confidence), and *p*-values less than 0.0001 between healthy adults (HV). HV N°6 (65-yo, male) exhibited high FF, low T_{1w} and low T_{2w} (65.0%/939ms/22ms, L5), whereas HV N°12 (22-yo, female) produced low FF, high T_{1w} and very high T_{2w} (24.5%/1605ms/39ms, L5).

Discussion: Even though heterogeneities in FF, T_{1w} and T_{2w} were about twice as high in BM than in GM, the repeatability between duplicate scans produced an adequate CV of less than 5%. FF, T_{1w} and T_{2w} produced significantly different results between participants. Differences in FF appeared to correlate with age and body fat. FF and T_{1w} results were also significantly different between BM anatomical sites. The large spread in T_{2w} values between healthy adults may be reduced by separating the cohort by sex, as differences in T_{2w} have been previously reported in BM between males and females[6]; the effect of BM anatomical site, age and body habitus should be investigated in more detail.

Additionally, the T_{1w} averaged over the BM anatomical sites revealed a strong correlation with mean T_{2w} (Fig. 3). It is possible that BM iron content varies significantly among healthy adults and exerts an effect, in which case the paramagnetic relaxivity of iron would affect both T_{1w} and T_{2w}.

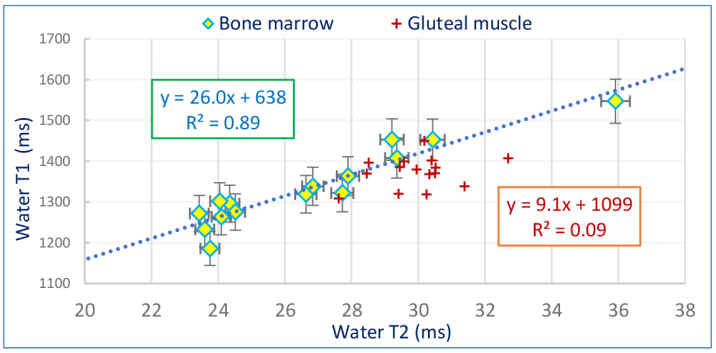

Fig. 3. Average over the BM anatomical sites of the mean T_{1w} of each ROI against the corresponding T_{2w} for each adult. Note the strong correlation in BM (r^2=0.89) compared to the mean T_{1w} (1373±7.5ms) vs. T_{2w} (29.9±1.2ms) in GM (r^2=0.09) for each adult.

Accounting for such confounding factors would have the benefit of narrowing the expected T_{1w}, T_{2w} and FF range in healthy adults and, through multivariate analysis, help diagnose abnormalities in BM resulting from haematopoietic disorders.

Conclusions: This evaluation demonstrates the adequate performance of T_1 mapping in BM by VFA 3D Dixon-SPGR and T_{2w} mapping by fat-suppressed, SE-EPI to complement FF assessment by IDEAL. The heterogeneity and extent of values between healthy adults remains a challenge for the use of qMRI in the diagnosis of BM disorders but the simultaneous acquisition of multiple quantitative parameters may offer diagnostic clarity.

Acknowledgements: This research is funded by a grant from the National Institute for Health and care Research (NIHR)/Oxford Biomedical Research Centre (BRC). Thanks to Dr Mark R. Symms for his help on the GE Premier.

References

[1] J.C. Dutoit JC, K.L. Verstraete *Insights Imaging*, 7(4):553-569 (2016). [2] Ö. Alpdogan *et al. Blood*, 92: 2995-2997 (1998). [3] S. Slot *et al. Cancer Imaging*, 21(1):36 (2021). [4] Y. Wang *et al. Quant Imaging Med Surg.* 13(2):912-923 (2023). [5] S.B. Reeder *et al. J Magn Reson Imaging.* 25(3):644-652 (2007). [6] M. Dieckmeyer *et al. NMR Biomed.* 28(4):432-439 (2015).

Off-Resonance Correction for Hyperpolarized Xenon-129 Imaging with Integrated B_0 Mapping and Pinv-Recon

Kylie Yeung[1,2], Fergus V Gleeson[2], Rolf F Schulte[3], Anthony McIntyre[2], Damian J Tyler[1], Florian Wiesinger[3], and James T Grist[1,2]

[1]Oxford Center for Clinical Magnetic Resonance Research (OCMR), University of Oxford, Oxford, UK
[2]Department of Radiology, Oxford University Hospitals NHS Trust , Oxford, UK
[3]GE HealthCare, Munich, Germany

Introduction: Hyperpolarized Xenon-129 is a gaseous MRI contrast agent that enables regional assessment of lung function[1]. Using spin-exchange optical pumping, its magnetic signal is temporarily enhanced above thermal equilibrium, enabling images to be acquired during a breath-hold before signal decay. This technique has shown utility in assessing conditions like long COVID[2], COPD[3] and asthma[4].

One of the challenges of lung imaging is the large B_0 inhomogeneity at the air-tissue interfaces, which results in image artifacts and blurring[5]. In this work, we present a straightforward approach to integrate a B_0 map acquisition in the same breath-hold as a hyperpolarized Xenon-129 ventilation scan, and a simple reconstruction approach with Pinv-Recon[6], [7], [8].

Methods: In the same breath-hold, a high-resolution ventilation image and an integrated B_0 map (low-resolution varied echo time (TE) acquisition) were acquired. 6 hyperpolarized Xenon-129 datasets were acquired on a 3T GE Premier scanner (GE HealthCare, Milwaukee, USA) and a flexible Tx/Rx Xenon-129 vest coil (PulseTeq, Cobham, UK). Xenon gas was polarized for approximately 30 minutes using a commercial polarizer (Polarean, NC, USA). Both sequences were stack-of-spirals, with parameters for the ventilation sequence: 12 arms, FOV 400 x 400 x 250 mm, matrix 80 x 80 x 51, FA = 4° per excitation, TR/volume ~ 10 s; and the varied TE sequence: 1 arm, FOV 400 x 400 x 250 mm, matrix 20 x 20 x 13, FA = 2° per excitation, TE = [0, 3, 5, 15] ms, TR/volume ~ 0.4s.

The low-resolution varied TE image was reconstructed with Pinv-Recon and the B_0 map was fitted using the MEDI toolbox[9]. The B_0 map was then masked, the signal outside of the mask was filled and the map was smoothed and interpolated to the reconstruction matrix size of the high-resolution dataset. To apply Pinv-Recon with B_0 correction to the high-resolution dataset, the encoding matrix was calculated using the known spiral trajectory ($\boldsymbol{k}$) and the known B_0 map (ΔB_0) as follows:

$$Encode = e^{-i\,2\pi\,\boldsymbol{k}\,\boldsymbol{r}} \cdot e^{-i\,\Delta B_0(r)\,t(k)}$$

where i is the imaginary unit, $\boldsymbol{r}$ is a vector of image space coordinates, and t is a time vector of the acquisition of each k-space point, and $\cdot$ indicates element-wise multiplication. The reconstruction matrix (i.e. the Moore-Penrose Pseudoinverse of *Encode*) was calculated using Cholesky decomposition with Tikhonov regularization, and multiplied with the raw data with depolarization accounted for [10]. To compare the images before and after B_0 correction, image sharpness was quantified using a gradient-based approach (*imgradient3* in MATLAB with the Sobel function).

Results: Figure 1a-b shows fitting the B_0 map from low-resolution varied TE images. Figure 1c-h shows an example of a ventilation image before and after B_0 correction, as well as the difference image between the two. Table 1 summarizes the sharpness of the 6 datasets before and after B_0 correction, with an average 0.56% increase in sharpness.

Discussion and Conclusion: B_0 off-resonance needs to be measured on a patient-by-patient basis, but it is challenging to map at the ^{1}H frequency due to the low proton density in the lungs. The presented method enables straightforward measurement and correction of B_0 off-resonance, showing improved sharpness for the present dataset. More noticeable improvement is expected in datasets with longer readout and more severe B_0 distortion. Pinv-Recon, unlike conventional approaches such as multifrequency interpolation[11], corrects the B_0 distortion as a continuous function, rather than

demodulating to discrete frequencies, offering a more direct and potentially more accurate correction of B_0 distortion. Further work will involve characterizing the impact of B_0 correction on quantitative metrics such as ventilation defect percentage calculation.

References

[1] L. Ebner *et al.*, *Eur. J. Radiol.*, vol. 86, pp. 343–352, Jan. 2017 doi:10.1016/j.ejrad.2016.09.015
[2] J. T. Grist *et al.*, *Radiology*, vol. 305, no. 3, pp. 709–717, May 2022 doi:10.1148/radiol.220069
[3] L. Myc *et al.*, *Thorax*, vol. 76, no. 2, pp. 178–181, Feb. 2021 doi:10.1136/thoraxjnl-2020-214924
[4] G. T. Mussell *et al.*, *ERJ Open Res.*, vol. 7, no. 3, pp. 00785–02020, Jul. 2021 doi:10.1183/23120541.00785-2020
[5] M. W. Haskell *et al.*, *NMR Biomed.*, vol. 36, no. 5, p. e4867, 2023 doi:10.1002/nbm.4867
[6] K. Yeung *et al.*, May 27, 2025, *arXiv*: arXiv:2410.06129.
[7] K. Yeung *et al.*, Abstract 2604 in *Proc. Annu. Meeting ISMRM 2025*, Hawaii, US, May 2025.
[8] K. Yeung *et al.*, Abstract 4487 in *Proc. Annu. Meeting ISMRM 2025*, Hawaii, US, May 2025.
[9] B. Kressler *et al.*, *IEEE Trans. Med. Imaging*, vol. 29, no. 2, pp. 273–281, Feb. 2010 doi:10.1109/TMI.2009.2023787
[10] J. W. Plummer *et al.*, *Magn. Reson. Med.*, vol. 92, no. 4, pp. 1363–1375, 2024 doi:10.1002/mrm.30188
[11] L.-C. Man *et al.*, *Magn. Reson. Med.*, vol. 37, no. 5, pp. 785–792, 1997 doi:10.1002/mrm.1910370523

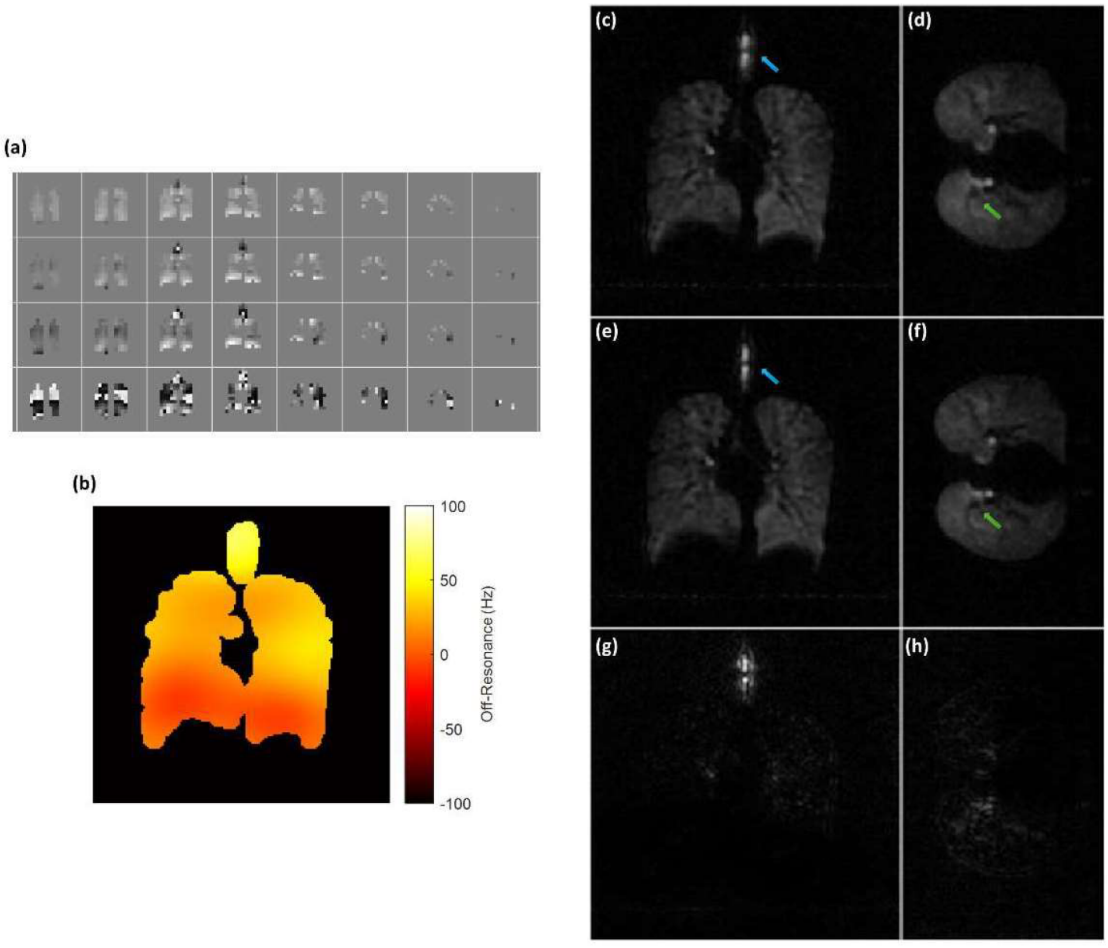

Figure 1 (a) Low-resolution, varied echo time acquisitions for B_0 map fitting (b) fitted B_0 map (c, d) coronal and axial views of ventilation image before B_0 correction, (e, f) coronal and axial views of ventilation image before B_0 correction (g, h) difference between and after correction.

Image	Dataset 1	Dataset 2	Dataset 3	Dataset 4	Dataset 5	Dataset 6
Sharpness (uncorrected)	18911	15782	11632	14360	15285	18432
Sharpness (B_0 corrected)	19022	15832	11707	14395	15431	18545
% increase	0.59	0.32	0.64	0.24	0.96	0.61

Table 1 Image sharpness before and after B_0 correction.

Optimization of [2-^{13}C]Pyruvate Hyperpolarization Via the Addition of Gadolinium

Zhuang Liu[1], Damian J Tyler[1], Ladislav Valkovič[1], James T Grist[1]
[1] Oxford Centre for Clinical Magnetic Resonance Research, Division of Cardiovascular Medicine, Radcliffe Department of Medicine, University of Oxford

Introduction: Hyperpolarized [2-^{13}C]pyruvate has recently been shown to be a feasible method for clinically assessing tricarboxylic acid (TCA) cycle intermediates and acetylcarnitine targeting different organs[1], [2], [3]. However, the achievable polarization for [2-^{13}C]pyruvate is lower than that of [1-^{13}C]pyruvate[4] and so methods to increase the level of enhancement are desired. Previously, Gadolinium(Gd)-based contrast agents have been used as an enhancer for [1-^{13}C]pyruvate polarization to significantly increase polarization and signal-to-noise ratio (SNR) achieved during dissolution dynamic nuclear polarization (dDNP) for real-time metabolic imaging[5]. The potential gains from the addition of Gd to [2-^{13}C]pyruvate preparations remain unstudied and so this work aims to optimize the polarization of [2-^{13}C]pyruvate through the addition of Gd.

Methods: A HyperSense hyperpolarizer (3.35T, 1.4K) (Oxford Instruments, UK) was used to polarize samples. AH111501 was used as the electron paramagnetic agent (EPA), and Dotarem (Guerbet, France) was used as the gadolinium-based contrast agent for the experiments. 15 mM EPA was used in previous [1-^{13}C]pyruvate studies and was found also to be the optimum for [2-^{13}C]pyruvate, and the Gd concentration was varied at 0, 0.5, 1, 2, and 3mM. Samples with each concentration underwent a microwave frequency sweep to determine the optimal frequency for build-up. A 5 MHz step size and 60-second step duration were used, and the optimal frequency was taken as the first peak observed during the sweep. Then, samples were polarized at their optimal frequency until they had reached 95% of their maximum polarization. The amplitude and build-up time constant were recorded. A Bruker BioSpin 11.7T vertical bore MRI system (AVANCE 500) was used to assess the liquid state polarization following dissolution. 8 mL of buffer made of 40 mM Tris Base, 250 µM of K_2EDTA, and 60 mM of NaOH was used for dissolution. 120 seconds of 1-degree excitations (TR=1s) were used to assess the polarization decay, followed by 10-, 20-, 30-, 10-, 20-, 30-, 40-, 50-, and 60-degree flips to assess B_1.

Results: [1-^{13}C]pyruvate and [2-^{13}C]pyruvate had an optimal Gd concentration of 2 mM and solid-state enhancement factors of around 1.5 (Figure 1). The dDNP polarization percentages of the baseline and optimal preparations were $17.7 \pm 3.1\%$ and $22.2 \pm 4.1\%$ (p=0.04) respectively for [1-^{13}C]pyruvate and $13.5 \pm 4.3\%$ and $26.3 \pm 8.1\%$ (p=0.02) for [2-^{13}C]pyruvate (Figure 2). [1-^{13}C]pyruvate had a $T_1 = 38.5 \pm 1.5s$ for baseline and a $T_1 = 32.3 \pm 3.8s$ (p=0.003) for the Gd optimized sample. [2-^{13}C]pyruvate had a $T_1 = 32.1 \pm 1.5s$ for the baseline and a $T_1 = 28.2 \pm 1.2s$ (p<0.001) for the Gd optimized sample at 11.7T.

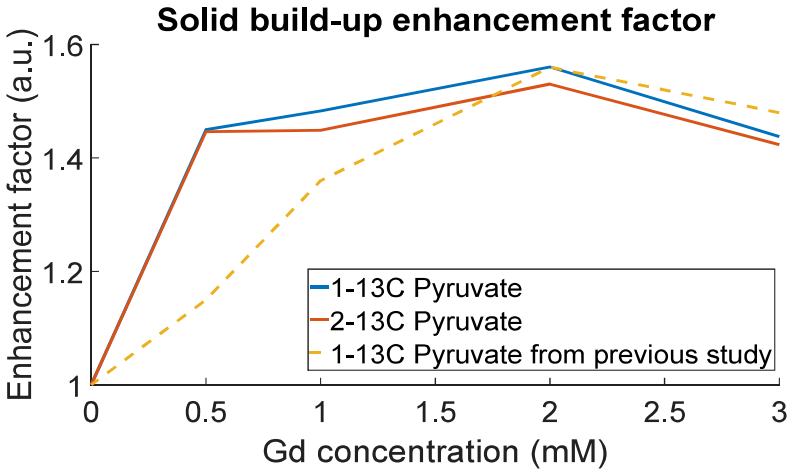

Fig.1. Solid build-up enhancement factor of [1-^{13}C] and [2-^{13}C] pyruvate comparing with the [1-^{13}C] pyruvate data from the previous study

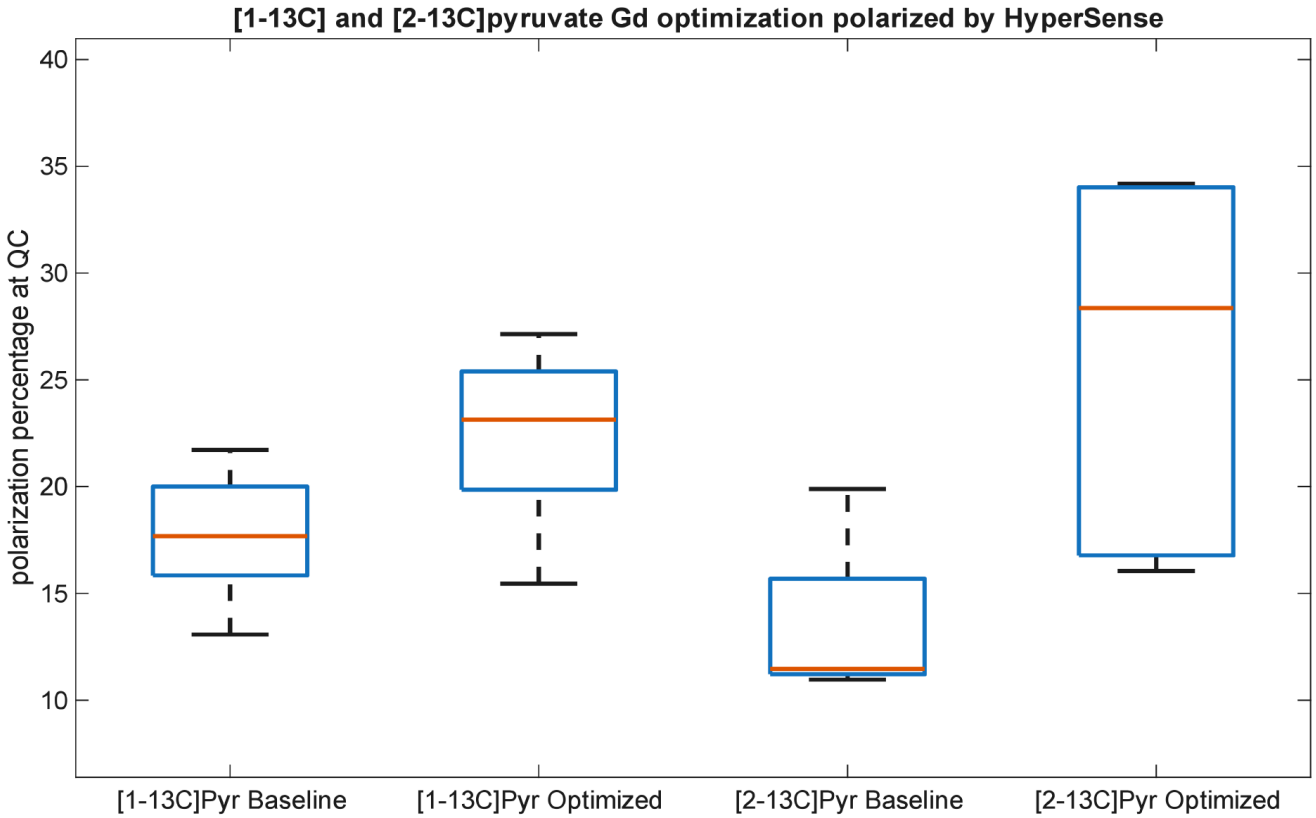

Fig. 2. [1-^{13}C] and [2-^{13}C]pyruvate Gd optimization by HyperSense box plots

Discussion: [1-^{13}C] and [2-^{13}C]pyruvate had a similar solid-state enhancement factor when doped with 2mM Gd. However, their liquid state enhancement factor varied. Given the fact that the polarized samples are vulnerable to the complex nature of the magnetic field within the lab where the 3.35T polarizer and the 11.7T MRI system are placed side by side, it is understandable that, despite the consistent solid-state results, the liquid-state results are more variable. Increasing the number of experiments would likely solve this issue; however, since this is a pilot project running on an outdated system, the results are satisfactory and clearly indicate the possible enhancement of [2-^{13}C]pyruvate through the addition of Gd. As expected, the T_1 values of [2-^{13}C]pyruvate were shorter than [1-^{13}C]pyruvate in baseline and Gd optimized samples. The decreasing trend of T_1 after the addition of Gd aligns well with previous work[5]. It also validates the dissolution experiment protocol to some extent – despite inconsistent liquid state polarization, the T_1 values were consistent and expected. Future experiments are planned to be performed on a higher field strength polarizer - SpinAligner (6.7T, 1.4K) (Polarize, Denmark), and a clinical polarizer, GE SpinLab (5T, 0.8K) (GE Healthcare, USA).

Conclusions: The addition of Gd to [2-^{13}C]pyruvate had a similar behaviour to [1-^{13}C]pyruvate in the solid and liquid states, in terms of the enhancement factors and optimal Gd concentration. Future work will assess Gd optimization on state-of-the-art higher-field-strength platforms.

References:

[1] T. B. Chung *et al.*, 'First hyperpolarized [2-13C]pyruvate MR studies of human brain metabolism', *J. Magn. Reson.*, vol. 309, p. 106617, 2019, doi: 10.1016/j.jmr.2019.106617.

[2] H. Chen *et al.*, 'Probing human heart TCA cycle metabolism and response to glucose load using hyperpolarized [2-13C]pyruvate MRS', *NMR Biomed.*, vol. 37, no. 3, Mar. 2024, doi: 10.1002/nbm.5074.

[3] S. K. Bech *et al.*, 'Myocardial metabolic flexibility following ketone infusion demonstrated by hyperpolarized [2-13C]pyruvate MRS in pigs', *Sci. Rep.*, vol. 15, no. 1, p. 5849, Feb. 2025, doi: 10.1038/s41598-025-90215-9.

[4] J. M. Park *et al.*, 'Measuring mitochondrial metabolism in rat brain in vivo using MR Spectroscopy of hyperpolarized [2-13C]pyruvate', *NMR Biomed.*, vol. 26, no. 10, pp. 1197–1203, 2013, doi: 10.1002/nbm.2935.

[5] L. Friesen-Waldner, A. Chen, W. Mander, J. T. Scholl, and A. C. Mckenzie, 'Optimisation of dynamic nuclear polarisation of [1-13C] pyruvate by addition of gadolinium-based contrast agents', *J. Magn. Reson.*, vol. 223, pp. 85–89, 2012, doi: 10.1016/j.jmr.2012.07.010.

Comparison of segmentation-based and ROI-based quantification of pancreatic PDFF

Yuchen Ma[1], George Ralli[1], Eve S. Shalom[1], Paul Aljabar[1], Edward Jackson[1], Michael Brady[1]
[1] Perspectum Ltd, Oxford, United Kingdom

Introduction: Studies have shown that pancreatic fat is both elevated in, and a risk factor for, type 2 diabetes [1]. Consequently, there is an increasing interest in accurately quantifying pancreatic fat. Three distinct types of pancreatic fat are recognized: intra-pancreatic fat (within the pancreatic tissue), inter-pancreatic fat (between lobules), and peri-pancreatic fat (surrounding the pancreas) [2].

Proton density fat fraction (PDFF) measured from chemical shifted-encoded MRI sequences are gaining in popularity due to their ability to non-invasively quantify fat in abdominal organs, including the pancreas [3]. Many studies use manually placed ROIs to quantify pancreatic fat in PDFF maps. In many ROI-based protocols, operators tend to place ROIs in more uniform regions of the pancreas with a lower signal as they appear on the PDFF maps and are therefore more tuned to measure intra-pancreatic fat [4]. More recently, methods using automated-segmentation masks have been proposed. As such methods cover the entire pancreas, they may capture multiple fat compartments, meaning that PDFF values measured from these two methods may not be directly comparable. Here, we investigate the differences in pancreatic PDFF measures obtained from ROI and segmentation-based approaches and propose a method to improve alignment between both approaches when quantification of intra-pancreatic fat is of particular interest.

Methods: 59 subjects with type 2 diabetes were scanned on a Siemens Prisma 3T scanner. Five PDFF slices were obtained using 2D multi-echo gradient echo acquisitions (12 echoes, TE/ΔTE/TR: 1.1,1.1,15ms, slice thickness 10mm) and processed with both an ROI-based and segmentation-based approach. In the ROI-based approach [4], a single rater placed three ROIs in the centre of the pancreatic head, body, and tail, avoiding regions of visceral fat. In the mask-based method, a pancreatic segmentation mask automatically generated from the water image of a 3D T1-weighted Dixon SPGR scan, using a previously described model [5] was re-sampled onto the five PDFF slices, using positional information from the DICOM headers. The slice with the largest pancreatic area was selected and the mask was further pruned by removing pixels with PDFF values >70% and a binary closing operation (using a circular structuring element with a radius of 1 pixel). Figure 1 (d) shows an example case processed with the ROI- and mask-based methods.

To compare the mask-based and ROI-based measurements, different percentiles of PDFF were extracted from the segmentation mask and compared with the ROI-based measurement using a Bland-Altman analysis and the intra-class correlation coefficient (ICC). To obtain the percentile minimising the bias, a training set of 39 cases was used. The remaining 20 cases were used as a validation set and processed with the ROI-based protocol by a second operator to measure inter-rater variability.

Results: Median segmentation mask PDFF was systematically higher than the ROI-based estimates with a bias [lower, upper limits of agreement (LoA)] of 8.50 [-4.09, 21.10], 7.07 [-4.14, 18.28] percentage points in the training and test cohorts, respectively. In the training cohort, the 25^{th} percentile was found to minimise both the bias and LoA. Within the testing cohort (see Figure 1), the bias [upper, lower LoA] between the PDFF mask 25^{th} percentile and ROI-based PDFF was 1.29 [-4.37, 6.95] percentage points. In the test dataset, ICC for the median and 25^{th} percentile PDFF vs the ROI-based PDFF was 0.60 and 0.91, respectively, and the ICC for the inter-rater ROI-based PDFF was 0.92.

Discussion: The median segmentation mask PDFF is systematically higher than manual ROI-based values. This is likely because the ROI-based measurements tend to capture intra-pancreatic fat, while

segmentation-based masks also encompass inter-lobular and peri-pancreatic fat. Taking the 25th percentile of PDFF from the masks provides closer alignment with the ROI-based approach, giving an ICC comparable to that of the inter-rater ROI-based analysis, and may therefore be preferable in studies which are focused on intrapancreatic fat specifically. We also observed that discrepancies between the ROI and mask-based measurements increased at higher PDFF values, as did the inter-rater variability. This likely results from the reduced visibility, and increased heterogeneity, of the pancreas in PDFF maps in high-fat cases, making ROI placement more challenging. In such cases, a mask-based approach obtained from segmentations of a different acquisition (e.g. the water DIXON images used here) may be more robust.

Conclusion: Measuring median pancreatic PDFF with a segmentation mask produces higher values than ROI-based approaches, most likely due to the latter capturing only the intra-pancreatic fat while the former also includes the inter-lobular and peri-pancreatic fat compartments. Using the 25th percentile from a mask-based approach may be preferable in studies focused specifically on intra-pancreatic fat.

References:

[1] Inaishi, Jun, and Yoshifumi Saisho. "Beta-cell mass in obesity and type 2 diabetes, and its relation to pancreas fat: a mini-review." Nutrients 12.12 (2020): 3846.
[2] Sakai, Naomi S., Stuart A. Taylor, and Manil D. Chouhan. "Obesity, metabolic disease and the pancreas—Quantitative imaging of pancreatic fat." The British journal of radiology 91.1089 (2018): 20180267.
[3] Yoshizawa, Eriko, and Akira Yamada. "MRI-derived proton density fat fraction." Journal of Medical Ultrasonics 48.4 (2021): 497-506.
[4] Al-Mrabeh, Ahmad, et al. "Quantification of intrapancreatic fat in type 2 diabetes by MRI." PloS one 12.4 (2017): e0174660.
[5] Triay Bagur, Alexandre, et al. "Standardized pancreatic MRI-T1 measurement methods: comparison between manual measurement and a semi-automated pipeline with automatic quality control." British Journal of Radiology 98.1170 (2025): 965-973.

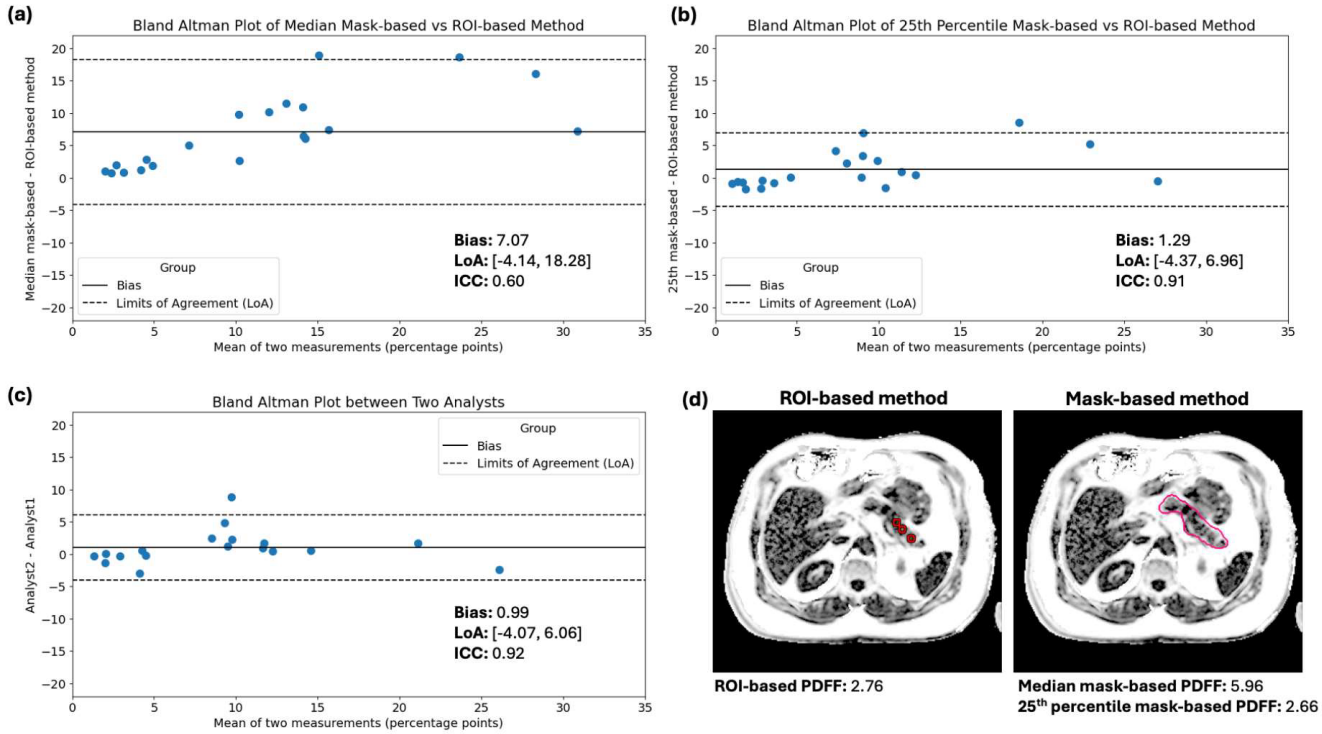

Figure 1: Bland-Altman plots comparing (a) median mask-based vs ROI-based PDFF (b) 25th percentile mask-based vs ROI-based PDFF (c) ROI-based PDFF from two different analysts, in the 20 test cases. (d) An example case showing ROI-based and mask-based method.

Variability in 13C MRS measurement of Liver Glycogen in Children.

Abi Spicer[1], Penny Gowland[1], Susan T Francis[1], Elizabeth J Simpson[2,3], Ian A Macdonald[2], Stephen J Bawden[1,3]

[1]Sir Peter Mansfield Imaging Centre, University of Nottingham, Nottingham, United Kingdom
[2]David Greenfield Human Physiology Unit, MRC/ARUK Centre for Musculoskeletal Ageing Research, University of Nottingham School of Life Sciences, Queen's Medical Centre, Nottingham, United Kingdom
[3]National Institute for Health Research Biomedical Research Centre, Queen's Medical Centre, Nottingham, United Kingdom

Introduction: Liver glycogen concentration (LGly) can indicate altered metabolism in children, and ^{13}C MRS is a non-invasive alternative to biopsy for measuring LGly (1). Currently reproducibility measures have only been performed in adults (2,3). This study aimed to assess inter- and intra- reproducibility for participants and raters of ^{13}C MRS LGly measures made in pre-pubescent children and to assess agreement between manual and automated analysis.

Methods: 24 healthy children aged 8-12yrs (13F,11M) were recruited as part of a larger study (2), each attended 2 visits (V1 and V2), with 2 session per visit, separated by ≥5days. Each visit comprised of 2 sessions, Figure 1.

Figure 1 – Study timeline

Acquisition: ^{13}C-MR spectra were collected using a 15cm single-loop ^{13}C surface coil (PulseTech) on a Philips 3T Achieva. A ^{13}C-labeled urea sample was used to confirm positioning and as a reference signal. Spectra were obtained using an unlocalized pulse-acquire sequence with narrow bandwidth pencil beam shimming. The urea signal was measured with TR=1500ms, FA=25°, bandwidth = 7kHz, sample points 1024, NSA =20. LGly were measured with TR=280ms, FA=95°, bandwidth =7kHz, sample points 1024, NSA = 3072. All spectra were analysed using in-house MATLAB (MathWorks, 2023b) scripts by two raters (Rater1 – newly trained and Rater2 – experienced and provided training) and by an automated analysis pipeline. For all analyses, LGly was estimated by comparison of the area under the glycogen doublets (scaled to the urea peak) to a 200mmol/Liver glycogen phantom.

Variability: Each rater performed glycogen fitting 3 times per spectra to assess intra-rater variability, all other variability measures used the average of repeats; automated analysis was performed once. This study assessed variability using Coefficient Of Variation (COV) and Intraclass Correlation Coefficient (ICC, IBM SPSS) values.

Results: LGly values ranged from 257-742 mM, 251-675 mM, and 263-705 mM at T-PM and 184-538 mM, 186-508 mM, and 180-509 mM at T-AM for Rater1 and Rater2 and automated analysis respectively (Figure 3). Variability measures are shown in Figure 4, Inter-rater ICC = 0.96.

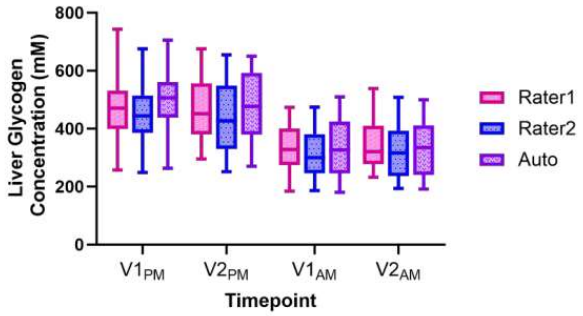

Figure 3 - Average hepatic glycogen concentrations from both raters (Rater1 was newly trained by Rater2) and automatic analysis for all visits and time points. Whiskers show the full range of data, the box expands from the 25th to 27th percentile, and the central line represents the median value.

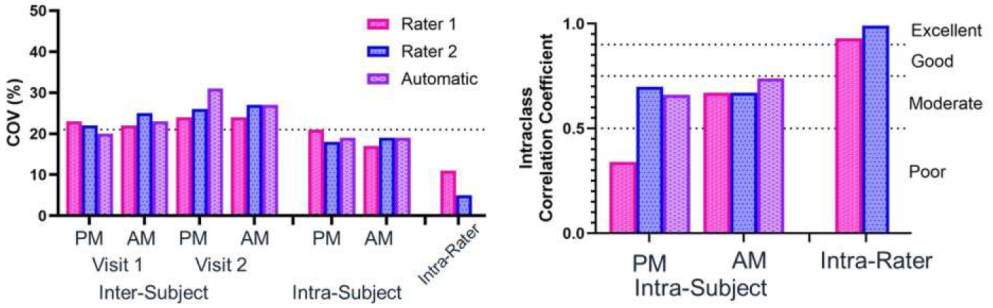

Figure 4 - Variability in measures, pink is used for rater 1, blue for rater 2 and purple for automatic analysis. Left – COV for inter-subject, intra-subject and intra-rater variability for Visit 1 and 2 for evening (PM) and morning (AM) scan sessions. Right- ICC values for intra-subject variability for evening (PM) sessions compared to morning (AM) and intra-rater variability across all visits and timepoints.

Discussion: Fasted and fed LGly in this study were larger than previously measured in children (3,4). Intra-subject ICC values showed moderate agreement (Rater1 T-PM showed poor agreement), and variability was similar (21 ±2 %) for T-PM and T-AM across all raters. The similar COV for T-PM and T-AM suggests that providing a tailored meal is adequate for ensuring reproducibility where an overnight fast is not possible. Intra-subject reproducibility was better than that seen in adults for fasted measures and worse after the tailored meal, (here ~ 19%, adults = 35% (5)), perhaps indicating greater variation in children's postprandial gastric emptying and metabolic rates. Inter-subject reproducibility was similar across all sessions and raters (23 ±3 %) and was equal to or slightly larger than intra-subject variations, as expected.

Intra-rater ICC values showed excellent agreement for both raters, demonstrating the robustness of the analysis method. However, the increased expertise of Rater2 is shown by their COV which was half that of Rater1 (5% and 11%, respectively). Across all analysis methods, the inter-rater ICC value suggests excellent agreement (0.96).

Conclusions: LGly were higher than previously measured in literature for children (3,4), though the paucity of literature makes it difficult to draw any conclusions. Overall, LGly in children were found to be reproducible across visits and raters. Effects of differences between raters were minimal compared to intra-subject and inter-subject variations and can be mitigated using automated analysis, which showed consistent agreement with both raters.

Acknowledgements: The authors want to thank Nestle for funding this work and the MRC IMPACT DTP for funding AS studies.

References

1. Taylor R, Price TB, Rothman DL, Shulman RG, Shulman GI. Validation of 13C NMR measurement of human skeletal muscle glycogen by direct biochemical assay of needle biopsy samples. Magn Reson Med [Internet]. 1992 [cited 2022 Jul 25];27(1):13–20. Available from: https://pubmed.ncbi.nlm.nih.gov/1435198/
2. Horstman AM, Bawden SJ, Spicer A, Darwish N, Goyer A, Egli L, et al. Liver glycogen stores via 13C magnetic resonance spectroscopy in healthy children: randomized, controlled study. Am J Clin Nutr. 2023 Apr 1;117(4):709–16.
3. Matyka K, Dixon RM, Mohn A, Rajagopalan B, Shmueli E, Styles P, et al. Daytime liver glycogen accumulation, measured by 13C magnetic resonance spectroscopy, in young children with Type 1 diabetes mellitus. Diabetic Medicine. 2001;18(8):659–62.
4. Flück CE, Slotboom J, Nuoffer JM, Kreis R, Boesch C, Mullis PE. Normal hepatic glycogen storage after fasting and feeding in children and adolescents with type 1 diabetes. Pediatr Diabetes [Internet]. 2003 Jun 1 [cited 2023 Dec 13];4(2):70–6. Available from: https://onlinelibrary.wiley.com/doi/full/10.1034/j.1399-5448.2003.00015.x
5. Stephenson MC, Leverton E, Khoo EYH, Poucher SM, Johansson L, Lockton JA, et al. Variability in fasting lipid and glycogen contents in hepatic and skeletal muscle tissue in subjects with and without type 2 diabetes: a 1H and 13C MRS study. NMR Biomed [Internet]. 2013 Nov [cited 2023 Nov 1];26(11):1518–26. Available from: https://pubmed.ncbi.nlm.nih.gov/23836451/

Evaluating the Stability and MRI Relaxation Properties of Alginate for Breast Phantom Development

Klara Mišak [1,2,3], Agnieszka Sierhej [2], Chris A Clark [2], Simon Walker-Samuel [1], and Matt T Cashmore [3]

[1] Centre for Computational Medicine, Division of Medicine, University College London [2] UCL Great Ormond Street Institute of Child Health [3] National Physical Laboratory, Teddington, UK

Purpose: Alginate hydrogels present potential for application in anthropomorphic tissue-mimicking phantoms due to their tuneable physical and magnetic properties [1]. Their capability to mimic tissue-relevant relaxation times makes them well-suited for applications in quantitative magnetic resonance imaging (qMRI), where inter-site reproducibility and consistency are essential for reliable biomarker validation and early cancer detection [2]. Despite their widespread use in biomedical applications [3], the long-term physical and functional stability of alginate-based phantoms needs to be fully characterized. This study aims to quantitatively assess the temporal stability of alginate breast phantoms by monitoring changes in MRI parameters, including longitudinal (T_1) and transverse (T_2) relaxation times, and RF field homogeneity, over an initial 28-day period. This work addresses the crucial need for standardized and reproducible qMRI calibration materials, especially in breast imaging applications, where reliable relaxation times reference values are needed for radiotherapy treatment planning and quantitative lesion assessment.

Figure 1: MR image of the phantom (TE = 7 and TR = 500 ms)

Methods: The prototype phantom consisted of twelve 15 mL Falcon tubes filled with 2% (w/v) alginate in saline (1.17% NaCl). To achieve target breast tissue relaxation times [4], two doping formulations were used: 0.42 mM $NiCl_2$ (for T_1 modulation) and 1.14 mM $MnCl_2$ (for T_2 contrast) to mimic fibroglandular tissue (FGT), and 3.10 mM $NiCl_2$ (T_1) and 1.13 mM $MnCl_2$ (T_2) to mimic adipose tissue characteristics. MRI data of the phantom (Fig. 1) were acquired on days 0, 14, and 28 using spin echo sequences (T_1: TR = 500–3500 ms, TE = 7 ms; T_2: TR = 500 ms, TE = 7–350 ms) on a 3 T Siemens Prisma. A freshly prepared phantom with the same composition was scanned at each timepoint to assess formulation reliability and temporal stability. Phantoms were equilibrated at scanner room temperature (19.2–20.2 °C) for at least 24 hours prior to imaging. Relaxation times were estimated using saturation recovery (T_1) and mono-exponential decay (T_2) models, with B_1 correction applied to account for RF inhomogeneity. Phantom reliability was assessed using the coefficient of variation (CV), whilst gel stability was evaluated using independent two-sample *t*-tests comparing days 0 and 28.

Results: Phantom reliability was high across sessions (days 0, 14, and 28), with T_1 and T_2 measurements demonstrating strong longitudinal consistency for both FGT- and adipose-mimicking phantoms (Fig. 2), particularly in the FGT phantoms (CV = 0.28%). Regarding phantom stability, a significant increase in T_1 was observed in adipose-mimicking phantoms ($p < 0.05$), while no significant change was detected in the FGT phantoms (Fig. 3). T_2 values declined in both phantom types (Δ = −10.44 ± 15.68% and −9.83 ± 12.67%), though these changes were not statistically significant.

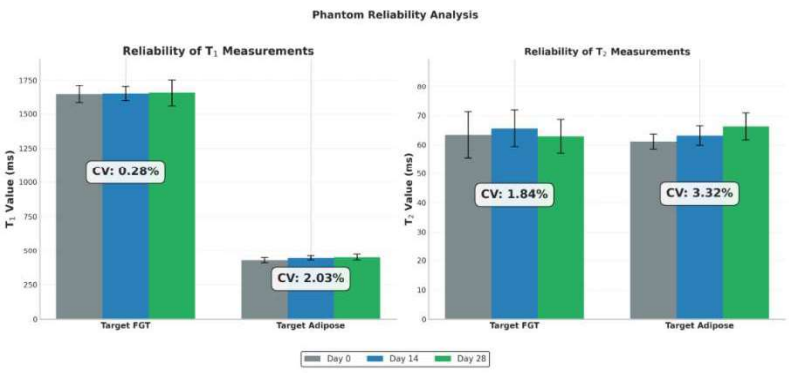

Figure 2: Reliability analysis of relaxation times for adipose and fibroglandular phantoms across three time points

Discussion: The phantoms demonstrated both reliability and gel stability, making them suitable tools for longitudinal qMRI assessment. The T_1 increase observed in adipose-mimicking phantoms likely reflects dopant redistribution or mild oxidation [5], whereas the greater stability (Δ = 6.66 ± 4.54%) of FGT-mimicking phantoms suggests that lower $NiCl_2$ content may inhibit such effects. T_2 reductions may reflect gel compaction or altered water mobility during aging [6], though high variability in standard deviation limits interpretation. The stable B_1 correction and narrow temperature range suggests that observed relaxation changes likely reflect intrinsic material behaviour rather than technical-induced variability. Despite relaxation times being systematically elevated (~13–15%) relative to literature

values (Fig. 4) [3], their internal consistency across phantom types supports their use in comparative or calibration-focused qMRI studies. These findings highlight the potential of alginate-based phantoms as low-cost, tuneable models for advancing qMRI, by providing a means to assess the reliability of MRI relaxation times that mimic those of breast tissue. However, the relatively short 28-day monitoring period may underestimate long-term degradation, and variability in T_2 measurements suggests that future work should investigate strategies to improve gel uniformity and chemical stability. Additionally, exploring a broader range of dopants and storage conditions could further refine phantom stability and extend applicability to a wider set of imaging contexts.

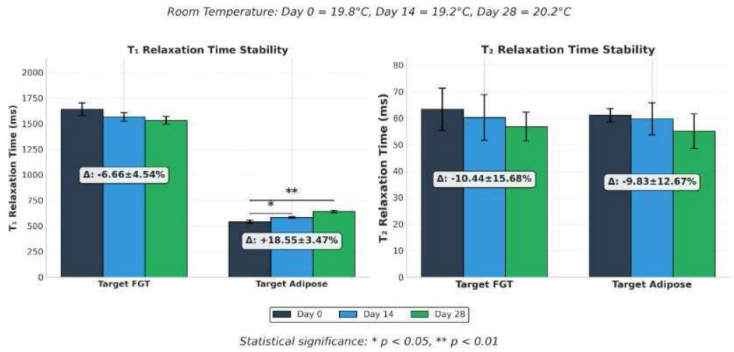

Figure 3: Longitudinal relaxation time analysis (gel stability) showing changes in T_1 and T_2 over 28 days, with statistical comparison between initial and final time points

Tissue Type	Metric	Phantom Value (ms)	Literature Value (ms)	% Difference ± SD
Target FGT	T_1	1643.1 ± 62.1	1444.8 ± 92.7	13.7% ± 7.4%
Target FGT	T_2	63.42 ± 7.89	54.36 ± 9.35	14.29% ± 3.03%
Target Adipose	T_1	428.38 ± 18.12	366.78 ± 7.75	15.50% ± 4.99%
Target Adipose	T_2	61.13 ± 2.53	52.96 ± 1.54	13.36% ± 0.68%

Figure 4: Deviation of phantom relaxation times from literature values for breast tissue relaxation properties

Conclusion: This study confirms that alginate-based breast phantoms provide reproducible qMRI measurements over short timescales while revealing sensitivity to material aging, particularly in T_1 behaviour. These results underscore the need for periodic reassessment of phantom properties in longitudinal or multi-centre qMRI studies to ensure sustained measurement reliability. Continued refinement of phantom composition will be key to enhancing long-term stability for use in standardizing breast imaging protocols and quantitative biomarker development.

References:

[1] Smith, A. M., & Senior, J. J. (2021). Alginate hydrogels with tunable properties. In A. Lavrentieva, I. Pepelanova, & D. Seliktar (Eds.), *Tunable hydrogels: Smart materials for biomedical applications* (Vol. 178, pp. 37–61). Springer. https://doi.org/10.1007/10_2020_161

[2] Keenan, K. E., Biller, J. R., Delfino, J. G., Boss, M. A., Does, M. D., Evelhoch, J. L., Griswold, M. A., Gunter, J. L., Hinks, R. S., Hoffman, S. W., Kim, G., Lattanzi, R., Li, X., Marinelli, L., Metzger, G. J., Mukherjee, P., Nordstrom, R. J., Peskin, A. P., Perez, E., … Sullivan, D. C. (2019). Recommendations towards standards for quantitative MRI (qMRI) and outstanding needs. *Journal of Magnetic Resonance Imaging, 49*(7), e26–e39. https://doi.org/10.1002/jmri.26598

[3] Lee, K. Y., & Mooney, D. J. (2012). Alginate: Properties and biomedical applications. *Progress in Polymer Science, 37*(1), 106–126. https://doi.org/10.1016/j.progpolymsci.2011.06.003

[4] Rakow-Penner, R., Daniel, B., Yu, H., Sawyer-Glover, A., & Glover, G. H. (2006). Relaxation times of breast tissue at 1.5T and 3T measured using IDEAL. *Journal of Magnetic Resonance Imaging, 23*(1), 87–91. https://doi.org/10.1002/jmri.20494

[5] Pan, D., Schmieder, A. H., Wickline, S. A., & Lanza, G. M. (2011). Manganese-based MRI contrast agents: Past, present and future. *Tetrahedron, 67*(44), 8431–8444. https://doi.org/10.1016/j.tet.2011.07.076

[6] Dhabalia, R., Kashikar, S. V., Parihar, P. S., & Mishra, G. V. (2024). Unveiling the intricacies: A comprehensive review of magnetic resonance imaging (MRI) assessment of T2-weighted hyperintensities in the neuroimaging landscape. *Cureus, 16*(2), e54808. https://doi.org/10.7759/cureus.54808

Enhanced SNR in Ultra-Low Field MRI using novel Composite Refocusing Pulses

Finn Aubrey Conboy [1,2] Samira Bouyagoub [1,2] Itamar Ronen [1,2] Ivor Simpson [3] Nicholas G Dowell [1,2]
[1] University of Sussex, Clinical Imaging Sciences Centre, Brighton, BN1 9RR, UK
[2] Brighton and Sussex Medical School, BSMS Teaching Building, Brighton, BN1 9PX, UK
[3] School of Engineering and Informatics, University of Sussex, BN1 9QJ, UK

Aim: To increase signal-to-noise ratio (SNR) in Ultra-Low Field (ULF) MRI by compensating for magnetic and radiofrequency field inhomogeneities (ΔB_0 and ΔB_1) using a novel composite refocusing pulse (CRP) developed through an optimization framework.

Introduction: ULF scanners offer greater accessibility, lower cost and mobility than high field (HF) systems. However, since NMR signal scales with magnetic field strength, ULF scanners suffer from reduced SNR, limiting clinical use. This low SNR is further reduced by two inhomogeneities: (1) ΔB_0, due to magnet design in ULF systems; (2) ΔB_1, highest in areas near or outside the coil. SNR can be improved by replacing square pulses with CRPs in a 50mT scanner [1]. CRPs, comprised multiple pulse segments with varying phase and flip angles, can offer greater insensitivity to ΔB_0 and ΔB_1 than square pulses. While CRPs are well-established in HF spectroscopy, their direct application to ULF is limited by longer pulse durations (t_{pulse}) leading to narrower excitation bandwidths. HF spectroscopy typically uses short pulses (10s of µs), whereas ULF systems use longer pulses (100s of µs).

$$FWHM = \frac{1.21}{t_{pulse}} \quad (1)$$

CRPs are often designed using average Hamiltonian theory to emulate RF pulses with improved insensitivity to ΔB_0 and ΔB_1. To simplify optimization, many CRPs use only 180° segments, since any odd number of elements - regardless of phase - produces a refocusing pulse. However, this approach results in longer pulses, limiting ULF performance (Eq.1). To address this, we developed a six-element CRP (6seg) not limited to 180° flip angles to enhance robustness to field inhomogeneities and so improve signal homogeneity and SNR across the imaging volume.

Method: Bloch equation simulations were used to evaluate magnetization evolution during pulse optimization. CRPs were optimized using scipy.minimize with the trust-constr method [2], a gradient-based optimizer that adjusts the flip angle and phase of each pulse element to minimize the loss function. This quantified deviation between final and target magnetization vectors. Each optimization iteration had two stages:

1. CRP was evaluated under ideal conditions (ΔB_0=0Hz and ΔB_1=100%) to determine whether it acted as an effective refocusing pulse. If the resulting loss exceeded 5%, the pulse was rejected by assigning a large penalty.
2. Pulses that passed the refocusing pulse check were evaluated for insensitivity by computing total loss across a range of ΔB_0 and ΔB_1 inhomogeneities, as given by:

$$\iota = \frac{1}{N_{combinations}} \sum_{i=1}^{N} \left\| M_{final}\left(\Delta B_0{}^{(i)}, \Delta B_1{}^{(i)}\right) - M_{target} \right\|^2 \quad (2)$$

(where $N_{combinations}$, M_{final} and M_{target} represent the number of combinations, final magnetization state and target state respectively). 6seg was optimized across 24 off-resonance frequencies (−2.5 to +2.5 kHz) and 8 B_1 scaling factors (0.8 to 1.2), resulting in 192 equally spaced combinations. The CRP, with the lowest loss function that satisfies the refocusing condition, was selected after several iterations. The final CRP included flip angles ranging from 75° to 180°, selected to improve robustness to ΔB_0 (Table 1).

Equipment: Data were collected using a 50mT MGNTQ scanner [3] equipped with a Halbach permanent magnet array and Kea2 Spectrometer with solenoid head coil using a Siemens spherical Phantom D170 (1.25 $NiSO_4 \cdot 6H_2O$ per 1000g distilled water).

Experiment: A 3D TSE pulse sequence was modified to incorporate the CRPs. Based on prior work, LT demonstrated highest SNR improvement and was used as a benchmark. We compared LT with 6seg, and a conventional square pulse. Phantom segmentation was manually performed using in-house

software.

Within the imaging volume, ΔB_0 reached up to 3 kHz off-resonance while the phantom extended beyond the coil leading to regions of high ΔB_1 (Fig. 1b). Signal drop-off was plotted along the phantom's superior–inferior axis (Fig. 2a).

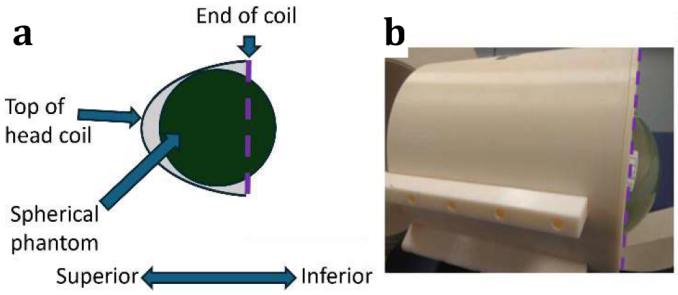

Designation	Composite Pulse (Flip angle° Phase°)	Reference
Square	$180°_{0°}$	N/A
6seg	$113°_{322°}\ 178°_{296°}\ 178°_{57°}\ 174°_{215°}\ 180°_{78°}\ 75°_{292°}$	This work
LT	$90°_{135°}\ 270°_{45°}\ 90°_{135°}$	[4]

Fig. 1. (a) labelled diagram of experiment. (b) Image showing phantom extruding from phantom.

Table 1: Refocusing pulses evaluated in this work

To assess voxel-wise signal distribution, a normalized histogram of phantom voxel intensities was generated (Fig.2b), showing probability density across the entire imaging volume showing signal intensity and homogeneity. To compare the pulses performance, the mean signal was used to show overall signal changes, and peak height was used to measure signal homogeneity in the histogram.

Results:

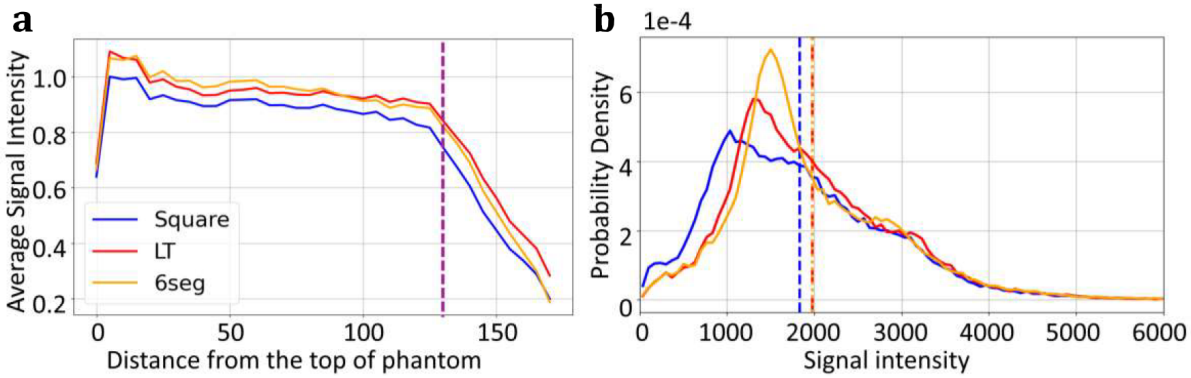

Fig.2. (a) Average signal of each slice against distance from top of the coil, normalized to peak square signal. Dashed line represents where the phantom leaves the coil. (b) Normalized histogram of signal intensity. TSE 3D sequence, with 150 bins, bin width of 67, TE of 20ms, Tr 500ms, ETL of 4, voxel size of 2x2x5mm. Lines represent mean signal intensity values of the histograms, Square=1834, LT=1975, 6seg=1977

LT and 6seg showed an 8% average signal increase over the square pulse across the entire phantom (Fig. 2b). However, 6seg showed greater insensitivity to ΔB_0 and ΔB_1 with peak height increases of 25% and 48% compared to LT and square. LT retained highest signal beyond the coil, with 10% increase over 6seg at 150 cm, indicating greater ΔB_1 insensitivity (Fig. 2a).

Discussion and Conclusion: We have shown that our approach, 6seg, can yield greater signal homogeneity for ULF MRI while maintaining increased signal of prior CRP, delivering superior signal homogeneity in the presence of ΔB_0 and ΔB_1, without extending scan time.

References:

[1] F. Aubrey Conboy et al, Improving SNR in areas of high inhomogeneity in Ultra-Low Field MRI using Composite Refocusing Pulses. Accepted for 41st ESMRMB. Marseille 2025

[2] P. Virtanen et al., SciPy 1.0: Fundamental Algorithms for Scientific Computing in Python, Nature Methods, vol. 17, pp. 261–272, 2020. DOI: 10.1038/s41592-019-0686-2

[3] Multiwave Imaging, Meet MGNTQ. Available at: https://multiwave.ch. Accessed 29/07/25

[4] R. Tycko, Broadband population inversion, Phys. Rev. Lett. 51 (1983) 775–77

MRI Fun Day: Pilot Study of a Paediatric-Focused Educational Event

Neslihan Isleyen[1], Laura Bortolotti[2], Adrian Tang[3], Joanne Smith[4] , Racheal Weithers[4], Mehvish Alavi[4]

[1]The Royal London Hospital, London, UK; [2]The University of Nottingham, UK; [3]The University of Manchester, UK; [4]South Tees Hospitals NHS Foundation Trust, Middlesbrough, UK

Introduction: MRI scans can trigger anxiety in paediatric patients due to loud noise, confined spaces, and unfamiliar environments, leading to motion artefacts, failed scans, and sedation-related risks [1–4]. The MRI Fun Day at James Cook University Hospital, supported by BIC- ISMRM, aimed to reduce scan anxiety and improve children's experience through play-based education [1–4].

Methods: The event included an inflatable mock scanner and interactive stations such as teddy bear scans, puzzles (**Figs 3 and 4**), roleplay, and colouring. Staff facilitated age-appropriate activities for children and parents prior to MRI appointments. Qualitative feedback was gathered from both groups (**Fig 1**). A clinical physicist captivated children with an interactive demonstration explaining MRI principles (**Fig 2**). Real brain scan images were displayed to spark curiosity and demystify the imaging process. A Spider-Man figure added a playful touch, helping children connect with the science in a fun, relatable way. The highlight for many was exploring the inflatable MRI scanner—an immersive, hands-on experience that allowed children to step inside a life-sized replica, easing anxiety and turning learning into adventure (**Fig 4**). Parental consent was obtained for use of all images.

Results: Eighteen children (aged 5–11) participated; 14 had scans the same day. All engaged with at least two activities, and all scanned successfully without sedation or early termination. Staff reported smoother handling and fewer motion artefacts (**Fig 6**). These findings support evidence linking patient-centred preparation with improved scan outcomes [1–3].

Discussion: MRI procedures can provoke anxiety due to noise, confinement, and unfamiliarity, often compromising image quality. Sedation or repeat imaging poses risks, especially for paediatric patients [3,4]. Literature highlights non-pharmacological strategies like behavioural preparation to improve compliance and scan success [1–4]. This initiative helped children build familiarity and control in a safe, non-clinical setting. Feedback suggested improved psychological readiness and perceptions of MRI—from intimidating to manageable and even fun. Results reflect broader evidence on the benefits of preparatory interventions [1–4], and demonstrate the potential of a scalable, low-cost model to enhance paediatric imaging care [4].

Conclusions: A play-based, educational approach can reduce anxiety, improve scan outcomes, and strengthen rapport with paediatric patients. Broader rollout is recommended to assess long-term effects on sedation rates, scan quality, and satisfaction [1–4].

Acknowledgements: We thank the British & Irish Chapter (BIC) ISMRM for their generous support.

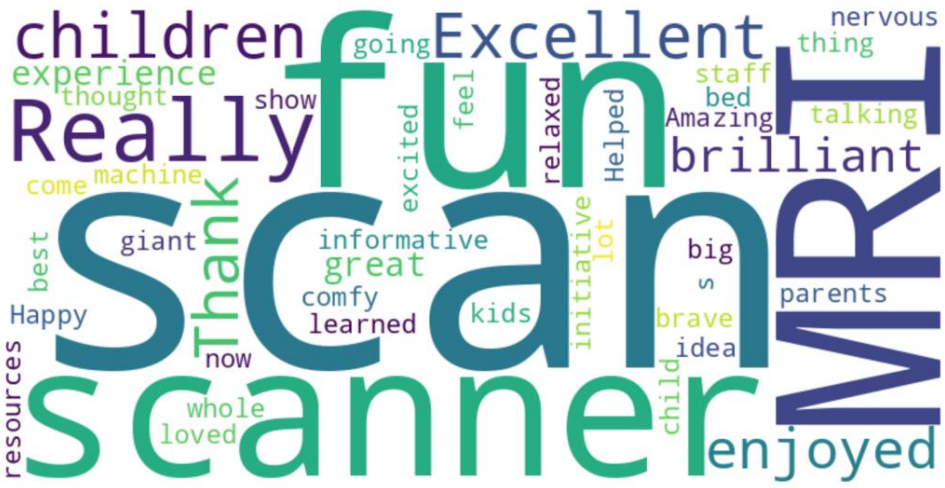

Fig 1

Fig 2

Fig 3

Fig 4

Fig 5

Fig 6

30

Imaging glucose uptake and lactate production in a chick CAM model of glioblastoma

Elisabeth N Gash[1], Jan Schulze1, Sarah E Barnett2, Mahon Maguire2, Mohesh Moothanchery2, Ian Scott3, Stephen Pickup4, Joseph Sacco1, Judy Coulson1, Sonia Rocha5, Harish Poptani1

[1]Molecular and Clinical Cancer Medicine, [2]Liverpool Shared Resource Facilities, [5]Biochemistry, University of Liverpool, [3]Walton Centre NHS Trust, Liverpool, [4]University of Pennsylvania, USA

IIntroduction: Glioblastoma (GBM) is an aggressive brain tumour characterised by extensive hypoxia and a metabolic shift towards glycolysis, contributing to treatment resistance. The chick chorioallantoic membrane (CAM) model is a valuable platform for studying tumour-host vascular interactions and is compatible with *in vivo* imaging. This study integrates [18F]FDG-PET and ^{1}H MRS to evaluate glucose uptake and lactate production in GBM-CAM xenografts and their association with hypoxia markers.

Methods: GBM xenografts were established by implanting 2×10^{6} U-251 cells onto the CAM at embryonic day 7 (E7). Tumours were imaged with [18F]FDG-PET on E12, followed by lactate MRS using image-selected in vivo spectroscopy (ISIS) and selective multiple quantum coherence (SelMQC) on E13–E14. 18 eggs were analysed with [18F]FDG-PET, and 13 survived to E13 for lactate MRS. Glucose uptake was quantified using the sum of the accumulated maximum standardized uptake values (SUVtotal), and lactate was assessed as lactate/water ratios (RelLac). A Pearson correlation was used to asses the correlation between SUVtotal and RelLac. Tumours were harvested for mRNA expression analysis and histological assessment (H&E and IHC staining).

Results: GBM xenografts exhibited increased expression of glycolytic genes GLUT1, PDK1, LDHA, and the proangiogenic marker VEGFA compared to U-251 cells *in vitro* (Figure 1A), indicating a metabolic shift towards glycolysis. [18F]FDG-PET detected glucose uptake in 94% (17/18) of tumours, while lactate MRS detected lactate in 69% (9/13). H&E staining revealed a highly cellular tumour morphology, and IHC showed strong CAIX staining (Figure 1B), a hypoxia marker localised to the tumour core. A significant negative correlation was observed between SUVtotal and RelLac ($R = -0.71$, $P = 0.033$) (Figure 2).

Discussion: The increased expression of glycolytic and proangiogenic genes suggests a metabolic adaptation of GBM cells upon implantation onto the CAM, perhaps occurring due to the hypoxic microenvironment. The negative correlation between FDG and lactate may suggest distinct spatial distributions of glucose uptake and lactate accumulation. Alternatively, this could be due to differences in glucose transporters (measured by PET) versus steady state lactate values (combination of production and clearance) measured by MRS. Given that lactate preferentially accumulates in necrotic, less cellular regions, whereas glucose uptake is associated with viable tumour tissue, these findings align with previous observations in patients and in rodent models. The presence of CAIX further supports the role of hypoxia in driving glycolytic metabolism. The negative correlation may warrant further investigation into vascularisation dynamics and lactate clearance mechanisms within the CAM model.

Conclusion: These findings demonstrate that GBM-CAM tumours are hypoxic and exhibit a metabolic shift to glycolysis. [18F]FDG-PET and lactate MRS provide complementary insights into tumour metabolism. Further studies on tumour-host vascular relationship are needed to better understand these metabolic changes within the tumour.

Meet the presenter bio (50 words)

I’m a final year PhD student investigating the role of hypoxia in GBM vasculature and glycolytic metabolism, two critical and highly connected facets of the tumour microenvironment. I’m based at University of Liverpool, Centre for Preclinical Imaging, where I investigate these features in a chick-CAM model using MRI, MRS and [18F]FDG-PET.

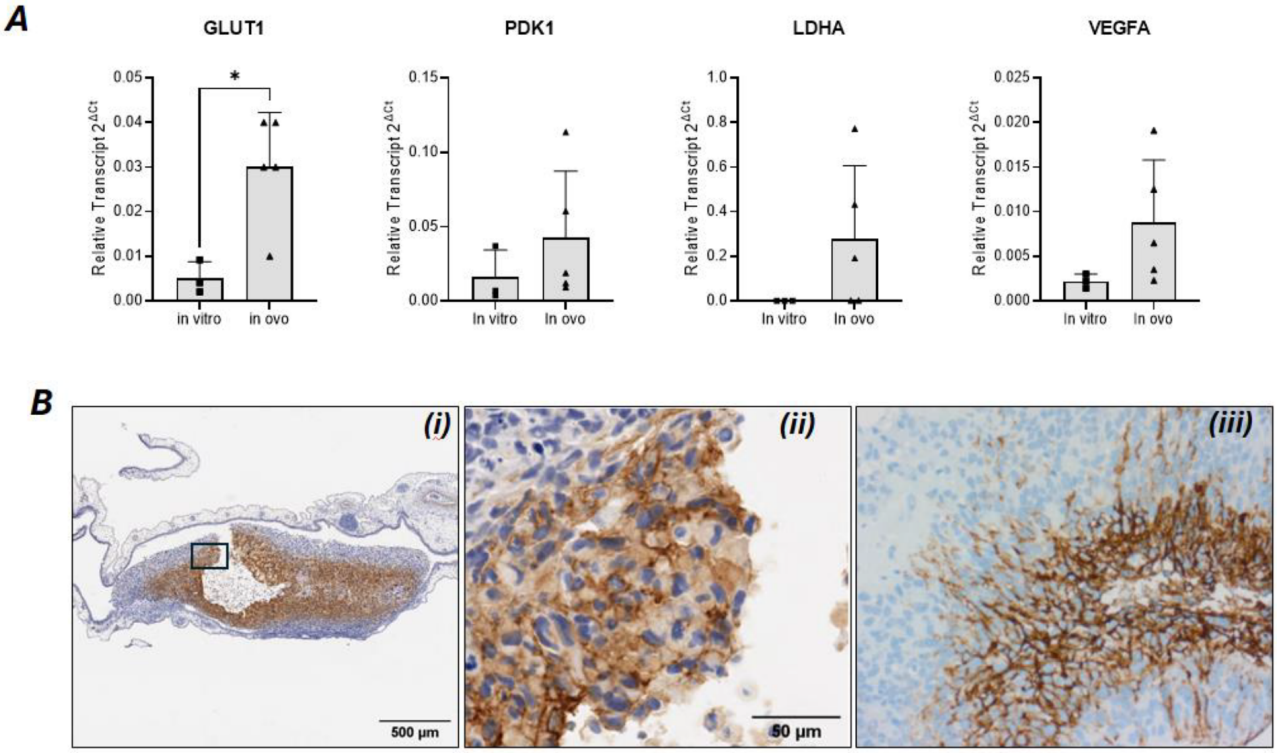

Figure 1. GBM-CAM xenografts are hypoxic and increase expression of genes involved in glycolytic metabolism. (A) GLUT1 involved in glucose transport; PDK1, phosphorylates pyruvate dehydrogenase for ubiquitination, preventing conversion of pyruvate to acetyl-coA; LDHA1, converts pyruvate to lactate; and VEGFA, promoting angiogenesis to restore oxygen and nutrient supply. (B) Representative image of strong CAIX staining in CAM tumour core, surrounding a necrotic core (500 µM) (i) and (50 µM)(ii). Patient GBM showing strong perinecrotic CAIX staining (X200), taken from Haapasalo et al., 2020 (iii).

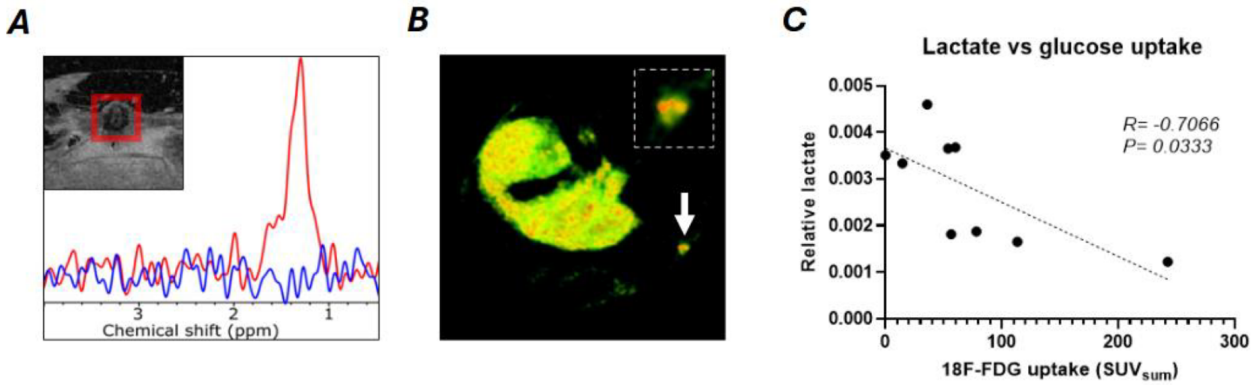

Figure 2. Lactate detection and [^{18}F]FDG uptake in GBM-CAM xenograft. (A) Representative image of voxel placement above the site of the tumour with red box denoting voxel placement and lactate peak at 1.3 ppm. (B) Uptake of [^{18}F]FDG into the xenograft after injection of 8 ±2 MBq [^{18}F]FDG into a large vessel on EDD13. (C) Strong negative correlation between SUVsum and relative lactate.

References:

Haapasalo, Joonas & Nordfors, Kristiina & Haapasalo, Hannu & Parkkila, Seppo. (2020). The expression of carbonic anhydrases II, IX and XII in brain tumors. Cancers. 12. 1723. 10.3390/cancers12071723.

Thank you

**On behalf of all the organisers,
thank you for participating in the BIC-ISMRM 2025 Annual Meeting in Brighton.**

We hope you have enjoyed your time with us.

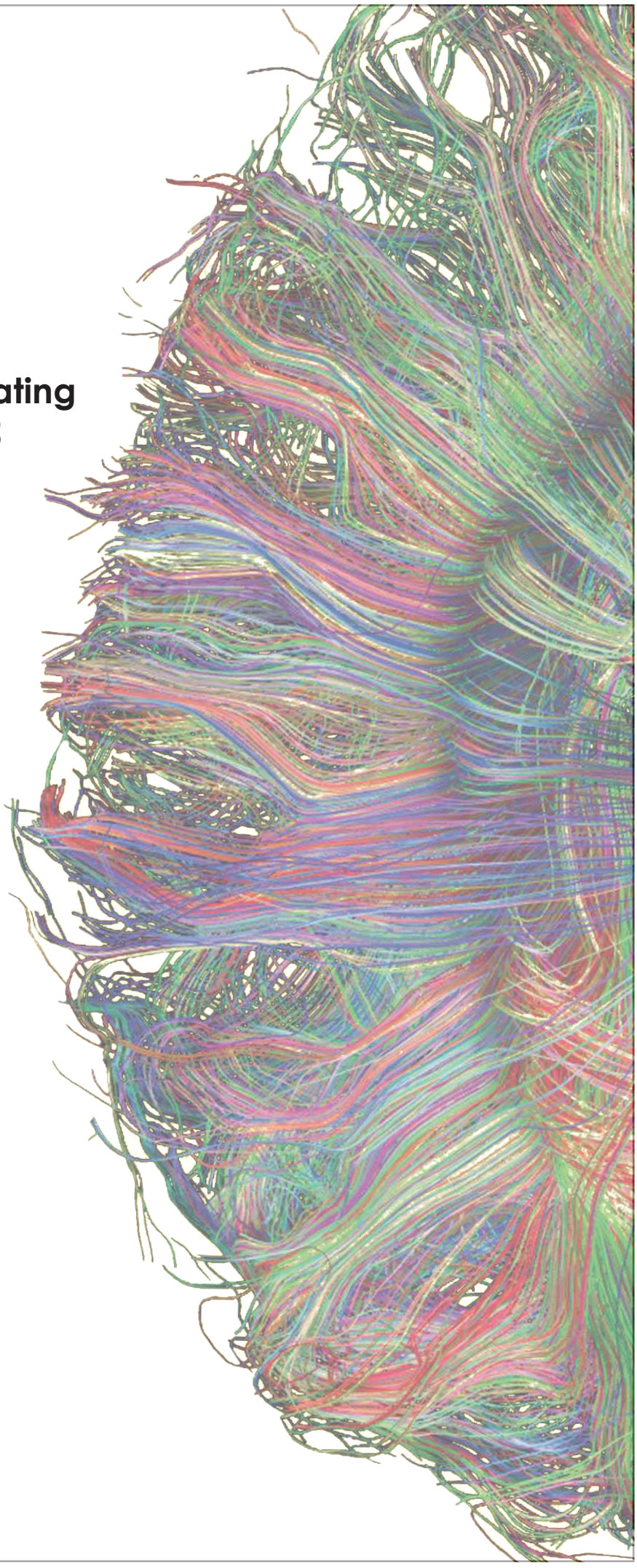

Brighton
ISMRM | British & Irish CHAPTER
2025